

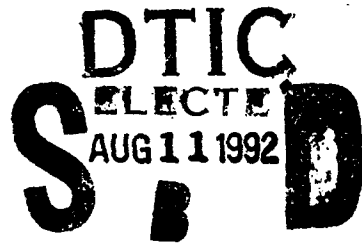
**AD-A253 975**



**Technical Report  
885**

2

# **Covalent Electron Transfer Theory of Superconductivity**



G.F. Dionne

19 June 1992

**Lincoln Laboratory**  
MASSACHUSETTS INSTITUTE OF TECHNOLOGY  
*LEXINGTON, MASSACHUSETTS*



Prepared for the Department of the Air Force under Contract F19628-90-C-0002.

Approved for public release; distribution is unlimited.

**92-21829**



02 8 6 002

This report is based on studies performed at Lincoln Laboratory, a center for research operated by Massachusetts Institute of Technology. The work was sponsored by the Department of the Air Force under Contract F19628-90-C-0002.

This report may be reproduced to satisfy needs of U.S. Government agencies.

The ESD Public Affairs Office has reviewed this report, and it is releasable to the National Technical Information Service, where it will be available to the general public, including foreign nationals.

This technical report has been reviewed and is approved for publication.

FOR THE COMMANDER

*Hugh L. Southall*

Hugh L. Southall, Lt. Col., USAF  
Chief, ESD Lincoln Laboratory Project Office

Non-Lincoln Recipients

PLEASE DO NOT RETURN

Permission is given to destroy this document  
when it is no longer needed.

**MASSACHUSETTS INSTITUTE OF TECHNOLOGY  
LINCOLN LABORATORY**

**COVALENT ELECTRON TRANSFER THEORY  
OF SUPERCONDUCTIVITY**

***G.F. DIONNE***  
***Group 61***

**TECHNICAL REPORT 885**

**19 JUNE 1992**

**Approved for public release; distribution is unlimited.**

**LEXINGTON**

**MASSACHUSETTS**

## ABSTRACT

Following a brief review of phenomenological origins, a comprehensive discussion of the physics and chemistry of superconducting metallic oxide systems is presented. The real-space covalent electron transfer (CET) theory, developed in 1987 after the discovery of high-temperature superconductivity (high- $T_c$ ) in cuprate systems, is based on the premise that superconductivity is created by spontaneous charge transfer through covalent bonds where large polarons are formed to compensate charge imbalances in mixed-valence molecular structures. Superconductivity is disrupted by the thermally activated mobility that causes normal-state conductivity. In this report, the CET theory is expanded to include a molecular-orbital analysis of the electron transfer probability (assumed to be unity in the original model). An examination of the local magnetic superexchange interactions between  $\text{Cu}^{2+}\text{-O}^{2-}\text{-Cu}^{2+}$  ions indicates that the onset of superconduction requires a breakdown in static antiferromagnetic order (the  $T_N, T_c = 0$  condition) to eliminate the exchange contribution to the polaron trap energy. This spin alignment frustration that was predicted in the 1987 version of this theory and later confirmed by several experimentalists is explained by the spontaneous action of mobile polaronic ions in zero-spin states. By comparing the covalent transfer (superconduction) and electron hopping (normal conduction) mechanisms, two important results are obtained. First, the thermal energy at the critical temperature ( $kT_c$ ) may be approximated by the hopping activation energy ( $E_{\text{hop}}$ ) magnified by the ratio of the supercarrier concentration ( $x$ ) at  $T = 0$  to the threshold concentration ( $x_t$ ) at  $T = T_c$ , i.e.,  $kT_c \approx E_{\text{hop}}(x/x_t)$ , where  $x_t \ll x$ . Second, a new two-fluid function is derived for the temperature-dependent population distribution between normal and superelectrons. From the fraction of carriers that is not thermally activated (hopping), condensation to the superconducting state occurs in the form of dynamic ferroelectricity with spin wave fluctuations along chains of ordered polaronic dipoles for which the condensation energy is directly proportional to the square of the supercarrier population. With this relation, it is then possible to derive direct expressions between the measurable superconduction parameters and the effective supercarrier density as functions of temperature. Based on these concepts, computed values of critical temperature, magnetic field, and supercurrent density, as well as specific heat, penetration depth, coherence length, and microwave surface resistance compare favorably with measured values, both in magnitude and as functions of temperature. The reported superconducting properties of the various high- $T_c$  systems are then examined in the context of this new model. To contrast with low- $T_c$  metals, the covalent transfer concept is applied qualitatively to systems with conduction electrons. Finally, the various topics are summarized and conclusions drawn concerning the limitations and applicability of superconduction phenomena, as interpreted by the CET theory.

## ACKNOWLEDGMENTS

The author recognizes contributions from the following members of the Lincoln Laboratory Analog Device Technology Group: Dr. A.C. Anderson, Dr. D.E. Oates, A.C. Westerheim, L.S. Yu-Jahnes, and Dr. R.S. Withers. Acknowledgments are also extended to Prof. J.M. Honig of Purdue University for providing information relating to the nickelate superconductors, Prof. S.M. Anlage of the University of Maryland for providing data from penetration depth measurements, and Dr. B.S. Ahern of the Rome Laboratory at L.G. Hanscom Air Force Base for general literature support. Finally, the author is grateful to Dr. G.N. Tsandoulas, D.H. Temme, and V. Vitto of Lincoln Laboratory for their encouragement throughout the course of this work.

DTIC QUALITY INSPECTED 8

<b>Accession For</b>	
NTIS GRA&I	<input checked="" type="checkbox"/>
DTIC TAB	<input type="checkbox"/>
Unannounced	<input type="checkbox"/>
Justification	
By	
Distribution/	
Availability Codes	
Dist	Avail and/or Special
A-1	

## TABLE OF CONTENTS

Abstract	iii
Acknowledgments	v
List of Illustrations	ix
List of Tables	xv
1. INTRODUCTION	1
2. PHENOMENOLOGICAL FOUNDATIONS	5
2.1 The London Equations	5
2.2 The Macroscopic Molecule Concept	7
2.3 Nonlocal Considerations	8
3. THERMALLY ACTIVATED SEMICONDUCTION	11
3.1 Mixed-Valence Orbital Carriers	11
3.2 Electrostatic/Elastic Trap Energy	15
3.3 Magnetic Exchange Trap Energy	17
3.4 Magnetic Frustration and Zero-Spin Polarons	22
3.5 Superconduction and Zero-Spin Polarons	26
4. MOLECULAR ORBITAL CONDUCTION	31
4.1 Covalent Transfer versus Thermal Hopping	31
4.2 Quantum Mechanical Transfer Efficiency	36
4.3 Large-Polaron Array Concept	39
4.4 Real-Space Electron Pairing and Antiferromagnetism	39
4.5 Polaron Carrier Statistics	41
5. SUPERCONDUCTION ELECTRICAL PHENOMENA	43
5.1 Critical Temperature and Polaron Concentration	43
5.2 Resistivity versus Temperature and Composition	52
5.3 Resistivity of Multiphase Superconductors	58
5.4 Microwave Surface Resistance $R_s$	62
6. SUPERCURRENTS AND MAGNETIC PHENOMENA	65
6.1 Supercurrent Formation and Effective Supercarrier Density $n_s^e$	65
6.2 Condensation Energy $\Delta G$	69

## TABLE OF CONTENTS (Continued)

6.3 London Penetration Depth $\lambda_L$	70
6.4 Thermodynamic Critical Magnetic Field $H_c$	73
6.5 Specific Heat Discontinuity $\Delta C$	75
6.6 Critical Current Density $i_c$	77
6.7 Intrinsic Coherence Length $\xi_0$	81
6.8 Type-II Superconductors	84
6.9 Magnetic Levitation	86
 7. LARGE-POLARON SUPERCONDUCTING SYSTEMS	 89
7.1 Systems with $3d-2p\sigma$ Bonds	90
7.2 Systems with $6s, 6p-2p\sigma$ Bonds	101
7.3 Systems with $3d-2p\pi$ or $3d-3d\sigma$ Bonds	103
 8. COVALENT ELECTRON TRANSFER IN METALS	 107
8.1 The Goodenough $b$ Parameter Model	107
8.2 Real-Space Pairing in Metals	110
8.3 $T_c$ and the $W$ Parameter	112
8.4 The Matthias Model and the Periodic Table	113
8.5 The Isotope Effect	116
8.6 Superconducting Compounds with $c \approx 0$	118
8.7 Comparison of Metal and Oxide Superconductors	119
 9. SUMMARY AND CONCLUSIONS	 123
 APPENDIX A. SELF-CONSISTENT MOLECULAR-ORBITAL THEORY	 129
APPENDIX B. THE $\text{Cu}^{2+}\text{O}^{2-}$ MOLECULE	133
APPENDIX C. THE FOUR-BODY $(\text{Cu}^{2+}\text{O}^{2-}) - (\text{Cu}^{2+}\text{O}^{2-})$ LINEAR MOLECULE	139
APPENDIX D. OXYGEN-COORDINATION INFLUENCE ON $E_{\text{hop}}$	143
APPENDIX E. EFFECTIVE AREA OF TYPE-I MAGNETIC FIELD AND SUPERCURRENT	145
APPENDIX F. THE LOW-SPIN STATES OF Ni CATIONS	147
APPENDIX G. EFFECTIVE DIELECTRIC CONSTANT OF Sn	151
 REFERENCES	 153

## LIST OF ILLUSTRATIONS

Figure No.		Page
1	Perpendicular relations between current and magnetic field for superconducting cylinders of large and small diameters.	6
2	Two types of charge transfer in oxides.	12
3	Origin of polarons in mixed-valence cation systems.	14
4	$E_{\text{hop}}$ versus polaron density for monoxides of Mn, Co, Ni, and Cu.	17
5	Schematic model of elastic and magnetic contributions to the hopping electron activation energy barrier.	20
6	Two-dimensional model of the intrasublattice passage of a "hole" in an antiferromagnetically ordered lattice.	21
7	Growth of magnetic frustration from (a) local spin canting caused by magnetic dilution to (b) regions of complete disorder defined by the boundaries of itinerant $S_p = 0$ polarons.	24
8	Cation sublattice projection of $\text{La}_{2-x}\text{Sr}_x\text{CuO}_4$ viewed along $c$ axis, with La and Cu ions in alternate planes.	25
9	Model curve of the decrease in activation energy with the increase in polaron concentration.	26
10	Influence of rare-earth (RE) magnetism on the semiconduction (activation energies) of an $(\text{RE})_2\text{CuO}_4$ series.	27
11	Schematic diagram of $S = 1/2 \rightarrow S = 0$ transfers among $3d^n$ group.	29
12	Experimental verification of the magnetic frustration requirement prior to the onset of superconductivity in $\text{La}_{2-x}\text{Sr}_x\text{CuO}_4$ and $\text{YBa}_2\text{Cu}_3\text{O}_y$ systems.	30
13	Essential definition of two alternative conduction mechanisms.	32
14	Conceptual description of the formation of a pair of molecular orbital states, and the growth of energy bands from the transfer integral energy $h$ .	33
15	Pictorial definition of small polaron limit, showing how covalent stabilization overcomes local polaron trap energy ( $h \geq E_{\text{hop}}$ ).	34
16	Two-dimensional description of large polaron cells amidst fixed polaron ionic sources.	35
17	Comparison of small and large polaron energies.	37
18	One-dimensional model of a large polaron chain indicating the merger of carrier density functions $ \psi_j ^2$ to establish a continuous molecular orbital state.	38
19	Large-polaron Coulomb potential $\Delta E_{1,\gamma}$ versus $\gamma$ for different reduced polaron source separations $\Gamma$ for $K = 16$ .	45



## LIST OF ILLUSTRATIONS (Continued)

Figure No.		Page
20	Transfer efficiency $\eta$ as a function of $\Gamma/2$ , for $K = 16$ and $b = 0.43$ eV.	46
21	Critical temperature $T_c$ versus $x$ for $\text{La}_{2-x}\text{Sr}_x\text{CuO}_4$ , $\text{La}_{2-x}\text{Sr}_x\text{CaCu}_2\text{O}_6$ , and $\text{YBa}_2\text{Cu}_3\text{O}_y$ (where $y$ has been converted to $x$ using the linear model $y = 0.25x - 1.5$ ).	49
22	Supercarrier concentration $x_s(0)$ versus $x$ for the $\text{La}_{2-x}\text{Sr}_x\text{CuO}_4$ and $\text{YBa}_2\text{Cu}_3\text{O}_y$ systems of Figure 21.	50
23	Comparison of theory with $T_c$ versus $y$ data from $\text{YBa}_2\text{Cu}_3\text{O}_y$ .	51
24	Projected $T_c$ versus $x$ curves based on CET theory over the range of $0 \leq \beta \leq 2$ for individual carriers and $0 \leq \beta \leq 1$ for pairs.	52
25	Generic plots of $\rho$ versus $T$ for $E_{\text{hop}} = 0$ and 10 meV, defining relations for $T_{\text{min}}$ , asymptote slope $\partial\rho/\partial T _{\infty}$ , and intercept $\rho_i$ .	54
26	Simple model of the segregation of superconducting and normal regions for the purpose of estimating electrical resistivity above the transition temperature.	54
27	Resistivity versus temperature for $0 \leq \eta P \leq 1$ , showing the influence of covalent transfer on the lowering of $T_{\text{min}}$ and $\rho_i$ .	56
28	Comparison of theory with experiment for the $\text{La}_{2-x}\text{Sr}_x\text{CuO}_4$ system.	57
29	Comparison of theory with experiment for bulk polycrystalline and oriented film $\text{YBa}_2\text{Cu}_3\text{O}_7$ .	57
30	Proposed phase diagram for the $\text{La}_{2-x}\text{Sr}_x\text{CuO}_4$ system.	58
31	Cross section of a multiphase insulator/superconductor network.	59
32	Sample resistivity versus temperature plots of a two-phase $\text{YBa}_2\text{Cu}_3\text{O}_y$ system over the range $0 \leq f \leq 1$ .	60
33	Theory fit to experiment for $\text{Pb}_2\text{Sr}_2(\text{Dy,Ca})\text{Cu}_3\text{O}_8$ single-crystal ( $f = 0.65$ ) and $\text{Pb}_2\text{Sr}_2(\text{Y,Ca})\text{Cu}_3\text{O}_8$ polycrystalline ( $f = 0.98$ ) specimens.	60
34	Curves of Figure 32, with $\rho(T)$ normalized to $\rho(300)$ .	61
35	$\rho(T)/\rho(300)$ versus $T$ curves for the $(\text{Tl}_{0.5}\text{Bi}_{0.5})(\text{Ca}_{1-z}\text{Y}_z)\text{Sr}_2\text{Cu}_2\text{O}_y$ family of mixed-phase superconductors.	61
36	Comparison of CET calculations and measurements of microwave surface resistance $R_s$ versus $t$ for films of $\text{YBa}_2\text{Cu}_3\text{O}_7/\text{LaAlO}_3$ and Nb.	63
37	Two-dimensional model of polaron condensation to superconducting state.	66
38	Superconducting polaron distribution and probability contour of the carrier density $n_s =  \psi_s ^2$ .	66

## LIST OF ILLUSTRATIONS (Continued)

Figure No.		Page
39	Two-dimensional model of partially condensed supercurrent.	67
40	Pictorial representation of the simultaneous decrease of $n_s^e(T)$ and the growth of $n_l(T)$ as $T \rightarrow T_c$ , where $n_s$ and $n_l$ converge to establish the threshold density for the onset of superconductivity.	68
41	Comparison of $n_s^e(t)/n_s^e(0)$ versus $t$ for $W = 0.5, 1$ , and $1.76$ with the BCS function and with the empirical $(1 - t^4)$ two-fluid function.	71
42	Comparison of calculated $\ln[\lambda_L(t)/\lambda_L(0) - 1]$ versus $t^{-1}$ curves with the YBa <sub>2</sub> Cu <sub>3</sub> O <sub>7</sub> /LaAlO <sub>3</sub> and YBa <sub>2</sub> Cu <sub>3</sub> O <sub>7</sub> /MgO film data for $W = 0.5$ and $1$ .	72
43	Comparison of calculated resonance frequency $f_o$ versus $t$ with YBa <sub>2</sub> Cu <sub>3</sub> O <sub>7</sub> /LaAlO <sub>3</sub> stripline resonator data for $W = 0.5, 1$ , and $1.76$ .	73
44	Change in Gibbs free energy as a function of $H$ , indicating a decreasing energy available for conversion to the kinetic energy of supercurrent as $H \rightarrow H_c$ .	74
45	Comparison of $H_c(t)/H_c(0)$ versus $t$ for $W = 1.76, 2$ , and the thermodynamic $(1 - t^2)$ function.	76
46	Generic curves of $\Delta C(t)/\Delta C(1)$ versus $t$ for $W = 1$ and $1.76$ , compared with data from Sn and Ga.	78
47	Normalized critical current density $i_c(t)/i_c(0)$ versus $t$ for $W = 0.5, 1$ , and $2$ .	79
48	CET universal plot of $i_c(t)/i_c(0)$ for the bulk case with $W = 1$ .	80
49	Variation of $H$ and $\psi_s$ at the fluxoid/superconductor interface for $\kappa \ll 1$ (type I) and $\kappa \gg 1$ (type II).	85
50	CET calculated curve of $H_{c2}(t)/H_{c2}(0)$ versus $t$ for $W = 0.8$ .	85
51	Diagrammatic representation of the Meissner flux expulsion/levitation effect from induced diamagnetism in a superconductor.	87
52	Generic MO energy level diagram for a $d^0$ cation in an oxygen octahedral complex.	89
53	Band model approximation of the MO states of a Cu perovskite, indicating a partially filled antibonding band.	90
54	Crystal-field diagrams for the $d^8$ low-spin ( $S = 0$ ) state: (a) free ion level as zero-energy reference and (b) least stable $d_{x^2-y^2}$ level as reference.	92
55	MO diagram for a tetragonally ( $D_{4h}$ ) distorted CuO <sub>6</sub> complex.	93
56	MO diagram for a square planar ( $C_{2h}$ ) CuO <sub>4</sub> complex.	94
57	$p$ -type $3d_{x^2-y^2}-2p_y\sigma$ Cu <sup>2+</sup> -O-Cu <sup>3+</sup> covalent transfer in 180-deg perovskite bond geometry for $d^9 \rightarrow d^8$ (low-spin).	95

## LIST OF ILLUSTRATIONS (Continued)

Figure No.		Page
58	Ordered A-layer structure of $\text{YBa}_2\text{Cu}_3\text{O}_y$ , showing breakdown of $\text{CuO}_6$ complexes as $y$ decreases from 9 (hypothetical in this case).	96
59	Proposed linear valence model of Cu(1) and Cu(2) as a function of the oxygen content variation and distribution depicted in Figure 58.	97
60	Nominal Cu valence as determined from linear model of Figure 59 compared with valence bond sum analysis for $\text{YBa}_2\text{Cu}_3\text{O}_v$ .	98
61	$n$ -type $3d_{x^2-y^2}-2p_y\sigma$ $\text{Cu}^{1+}$ -O- $\text{Cu}^{2+}$ covalent transfer in 180-deg perovskite bond geometry for $d^{10} \rightarrow d^9$ .	100
62	$n$ -type $3d_{z^2}-2p_y\sigma$ $\text{Ni}^{2+}$ -O- $\text{Ni}^{3+}$ covalent transfer in 180-deg perovskite bond geometry for $d^8(\text{low spin}) \rightarrow d^7(\text{low spin})$ .	101
63	MO diagram for a $\text{Bi}^{4+}$ , $\text{Pb}^{3+}$ in an octahedral $\text{O}^{2-}_6$ complex.	102
64	Covalent transfer paths for $t_{2g}$ -occupied cations.	104
65	MO diagram for the octahedral $\text{Ti}^{3+}\text{O}^{2-}_6$ complex $t_{2g}-2p\pi$ states.	105
66	Variation of resistivity minimum as a function of $E_{\text{hop}}$ .	108
67	Energy band diagram based on Goodenough's $c = 0$ case of excited charge transfer ( $\Delta U \neq 0$ ).	109
68	Conceptual model of the condensation of virtual dipole with $S = 0$ sites.	111
69	$W$ parameter as a function of $x_i/x_{\text{eff}}$ with regimes of oxides and metals indicated. Note that linear approximation may apply only to oxides.	113
70	Matthias empirical function $F(n)$ relating $T_c$ to the average number $n$ of valence electrons per atom.	114
71	Superconducting elements in the periodic table.	115
72	Dipole arrangements before superconduction condensation.	120
73	Temperature dependence of supercarrier density for values of dispersal parameter.	122
74	Partial historical summary of superconductivity theory development.	123
A-1	Definitions of MO bonding $\Lambda_-$ and antibonding $\Lambda_+$ states.	129
B-1	Crystal-field and covalent contributions to the semiempirical $10 Dq$ splitting between $t_{2g}$ and $e_g$ bands.	134
B-2	$\text{CuO}$ molecule approximation to the complete lattice energy $E_{\text{latt}} \approx -43$ eV, using a Madelung constant $M \approx 1.5$ to represent the effective electrostatic fields that determine the respective cation and anion energies.	134

## LIST OF ILLUSTRATIONS (Continued)

Figure No.		Page
B-3	Born-Mayer function for CuO, indicating corrected Coulomb attraction curve of Madelung energy to fit the $E_{\text{latt}} \approx -43$ eV result.	135
B-4	Composite energy level diagram for CuO model, combining lattice energy estimates, point-charge crystal field splittings, and MO splittings.	136
C-1	CuO-CuO two-molecule chain.	140
D-1	Growth of $e_g$ doublet splitting as the tetragonal crystal field component increases through $D_{4h} \rightarrow C_{4v} \rightarrow C_{2h}$ to provide stabilization for the $d^8$ low-spin state.	144
E-1	Effective flux penetration regions for a rectangular cross-section model.	145
F-1	Ground state crystal-field orbital occupancy diagrams for $d^7$ and $d^8$ spin states.	148
F-2	Empirical fit of theory to data indicating dual activation energies of $\text{Li}_x\text{Ni}_{1-x}\text{O}$ system.	149
F-3	Effects of Jahn-Teller distortion of $\text{Ni}^{3+}$ (low spin) octahedral complex.	150

## LIST OF TABLES

Table No.		Page
1	Polaron Electrostatic/Elastic Trap Parameters	16
2	Octahedral-Site $d^n$ Superexchange Couplings for 180-deg Bonds (High Spin)	18
3	Octahedral-Site $d^n$ Superexchange Couplings for 180-deg Bonds (Low Spin)	19
4	Magnetic Trap Energies $E_{\text{mag}}$ for $z = 6$	23
5	Zero-Spin Polarons for Covalent Transfer	28
6	Superconductor Parameter Values and Dependence on Carrier Density	87
7	Cu Perovskite Superconduction Parameters	99
8	Isotope Effect in Superconductors	116
9	Dielectric Data for Ionic Compounds	118
10	Qualitative Comparison of Superconduction Parameters	121
11	Superconduction Pairing Arrangements	127
B-1	(CuO) <sup>+</sup> Ionic Stabilization Energies	138

## 1. INTRODUCTION

In a recent study of high-temperature superconductivity in transition-metal oxides [1], a theory that originated from the electrical conduction in the normal state was developed to interpret the reported superconduction phenomena as functions of temperature and chemical composition [2–6]. The motivation for this first exercise grew from the author's familiarity with the behavior of inhomogeneous and magnetically dilute ferrimagnetic oxides, to which the newly discovered superconducting perovskites bear a strong resemblance, through frustration of long-range magnetic order from spin canting and electron conduction associated with mixed cation valence. In contrast to the microscopically uniform structure of elemental superconductors, which can be analyzed by standard periodic-lattice band theory, the complex multication perovskites are not only superconductors in spite of their inhomogeneities, but because of them. Another marked difference from the low temperature systems is that the carriers are not drawn from a free electron gas, but rather exist as orbitally bound electrons with transport determined in its simplest form by the thermally activated charge transfer process called hopping. Consequently, the covalent chemical bond, so often ignored in the physics of metals, emerged as the most probable avenue of electron transport in accord with the macroscopic molecule concept that flows from the phenomenology of the London theory.

To account for the observed effects of systematic chemical substitutions in the oxide compounds, the problems had to be worked out in real space. In contrast to the conventional many-body approach, the charge carriers were treated as isolated polarons created by the specific nature of the formal ionic valence states. The theory, therefore, began with the following premise: If electrical resistance results from collisions of free electrons with phonons, then superconduction does not involve free electrons, but rather valence electrons bound in orbital states and affected by phonons indirectly through a statistically limited activation process. As a result, the occurrence of the superconducting state over the normal state would arise from competition between two conduction mechanisms, (1) transfer of covalent electrons through orbital overlaps that create a stabilization energy proportional to the transfer integral  $b$ , independent of electron-lattice coupling, and (2) electron hopping limited by an activation energy  $E_{\text{hop}}$ . Because the spatial order of the electrons in the superconducting state is destroyed by random thermally activated hopping, therefore, an analysis of the critical temperature  $T_c$  revealed a direct dependence on the magnitude of  $E_{\text{hop}}$ ; because the superconducting state evolves from orbital transfer through spatially ordered mobile polarons formed from mixed-valence ions occupying similar lattice sites, dispersal of polaron sources (fixed-valence cations and/or anion vacancies) was shown to have an important influence on  $T_c$ .

Covalent conduction can emerge from the notion of a Mott insulator, where the overlapping of localized states causes the removal of energy gaps to form a collective electron system. This concept led to Goodenough's model [7] of orbital interaction that included both single and mixed valences, in which the magnitude of the covalent transfer integral  $b$  was used as a measure of the relative degree of localized and collective conduction likely for a particular system. In the initial version of the covalent electron transfer (CET) theory [1], the focus was on the mixed-valence case, for which a phenomenological theory derived from the above concepts was applied to critical temperature and normal resistivity data of the

$\text{La}_{2-x}\text{Sr}_x\text{CuO}_4$ ,  $\text{YBa}_2\text{Cu}_3\text{O}_y$ , and  $\text{Bi}_2\text{Sr}_2\text{CaCu}_2\text{O}_8$  perovskite-related systems that involve  $\text{Cu}^{2+}\text{-O}^{2-}\text{-Cu}^{3+}$  (low-spin,  $S = 0$ ) cation-anion-cation transfers in 180-deg configurations.

For the likely case of antiferromagnetic coupling, electron hopping occurs between sites of the same sublattice, i.e., hops of two metal-oxygen bond lengths to satisfy the selection rule  $\Delta S = 0$  of maintaining parallel spin alignments; for CET, adjustments in local spin directions (causing spin wave fluctuations) require double electron transfers that represent electron pairing in real space. In practical terms, the effect of this pairing would be to double the size of the smallest current entity, a result that would account for the factor of 2 that appears to modify the electronic charge in flux quantization and quasi-particle tunneling experiments. Apart from the Bardeen-Cooper-Schrieffer (BCS) theory requirement [8] of  $k$ -space pair correlation dependence on phonons, both theories are similar in their relation to lattice thermal energy; the BCS theory is based on pairs that condense into an ordered superconducting state below the thermal energy of a threshold "gap," while the supercarriers of the CET correlate for thermal energies less than the "trap" energy ( $E_{\text{hop}}$ ). There is no requirement for phonons to exist as  $T \rightarrow 0$  K in the CET theory.

In this report, the original model that was developed from the covalent transfer concept is first refined and then applied to interpret a broader spectrum of superconductor behavior. Initially, traditional superconduction phenomenology relevant to the new theory is reviewed in Section 2. For testing compatibility with the CET theory, the London theory is examined in the context of giant molecular wavefunctions that automatically result from the requirement of spatially ordered carriers (the classical basis for the coherent wavefunction concept of a boson fluid used in quantum mechanical theory).

From analyses of the magnetic couplings in Section 3, the main contribution to  $E_{\text{hop}}$  is attributed to antiferromagnetic exchange, which becomes diluted with increasing density of zero-spin polarons, leaving only the small electrostatic contribution associated with the local electrostatic/elastic distortion. For this reason, superconduction arises from an ionic/covalent bonding duality. With only ionic bonding, there is no covalent transfer; with both types of bonding, hopping and covalent transfer coexist, and supercurrents can form where the probability of covalent transfer reaches a minimum threshold.

In Section 4 the original crystal-field approach that was applied to the layered cuprates is placed in the more general context of molecular-orbital (MO) theory that allows the orbital transfer efficiency to be defined in quantum mechanical terms. With the conduction perceived as originating from isolated dipoles, e.g.,  $(\text{LaSr})^--(\text{CuO})^+$ , the  $(\text{CuO})^+$  molecular ion becomes the mobile polaron in  $p$ -type compositions. To this end, a calculation based on self-consistent perturbation theory is carried out to determine the transfer wavefunction and to arrive at an estimate of the orbital transfer integral energy  $b$  for the  $\text{CuO-CuO}$  molecule. For the lattice energy parameters chosen in the calculation, the MO state in which the "hole" carrier would reside is dominated by the  $\text{Cu } d_{x^2-y^2}$  orbital, and the polaron would be mainly  $\text{Cu}^{3+}\text{O}^{2-}$ , with  $\text{Cu}^{3+}$  in a low-spin  $S = 0$  state. A different set of lattice energies could place the hole in the oxygen lattice, a peroxide polaron  $\text{Cu}^{2+}\text{O}^{1-}$ , with the  $S = 1/2$  spins of both  $\text{Cu}^{2+}(\uparrow)$  and  $\text{O}^{1-}(\downarrow)$  in opposition to form a net  $S = 0$ .

In Section 5 the effects of the  $b$ -dependent transfer efficiency and large-polaron cell radii are then woven into the original phenomenological model used to compute critical temperature as functions of  $E_{\text{hop}}$  and effective polaron density. The parameter values determined by matching theory to experiment

are then used to compute (as functions of temperature) the normal electrical conductivity of multiphase superconductors and the microwave surface resistance of high quality superconducting films.

Because the percolation of polaron cells is a necessary condition for superconduction in Section 6, the condensation to the superconducting state is defined as the alignment of polaron dipoles into dynamic chains in which the Gibbs free energy is converted to the energy of the supercurrent. The dipolar condensation is analogous to the spontaneous occurrence of ferroelectricity (or ferromagnetism), except that energy release associated with electrocaloric or magnetocaloric effects is converted into kinetic energy — dynamic ferroelectricity with associated spin waves. Based on comparisons with reported experimental findings, all specific results from this work are shown to be dependent on the density of supercarriers, including the derivation of expressions for critical magnetic field and current; their variation with temperature, including their favorable comparison with experiment; the determination of coherence lengths and penetration depths and their relation to each other; the theory of type-II superconductors, including an examination of the source and rigidity of the fluxoid lattice; and the mechanical aspects of the Meissner flux-exclusion phenomenon.

On the basis of these theory refinements, the properties of high temperature superconducting perovskites are examined in Section 7 through comparisons with experimental results. The discussion of orbital transfer superconduction is also extended to include lower temperature oxide superconductors, including  $\text{LiTi}_2\text{O}_4$  spinel and the nontransition-metal Bi and Pb perovskites (e.g.,  $\text{BaBi}_x\text{Pb}_{1-x}\text{O}_3$ ).

Section 8 examines the implications of the CET mechanism in the case of metals based on the speculation that before superconduction can occur, they “condense” to an insulating state through delocalized electrons returning to their parent ions. In this context, some standard topics are discussed, such as the isotope effect and the correlation of superconduction properties to element groups of the periodic table. The origins of superconductivity in metals and oxides are compared with the focus on the reasons for the exaggerated  $T_c$  values of the polaronic cuprates. Finally, a figure-of-merit temperature that is proportional to the activation energy is proposed as a basis for comparing the effectiveness of superconductors.

In Section 9, the essential features of the CET theory are summarized and conclusions are made. The fundamental tenet is repeated: Superconductivity is a natural state at low temperatures; the thermal activation that destroys the ordered carrier state becomes the source of the mobility-limited carriers of the normal conductivity at higher temperatures.

Since the original report [1] discussing CET was published, a number of theoretical results from that work have been confirmed by experiment. These include:

- The prediction that high- $T_c$  superconductivity with electron carriers ( $n$ -type) would be possible with  $d^{10} \rightarrow d^9$  cation transfer combinations, which was discovered in  $\text{Nd}_{2-x}\text{Ce}_x\text{CuO}_{4-y}$ , as discussed in Section 7.
- The conclusion that long-range static antiferromagnetic order would have to break down before the superconducting state could be established, which was subsequently verified by Néel temperature measurements.



- The result from the preliminary theoretical model for critical current density that indicated an early fall off and tail as a function of temperature that has now been established by many experiments.
- The accurate prediction of microwave surface resistance measurement results over the complete temperature range by means of a normal electron hopping conduction model.

Background to this research has been drawn from the works of J.B. Goodenough on the subject of electrical conduction in metal oxides, from P.W. Anderson and Goodenough on the principles of magnetic superexchange, from R.R. Heikes, W.D. Johnston, and P.-G. de Gennes on the hopping conduction in mixed-valence oxides, and from J.H. Van Vleck, L.G. Orgel, and C.J. Ballhausen on matters pertaining to crystal-field and MO theory. On the specific subject of superconductivity, several excellent reference texts were consulted by authors who include F. London, M. Tinkham, C. Kittel, D. Schoenberg, J.M. Blatt, and J.R. Schrieffer.

## 2. PHENOMENOLOGICAL FOUNDATIONS

To relate the mechanism of the covalent electron transfer theory to traditional superconductor phenomenology, it is first necessary to review the basic macroscopic concepts on which any microscopic theory must be founded.

### 2.1. THE LONDON EQUATIONS

The magnetic flux density  $B$  must be constant to satisfy Faraday's law  $\nabla \times E = -(1/c)\partial B/\partial t$ , because the electric field  $E = 0$  in a hypothetical perfect conductor. For this reason, such a material would also be described as a perfect magnetic shield. An unchanging value of  $B$ , however, is not a sufficient condition for superconduction, because the Meissner effect requires the expulsion of flux from the interior of the specimen as it becomes superconducting, i.e.,  $B \rightarrow 0$ . When an external field  $H$  is removed from a normal conductor that might have attained a zero resistance state, the existing  $B$  would be sustained (flux trapping) by induced surface eddy currents. It follows, therefore, that a superconductor differs from a normal "perfect" conductor by the manner in which currents induced by changes in  $H$  are somehow constrained to ensure the  $B = 0$  condition.

Because superconducting materials are never spontaneously magnetic,  $B \sim H = 0$  (i.e., permeability  $\mu \sim 1$ ). It follows from the Maxwell equation of magnetic induction  $\nabla \times H = -(4\pi/c)i_s$  that the current density  $i_s$  is also zero in the interior, where  $B = 0$ , that the current must exist only at the surface, and that the material behaves as a perfect diamagnet with  $i_s$  inducing a field exactly equal and opposite to  $H$ . It is clear from inspection that Faraday's law alone cannot account for the  $E = B = 0$  condition. To describe these phenomena London [9] devised two relations to augment the Maxwell equations:

$$E = (4\pi\lambda_L^2/c^2) (\partial i_s/\partial t) \quad , \quad (1a)$$

and

$$H = -(4\pi\lambda_L^2/c) (\nabla \times i_s) \quad , \quad (1b)$$

where the London penetration depth  $\lambda_L = (mc^2/4\pi e^2 n_s)^{1/2}$  is a constant inversely dependent on the square root of carrier density  $n_s$ , with  $m$  and  $e$  as the electron mass and charge, respectively. In a more general context,  $m$  would be treated as the effective mass  $m^*$ , but this refinement will not enter the discussions or calculations throughout this work. For a stationary state,  $\partial i_s/\partial t = 0$ , and Equation (1a) fulfills the  $E = 0$  requirement. If Equation (1b) is then combined with  $\nabla \times H = -(4\pi/c)i_s$ , the following differential equations emerge, provided that  $\nabla \cdot H = 0$  and  $\nabla \cdot i_s = 0$ :<sup>1</sup>

$$\nabla^2 H = H/\lambda_L^2 \quad ,$$

and

$$\nabla^2 i_s = i_s/\lambda_L^2 \quad . \quad (2)$$

The solutions of Equation (2) yield  $H$  and  $i_s$  as exponential functions of distance  $x$  from the specimen surface, e.g.,  $H = H_0 \exp(-x/\lambda_L)$ ; therefore, both  $H$  and  $i_s$  are maxima at the surface and decay inward with

<sup>1</sup> It is necessary to use the vector identity:  $\nabla \times (\nabla \times V) = \nabla(\nabla \cdot V) - \nabla^2 V = -\nabla^2 V$ , with  $\nabla \cdot V = 0$ .

a profile characterized by London penetration depth  $\lambda_L$ . If flux and current are expelled from the interior of the material from  $B = E = 0$  conditions, they coexist in surface layers of depth  $\lambda_L$  as solenoidal vectors normal to each other, i.e.,  $\nabla \cdot \mathbf{H} = 0$ ,  $\nabla \cdot \mathbf{i}_s = 0$ , and may be illustrated by the simple geometries of Figure 1.

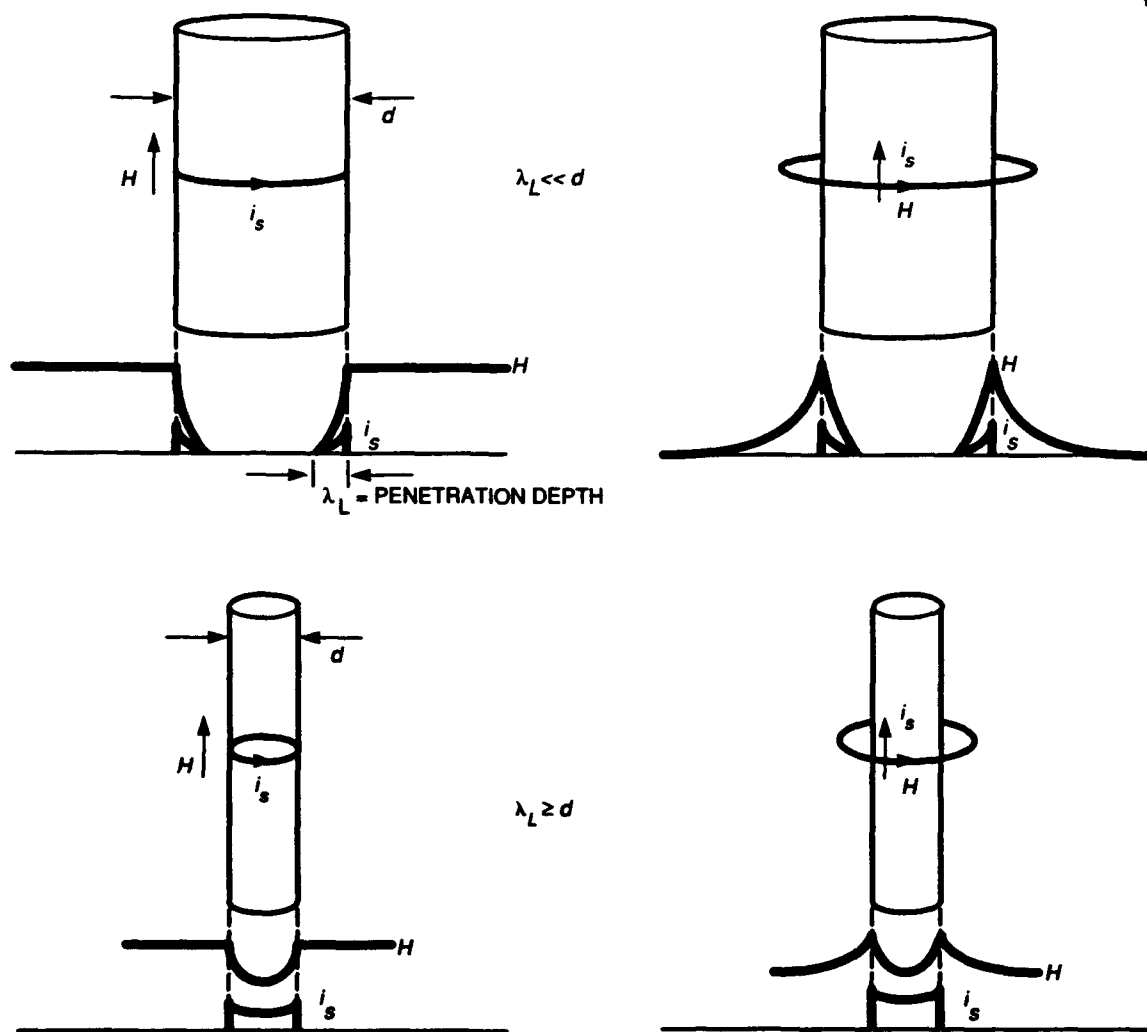


**Figure 1. Perpendicular relations between current and magnetic field for superconducting cylinders of large and small diameters. In the upper cases, the current responds to an applied external field within a depth  $\lambda_L$ , and in the lower ones the field is generated to a depth  $\lambda_L$  by a current passed through the superconductor. For the thin cylinders where  $\lambda_L \geq d$ , the penetration can be almost complete.**

A more useful relation is the interdependence of  $i_s$  and  $H$  in a superconducting environment, where  $E = 0$ . Because  $\nabla \cdot H = 0$ ,  $H$  may also be defined in terms of the magnetic vector potential according to  $H = \nabla \times A$ , and it follows from Equation (1b) that

$$i_s = -c/(4\pi\lambda_L^2) A$$

or

$$= -(e^2/mc) n_s A, \quad (3)$$

which is a relation analogously referred to as the "Ohm's law of superconductivity," where the supercurrent is controlled by magnetic instead of electric fields. It should be noted that Equation (3) is not gauge invariant, and that a further constraint must be placed on  $A$  for application of this relation to specific phenomenology. In the most general case of simply connected superconductors, the London gauge  $\nabla \cdot A = 0$  is chosen to conform to the  $\nabla \cdot i_s = 0$  condition that defines the observed supercurrent rigidity, i.e., no current components normal to surface.

## 2.2 THE MACROSCOPIC MOLECULE CONCEPT

A more fundamental physical derivation of Equation (3) may be obtained from classical electrodynamics, where the mean local canonical momentum of individual carriers  $\langle p \rangle = m\langle v \rangle + (e/c)A$ , with  $\langle v \rangle$  as the local mean carrier velocity. Statistical mechanics dictates that  $\langle v \rangle = 0$  in a normal conductor, therefore it follows that  $\langle p \rangle = (e/c)A$  in the normal state. For a superconducting ground state, however, a Bloch theorem [10] concluded that  $\langle p \rangle = 0$ , implying a certain rigidity or inability of the momentum to respond to  $H$ , therefore establishing that  $\langle v \rangle = (e/mc)A$ . For a chain of ordered carriers of number density  $n_s$ , it follows that the supercurrent density  $i_s = -n_s e \langle v \rangle = -(n_s e^2/mc)A$ , thereby producing an alternate derivation of Equation (3). For this electrodynamic approach to comply totally with the constraints of the phenomenological result that  $\nabla \cdot i_s = 0$ , it is not only necessary that the gauge condition  $\nabla \cdot A = 0$  apply, but also that  $\nabla n_s = 0$ .<sup>2</sup> Therefore, the basis for describing the supercurrent as spatially rigid, i.e., the  $\langle p \rangle = 0$  condition, must include the condition that the distribution of carriers be uniform (ordered) along the current path.

The notion of spatially ordered carriers is not readily applicable to a free-electron gas. Because the first superconductors were metals, a quantum mechanical alternative to this classical concept evolved from the nonlocal ideas of Pippard [11], i.e., the analogy of supercarrier coherence length  $\xi_0$  to normal carrier mean-free-path, giving rise to the Ginsburg-Landau [12] ensemble-average wavefunction  $\psi_s$ , which in turn is related to the supercurrent electron density by the standard expectation value relation

$$|\psi_s|^2 = n_s, \quad (4)$$

<sup>2</sup> Recall that  $\nabla \cdot i_s = (e^2/mc) (n_s \nabla \cdot A + A \cdot \nabla n_s)$  and for  $\nabla \cdot i_s = 0$ , both  $\nabla \cdot A$  and  $\nabla n_s = 0$ . This latter condition is not only necessary for supercurrent rigidity in the classical argument but also sufficient, because a carrier distribution dynamically ordered in real space is a rigid current by definition. In effect it should be considered the fundamental physical requirement for the applicability of Equation (3) to superconductivity.

where the number density  $n_s$  now represents the instantaneous probability of a supercarrier existing at a position vector  $r$ . As a result, Equation (3) may be written as

$$\mathbf{i}_s = -(e^2/mc) |\psi_s|^2 \mathbf{A} \quad , \quad (5)$$

with the attendant implication that  $\nabla \psi_s = 0$  to satisfy the condition that  $\nabla n_s = 0$ .

Four important conclusions are deduced from this wavefunction rigidity concept:

- The current density vector  $\mathbf{i}_s$  is directly and exclusively controlled by the magnetic field through the vector potential  $\mathbf{A}$ .
- The eigenstate of the supercurrent has the properties of a space-invariant wavefunction with zero average mechanical momentum ( $\langle p \rangle = \nabla \psi_s = 0$ ).
- The resulting spatial invariance of the carrier density  $n_s$  implies ordered or equispaced supercarriers.
- Superelectrons cannot be part of the normal free-electron gas.

If the carriers have similar quantum states that may be described in terms of a single giant MO wavefunction, the current rigidity imposed by the fixed wavefunction provides an immediate explanation for the absence of eddy currents and the presence of flux trapping in the superconducting state.

## 2.3 NONLOCAL CONSIDERATIONS

In a manner similar to the nonlocal arena of normal electrons that move independently within the range of a mean-free-path  $\ell$ , Pippard [11] suggested that a sphere of radius  $\xi_0$  be considered as a nonlocal region in which each superelectron would exist within the correlation scheme. For normal conduction,  $\ell$  is the average distance that an electron can be transported without scattering; for superconduction,  $\xi_0$  is the average distance that a superelectron can remain in coherence with the ensemble as part of the giant molecular state. As examined in Section 6.7, the coherence length  $\xi_0$  may be estimated from the uncertainty principal once a value for momentum  $p_s$  is determined.

Ginsburg and Landau [12] reasoned that because wavepackets have a spatial profile, the coherence length could be readily introduced through a generalized form of  $\psi_s$  with an exponential decay and proposed a solution of a Schrodinger-type equation with

$$\psi_s(r) \sim \psi_s(0) \exp(-r/\xi) \quad , \quad (6)$$

where  $\xi$  is a more generalized coherence length. In this context,  $\xi$  represents the smallest size of wavepackets that the superconducting charge carriers can form. In a context more appropriate to the discussions that follow, the gradient of the superconduction carrier number density wavefunction may be expressed as

$$\nabla n_s \sim (2/\xi) |\psi_s|^2 \sim (2/\xi) n_s \quad . \quad (7)$$

As  $\xi \rightarrow \infty$ ,  $\nabla n_s \rightarrow 0$ , to approach the condition for spatial ordering of carriers.

In band-theoretical terms that have been applied to conventional metal superconductors, an intrinsic coherence length  $\xi_0 \sim (h/2\pi)v_F/kT_c$  is defined in terms of the Fermi velocity  $v_F$  and superconduction critical temperature  $T_c$ . A more general definition was pointed out by Pippard for materials where the coherence length is reduced by impurities that limit the electron mean-free-path  $\ell$ , according to  $1/\xi \approx 1/\xi_0 + 1/\ell$ . As a consequence, superconductors may be categorized as:

- Class 1. Type-I pure superconductors with large  $\xi_0 \gg \lambda_L$  that require a full nonlocal theory treatment (Pippard superconductors)
- Class 2. Impure superconductors with  $\xi_0 \sim \ell$  that are controlled by the mean-free-path (London limit, where  $\xi < \xi_0$ )
- Class 3. Pure superconductors with  $\xi_0 \ll \lambda_L$ .

For Class 2, Equation (3) is modified to read  $i_s = -(n_s e^2 / mc) (\xi / \xi_0) A$ , where  $\xi^3 \ll \xi_0 \lambda_L^2$ ; only for Class 3 is Equation (3) valid as stated. In practice, Classes 2 and 3 are type-II superconductors, the former resulting from impurities and the latter representing the case of small intrinsic coherence length, which is the focus of this report.

In Section 6 the ratio  $\kappa = \lambda_L / \xi_0$  is shown to be effectively constant with temperature. In physical terms, the ideal type-I superconductor features  $\kappa \ll 1$  with  $\xi_0 \rightarrow \infty$  and  $\lambda_L \rightarrow 0$ ; in the opposite extreme, the magnitudes of these quantities reverse,  $\kappa \gg 1$ , with  $\xi_0 \rightarrow 0$  and  $\lambda_L \rightarrow \infty$  in the natural type-II case (Class 3). The essential point is that the coherence length represents a measure of the wavefunction uniformity; it is the quantum mechanical equivalent of the spatially ordered carrier concept of the classical London theory, which will be examined further in the context of CET.

### 3. THERMALLY ACTIVATED SEMICONDUCTION

As described in an earlier report [1], electrical properties of insulating oxides may be approached from either a localized extreme, where the carriers are bound to their sites in a largely ionic bonding scheme, or from the collective carrier extreme that implies sufficient covalent bonding to warrant the consideration of energy bands. From Section 2, it is apparent that the giant molecular system described by the Londons must involve a dual character that includes both a quasi-discrete energy level structure (narrow bands from tight binding) and covalent bonding to permit the formation of a continuous chain. As a result, it is logical to begin with the localized case and then add covalent effects as an increasing perturbation.

Where a fixed impurity ion or defect is present at a lattice site, the charge imbalance may be compensated by an electron (or hole) induced on a neighboring site. This charge forms the opposite half of a dipole and is, therefore, coupled electrostatically to the fixed charge. As part of the local lattice accommodation it is also trapped in its site by a deformation of its surroundings. Because it is mobile through thermal activation, the charge with its trap is a polaron; where the trap involves magnetic exchange stabilization, the polaron may be described as magnetic. The significance of the polaron concept in superconductivity is that it represents the source of electrical conduction for bound electrons. A general theory of polarons has been outlined by Fröhlich [13]. More relevant to the current work, however, is the molecular-crystal model developed by Holstein [14], where two polaron extremes were defined: a small polaron, in which the carrier is localized within a lattice parameter of the polaron source, and a large polaron, which can become itinerant within several lattice parameters radius surrounding its fixed source. In both cases, however, thermally activated electron hopping is a principal cause of conduction.

Semiconduction in metal oxides, therefore, represents the intermediate coupling (large polaron) regime that interfaces between the purely localized (small polaron) and the fully collective situation usually interpreted by band theory. In the analyses to follow, the large polaron case will be explored with the assumption that the band is narrow enough to be approximated by the individual molecular orbital states. For the purpose at hand, the chemical origins and physical phenomena associated with large itinerant polarons will be examined first.

#### 3.1 MIXED-VALENCE ORBITAL CARRIERS

Of the two situations where bound electrons transfer between similar sites, one is a general case that is illustrated in Figure 2(a) (from Tilley [15]), consisting of transfer between similar ions  $M^{n+}$  that creates two different ions  $M^{(n-1)+}$  and  $M^{(n+1)+}$  of the same element and requires a net energy expense (excitation) according to the relation

$$2M^{n+} \leftrightarrow M^{(n-1)+} + M^{(n+1)+} - \Delta U \quad , \quad (8)$$

where  $\Delta U$  is the net transfer energy required, closely related to the algebraic sum of the ionization potentials (corrected for screening effects of the lattice) and typically measuring several electron volts.

The other case and the mechanism of interest in this report was postulated originally by Verwey [16] for the  $\text{Li}^{1+}_x\text{Ni}^{2+}_{1-2x}\text{Ni}^{3+}_x\text{O}$  system<sup>3</sup> and examined by Zener [17] and de Gennes [18], is a special case of Equation (8) that involves the transfer of an electron between different ions of the same element (i.e., a mixed-valence situation that creates a polaron), according to

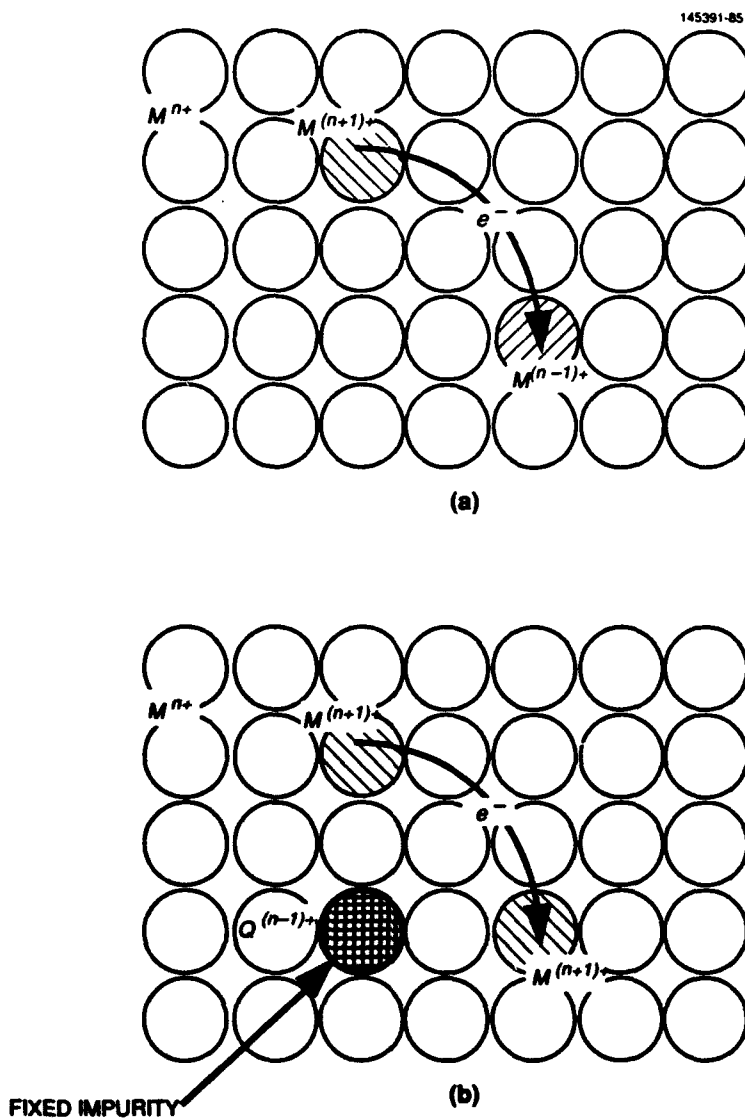


Figure 2. Two types of charge transfer in oxides: (a) excitation ( $> 1$  eV) in the uniform valence case where the electron transfer creates two "new" ions  $M^{(n-1)+}$  and  $M^{(n+1)+}$  requiring energy  $\Delta U$ , and (b) activation ( $< 1$  eV) occurring with mixed-valence cations, where the transfer causes only a change in carrier location.

<sup>3</sup>The  $\text{Li}^{1+}$  ion acts as an acceptor relative to the divalent cation lattice to create a  $p$ -type hopping semiconductor. Because metal ions are normally less stable than filled-shell  $\text{O}^{2-}$  anions in the ionic lattice, the electrons are removed from the  $\text{Ni}^{2+}$  rather than the  $\text{O}^{2-}$ .



The initial and final energy states of the system are unchanged ( $\Delta U = 0$ ) because the two sites are equivalent; only the participating ions have exchanged positions in the lattice, as shown in Figure 2(b), and only one band (usually narrow) is required to describe the conduction states. For unequal populations of  $M^{n+}$  and  $M^{(n-1)+}$ , the minority ion is the mobile half of a dipole electrostatically coupled to a fixed source with its ratio to the total population of its particular sublattice indicated by  $0 \leq x \leq 0.5$ . (If  $x \geq 0.5$ , the other ion will be the mobile half and will be designated as the polaron, either  $n$  or  $p$  type, depending on the sign of its charge.) Where  $x$  is small, the carrier states are localized as individual energy levels in the manner suggested by Goodenough [7].

The occurrence of mixed valence is restricted to a select group of ions, particularly those of the  $d^n$  series transition elements. There are two common situations of mixed-valence cations in a crystal lattice: (1) where the natural stoichiometry calls for a nonintegral average valence in a cation sublattice (e.g.,  $\text{Fe}_3\text{O}_4$ ,  $\text{Mn}_3\text{O}_4$ ), and (2) where a mixture of fixed-valence ions or lattice vacancies force a variation in cation valence within a sublattice to preserve stoichiometry (e.g., the magnetically altered ferrimagnetic spinels and garnets [19]).

Where mixed valence exists, the imbalance in the numbers of the two valence states determines whether the conductivity is  $n$  or  $p$  type. In the example presented in Figure 3(a), where  $\text{Sr}^{2+}$  ions are substituted for  $\text{La}^{3+}$  in the  $\text{La}^{3+}_{2-x}\text{Sr}^{2+}_x\text{Cu}^{2+}_{1-x}\text{Cu}^{3+}_x\text{O}_4$  system, an equal number of  $\text{Cu}^{3+}$  ions must be created to reestablish electrostatic neutrality.<sup>4</sup> Because the  $\text{Sr}^{2+}$  ions occupy a minority of the  $A$  sublattice dominated by  $\text{La}^{3+}$ , they represent isolated sites of fixed negative charges; the corresponding  $\text{Cu}^{3+}$  ions, however, represent positive charges in the  $B$  sublattice, i.e., the other halves of the dipoles formed with the  $\text{Sr}^{2+}$  polaron sources, and will occur in closest proximity to the  $\text{Sr}^{2+}$  site to reduce the Madelung energy. Moreover, the  $\text{Cu}^{3+}$  ion can occupy with equal probability any of four geometrically equivalent sites around the  $\text{Sr}^{2+}$  ion in this particular lattice, and the positively charged hole carrier associated with the  $\text{Cu}^{3+}$  ion can move between them through the thermally activated mobility mechanism. With the application of an external electric field, the hole can move away from the  $\text{Sr}^{2+}$  negative charge, extending the dipole and increasing the energy. For this reason, the hole is considered to be tethered to a fixed negative source ( $\text{Sr}^{2+}$ ), and the conductivity is  $p$ -type because the polaron is positively charged. In Figure 3(b), the case of a negative polaron that would give rise to  $n$ -type conduction is shown. Instead of  $\text{Sr}^{2+}$ , the fixed-valence ion is tetravalent, e.g.,  $\text{Ce}^{4+}$  or  $\text{Pr}^{4+}$ , representing a positive charge, and the mobile ion then becomes  $\text{Cu}^{1+}$ , representing a negative polaron and providing an  $n$ -type conductivity.

Thermally activated electron hopping is a form of conduction that is peculiar to metal oxides with cations of mixed (dual) valence. Because conductivity increases with temperature for thermal energies below the level of activation, it is described by a relation similar to the familiar law of diffusion [15,20,21],

$$\sigma = Ne \mu(T) = Ne (eD/kT) \exp(-E_{\text{hop}}/kT) \quad , \quad (10)$$

<sup>4</sup>The assignment of the 3+ charge to Cu in the  $(\text{CuO}_4)^+$  ion emerges from the MO analysis carried out in Appendices A, B, and C. In polaron notation the chemical formula  $\text{La}^{3+}_{2-x}\text{Sr}^{2+}_x\text{Cu}^{2+}_{1-x}\text{Cu}^{3+}_x\text{O}_4$  becomes  $(\text{La}^{3+}_{2-x}\text{Sr}^{2+}_x)^{x-}(\text{CuO}_4)^{x+}$ .

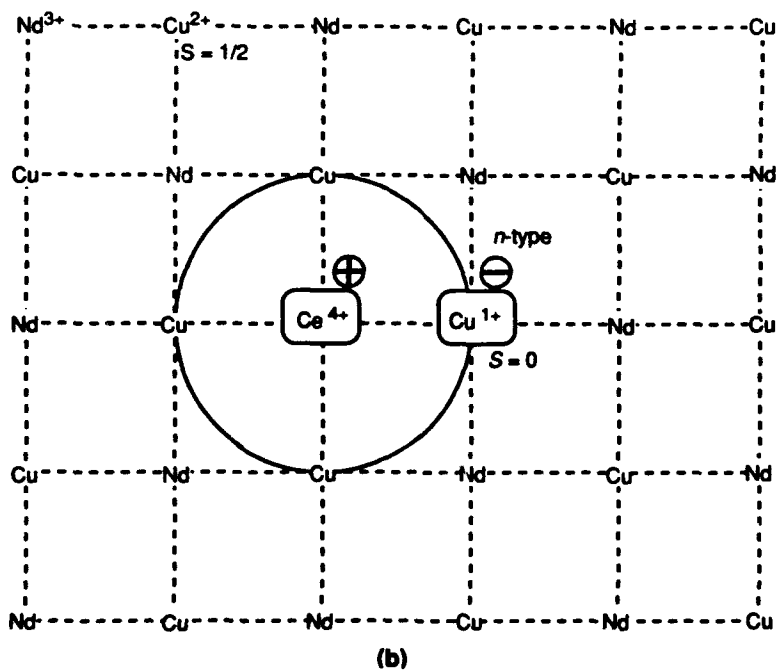
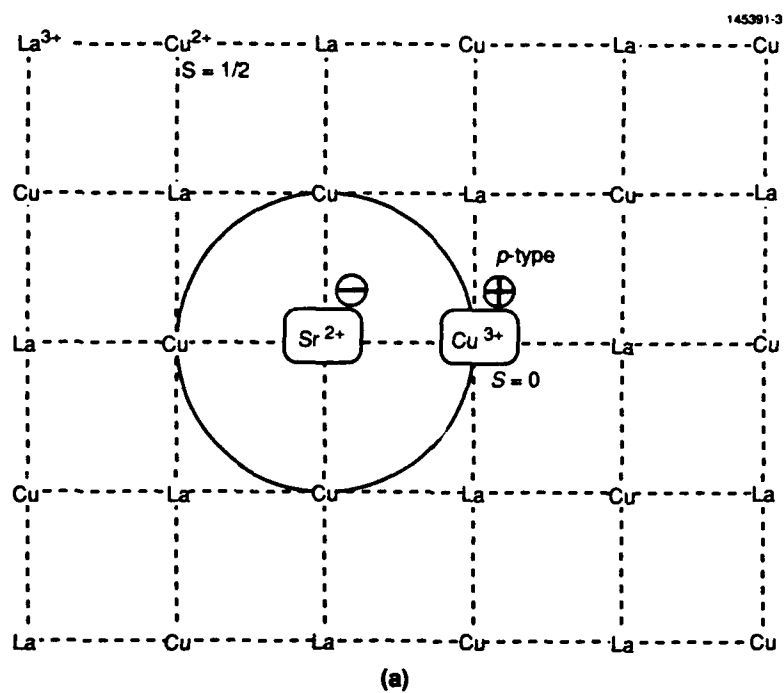


Figure 3. Origin of polarons in mixed-valence cation systems: (a) *p*-type conduction, e.g.,  $(La^{3+}Sr^{2+})^{+}-(CuO_4)^{-}$ , and (b) *n*-type conduction, e.g.,  $(Nd^{3+}Ce^{4+})^{+}-(CuO_4)^{-}$ . Cu ions are typically in separate planes from the alternate cations; O ions are omitted for clarity.

where  $N$  is the total number of carriers,  $\mu(T)$  is the thermally activated mobility,  $D$  is the diffusion constant, and  $E_{\text{hop}}$  is the activation energy. The polaron ion harbors a trapped carrier that is isolated from other carriers by the average polaron separation distance; the conduction is intrinsically local and is treated as such theoretically.

Conductivity as expressed by Equation (10) resembles that of band semiconductors, where an exponential factor also controls the carrier density  $n$ . For the case of a degenerate semiconductor with large impurity density  $N_i \gg n$  and impurity ionization energy  $E_i$  much smaller than the gap energy,  $n(T) \sim N_i T^{3/4} \exp(-E_i/kT)$ , with the mobility influenced by temperature as determined from standard conductivity theory  $\mu(T) \sim T^{3/2}$ , yielding a result similar to Equation (10) if  $E_i = E_{\text{hop}}$ , with  $\sigma \sim \sigma_0 T^{3/4} \exp(-E_{\text{hop}}/kT)$ . In the limit as  $T \rightarrow 0$ , however, excited carrier density  $n \rightarrow 0$ , thereby eliminating any possibility of spontaneous conduction by an alternate mechanism. At extreme doping levels, however, one is tempted to speculate on the possibility that tunneling between impurity sites may provide such a temperature-independent conduction mechanism. The  $p$ -type compound  $\text{AlGe}_2$ , for example, has  $T_c = 1.75$  K.

### 3.2 ELECTROSTATIC/ELASTIC TRAP ENERGY

The magnitude of  $E_{\text{hop}}$  involves a combination of several factors, most of which can be treated only semiempirically. In physical terms, it is the polaron trap energy (the stabilization energy difference between the two valence states in the lattice) with a basic contribution  $E_{\text{el}}$  that arises from the electrostatic coupling between cation ligands. Among the effects that contribute to  $E_{\text{el}}$  are the ionization potential (electronegativity) differences, the MO and crystal-field stabilization energies, and the compensating effects of lattice elastic strains that occur spontaneously around the carrier site, e.g., static Jahn-Teller effects in  $\text{Cu}^{2+}$  and  $\text{Ni}^{3+}$  (low spin), or through physical accommodation for differing ion sizes and valences in mixed-cation systems.

From considerations of lattice electrostatic energy minimization, the attractive potential of the polaron ion to its source represents a major energy-compensating influence that will be optimized by keeping the effective dipole separation as small as possible. Hence, there emerges the concept of the polaron tethered to its source by the Coulomb inverse square law. Extending the general rule that local energy differences will tend to be minimized, one would expect site stabilization energy differences of electrostatic origin to be reduced through lattice elastic adjustments. For this reason, measured activation energies are small in comparison with the electronegativity and other energies that make a contribution to the overall stabilization.

The transport of electrons trapped in a crystal lattice evolves from polaron theory, and the reader is encouraged to consult standard articles [13,22,23]. For the purpose at hand, however, it is sufficient to recognize that a carrier created by the mixed-valence condition is indeed a polaron (defined as the mobile charge and its surrounding cloud of optical phonons) and that the weak-coupling solution for the polaron ground state may be used to describe  $E_{\text{el}}$  according to the relation [13].

$$E_{\text{el}} \approx (\alpha/2) (h\nu_D) \quad , \quad (11)$$

where the coupling constant<sup>5</sup>  $\alpha$  is expected to be less than unity for  $3d^n$ -series oxides (see selected examples in Table 1 [23] where  $\alpha$  is also seen to decrease with the amount of covalence or polarizability), and  $\nu_D$  is the

---

<sup>5</sup>The magnitude of this dimensionless constant is related to the density of the phonon cloud surrounding the trapped carrier and is, in general, inversely proportional to the dielectric constant, as discussed in Section 8.5.

maximum phonon (Debye) frequency  $\sim 10^{13}$  Hz, yielding a Debye energy  $\hbar\nu_D \sim 40$  meV. For the oxides,  $E_{el}$  would typically fall below 100 meV, and for the superconducting Cu perovskites that feature  $e_g$  orbital covalence,  $E_{el}$  can fall below 10 meV. For metals, where screening by conduction electrons causes local dielectric constants to become large to the point of being undefined,  $\alpha$  and consequently  $E_{el}$  would be substantially smaller.<sup>6</sup> In anticipation of the theoretical development to follow, note that a qualitative correlation appears to exist between  $E_{el}$  and the superconduction critical temperature  $T_c$ ; in both cases the highest values tend to occur for materials with the lowest normal conductivity.

**TABLE 1**  
**Polaron Electrostatic/Elastic Trap Parameters<sup>a</sup>**

Compound	Ionic	Ionic	Ionic	Mixed <i>d-p</i>	Mixed <i>s-p</i>	Covalent <i>s-p</i> <sup>3</sup>
	LiF	AgCl	ZnO	CuO <sup>b</sup>	PbS	GaAs
<i>K</i>	9.3	12.3	8.5	15 to 20 <sup>c</sup>	17.9	13.5
$\nu_D (\times 10^{13} \text{ Hz})$	2	0.5	2		0.5	1
$\alpha$	5.2	1.7	0.85	<1 (est)	0.16	0.06
$\hbar\nu_D$ (meV)	81	24	83		18	3
$E_{el}$ (meV) <sup>d</sup>	210	20	36	(3) <sup>e</sup>	1.5	1

<sup>a</sup> Derived (except for CuO) from tabulated data in Brown [23], Table 1.

<sup>b</sup> With *d-p* covalence through the  $e_{x^2-y^2}$  orbital in a 180-deg Cu-O-Cu bond, it is reasonable for CuO to fall in the regime of at least moderate covalence for this particular orbit.

<sup>c</sup> For Cu<sub>2</sub>O<sub>3</sub>,  $K = 18.1$  (*Handbook of Physics and Chemistry*, CRC Press, 62nd Ed.).

<sup>d</sup> Calculated from  $(\alpha/2)\hbar\nu_D$ .

<sup>e</sup> Measured as  $E_{hop}$  in Goodenough et al. [24].

<sup>6</sup> It is appropriate to recall the approximation often used to estimate potentials of impurity atoms in semiconductor hosts,

$$E_i \sim 2\pi^2 m Z^2 e^4 / K^2 \hbar^2 ,$$

which represents the expression for the ionization potential of a hydrogen atom ( $Z = 1$ ) with the Coulomb field reduced by the square of the host dielectric constant.

To calculate accurately  $E_{\text{hop}}$  for a particular situation is a formidable task. A more reasonable approach to gaining insight about its relative magnitude in transition metal oxides may begin with the experimental observation that the activation energies are typically 0.1 to 1 eV at low polaron concentrations, as evidenced in the data of Heikes and Johnston [20] shown in Figure 4. Because this range of values is substantially larger than the energies expected for pure elastic stabilization in metal oxides, an additional contribution from magnetic exchange must be considered.

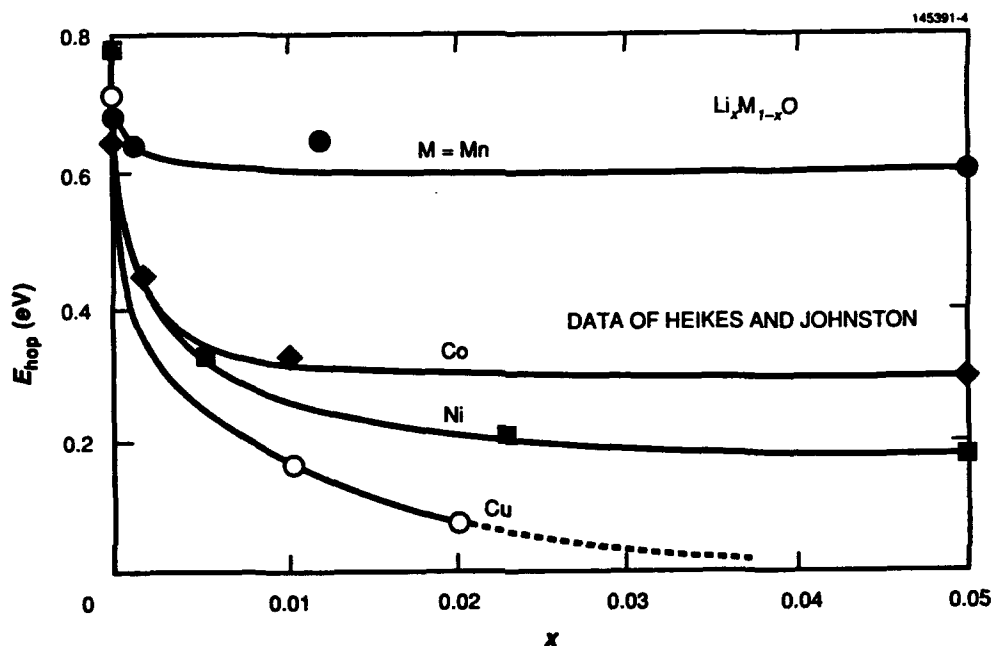


Figure 4.  $E_{\text{hop}}$  versus polaron density for monoxides of Mn, Co, Ni, and Cu (from Heikes and Johnston [20]).

### 3.3 MAGNETIC EXCHANGE TRAP ENERGY

According to Goodenough's qualitative summary for 180-deg superexchange [25] presented in Tables 2 and 3, all the couplings for the  $3d^n$  transition series  $e_g$ -occupied ions relevant to this investigation favor antiferromagnetic alignment. If one begins with the premise that at least partial short-range antiferromagnetic order is always present, particularly between the polaron ion of spin  $S_p$  and its neighboring lattice ions of spin  $S_L$ , the trap boundaries are formed by lattice spins of opposite polarity. Under these conditions a basic magnetic contribution to the activation energy emerges: The transfer electron will be destabilized internally on its new site because its spin direction opposes the existing net spin alignment. If the transfer ions are in turn coupled antiferromagnetically to the molecular field from the surrounding neighbors, the transferred electron spin causes an additional destabilization through its coupling to this external exchange field. It must be concluded, therefore, that as long as antiparallel spin alignments are ordered in two distinct sublattices, the energies between initial and final states of intersublattice transfers are unequal by a magnetic exchange energy

**TABLE 2**  
**Octahedral-Site  $d^n$  Superexchange Couplings for 180-deg Bonds (High Spin)**

	$e_g$		$d^0$	$d^1$	$d^2$	$d^3$	$d^4$	$d^5$	$d^6$	$d^7$	$d^8$	$d^9$
	$t_{2g}$											
	$d^1$	<div>S = 0 CET</div>	NEGL	$\uparrow\downarrow$ W	$\uparrow\downarrow$ W	$\uparrow\uparrow$ ~	$\uparrow\uparrow$ M	$\uparrow\uparrow$ M	$\uparrow\uparrow$ M	$\uparrow\uparrow$ M	NEGL	
	$d^2$			$\uparrow\downarrow$ W	$\uparrow\downarrow$ W	$\uparrow\uparrow$ ~	$\uparrow\uparrow$ M	$\uparrow\uparrow$ M	$\uparrow\uparrow$ M	$\uparrow\uparrow$ M	$\uparrow\uparrow$ W	
	$d^3$				$\uparrow\downarrow$ W	$\uparrow\uparrow$ ~	$\uparrow\uparrow$ M	$\uparrow\uparrow$ M	$\uparrow\uparrow$ M	$\uparrow\uparrow$ M	$\uparrow\uparrow$ W	
	$d^4$					$\uparrow\uparrow$ ~M	$\uparrow\downarrow$ ~	$\uparrow\downarrow$ ~	$\uparrow\downarrow$ ~	$\uparrow\downarrow$ ~	$\uparrow\downarrow$ ~	
	$d^5$						$\uparrow\downarrow$ S	$\uparrow\downarrow$ S	$\uparrow\downarrow$ S	$\uparrow\downarrow$ S	$\uparrow\downarrow$ ~	
	$d^6$							$\uparrow\downarrow$ S	$\uparrow\downarrow$ S	$\uparrow\downarrow$ S	$\uparrow\downarrow$ ~	
	$d^7$								$\uparrow\downarrow$ S	$\uparrow\downarrow$ S	$\uparrow\downarrow$ ~	
	$d^8$									$\uparrow\downarrow$ S	$\uparrow\downarrow$ ~	
	$d^9$										$\uparrow\downarrow$ ~	
	$d^{10}$										<div>S = 0 CET</div>	

S = STRONG; M = MODERATE; W = WEAK; ~ = QUASI-STATIC

**TABLE 3**  
**Octahedral-Site  $d^n$  Superexchange Couplings for 180-deg Bonds (Low Spin)**

	$e_g$												
	$t_{2g}$												
		$d^4_{hs}$	$d^5_{hs}$	$d^6_{hs}$	$d^7_{hs}$	$d^8_{hs}$	$d^9_{hs}$		$d^4_{ls}$	$d^5_{ls}$	$d^6_{ls}$	$d^7_{ls}$	$d^8_{ls}$
	$d^4_{ls}$		$\uparrow\uparrow$ M	$\uparrow\uparrow$ M	$\uparrow\uparrow$ M	$\uparrow\uparrow$ M	$\uparrow\uparrow$ ~W		$\uparrow\downarrow$ W	$\uparrow\downarrow$ W		$\uparrow\uparrow$ ~	
	$d^5_{ls}$			$\uparrow\uparrow$ W	$\uparrow\uparrow$ M	$\uparrow\uparrow$ M	$\uparrow\uparrow$ ~W			NEGL		NEGL	
	$d^6_{ls}$				$S=0$ CET?					$S=0$ CET		$S=0$ CET	
	$d^7_{ls}$	$\uparrow\downarrow$ ~	$\uparrow\downarrow$ ~	$\uparrow\downarrow$ ~		$\uparrow\uparrow$ ~	NEGL					$\uparrow\downarrow$ ~	$S=0$ CET
	$d^8_{ls}$						$S=0$ CET						

S = STRONG; M = MODERATE; W = WEAK; ~ = QUASI-STATIC

$E_{mag}$ . According to de Gennes [18], energy-conserved transfers must take place within the same sublattice, and such events can occur through electron hops between next-nearest neighbors over a barrier of energy

$$E_{hop} = E_{el} + E_{mag} \quad , \quad (12)$$

depicted in the rectangular barrier model of Figure 5.

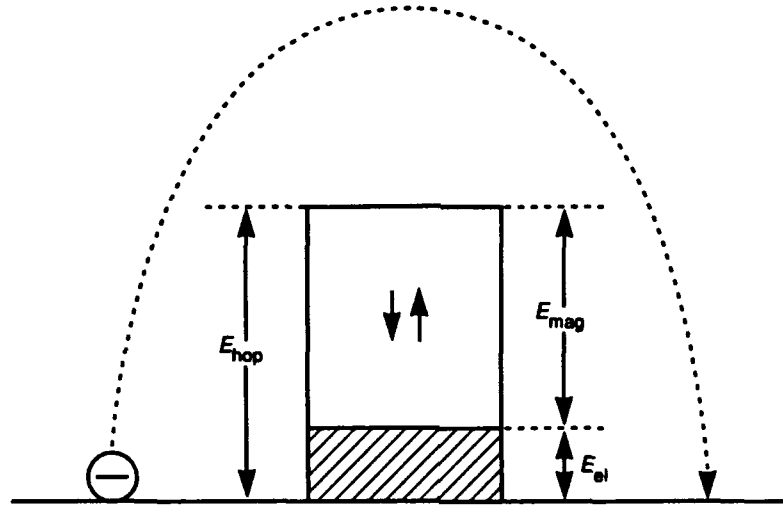


Figure 5. Schematic model of elastic and magnetic contributions to the hopping electron activation energy barrier.

For the energy-conserved transfer of  $S_p$  to a site two lattice lengths away, the two electrons of the  $S_L$  ions form a pair that creates a moving spin fluctuation as they reverse their spin directions to satisfy an internal exchange requirement — Hund's rule for maximum  $S$  in the case of a half-filled/empty orbital combination or the Pauli principle in the case of a filled/half-filled combination. (An alternative way of describing how this  $\Delta S = 0$  selection rule is satisfied is that one electron moves in two consecutive steps, temporarily occupying the empty state of the intermediate ion.) To analyze the energy of electron transfer between next-nearest-neighbor ions in an antiferromagnetically aligned lattice, consider the virtual process depicted in Figure 6, where  $S_L = S_p + 1/2$  and  $S_L' = S_p - 1/2$  represent the condition of maximum energy prior to spin reversals. This case discusses the problem of a hole polaron in a  $p$ -type hopping semiconductor, but the rationale would apply equally well to an electron polaron in an  $n$ -type material). If  $E_{\text{mag}}$  is assumed to be equivalent to the energy required for the passage of a polaron  $S_p$  directly through the opposing sublattice, the exchange interactions associated with a basic three-ion chain must be examined. After summing each of the individual exchange terms  $2J\mathbf{S}_i \cdot \mathbf{S}_j$  between six next-nearest neighbors<sup>7</sup>  $i$  and  $j$  linked by 180-deg M-O-M bonds among the three ion sites involved, and then subtracting the total energies of the initial ( $S_p\uparrow - S_L\downarrow - S_L\uparrow$ ) and final ( $S_L'\uparrow - S_L'\downarrow - S_p\uparrow$ ) states, the net magnetic destabilization energy is obtained:

$$E_{\text{mag}} = 2J[(2z - 3)S_L + 3S_p] \quad , \quad (13)$$

where  $J$  is the exchange constant (normally  $< 0$ , but here only its magnitude is used), and  $z$  is the number of next-nearest neighbors. With  $z = 6$ ,  $E_{\text{mag}} = 9J$  for  $S_L = 1/2$ ,  $21J$  for  $S_L = 1$ ,  $33J$  for  $S_L = 3/2$ ,  $45J$  for  $S_L = 2$ , and  $57J$  for  $S_L = 5/2$ .

<sup>7</sup> Twelve nearest-neighbor cations are linked by direct cation-cation  $t_{2g}$  orbitals across cube face diagonals and play a role in the overall exchange where half-filled  $t_{2g}$  orbitals are involved.



According to Anderson's theory of superexchange [26] as applied to these simple oxides,

$$b_{\text{tot}} \approx (2JS_L^2 U)^{1/2} \quad , \quad (14)$$

where  $U$  is the ionization potential involved in the electron exchange, and  $b_{\text{tot}} = b_{x-y}^2 + b_z^2 + b_l$  ( $b_l$  is the effective contribution from partially filled  $t_{2g}$ - $2p\pi$  states) and is the combined transfer integral for the particular cation-anion interaction in the  $x$ - $y$  plane. The origin of this definition of  $b_{\text{tot}}$  requires some explanation. In his original work Anderson reasoned that the  $b$  integrals could be estimated from simple relations to the optical splitting parameter  $Dq$ , according to  $b_{\text{tot}} = (10/3)Dq$  with individual orbitals weighted by coefficients determined from the size and directions of the respective  $e_g$  wavefunction lobes. For example, along the  $x$  or  $y$  directions the coefficients would be  $5/2$  and  $5/6$ , respectively, for the  $d_{x^2-y^2}$  and  $d_z^2$  states. To remain consistent with Equation (14), therefore, the contributions to  $b_{\text{tot}}$  from the two  $e_g$  orbitals would be expressed as  $b_{x-y}^2 = (3/4)b_{\text{tot}}$  and  $b_z^2 = (1/4)b_{\text{tot}}$ .

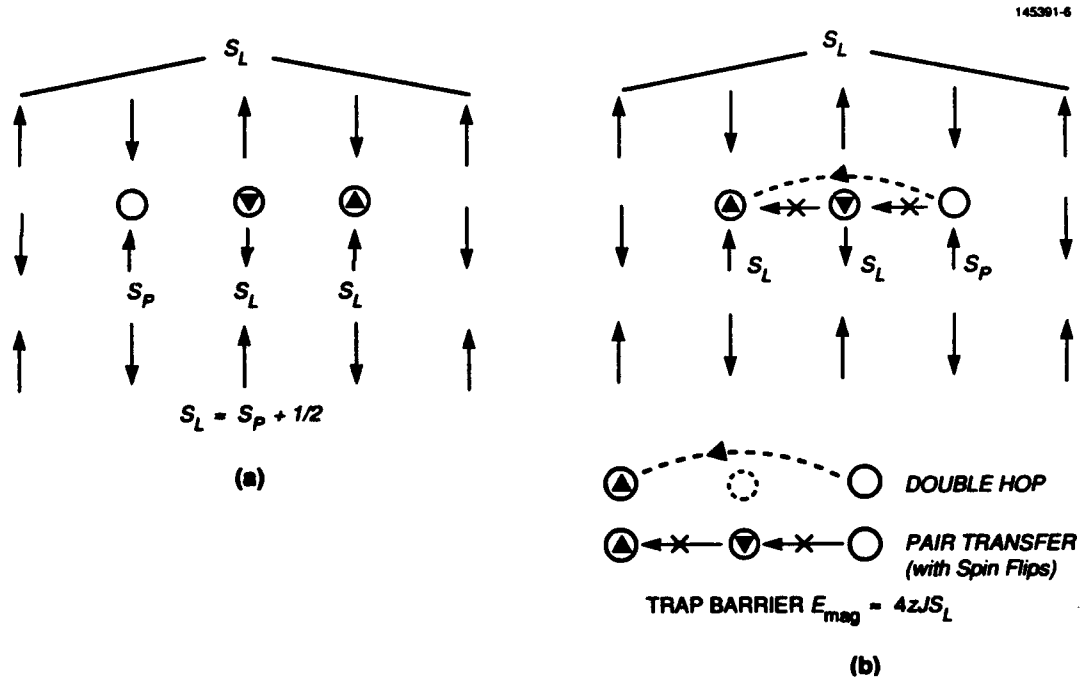


Figure 6. Two-dimensional model of the intrasublattice passage of a "hole" in an antiferromagnetically ordered lattice: (a) initial state, and (b) virtual destabilized state with two electron spins reversed to create possible spin wave fluctuation.

As a test for his theory, Anderson attempted to calculate the Néel temperatures from the standard relation of classical molecular-field ferromagnetism theory.<sup>8</sup> To this end, he estimated the  $J$  values from  $h_{\text{tot}}$  through Equation (14). Although the calculated  $T_N$  values were more than 50% higher than their measured counterparts, the qualitative trends served to verify his theory. One of several possible sources of the discrepancy may be seen in the analysis of the one-dimensional MO approximation in Appendix C, where the relation between  $h$  and  $Dq$  is determined after application of self-consistent perturbation theory that reveals only an indirect connection between  $h$  and  $Dq$  for these compounds.

A consistent set of  $J$  values is desired for the present discussion, and a reasonable value for  $h_{x-y}^2$  will be necessary for computations later in this report. Therefore Anderson's approach will be used in reverse, beginning with the well-established Néel temperature of NiO applied to the specific relation for the face-centered antiferromagnet family<sup>8</sup>

$$J = 6kT_N/zS_L(S_L + 1) \quad (15)$$

For  $T_N = 520$  K,  $z = 6$  nearest neighbors,  $S_L = 1$  (for high-spin  $\text{Ni}^{2+}$ ), it follows that  $J = 0.022$  eV. With these values of  $J$  and  $S_L$  combined with  $U = 7.3$  eV,<sup>9</sup> Equation (14) then yields  $h_{\text{tot}} = 0.57$  eV, leading to  $h_{x-y}^2 = 0.43$  eV and  $h_z^2 = 0.14$  eV. From these basic  $h$  values, effective  $h$  values may be constructed for other transition-metal oxides, as shown in Table 4. In the important case of CuO, only  $h_{x-y}^2 = 0.43$  eV applies. For CoO and MnO, where it is estimated that partially filled  $t_{2g}$  states make a 25% contribution through  $\pi$  bonding,  $h_{\text{tot}} = 0.57(1 + 0.25\tau)$  is used, where  $\tau$  is the number of active  $t_{2g}$  states, i.e.,  $\tau = 1$  for  $\text{Co}^{2+}$ , and  $\tau = 3$  for  $\text{Mn}^{2+}$ .

In general, the agreement between calculation and experiment is probably better than it deserves to be, based on the uncertainties involved. As commented in the footnotes to Table 4,  $E_{\text{mag}}$  numbers based on Heikes and Johnston data at  $x = 0$  are about a factor of 2 higher than what is typical for this group of materials.

### 3.4 MAGNETIC FRUSTRATION AND ZERO-SPIN POLARONS

As determined in several studies of ferrimagnetic spinels and garnets [29,30], the presence of a diamagnetic impurity in a magnetic sublattice directly reduces the molecular-field coefficient  $N_{jj}$  of the opposing sublattice and indirectly reduces the coefficient  $N_{ij}$  between the sublattices, causing decreases in the Curie temperature and controlling the contour of the thermomagnetization curve. This result may be readily

<sup>8</sup> The standard formula for the ferromagnetic ordering temperature derived from the Curie-Weiss molecular field theory is

$$T_{\text{CW}} = 2JzS(S + 1)/3k$$

In the case discussed here, Equation (15) was chosen instead of the above relation, because it applies directly to the face-centered antiferromagnetic structures of the Mn, Co, and Ni oxides. The derivation of Equation (15) was taken from Equations (6-3.27), (8-3.6), and (8-3.24) in A.H. Morrish, *The Physical Principles of Magnetism*, (New York: John Wiley & Sons [1965]).

<sup>9</sup> This value replaces  $U = 6.3$  eV originally used by Anderson (see Table 1 in Anderson [26]), which appears to have resulted from an error in subtraction.

**TABLE 4**  
**Magnetic Trap Energies  $E_{\text{mag}}$  for  $z = 6$**

Ion	Config	$S_L$	$S_p$	$U$	$b_{\text{tot}}^a$	$J$	$E_{\text{mag}}(\text{cal})$ ( $x = 0$ )	$E_{\text{mag}}(\text{exp})$ ( $x = 0$ )	$E_{\text{mag}}(\text{cal})$ $F_\theta \rightarrow 0$	$E_{\text{hop}}(\text{exp})$ ( $x = 0.05$ )
				(eV)						
Mn <sup>2+</sup>	$d^5$	5/2	2	9.9	1	0.008	0.46	0.67	0.10	0.60
Mn <sup>3+</sup>	$d^4$									
Co <sup>2+</sup>	$d^7$	3/2	1	5.8	0.71	0.019	0.64	0.66	0.11	0.30
Co <sup>3+</sup>	$d^{6b}$									
Ni <sup>2+</sup>	$d^8$	1	1/2	7.3	0.57	0.022	0.54	1.21 <sup>c</sup>	0.07	0.20 <sup>d</sup>
Ni <sup>3+</sup>	$d^7 \text{ ls}$									
Cu <sup>2+</sup>	$d^9$	1/2	0	5.9	0.43	0.063	0.55	0.69	0	~0
Cu <sup>3+</sup>	$d^8 \text{ ls}$									

<sup>a</sup> The value of  $b_{\text{tot}}$  varies somewhat among these ions and depends on the distribution of  $d$  electrons. For  $d^9$  and  $d^7$  (low spin), there is only one possible coupling and the maximum  $b$  is estimated as  $(5/2)Dq$  for the  $d_{x^2-y^2}-\sigma-d_{x^2-y^2}$  bonds; for  $d^8$  (high spin), two orbitals ( $d_{x^2-y^2}$  and  $d_{z^2}$ ) participate and the maximum is  $(10/3)Dq$ ; for  $d^7$  (high spin),  $d^6$ ,  $d^5$ , and  $d^4$  (high spin) all include smaller ( $\sim 25\%$ ) contributions from the usually neglected  $\pi$ -bonding  $t_{2g}$  states. The average  $Dq$  value  $\sim 0.1$  eV, but varies by about  $\pm 25\%$  among the group.  $b_{\text{tot}}$  is scaled to 0.57 eV of NiO, with adjustments for Co<sup>2+</sup> and Mn<sup>2+</sup> to account for the contributions from half-filled  $t_{2g}$  states, as described in the text. For Cu<sup>2+</sup> with a half-filled  $d_{x^2-y^2}$  orbital,  $b_{\text{tot}} = b_{x^2-y^2}$ .

<sup>b</sup> Co<sup>3+</sup> ( $d^6$ ) will condense to a low-spin  $S = 0$  state at low temperatures [27] with an energy of 20 kcal/mole  $\sim 0.86$  eV. In this event, both  $e_g$  electrons would undergo the transition in contrast to only one for the  $d^8$  case.

<sup>c</sup> This value for Ni<sup>2+</sup> is anomalously high in comparison with others, e.g., the Springthorpe et al. value of 0.28 eV for  $x = 0.002$  [28], suggesting that the polaron concentration may be smaller than believed and that the hopping mechanism may not yet be influencing the conductivity. The other values in this series are also somewhat high, raising the possibility of a systematic error in measurement or data reduction (e.g., a factor of 2) affecting all these results.

<sup>d</sup> At temperatures below 100 K,  $E_{\text{hop}}$  was measured as 0.009 eV [28], as discussed in Appendix D.

explained by the notion of local spin canting (with angle  $\theta$  to the alignment direction) surrounding the dilutant ion, where the loss of exchange linkages at neighbor sites reduces their spin commitments to the magnetic order and their contributions to the molecular (exchange) field. In Figure 7(a), this effect is represented by

an angular dispersal of the spins immediately surrounding the three ions involved in the transfer process, with the transfer ions themselves remaining in momentary 180-deg alignments (as in the snap-shot of a transfer event). For this situation, Equation (13) can be modified according to

$$E_{\text{mag}} = \underbrace{2J[(2z-3)S_L F_\theta]}_{\text{external}} + \underbrace{3S_p}_{\text{internal}} \quad (16)$$

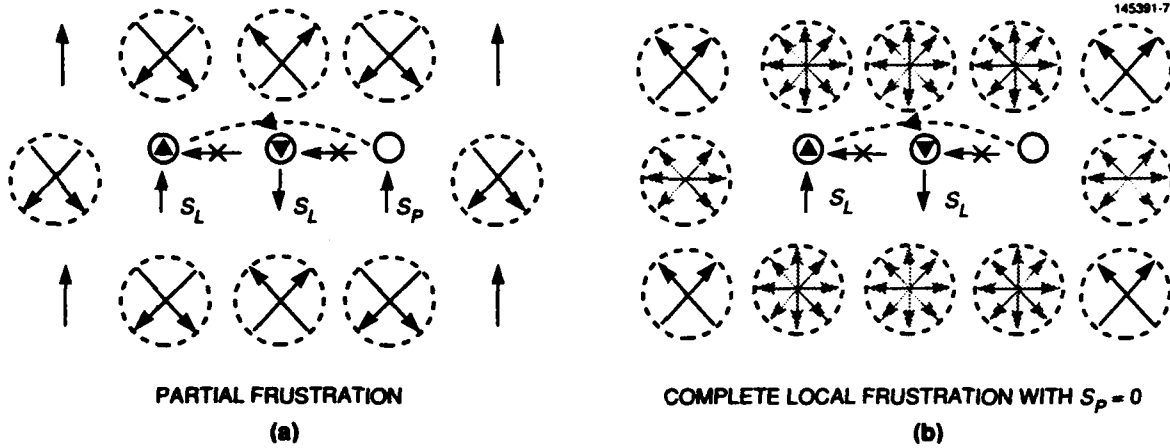


Figure 7. Growth of magnetic frustration from (a) local spin canting caused by magnetic dilution to (b) regions of complete disorder defined by the boundaries of itinerant  $S_p = 0$  polarons.

where  $F_\theta \leq 1$  is a canting factor related to the average alignment component  $\langle \cos\theta \rangle$  that depends on the amount of magnetic dilution.

With  $F_\theta < 1$ , Equation (16) indicates that  $E_{\text{mag}}$  will decrease accordingly as the antiparallel ordering breaks down. Because  $F_\theta$  would decrease with  $x$  in the  $\text{Li}_x\text{M}_{1-x}\text{O}$  systems from Li dilution, the Heikes and Johnston data [20] would be explained by the decrease in the external part of Equation (16), trending toward a limiting value of  $E_{\text{mag}} \approx 6JS_p$ . For the polaron ions involved in this study, comparison between theory and experiment is also presented in Table 4, where at least qualitative agreement is established. The failure of Ni, Co, and Mn to reach calculated levels suggests that only for Cu with  $S_p = 0$  does  $F_\theta \rightarrow 0$  and gives credence to the notion that diamagnetic polarons are required for a complete local breakdown of magnetic order.

Two conditions necessary for the minimization of  $E_{\text{mag}}$  emerge from Equation (16),  $F_\theta \rightarrow 0$  and  $S_p = 0$  (thereby setting  $S_L = 1/2$ ). If  $S_L = 0$ , the magnetic alignment requirement is erased. The effects of canting are somewhat more subtle, but nonetheless play an important role in the ability of some systems to support activationless current transport. As depicted in Figure 7(b) for the real case of  $S_L = 1/2$ ,  $S_p = 0$ , the polaron has a double-barreled effect on neighboring lattice spin alignments that can lead to a total breakdown in static magnetic order. In this situation, the intrinsic part of Equation (16) drops out, and (12) can be approximated by

$$E_{\text{hop}} = E_{\text{el}} + (2z-3)JF_\theta \quad (17)$$

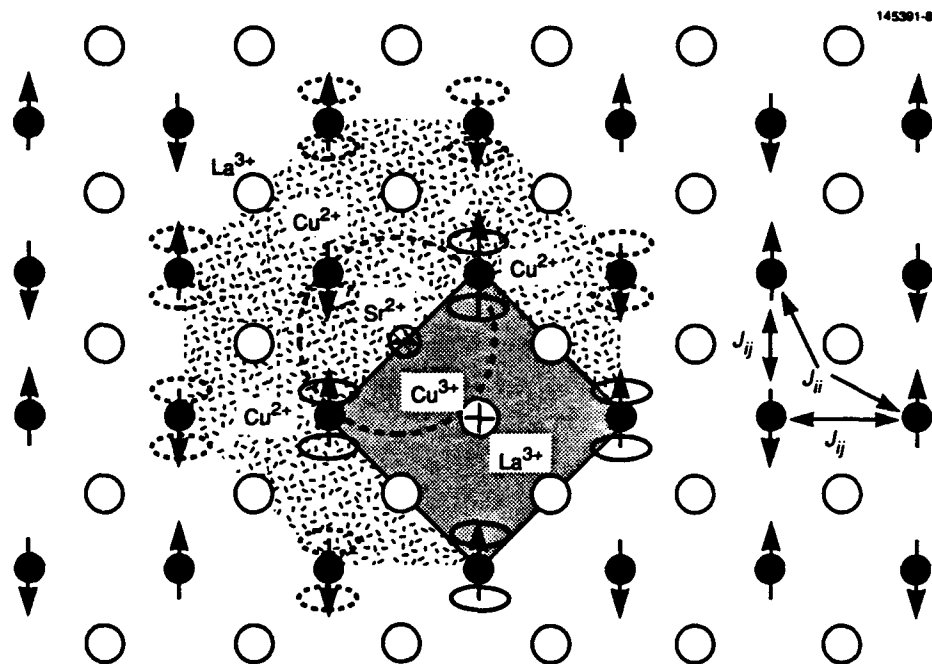


Figure 8. Cation sublattice projection of  $\text{La}_{2-x}\text{Sr}_x\text{CuO}_4$  viewed along  $c$  axis, with La and Cu ions in alternate planes. Note the canted spins about the  $S_p = 0$   $\text{Cu}^{3+}$  hole (at corners of shaded square) and the four small polaron Cu sites around  $\text{Sr}^{2+}$  that provide a region of frustration that encloses 12 spins.

With an  $S_p = 0$  polaron, it follows that its diamagnetism will also create a region of local frustration around the polaron source. Because the exchange isolation [29] from the missing couplings will also induce canting in the spins immediately surrounding the zero-spin polaron site [30], each polaron can produce an extended region of magnetic disorder.

In the superconducting perovskites, there is no direct dilution of the Cu sublattices. As examined at length in the original report [1], it is the minority  $\text{Cu}^{3+}$  ions in low-spin ( $S_p = 0$ ) states that provide the cause of spin canting. Unlike the case of fixed magnetic dilutants, the itinerance of the  $\text{Cu}^{3+}$  ions can cause the greatly enhanced region of frustration. Transfer of the polaron also means that the elastic deformations of the trap form a "wake" of canting ( $F_\theta \rightarrow 0$ ) that relaxes at a rate determined by the strength of spin-lattice coupling, thus creating a persistence to the region of frustration that could be sustained until the polaron returns to the same site (similar in principle to the raster of a television screen). At low temperatures the relaxation time increases, thereby offsetting the tendency for magnetic ordering to stabilize as  $T \rightarrow 0$ , and raising the likelihood of continued frustration within the region affected by the movement of the diamagnetic polaron.

Within the small polaron limit depicted in Figure 8 for  $\text{La}_{2-x}\text{Sr}_x\text{CuO}_4$ , a total of 12 spins are subjected to at least partial magnetic frustration.<sup>10</sup> As the density of moving polarons increases and the average value of  $F_\theta \rightarrow 0$ , the net exchange field would be canceled at  $x = 0.08$ , with individual spins forming a type of fluid state that is uncommitted to any single direction [31].

<sup>10</sup> In an antiferromagnetic system, a common condition for the breakdown of magnetic ordering is  $N_{ij} > (3/4)N_{ii}$ , as pictured in Figure 8 in terms of the respective  $J$  constants.

### 3.5 SUPERCONDUCTION AND ZERO-SPIN POLARONS

A generic representation of Equation (17) is presented in Figure 9 to suggest the manner of the decrease in  $E_{\text{hop}}$  with the growth of spin disorder as the polaron density increases. In conjunction with the Figure 4 data, the effects of spin canting are suggested by the decrease in  $E_{\text{hop}}$  with polaron concentration, where the most pronounced effect appears with the  $\text{Cu}^{2+(3+)}$  combination. (Note that each  $\text{M}^{3+}$  polaron is accompanied by a diamagnetic  $\text{Li}^{1+}$  ion that likely occupies an adjacent site to minimize electrostatic energy.) Here the spin state of  $\text{Cu}^{3+}$  is most likely  $S_p = 0$ , in accord with the noncubic symmetry of the  $\text{CuO}$  lattice that should result from a static Jahn-Teller effect. Because the activation energy of the Cu system decreases to values in the millielectron volt range as the exchange interactions erode with increasing  $x$ , it is concluded that the major part of  $E_{\text{hop}}$  in transition metal oxides is contributed by magnetic exchange.<sup>11</sup> Additional support for this conclusion appears in the data of George et al. [32], shown in Figure 10, where the activation energy above room temperature is seen to increase with the spin of the rare earth perovskite  $(\text{RE})_2\text{CuO}_4$ , in which the RE ions exchange with  $\text{Cu}^{2+}$  ions. Only the composition with diamagnetic  $\text{La}^{3+}$  produces an  $E_{\text{hop}}$  in the millielectron volt range, exposing a metallic slope of  $\rho$  versus  $T$  in the regime below 600 K.

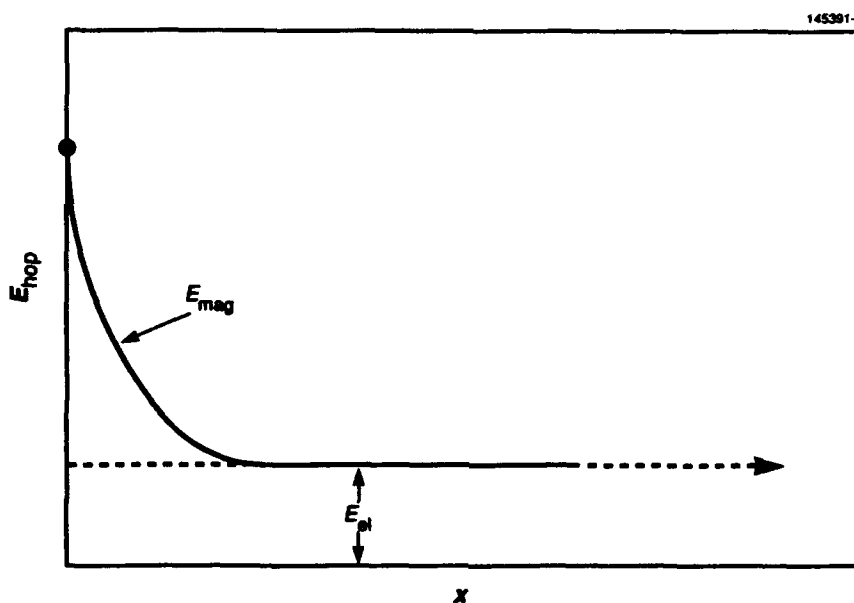


Figure 9. Model curve of the decrease in activation energy with the increase in polaron concentration.

<sup>11</sup> A more comprehensive summary of the  $E_{\text{hop}}$  values for these simple transition-metal oxides may be found in Schieber [19], Section V.A.

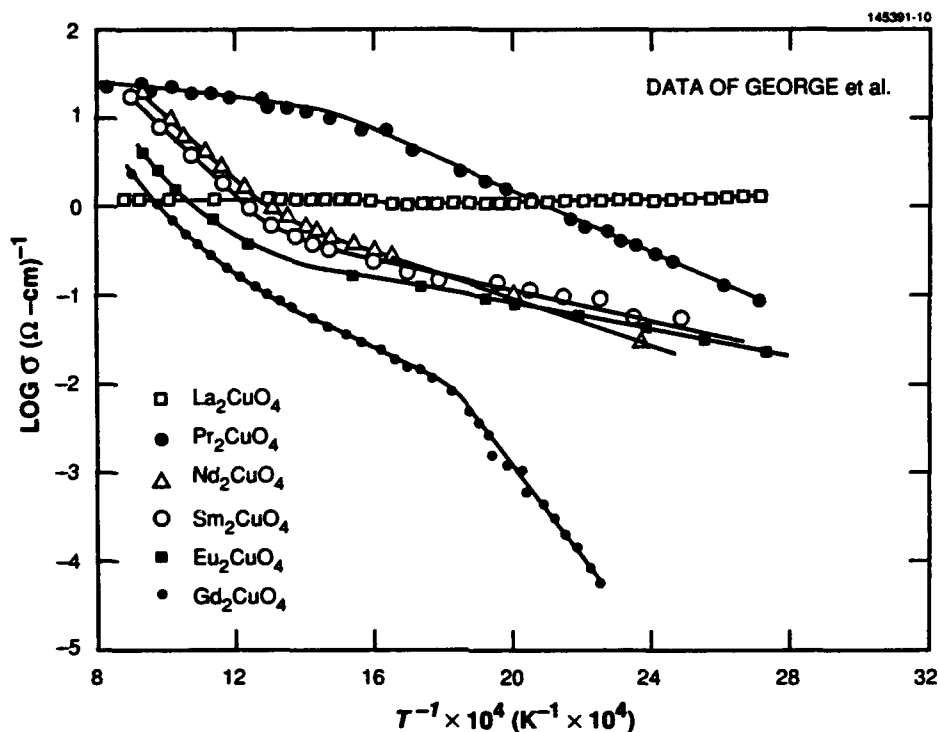


Figure 10. Influence of rare-earth (RE) magnetism on the semiconduction (activation energies) of an  $(RE)_2CuO_4$  series (George et al. [32]).

As summarized in Table 5, only a select number (see Figure 11) of mixed-valence pairs may be capable of satisfying the zero-spin condition for covalent transfer. These situations arise in transition metals where crystal-field stabilization energy of the higher energy electrons is comparable to the mutual repulsion energy (internal exchange) of electrons orbiting the same nucleus, i.e., the basis for Hund's rule. In order of descending  $d$  electron population:  $d^{10} \rightarrow d^9$ ,  $d^9 \rightarrow d^8$  (low spin),  $d^8$  (low spin)  $\rightarrow d^7$  (low spin),  $d^7$  (low spin)  $\rightarrow d^6$  (low spin), and  $d^1 \rightarrow d^0$ . The  $s^1 \rightarrow s^0$  is included, because it will be shown later that the covalent transfer mechanism can apply for  $Pb^{3+(4+)}$  and  $Bi^{4+(5+)}$  in perovskites [also  $Tl^{2+(3+)}$  if it can be found in a suitable compound].

**TABLE 5**  
**Zero-Spin Polarons for Covalent Transfer<sup>a</sup>**

Spin States <b>S = 1/2</b> <b>S = 0</b>	Coordination <sup>b</sup>	Cations <sup>c</sup>	Orbital <sup>d</sup>	Delocalization	Polaron Type <sup>e</sup>
<b><math>d^1 \rightarrow d^0</math></b>	<b>Octahedral</b>	<b>Ti<sup>3+(4+)</sup></b> <b>V<sup>4+(5+)</sup></b> <b>Nb<sup>4+(5+)</sup></b> <b>Ta<sup>4+(5+)</sup></b>	<b><math>d_{xy,xz,yz}</math></b>	<b>half-filled/empty</b>	<b><math>n</math> and <math>p</math></b>
$d^5(1s) \rightarrow d^4(1s)$	Tetrahedral	Fe <sup>3+(4+)</sup>	$d_{z^2}, x^2-y^2$	half-filled/empty	
$d^7(1s) \rightarrow d^6(1s)$	Octahedral	Co <sup>2+(3+)</sup>	$d_{x^2-y^2}$	half-filled/empty	
<b><math>d^7(1s) \leftarrow d^8(1s)^f</math></b>	<b>Octahedral</b>	<b>Ni<sup>3+(2+)</sup></b>	<b><math>d_{z^2}</math></b>	<b>half-filled/filled</b>	<b><math>p</math></b>
$d^9 \rightarrow d^8(1s)^f$	Octahedral	Cu <sup>2+(3+)</sup>	$d_{z^2}$	half-filled/empty	$p$
$d^9 \leftarrow d^{10}$	Octahedral	Cu <sup>2+(1+)</sup>	$d_{x^2-y^2}$	half-filled/filled	$n$
<b><math>s^1 \rightarrow s^0</math></b>	<b>Octahedral</b>	<b>Pb<sup>3+(4+)</sup></b> <b>Bi<sup>4+(5+)</sup></b>	<b><math>s(p)^g</math></b>	<b>half-filled/empty</b>	<b><math>p</math></b>

<sup>a</sup> Entries in **bold type** indicate cases where superconduction has been reported in an oxide. For  $d^1 \rightarrow d^0$  and  $d^{10} \rightarrow d^9$ , the relative distribution of the mixed valence creates  $n$ -type polarons.

<sup>b</sup> Octahedral sites reduce to planar coordinations where the c-axis ligands move to infinity.

<sup>c</sup> Bracket values represent the  $S = 0$  state, which is the polaron in all cases except Ni<sup>3+(2+)</sup> where  $S = 0$  clusters exchange isolate an  $S = 1/2$  polaron.

<sup>d</sup> For  $d_{xy,xz,yz}$  orbitals, transfer is by direct cation-cation exchange and should be less efficient in oxides.

<sup>e</sup> The polaron is defined as the minority ion. If it donates the electron, material will behave as  $n$ -type; if it receives the electron, it is  $p$ -type, regardless of its spin state.

<sup>f</sup> Low-spin  $d^8$  ( $S = 0$ ) requires planar symmetry or a strong tetragonal c-axis distortion.

<sup>g</sup> In an ionic model, the transfer electrons are in  $6s$  states, but in a molecular orbital model the  $6p$  states become more stable, as discussed in Section 7.1.

It is clear from an examination of the orbital occupancies (see Table 2) of Cu<sup>1+</sup> (filled  $d$  shell,  $d^{10}$ ), Ti<sup>4+</sup>, V<sup>5+</sup>, Nb<sup>5+</sup> (empty  $d$  shells,  $d^0$ ), and Pb<sup>4+</sup> and Bi<sup>5+</sup> (empty  $s$  shells,  $s^0$ ) that an  $S = 0$  state is fixed. More interesting situations develop, however, where the ions can assume dual spin configurations,<sup>12</sup> e.g.,  $d^8$ ,  $d^7$ , and  $d^6$ . Based on the diamagnetic behavior of La<sup>3+</sup><sub>2</sub>[Li<sup>1+</sup><sub>0.5</sub>Cu<sup>3+</sup><sub>0.5</sub>]O<sub>4</sub> [34] and the weak paramagnetism of La<sup>3+</sup>Sr<sup>2+</sup>Cu<sup>3+</sup>O<sub>4</sub> [24], the orbital occupancy of Cu<sup>3+</sup> was judged to produce  $S = 0$  state. Because a 3+ charge on the Cu ion would substantially increase the tetragonal field splitting of the  $e_g$  states over that of the host Cu<sup>2+</sup> ion, this finding is consistent with theory. Furthermore, low-spin Cu<sup>3+</sup> could not explain the magnetic properties of the nearly cubic La<sup>3+</sup>Cu<sup>3+</sup>O<sub>3</sub> compound [34]. In addition,  $E_{\text{hop}}$  has been inferred [1] from  $T_c$  data to be approximately 3 meV in the La<sub>2-x</sub>Sr<sub>x</sub>CuO<sub>4</sub> system, in accord with the 3-meV value determined for LaSrCuO<sub>4</sub> [24], further indicating that  $E_{\text{mc,g}}$  has been quenched by the presence of zero-spin cations and suggesting that  $E_{\text{hop}} \approx E_{\text{el}}$ .

<sup>12</sup> In general, Hund's rule of maximum spin polarization can be violated if the crystal-field splitting is large enough to offset the electrostatic repulsion energy of the unpaired electrons (internal exchange). This occurs where the cubic splitting parameter  $Dq$  is large, usually for high cation valence [33]. In the case of  $d^8$ , an additional tetragonal splitting  $> 0.1$  eV is required to relax the aligned  $S = 1$  pair to  $S = 0$  in the  $e_g$  shell.



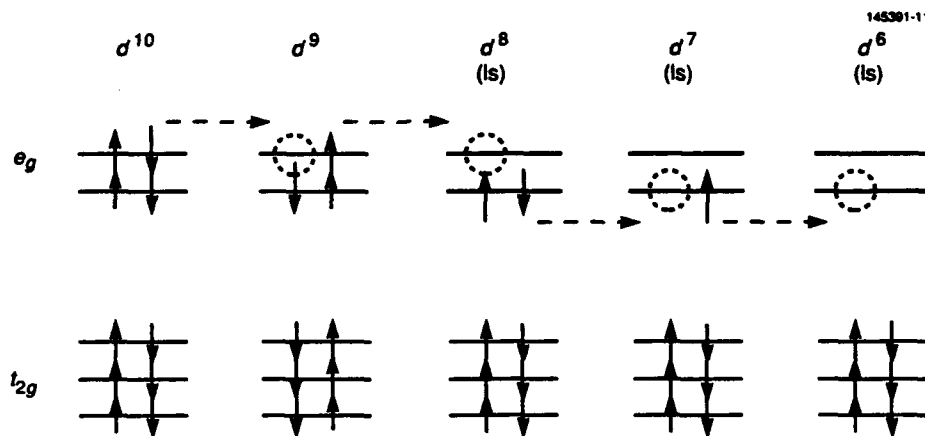


Figure 11. Schematic diagram of  $S = 1/2 \rightarrow S = 0$  transfers among  $3d^n$  group.

Another case worthy of discussion, which will be examined in Section 7.1 and Appendix F, is that of  $\text{Ni}^{3+(2+)}$ . Previously studied by Morin [35], Goodenough et al. [36], and Springthorpe et al. [28] in  $\text{Li}^{1+}_x\text{Ni}^{2+}_{1-2x}\text{Ni}^{3+}_x\text{O}$ ,  $\text{Ni}^{3+}(d^7)$  favors a low-spin state ( $S = 1/2$  instead of  $3/2$ ), as interpreted from the ferromagnetic behavior at  $x > 0.3$  [36]. With low-spin  $\text{Ni}^{3+}$ , the attendant Jahn-Teller effects originating from the single electron occupying the degenerate  $e_g$  states may become static at lower temperatures, and thereby create a local tetragonal component to the crystal field of neighboring  $\text{Ni}^{2+}$  ions, with the expectation of driving them also into a low-spin ( $S = 0$  instead of 1) state. Such an occurrence would immediately create transfer pairs of low activation energy that would not only alter the normal conduction behavior with temperature, but could also permit the creation of superconducting polaron cells. The radical decrease in the slope of  $\log(\rho/T)$  versus  $1/T$  data of Springthorpe et al. for  $T < 100$  K suggests that small amounts of low-spin  $\text{Ni}^{2+}$  are created at low temperatures even in this simple cubic material. More compelling evidence of nickel low-spin states was recently reported in the results Kakol et al. [37] of a series of experiments with  $\text{La}_{2-x}\text{Sr}_x\text{Ni}_x\text{O}_4$ , which yielded  $p$ -type semiconduction with  $E_{\text{hop}} \approx 20$  meV at room temperature, as well as a superconduction  $T_c < 70$  K. Because the  $B$ -site  $\text{Ni}^{2+}$  ions experience a strong tetragonal crystal field even before enhancement by  $\text{Ni}^{3+}$  Jahn-Teller stabilization, a sizeable population of zero-spin  $\text{Ni}^{2+}$  ions is a strong possibility.

For the case of  $\text{Co}^{2+(3+)}$ , the low-spin state ( $S = 0$ ) of  $\text{Co}^{3+}(d^6)$  in octahedral sites was established by Bongers [27] and Blasse [38]. The occurrence of low-spin ( $S = 1/2$ )  $\text{Co}^{2+}(d^7)$  is less probable because its smaller ionic charge leads to a reduced  $Dq$ , therefore covalent transfer with this ionic combination is not expected. Mixed-valence combinations involving Mn and Fe are also unlikely to provide covalent transfer;  $\text{Mn}^{3+}$  and  $\text{Fe}^{4+}$  (both  $d^4$ ) can theoretically assume  $S = 0$  configurations but only in tetrahedral sites,<sup>13</sup> where 180-deg  $\sigma$  bonding to oxygen ligands is not available.

<sup>13</sup>An interesting possibility for an  $\text{Fe}^{4+}(d^4)$  low-spin state in  $\text{Y}^{3+}_{3-x}\text{Ca}^{2+}_x\text{Fe}^{3+}_{5-x}\text{Fe}^{4+}_x\text{O}_{12}$  garnet [39] was suggested by a decrease in magnetization at low temperatures, signaling a possible change to the  $S = 0$  state. In spite of the large ionic charge, however, the  $Dq$  value for a tetrahedral site is only  $4/9$  that of an octahedral site, and the interpretation that is based on ferromagnetic alignment between high-spin  $\text{Fe}^{4+}$  ions ( $S = 2$ ) in tetrahedral sites and  $\text{Fe}^{3+}$  ions ( $S = 5/2$ ) in octahedral sites is more reasonable.

Experimental confirmation of the incompatibility between antiferromagnetic order ( $E_{\text{mag}} > 0$ ) and superconduction (requiring  $E_{\text{mag}} \rightarrow 0$ ) was clearly established for the  $\text{La}_{2-x}\text{Sr}_x\text{CuO}_4$  and  $\text{YBa}_2\text{Cu}_3\text{O}_y$  cuprate systems [40–42], as shown in Figure 12, where the appearance of a measurable  $T_c$  begins only after the Néel temperature  $T_N$  falls to zero at  $x \approx 0.05$ . This value of  $x$  is compatible with the prediction of 0.08 deduced in Section 3.4 [31]. The coincidence of these two effects will be explained later on the basis of large polaron radii, which determine both the volume of local magnetic frustration and the threshold concentration for superconduction. Observed changes in crystallographic symmetry (the tetragonal to orthorhombic phase transition) could be interpreted as resulting from the onset of magnetic frustration and is often associated with the appearance of cooperative Jahn-Teller effects in systems where Jahn-Teller ions are present.

The implications of this rationalization for superconduction in the presence of magnetic ions follow directly: Where static antiferromagnetism exists through long-range spin ordering ( $T < T_N$ ), there can be no superconduction; where residual dynamic antiferromagnetic exchange remains locally, superconduction can occur through covalent transfer by two electrons (real-space pairs) moving in correlation to permit the hole to transfer within the same magnetic sublattice in concert with spin wave fluctuations that satisfy local antiferromagnetic requirements, as discussed in Dionne [1].

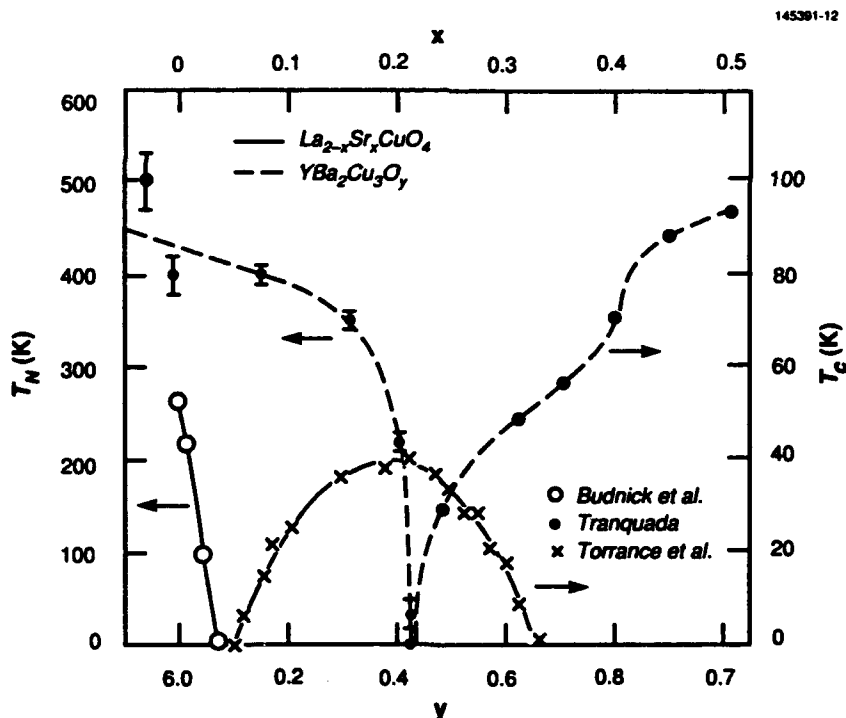


Figure 12. Experimental verification of the magnetic frustration requirement prior to the onset of superconductivity in  $\text{La}_{2-x}\text{Sr}_x\text{CuO}_4$  and  $\text{YBa}_2\text{Cu}_3\text{O}_y$  systems (data of Budnick et al. [40], Tranquada [41], and Torrance et al. [42]).

## 4. MOLECULAR ORBITAL CONDUCTION

The implications of the London theory were reviewed in Section 1.2, where it was pointed out that because of the spatial rigidity constraint, supercurrents could not comprise normal free electrons in a conduction band. Thus, either the free electrons would have to alter their collective state or bound electrons would have to be involved. The principal difference between the CET and the theories used to interpret lower temperature superconduction in metals and intermetallic compounds is that supercurrents (or superelectrons) are not formed from a free-electron gas. As proposed in the previous report [1], activationless transfer of bound electrons between covalent orbitals may be the superconduction mechanism in mixed-valence insulator hosts. This concept departs from the Bardeen-Cooper-Schrieffer idea that paired electrons (bosons) condense from the free-electron gas and returns to some of the earlier views of the Londons [9]. Instead of electrons correlated as pairs in  $k$  space, the correlation exists in real space for an entire chain of polarons in the same sublattice, as the associated electrons (or holes) move in ordered cadence through the covalent bonds of a single giant molecule.

### 4.1 COVALENT TRANSFER VERSUS THERMAL HOPPING

As pointed out in Section 2.1, the electron hopping mechanism that is responsible for the semiconduction properties of oxides is energy conserving when the initial and final states are equivalent with respect to the polaron source.<sup>14</sup> Such is the case where the ions represent different valence states of the same atom. In a quantum mechanical sense, the carrier can occupy either site with equal probability and no net energy expense is involved in a transfer. As long as phonons are available to provide activation, the equivalent sites surrounding the polaron source are in dynamic equilibrium, similar to an electron being shared among atoms in a molecular covalent bond. An important fundamental distinction between a molecule and the hopping transfer situation, however, lies in the fact that covalent sharing is spontaneous, while hopping requires activation. Spontaneous transfer occurs where the covalent state with the electron that is shared among equivalent ions is more stable than localization of the electron on any single ion.

The difference may therefore be stated as follows: With covalent sharing, the electron exists as a statistical probability among the ions of a polaron cell, independent of electron-lattice interaction; with thermal hopping, the electron is transferred between ions through an energy activation from phonons.<sup>15</sup>

---

<sup>14</sup>As background to this topic, the reader is advised to consult the comprehensive discussion of this problem set forth by Goodenough [43], particularly in relation to the localized versus collective electron situations and how the covalent transfer integral  $b$  might influence not only electrical conduction through band broadening (and energy gap narrowing), but also magnetic order and lattice elastic deformations. In the basic CET theory, only the special case of mixed valence is involved ( $c \neq 0$ ), and it is assumed that the carriers are at least quasi-localized, with bandwidths that may still be approximated by discrete levels.

<sup>15</sup>The concept of polaron hopping in nonsuperconducting  $\text{La}_{2-x}\text{Ca}_x(\text{Mn}^{2+}_{1-x}\text{Mn}^{3+}_x)\text{O}_4$  was examined in detail by de Gennes [18]. One important difference from the CET model is his use of the parameter  $b$  as a hopping integral rather than a covalent transfer energy. Hopping may have been considered by de Gennes as the only conduction mechanism here, but it must also be remembered that his work was carried out long before superconduction in these materials was considered possible.

Transition-metal oxides have been analyzed according to orbital energy-level structures described by the point-charge crystal-field model [1]. A schematic diagram showing the alternate conduction mechanisms of the  $\text{Cu}^{2+}\text{-O}^{2-}\text{-Cu}^{3+}$  is given in Figure 13. Because the discussion was primarily qualitative, this approximation was quite sufficient. Where the chemical systems are more strongly covalent or where a more quantitative examination of the covalent component of the orbital stabilization is desired, an MO model can provide information about the mixing of the individual wave functions that comprise the covalent bond [44–46]. In Figure 14, the formation of bonding and antibonding MO states are adjusted for slightly covalent (ionic insulators) and covalent (band model) semiconductors and collective electron conductors (metals). If an MO formalism is adopted according to the analyses in Appendices A, B, and C, the problem may also be generalized to include both cation-anion-cation and direct cation-cation transfers.

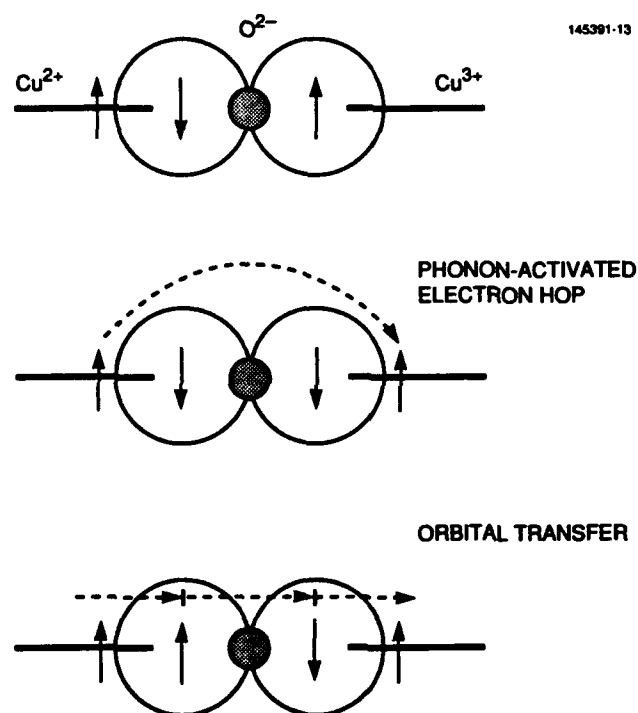


Figure 13. Essential definition of two alternative conduction mechanisms (shown as single transfers in a ferromagnet or paramagnet). Hopping requires external activation, while covalent transfer is spontaneous.

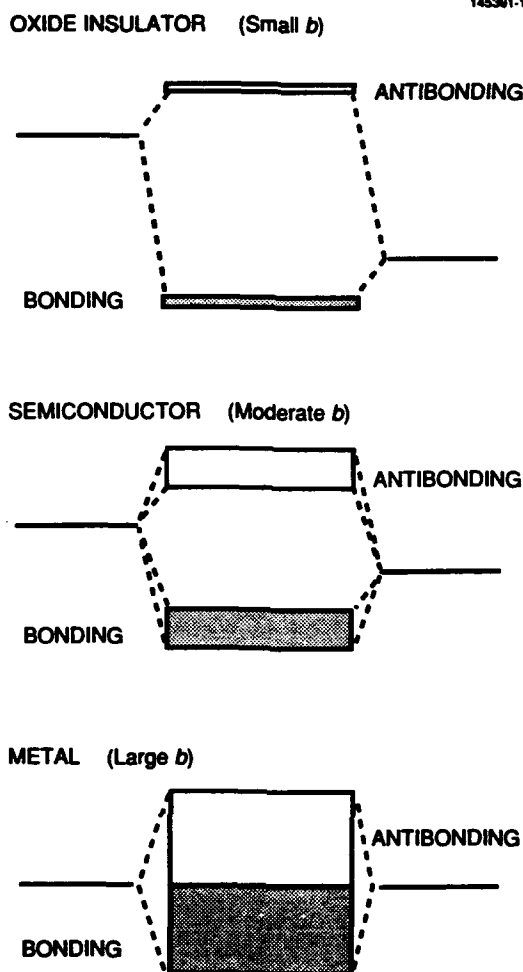


Figure 14. Conceptual description of the formation of a pair of molecular orbital states, and the growth of energy bands from the transfer integral energy  $b$ .

For a purely ionic bond there is no covalence, and the activation barrier between the two equivalent sites can be represented by Figure 15(a). If covalent stabilization is then "switched on" (assuming the addition of the necessary orbital overlaps), the bonding energy level is lowered by  $b/2$  with  $b$  as the effective transfer energy integral (see Appendix C) for the case where the two metal cations have the same stabilization energy, i.e.,  $E_M = E_{M'}$ . In Figure 15(c), the MO stabilization is shown to reduce the energy of the hybrid bond level with the result that the activation barrier is compromised by the energy made available through the covalent stabilization. Where the transfer integral exceeds the hopping barrier energy [Figure 13(d)], electron transfer is spontaneous because covalent sharing between ions is a more stable state than localization on an individual

cation. The threshold for covalent (activationless) transfer is therefore  $b \geq E_{\text{hop}}$ , under which conditions the individual transfer ions may no longer claim stationary valence states but become part of a cation sublattice of average positive charge in the manner of any quantum mechanical eigenstate.<sup>16</sup>

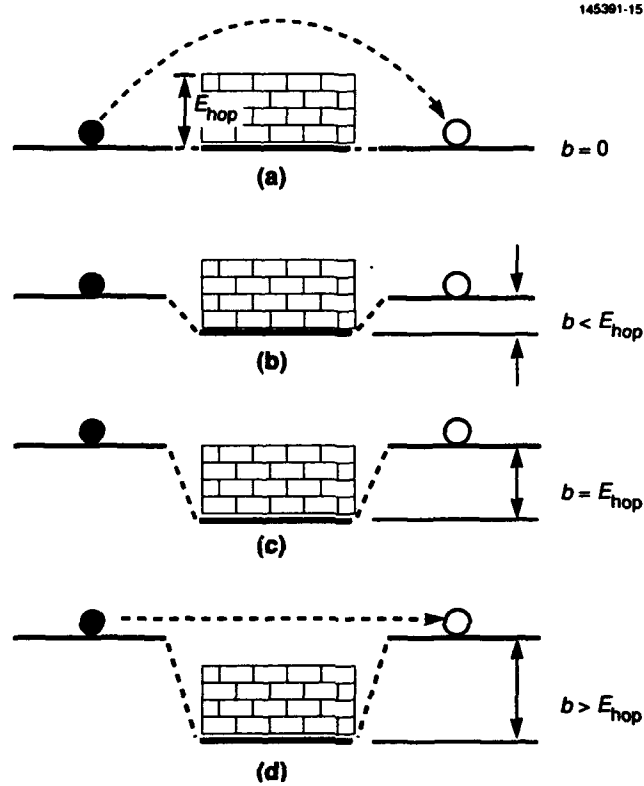


Figure 15. Pictorial definition of small polaron limit, showing how covalent stabilization overcomes local polaron trap energy ( $b \geq E_{\text{hop}}$ ).

There is an obvious trade-off between the covalent transfer energy  $b$  and the magnetic exchange integral  $J = \hbar^2 / 2S_L^2 U$  that emphasizes the need for frustration to occur. Because the combined transfer integral  $b_{\text{tot}} > b$  in all cases with  $S_L > 1/2$ , where unpaired spins occupy orbitals in addition to the transfer orbital ( $d^5$ ,  $d^6$ ,  $d^7$ , and  $d^8$ ), the CET condition may be stated as

$$b \geq (b_{\text{tot}} / 2S_L^2 U) [(2z-3)S_L F_\theta + 3S_p] \quad (18)$$

<sup>16</sup> To the extent that the carriers exist in  $d$ -electron energy bands that result from significant covalent interaction through  $b$ , they may be considered as collective according to the Goodenough criteria [43]. Although it is still convenient to discuss the ionic character of the materials in terms of specific valence states (e.g.,  $\text{Cu}^{2+}$ ,  $\text{Cu}^{3+}$ ), it is unrealistic to expect experimental identification of individual ionic species when they exist only in a state of transient equilibrium, as a wave function that is neither here nor there, but simultaneously everywhere!

Equation (18) reemphasizes the necessity of  $F_\theta \rightarrow 0$  and a zero-spin presence ( $S_L$  or  $S_p = 0$ ) in the transfer ion pair. This inequality also defines a *small* polaron limit in the sense of Holstein,<sup>17</sup> as depicted in Figure 16, because spontaneous polaron movement among equivalent sites requires that  $h \geq E_{\text{hop}}$ . Moreover, it allows condition for the formation of a *large* polaron cell for which the carrier becomes itinerant within a range determined by the strength of the dipole attractive field, causing magnetic frustration (where  $S = 0$ ) that serves as a necessary superconducting state.

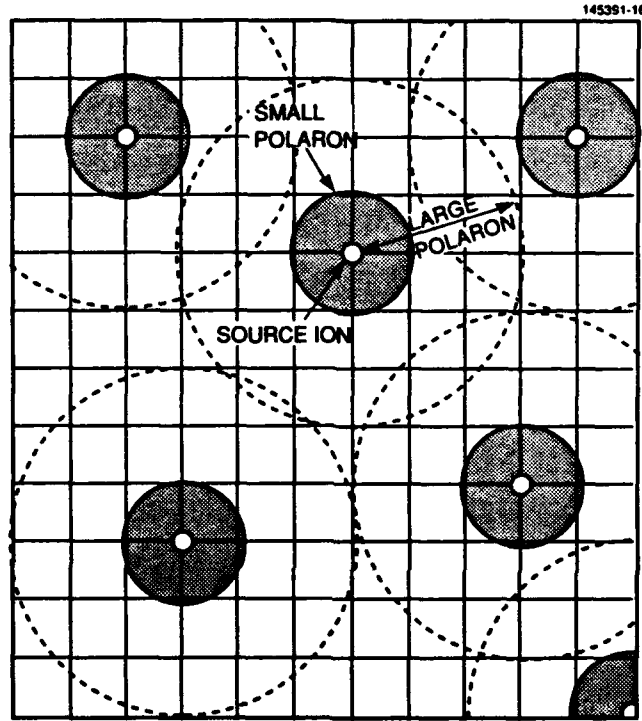


Figure 16. Two-dimensional description of large polaron cells amidst fixed polaron ionic sources.

<sup>17</sup> This result strongly resembles the small polaron limit determined by Holstein's model [14], in which the net polaron trapping energy  $E_p$  [from his Equation (46)] in the absence of magnetic ordering reduces to

$$E_p = E_{\text{el}} - 2J,$$

where  $J = h/2$ , and  $E_{\text{el}} = (1/2)(e^2/\pi 3aK_{\text{eff}})$ . Note that  $E_{\text{el}}$  varies inversely with the lattice distance  $a$  and the effective dielectric constant  $K_{\text{eff}}$ .

There is also a fundamental difference in Holstein's use of the transfer integral  $h$  for the large polaron case (his band-type solution) in which the covalent energy is treated as a perturbation that reduces the magnitude of the trapping energy according to [from his Equation (37)]

$$E_p = (e^2/2\pi^3 a K_{\text{eff}})^2 / 48h.$$

In this case, it will be seen that the basic elastic/electrostatic trapping energy ( $E_{\text{el}}$ ) is not viewed as dependent on  $h$ , instead the influence of covalence enters through a molecular orbital stabilization/destabilization splitting that raises the effective energy of the carrier state, as analyzed in Section 4.2. The most important difference, however, arises from the use of the CET mechanism as a competitor to thermal hopping.

## 4.2 QUANTUM MECHANICAL TRANSFER EFFICIENCY

In Appendices A and B, molecular-orbital theory is first applied to the simple case of a metal-ligand molecule to establish the basic MO functions of the bonding and antibonding  $d_{x^2-y^2} - p_{xy}$   $\sigma$  states of  $\text{Cu}^{2+}\text{-O}^{2-}$ . In Section 4.1, the requirement for activationless transfer between equivalent polaron sites was defined as  $b \geq E_{\text{hop}}$ . If  $E_{\text{hop}}$  is largely of magnetic origin, this condition represents the situation where covalent stabilization exceeds magnetic exchange destabilization, where orbital overlap can permit electron transfer without intermediate spin realignments.

If the two sites are not equivalent with respect to the polaron source, there is a net energy defined as  $\Delta E$  resulting from the change in Coulomb attractive force ([1], p. 35). In the absence of covalent orbital overlap ( $b = 0$ ), thermally activated hopping may transfer electrons by surmounting the energy barrier of the model in Figure 15; therefore, transport to sites of higher energy requires the energy input of an accelerating field.

With the covalent transfer energy  $b \rightarrow E_{\text{hop}}$ , the possibility of tunneling grows until the equivalent sites merge as a single molecule, with an equal probability of a mobile polaron occupying any of the sites. For transfer between inequivalent sites (where  $\Delta E > 0$ ), the  $b \geq E_{\text{hop}}$  condition is not sufficient. To compute the transfer efficiency as a function of changing polaron energy, the molecular orbital eigenfunction for the linear pair of CuO molecules constructed in Appendix C will be used as a building block to establish a general relation for a continuous chain. From Equation (C-10), the MO state where the transfer electron (or hole) resides is restated:

$$\psi_- = 0.24 (k_{21}\chi_L + k_{22}\chi_{L'}) - 0.99 (k_{21}\chi_M + k_{22}\chi_{M'}) \quad , \quad (19)$$

where  $\chi_M$  and  $\chi_{M'}$  are the respective copper  $3d_{x^2-y^2}$  orbitals, and  $\chi_L$  and  $\chi_{L'}$  are the oxygen  $2p_{xy}$   $\sigma$  orbitals that form the overlaps. For covalent electron transfer between nearest-neighbor cations, the carrier density reduction factor (or transfer efficiency) at  $\chi_{M'}$  was determined from the occupation probability  $k_{12}^2$  as [see Equation (C-11)]

$$\eta_{12} = k_{12}^2 / 0.5 = 1 - 1/G_{12} \quad . \quad (20)$$

Consider now the question of successive transfers between large polarons along a continuous chain (see Figure 17). The polaron energy increase as a function of distance from its source may be expressed as

$$\Delta E_{1,\gamma} = - (e^2/Ka) (1/\gamma - 1) \quad , \quad (21)$$

where  $K$  is the dielectric constant. For the energy increase between two consecutive sites,

$$\Delta E_{\gamma,\gamma+1} = - (e^2/Ka) [1/(\gamma+1) - 1/\gamma] = (e^2/Ka) [1/\gamma(\gamma+1)] \quad , \quad (22)$$

where  $\gamma$  is an integer that counts the number of consecutive transfers of length  $a$  away from the polaron source. From Equation (22),  $G_{12}$  from Appendix C may now be generalized according to

$$G_{\gamma,\gamma+1} = b_{\gamma,\gamma+1} / \Delta E_{\gamma,\gamma+1} \quad . \quad (23)$$



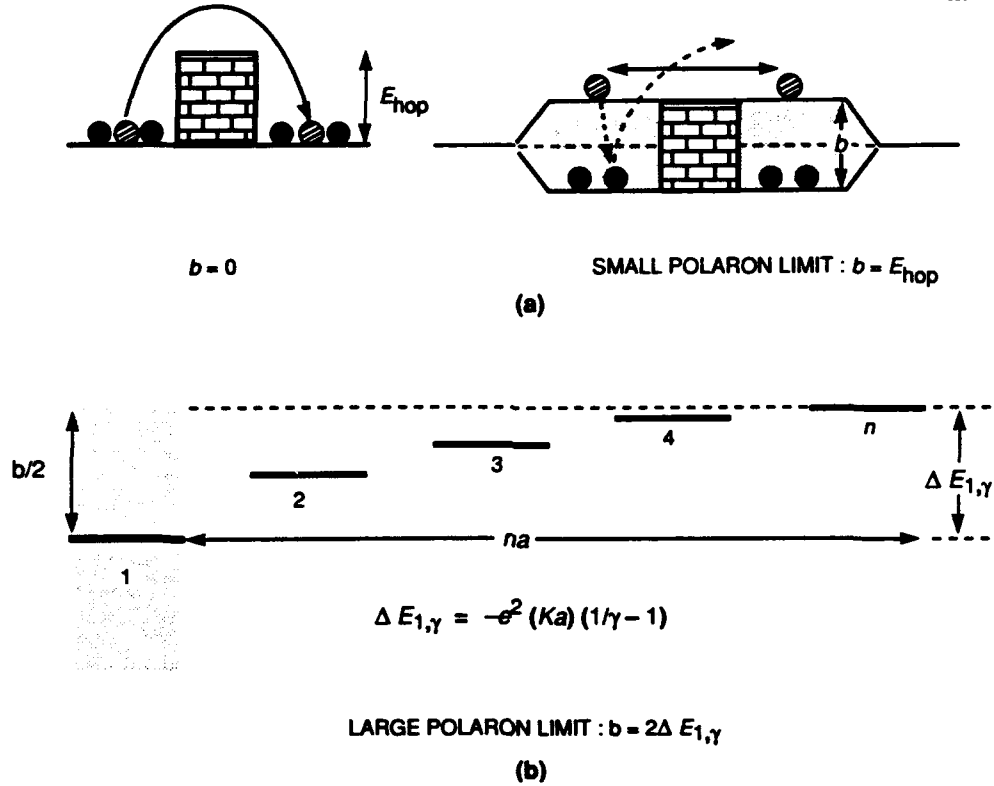


Figure 17. Comparison of small and large polaron energies: (a) carrier may transfer among equivalent sites across top of band if  $b \geq E_{hop}$ , unless it relaxes to fill state vacated by a hopping electron from bottom of band; (b) carrier may increase energy quantum mechanically in cumulative steps away from polaron source up to a limit determined by Equation (21).

From Equations (20) and (23), the transfer efficiency between  $\gamma = 1$  and  $\gamma + 1$  may be expressed as a product series

$$\eta_{1,\gamma+1} = \prod_1^{\gamma} \eta_{\gamma,\gamma+1} = (1 - G_{12})(1 - G_{23}) \dots (1 - G_{\gamma,\gamma+1}). \quad (24)$$

If  $G_{\gamma,\gamma+1} \gg 1$  (a good assumption for large  $\gamma$ ), Equation (24) simplifies to<sup>18</sup>

$$\eta_{1,\gamma+1} = 1 - \sum_1^{\gamma} 1/G_{\gamma,\gamma+1} = 1 - \sum_1^{\gamma} \Delta E_{\gamma,\gamma+1} / b_{\gamma,\gamma+1}. \quad (25)$$

<sup>18</sup>This relation follows from the theorem  $\prod_1^n (1 + u_n) = \prod_1^n (1 + x_n)$ , where

$$u_n = \frac{x_n}{\sum_1^{n-1} (1 + x_n)}$$

if  $x_1 \ll 1$ .

Because  $b_a = (\Lambda_+ + \Lambda_+' )s_a$  from Equation (C-2), we can define

$$b_{\gamma,\gamma+1} = (\Lambda_\gamma + \Lambda_{\gamma+1})s \quad (26)$$

To a good approximation,  $\Lambda_\gamma \approx \Lambda_1 + \Delta E_{1,\gamma}$  (where  $\Lambda_+$  is now relabeled as  $\Lambda_1$ ) and  $b_{\gamma,\gamma+1} \approx (2\Lambda_1 + \Delta E_{1,\gamma} + \Delta E_{1,\gamma+1})s$  with the subscript dropped from  $s_a$ . Because  $\Lambda_1 \gg \Delta E_{1,\gamma}$  (in the present case,  $|\Lambda_1| \approx 4 \text{ eV}$  and  $|\Delta E_{1,\infty}| \approx 0.5 \text{ eV}$ ), Equation (25) can be simplified to

$$\eta_{1,\gamma+1} \approx 1 - \sum_1^\gamma \Delta E_{\gamma,\gamma+1} / 2\Lambda_1 s \approx 1 - \Delta E_{1,\gamma+1} / 2\Lambda_1 s, \quad (27)$$

or

$$\eta_{1,\gamma} \approx 1 - \Delta E_{1,\gamma} / b, \quad (28)$$

where  $\Delta E_{1,\gamma} \approx -(e^2/Ka)(1/\gamma - 1)$  and  $b \approx 2\Lambda_1 s$ , and both quantities are treated as positive. [For computational purposes, a term  $\sim +0.4(e^2/Kab)^2$  will be added to Equation (28) to correct for a small second-order contribution that was lost in the approximation.]

This carrier reduction factor will later be expressed as a function of polaron density and used to modify the superconducting carrier concentration in the phenomenological model for determining the critical temperature. Because  $\eta_{1,\gamma}$  is related to the carrier wavefunction profile away from the site of minimum energy (i.e., closest to the polaron source), it also represents the short-range decay of the normalized charge density  $|\psi_s|^2$  as a function of distance (Figure 18), and therefore, may be used to define the radius of a large polaron cell that would determine the region of local magnetic frustration.

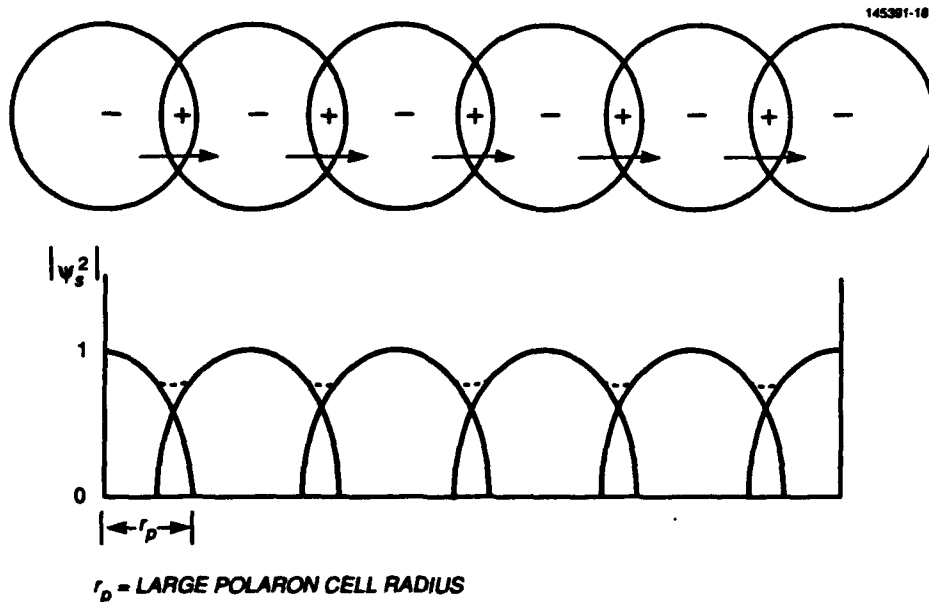


Figure 18. One-dimensional model of a large polaron chain indicating the merger of carrier density functions  $|\psi_s|^2$  to establish a continuous molecular orbital state.

### 4.3 LARGE-POLARON ARRAY CONCEPT

From the idea that the carriers reside in the orbital wavefunctions of CuO layers, under the attractive influence of isolated fixed charges, e.g.,  $\text{Sr}^{2+}$  ions in a  $\text{La}^{3+}$  sublattice, there emerges a rationale for describing the conduction activity in real space rather than employing conventional band theory where the role of discrete charges is lost in  $k$  space.

If the CuO molecules are used as building blocks, the lattice may be divided into polaron cells consisting of connected CuO molecules arrayed about their respective stationary source charges. As depicted in Figure 16, each cell would contain one carrier that orbits the source charge in the guise of a zero-spin  $(\text{CuO})^+$  ion,<sup>19</sup> beginning as a small polaron that is transported among equivalent sites by thermal activation where  $h < E_{\text{hop}}$ , and then expanding into regions of molecular orbital conduction as  $E_{\text{hop}}$  decreases below  $h$  through the onset of magnetic disorder where the polaron carrier is associated with an  $S = 0$  situation as described above. For this to occur,  $E_{\text{hop}}$  need not reach its minimum value  $E_{\text{el}}$ . Only the threshold for MO transfers  $h \geq E_{\text{hop}}$  is required to begin the process of breaking down the magnetic order within the spatial limits of the polaron to be discussed in Section 5.1.

For complete MO conduction and magnetic frustration throughout the lattice, therefore, it is important that the polaron cells be uniformly dispersed. A material in which the polaron sources are clustered would logically have fewer carriers that are isolated from each other and the polaron lattice concept would not readily apply. To account for the effect of inhomogeneous dispersal of the polaron sources, the concentration  $x$  will be modified in Section 5.1 by a semiempirical ordering factor  $P$ , based on the same elementary probability arguments used originally in Appendix C of Dionne [1].

### 4.4 REAL-SPACE ELECTRON PAIRING AND ANTIFERROMAGNETISM

With the MO mechanism of transfer now defined, the observed superconduction critical phenomena can be interpreted. Before this subject is addressed, however, it might be prudent to introduce briefly the longstanding question of whether a supercurrent is a true superfluid in all cases, i.e., whether the boson particle condensation characteristic of superfluids is a universally necessary condition for superconduction. The introduction of this topic at this juncture arises from the nature of the charge carriers to be used in the theoretical modeling to follow. If the supercarriers must be boson pairs, as widely believed, how is the electron pairing physically realized in the CET scheme? Or are there situations where the carriers are correlated as individuals?

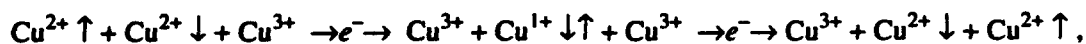
---

<sup>19</sup> It is appropriate here to remind the reader of the position taken in Appendix B, that localization of the hole in the CuO MO state could in theory favor the oxygen instead of the copper lattice for a different set of initial lattice energy parameters. To establish a zero-spin in this case, the  $\text{Cu}^{2+}$  spin ( $= 1/2$ ) would have to oppose the single spin of the now-paramagnetic  $\text{O}^{1-}$  ion. In terms of the  $\text{LaSrCuO}_4$  compound discussed in Section 3.5, valences and spin alignments might be expressed as  $\text{La}^{3+}\text{Sr}^{2+}\text{Cu}^{2+}(\uparrow)\text{O}^{1-}(\downarrow)\text{O}^{2-}_3$ . This model, however, does not easily explain the magnetic behavior of  $\text{LaCuO}_3$  or the superconduction of  $n$ -type  $\text{Nd}_{1.8}\text{Ce}_{0.2}\text{CuO}_4$ , to be discussed in Section 7.1.

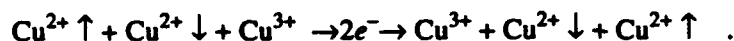
The BCS theory of superconductivity is predicated on the existence of conduction band electrons paired in  $k$  space through the mediation of lattice vibrational modes (phonons). Because the two electrons have  $+\mathbf{k}$  and  $-\mathbf{k}$  deBroglie momentum vectors, this device creates a carrier that immediately satisfies the basic macroscopic local requirement of superconduction, that is  $p$  (or  $k$ ) = 0, to yield a spatially rigid wavefunction. In addition, this concept automatically satisfies the spin pairing requirements (in  $k$  space) of the Pauli principle by assigning a resultant  $S = 0$  to the carrier. The paired electron carrier also provides the  $2e^-$  effective charge that is important for interpreting flux quantization and quasi-particle tunneling (Josephson effect) experiments.

In Dionne [1], paired carriers are discussed only in connection with double-charged mixed-valence polarons. In the basic description of the CET model, the carriers have been treated as individuals that move in correlation through a molecular orbital chain without concern for the disposition of electron spin states. In Sections 3.3 and 3.4, where the question of magnetic exchange interactions and their contributions to the stabilization energy  $E_{\text{hop}}$  was examined [1], it was pointed out that internal energy conservation could only be maintained in the absence of static cooperative antiferromagnetic ordering. Even if long-range ordering breaks down (above the Néel temperature), local exchange coupling can still contribute to  $E_{\text{hop}}$  and the superconduction can be quenched if  $h \leq E_{\text{hop}}$ .

A refinement to the single carrier transfer model that would account for both the spin coupling compensation and the paired-charge phenomena would logically consist of double electron transfer events. The most obvious (but least probable) scenario is the double mixed-valence transfer examined in Appendix B of Dionne [1] for the  $\text{Cu}^{1+}(d^{10}) \rightarrow \text{Cu}^{3+}(d^8) + 2e^-$  case; here both ions have  $S = 0$ , and the question of magnetic coupling is moot. The more likely double transfer scheme appropriate for an antiferromagnetic system would involve a two-electron energy-conserved event, where a singly charged polaron carrier (with  $S_p = 0$  that leads to magnetic frustration) moves in consecutive single-electron shifts to the closest magnetically equivalent site two bond lengths away through the formation of a virtual  $\text{Cu}^{1+}$  ion as an intermediate state according to



or two individual electrons moving in tandem by simultaneously trading spin states in the process, as depicted earlier in Figure 6(b), according to



Reference to the likelihood of some form of local electron pair formation in CuO is also mentioned in Goodenough's review [47]. In either case, the transfer event represents the minimum current unit and involves an effective charge of  $2e^-$ , in accord with the requirements for explaining flux quantization, quasi-particle tunneling and any other experiments that support the electron pair postulate.

Although it may be argued that this pair scheme could form the boson carriers required by the BCS theory, the pairs proposed here differ substantially from the phonon-mediated conduction electron Cooper pairs in  $k$  space. The electrons are part of the covalent bonding orbitals, the coupling is of local magnetic origin associated with spin polarization in real space, and the carriers (individuals or pairs) move as part of a correlated molecular chain, either in double steps or as real-space pairs exchanging spin states during transit.

In the context of the CET model, there is another situation that may challenge the basic boson requirement of superconduction. In oxide systems that feature a mixed-valence  $\text{Ti}^{4+(3+)}$  transfer,  $S_L = 0$  and the superconductor is  $n$  type. As a consequence there is neither a real-space requirement nor an obvious mechanism for pairing to occur. These materials will be examined in Section 7 together with a number of other superconducting systems.

#### 4.5 POLARON CARRIER STATISTICS

The microscopic view of superconductivity in metals is that boson carriers are created from the free electrons of the conduction band with energies near the Fermi level. Because the quantum electrodynamic version of the London theory requires that the carrier ensemble form a single wavefunction ( $n_s = |\psi_s|^2$ ), the individual carriers cannot be fermions because of the Pauli principle restriction that only one fermion can occupy a state at one time. Supercurrents, therefore, would occur in the form of bosons that condense through the attractive action of the Pauli principle to form a superfluid (boson condensation). In the BCS theory, the bosons are paired electrons with opposite spins so that the particles or carriers have a double electron charge and zero-spin quantum number ( $S = 0$ ). If the electrons are not paired, the carriers are fermions and the Pauli principle can only apply as a repulsive force, with electrons collectively competing for a limited number of quantum states.

If the ensemble wavefunction is replaced by uniformly spaced polaron carriers moving in unison under the influence of local electrostatic fields, however, there is also no competition for quantum states; carriers entering cells occupy states vacated by simultaneously exiting carriers. This situation is analogous to a vacuum diode without space charge, where each electron emitted from the cathode arrives at the anode before the next one is emitted. With only one carrier per cell, the scattering action among fermions with parallel spins by the Pauli exclusion principle does not produce impedance unless overlapping clusters of cells begin to create a local Fermi gas.

The CET concept is approached from the classical version of the London theory ( $\nabla n_s \sim 0$  instead of  $\nabla |\psi_s|^2 \sim 0$ ), therefore the carriers are not assumed to be free electrons, and there is no requirement for paired electrons mediated by phonons or other entities in  $k$  space; in fact, there is no requirement for paired electrons based on purely electrostatic grounds. Instead the individual polarons may be ordered electrostatically by repulsion within a chain of covalent bonds (the giant molecule concept), and real-space spin pairing in a supercurrent could be required only to maintain any existing dynamic antiferromagnetic order (e.g., spin waves) along the molecular transfer paths. As discussed in Section 3.4, the Pauli principle is satisfied if either the polaron has  $S_p = 0$  and magnetic disorder prevails where the lattice favors antiferromagnetic coupling in an undiluted state, or the lattice ions themselves have  $S_L = 0$ . Where the carriers transfer as real-space pairs with the double electron transfer of an  $S_p = 0$  polaron, the single ensemble wavefunction solution of Ginsburg and Landau becomes applicable because the limitations of Fermi statistics are circumvented by  $S = 0$  bosons. Because these bosons are local and would condense in real space, the overlapping necessitated by the  $k$ -space Cooper pair correlation is no longer of concern, and the question of a Schafroth condensation<sup>20</sup> is moot. Bose-Einstein statistics could also apply as in the quantum boson fluid formalism required by the Bardeen-Cooper-Schrieffer theory. Whether as individuals or pairs, however, covalent rather than conduction electrons are involved, and the superconduction system proposed is more localized than collective, particularly in the systems of low polaron density to be discussed later.

---

<sup>20</sup> See for example, J.M. Blatt, *Theory of Superconductivity* [New York: Academic Press, Inc. (1964)], p. 129.

Based on the earlier discussion of the nature of superconductivity, the question of carrier statistics alone poses a fundamental paradox. According to the Londons' [9] phenomenological assessment discussed in Section 2, the superconducting state requires that carriers move with spatial ordering (the  $\nabla n_s = 0$  constraint). Such a constraint implies order as opposed to randomness, and localization as opposed to collectiveness. Although statistics are required to describe quantum state occupation probabilities of collective systems, does it follow that statistics of any kind can play a role in an ideally ordered system? Does it matter whether particles are fermions or bosons if they are isolated, or even localized in an ordered chain, where there is no competition for quantum states? One further question follows directly: If electron pairing, as evidenced by the apparent double-electron charge phenomena, does not result from a requirement to satisfy boson statistics, can there be superconduction situations where pairing is not present in any form? Or does some form of spin pairing occur simply as part of the  $\nabla n_s = 0$  ordering requirement?

Whether the electrons are individual or paired, however, the mechanism of bound electron transfer is the same, involving part of the fundamental binding of the crystal lattice — the covalent bond.

## 5. SUPERCONDUCTION ELECTRICAL PHENOMENA

Up to this point the emphasis has been on defining the conditions for a covalent transfer conduction mechanism that can coexist with thermally activated hopping. To explain the origin of superconductivity, the discussion continues in two steps: First, threshold conditions for the zero resistivity observed below the critical temperature will be described, and second, the corresponding resistivity behavior above the critical temperature will be examined.

### 5.1 CRITICAL TEMPERATURE AND POLARON CONCENTRATION

Where covalent transfer is possible, zero resistance may be established when a threshold combination of polaron density and dispersal permit the formation of a continuous molecular chain [1]. Above a critical temperature, thermally activated hopping increases to the point where the effective transfer carrier population falls below the required minimum value. According to the original model, Equation (14) in Dionne [1], the instantaneous population of polarons engaged in random hopping is

$$n_n = N \exp(-E_{\text{hop}}/kT) \quad , \quad (29)$$

where  $N$  is the mean polaron density, and the exponential factor represents the probability of a hopping event as dictated by the familiar law of diffusion by thermal activation. Participation in covalent transfer by the remaining polarons<sup>21</sup> is jointly dependent on the dispersal of polaron sources (to satisfy the ordering requirement) and the degree of covalence. The maximum density of superconducting polarons is defined as

$$n_s = \eta PN [1 - \exp(-E_{\text{hop}}/kT)] \quad , \quad (30)$$

where  $N$  is decreased by the transfer efficiency  $0 \leq \eta \leq 1$  (previously assumed to be unity [1]) and the polaron dispersal factor  $0 \leq P \leq 1$ .

The statistics that are required to describe state occupancies of collective electrons are not invoked here because the model involves only isolated polarons. Each mobile polaron (which may move through paired electrons or in double transfer events) is an individual carrier that does not have to compete for an available state; when it moves into an adjacent cell it inherits the environment of the exiting polaron that is being expelled through electrostatic repulsion. The basic concept is stated as follows: Where orbital overlap between mixed-valence cations satisfies the transfer condition ( $h \geq E_{\text{hop}}$ ) in a system where polaron cells can merge into a single MO chain, superconduction can be an operating mechanism; superconduction, therefore, can be destroyed by thermal excitation of the electrons out of their bonding orbitals into the semiconductor hopping mode.

---

<sup>21</sup> For the sake of completeness, a third group of localized polarons may be defined as  $n' = N - (n_n + n_s)$ , which would be zero if both  $\eta$  and  $P$  were unity.

In terms of fractional populations, with  $x$  as the nominal polaron concentration per chemical formula unit, Equation (30) may be expressed as

$$x_s/x_{\text{eff}} = n_s/N_{\text{eff}} = [1 - \exp(-E_{\text{hop}}/kT)] \quad (31)$$

where  $x_{\text{eff}} = \eta Px$  is the effective polaron concentration at  $T = 0$ . It is instructive to recognize the statistical meanings of the three factors in Equations (30) and (31):  $\eta$  determines the relative occupation probability (in a quantum sense) of the electron being present at the junction of the two polaron cells in order to undergo covalent transfer,  $P$  is the polaron isolation probability, and the bracketed factor is the probability of the polaron carrier not being in the process of thermal activation.

### 5.1.1 Transfer Efficiency $\eta$

In the mixed-valence  $p$ -type Cu perovskites, it was concluded from the MO calculation that  $\eta_{1,\gamma} \approx 1 - \Delta E_{1,\gamma}/b$  [see Equation(28)]. For a one-dimensional approximation of a polaron carrier between two source charges separated by  $R$  and the carrier a distance  $r$  from the nearest source,

$$\Delta E_{1,\gamma} = -(e^2/Ka)[1 + (\Gamma-1)^{-1} - \gamma^{-1} - (\Gamma-\gamma)^{-1}] \quad (32)$$

where the reduced distances  $\gamma = r/a$  and  $\Gamma = R/a$ , with lower limits of 1. The repulsive energy between the carriers is assumed to be fixed because the fixed source charges are stationary and the supercurrent occurs through mutual repulsion of the mobile charges with the correlated polarons retaining their separation as they propagate.

For  $a = 4 \text{ \AA}$  (the approximate Cu-O-Cu bond length) and  $K = 16$ , for example,  $\Delta E_{1,\gamma}$  is plotted as a function of  $\gamma$  in Figure 19 to illustrate the polaron electrostatic potential barriers for various values of  $\Gamma$ . A threshold of  $b/2$  based on  $b = 0.43 \text{ eV}$  corresponding to the value of  $b_{x,y}^2$  for CuO determined in Section 3.3, is included to suggest the appropriate range of  $\Gamma$  values for this system.<sup>22</sup> The Coulomb energy peaks at  $\gamma = \Gamma/2$ , half the reduced distance to the junction between cells, therefore the energy barrier  $\Delta E_{\text{max}}$  at the cell boundary may be expressed as

$$\Delta E_{\text{max}} = -(e^2/Ka)[1 + (\Gamma-1)^{-1} - 4\Gamma^{-1}] \quad (\text{for } \Gamma \geq 2) \quad (33)$$

Because the concentration  $x = a/R$  (which also applies in three dimensions),  $\Gamma = 1/x$ , and Equation (33) may be written in terms of the polaron concentration,

$$\Delta E_{\text{max}} = -(e^2/Ka) [(1-2x)^2/(1-x)] \quad (\text{for } x \leq 0.5) \quad (34)$$

---

<sup>22</sup>This value of  $b$  is chosen in preference to the calculated  $b = 0.67 \text{ eV}$  that is determined from the MO model developed in Appendix C, although the two values are close enough to produce qualitatively similar results throughout this text. Although  $b$  is a negative energy, the minus sign is being dropped throughout this text because only the magnitude of  $b$  is used in any calculations.



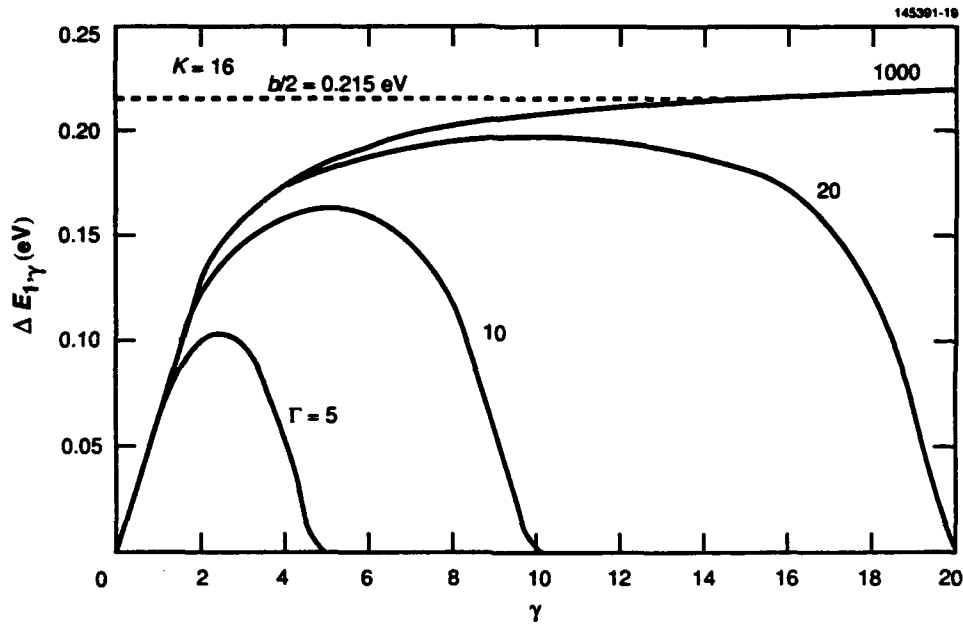


Figure 19. Large-polaron Coulomb potential  $\Delta E_{1,\gamma}$  versus  $\gamma$  for different reduced polaron source separations  $\Gamma$ , based on Equation (32), for  $K = 16$ .

A four-polaron relation that comes closer to the actual geometry of the layered perovskite-type compounds was derived in Dionne [1]; an abbreviated two-polaron version that produces similar computational results is expressed as

$$\Delta E_{\max} = -(e^2/Ka)[2(1 + \Gamma^2/4)^{-1/2} - (1 + \Gamma^2)^{-1/2} - 1] \quad (35a)$$

or

$$\Delta E_{\max} = -(e^2/Ka)[4x(1 + 4x^2)^{-1/2} - x(1 + x^2)^{-1/2} - 1] \quad (35b)$$

Through Equations (28) and (35) the transfer probability as a function of concentration can be summarized as

$$\eta = 1 - \Delta E_{\max}/b \quad (36)$$

In Figure 20, Equation (36) is plotted as a function of  $\Gamma/2$  for  $b = 0.43$  eV,  $a = 4$  Å, and  $K = 16$ , to illustrate a typical variation in  $\eta$  for the high- $T_c$  perovskites.

### 5.1.2 Isolation Probability $P$

For the isolated polaron concept to apply, a high degree of dispersal must exist. The MO cell model has meaning where the isolation probability factor  $P \rightarrow 1$ , and to the extent that  $P$  is less than unity, the effective density of potential supercarriers is reduced accordingly. If conduction takes place by linkages of these single-carrier cells, it follows that Pauli principle concerns become important where cation clustering causes cells

to overlap, thereby forcing multiple carriers to compete for states within the same regions of the lattice, invoking the need for Fermi statistics.

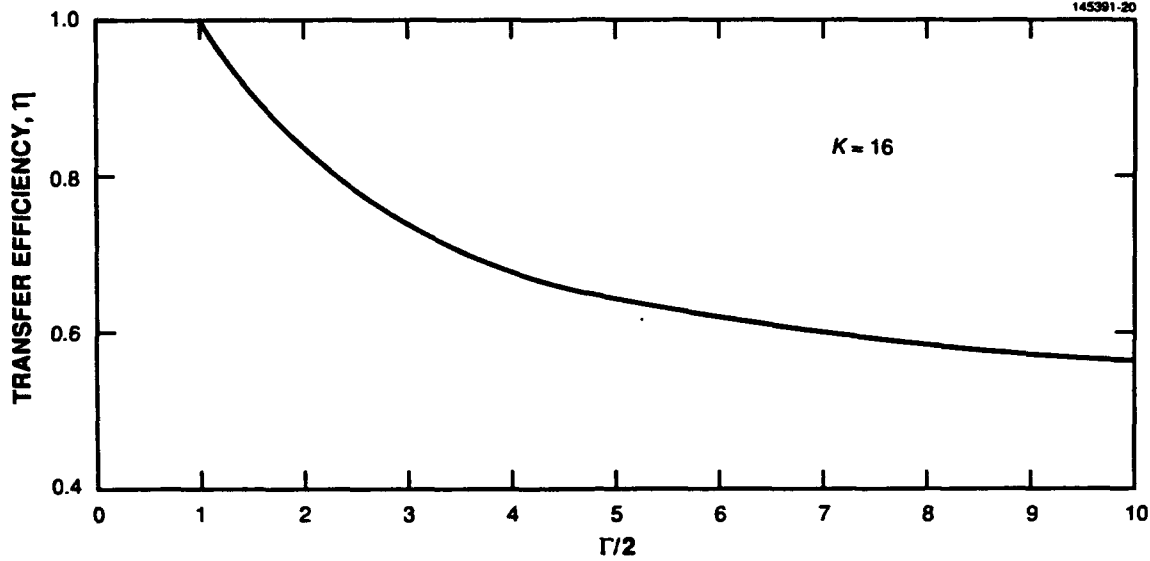


Figure 20. Transfer efficiency  $\eta$  as a function of  $\Gamma/2$ , for  $K = 16$  and  $h = 0.43$  eV.

The estimation of  $P$  must be adjusted according to whether the smallest transfer event involves one or two electrons. According to the rationale developed earlier (Dionne [1], Appendix C), it follows that

$$P_1 = 1 - 2\beta x \quad \text{for } 0 \leq x \leq 1/2 \text{ (single transfers)} \quad , \quad (37a)$$

or

$$P_2 = 1 - 2\beta x - 2\beta' x \approx 1 - 4\beta x \quad \text{for } 0 \leq x \leq 1/3 \text{ (pairs)} \quad , \quad (37b)$$

where the variable term in the equation for  $P_1$  is the probability of a second polaron occurring adjacent to the initial one, and  $\beta \geq 0$  is a dispersal parameter that is unity for a random distribution, less than unity for higher dispersal, and greater than unity for clustering.<sup>23</sup> The factor of 2 in Equation (37a) accounts for the removal of the pair of adjacent polarons as possible supercarriers. In the case of  $P_2$ , the two variable terms represent the probability of a polaron source appearing at least once on two consecutive sites from the initial polaron. For this simple first approximation, we assume that  $\beta \approx \beta'$  (the respective dispersal parameters for nearest and next-nearest neighbors).

<sup>23</sup>This model replaces that of Dionne [1], Appendix C, where  $-1 \leq \alpha \leq 1$  was defined as the dispersal parameter.

### 5.1.3 $T_c$ and Threshold Carrier Concentration $x_t$

From Equation (31) the condition for the onset of zero resistance may be set by defining a polaron transfer threshold density  $n_t$  (or concentration  $x_t$ ) for the completion of a current path. As discussed earlier, this threshold is contingent on a number of events taking place, principally the dipole alignments of the itinerant polarons and the presence of at least partial magnetic frustration. Assigning the critical temperature  $T_c$  to the threshold concentration condition,

$$x_t/x_{\text{eff}} = n_t/N_{\text{eff}} = [1 - \exp(-E_{\text{hop}}/kT_c)] \quad , \quad (38)$$

and the basic relation for critical temperature may be expressed as

$$T_c = E_{\text{hop}}/kW \quad , \quad (39)$$

where  $W = \ln[1 - n_t/N_{\text{eff}}]^{-1} = \ln[1 - x_t/x_{\text{eff}}]^{-1} \approx x_t/x_{\text{eff}}$  for  $x_t \ll x_{\text{eff}}$ . If  $\beta \ll 1$  and  $b$  is large,  $\eta P \rightarrow 1$  and  $x_{\text{eff}} \approx x$ . Equation (39) may then be reduced to the ideal case of  $T_c = (E_{\text{hop}}/k)(x/x_t)$ , with  $W \approx x_t/x$ . Thus, high  $T_c$  values for large  $E_{\text{hop}}$ , but also for large polaron concentrations  $x$  and small thresholds  $x_t$ . This last condition may be exploited by large  $b$  values, which also serve to raise  $\eta$  and optimize the effective carrier concentration, i.e.,  $x_{\text{eff}} \rightarrow x$ . Therefore, a simple rule for obtaining high  $T_c$  values would be high  $E_{\text{hop}}$  (small  $K$ ) and large  $b$  (large covalent stabilization energies). According to Equations (38) and (39),  $T_c$  represents the temperature at which  $x_s = x_t$ . As  $x$  varies, the function  $\eta Px = \eta(1 - 4\beta x)x$  follows a parabolic-type curve, reaching a peak at  $x_{\text{max}} = (8\beta)^{-1}$ .

If small threshold carrier concentrations lead to large  $T_c$  values, it follows that large polaron radii are the principal reasons for the high- $T_c$  oxide superconductors. Analogous to the small polaron  $b$  limit introduced by Holstein [48] i.e.,  $b \leq E_{\text{hop}}$ , a large polaron  $b$  range will be defined as  $E_{\text{hop}} \leq b \leq 2\Delta E_{1,\gamma}$  as depicted in Figure 17.<sup>24</sup> From this concept we may set an effective radius of isolated polarons from the definition of  $\Delta E_{1,\gamma}$  in Equation (28), according to

$$\gamma_p = 2\Omega/(2\Omega - 1) \quad , \quad (40)$$

<sup>24</sup>In a quantitative sense, the polaron radius is only figurative. As defined here, it means that the displacement of the polaron carrier at which the Coulomb destabilization energy step ( $\Delta E$ ) becomes equal to the covalent stabilization ( $\sim b/2$ ). In terms of the simple quantum mechanical approximation used to estimate  $\eta$ , the polaron wavefunction decays relatively according to Figure 20 and reaches a minimum at  $\Delta E_{\text{max}}$  but only reaches zero if  $\Delta E_{\text{max}} \geq b$ . An absolute polaron radius would therefore be defined by  $b = \Delta E_{1,\gamma}$  but an effective radius that is consistent with the onset of superconduction is  $b = 2\Delta E_{1,\gamma}$ . More helpful from a conceptual standpoint would be an exponential dependence in which the radius appears as a characteristic decay length, in the manner of a penetration depth or coherence length, but unfortunately this simple model of the CET mechanism does not readily permit this.

From Holstein's work [14], it is worth noting that the effective length of a large polaron in a linear chain may be approximated by

$$L_p \approx a (2b\pi a^3/e^2 K_{\text{eff}}) \quad ,$$

where  $\Omega = e^2/Kab$ . From this definition it follows that the reduced threshold polaron separation  $\Gamma_p$  would be twice the reduced radius (or  $2\gamma_p$ ), and the transfer threshold concentration in a perovskite could be approximated by

$$x_t = 1/\Gamma_p = 1/2\gamma_p = (2\Omega - 1)/4\Omega. \quad (41)$$

Note that within the approximations of this simple model,  $\gamma_p \rightarrow \infty$  in Equation (40), and  $x_t \rightarrow 0$  in (41), where  $2\Omega - 1 \leq 0$ . This result is not unreasonable, however, when one recalls that a second condition for superconduction is the breakdown of long-range antiferromagnetic order. In effect,  $x_t$  would be the larger of the  $x$  value at which  $T_N \rightarrow 0$  and the result of Equation (41).

#### 5.1.4 Polaron Concentration $x_0$ for the $T_N, T_c = 0$ Condition

Because the polaron dimension also influences the spatial extent of local magnetic frustration discussed in Section 3.4, it follows directly that the Néel temperature would decrease monotonically with polaron density and reach zero where the polaron cells merge or percolate. As a consequence, a minimum concentration for superconduction at  $T_c = 0$  (and a maximum for magnetic order at  $T_N = 0$ ) will be defined as

$$x_0 = \eta P/x_t, \quad (42)$$

with  $\eta$  and  $P$  evaluated at  $x = x_t$ . Because  $\eta P \leq 1$ ,  $x_0$  will be greater than  $x_t$ , particularly in the oxides if  $\eta$  is small due to a larger polaron radius. In the data to be examined next,  $x_t \sim 0.04$  and  $x_0 \sim 0.075$ , consistent with the range of minimum polaron concentrations ( $0.02 \leq x_0 \leq 0.09$ , from various publications) that also represent the point of total breakdown in static magnetic order ( $T_N = 0$ ) as verified by the data in Figure 12.

#### 5.1.5 Interpretation of $T_c$ versus $x$ Data

To test this theory, Equation (39) with  $P = P_2$  is fitted to experimental results for high-temperature superconducting systems. In Figure 21,  $T_c$  versus  $x$  data from the  $\text{La}_{2-x}\text{Sr}_x\text{CuO}_{4-y}$  system (with tetragonal  $\text{Cu-O}_6$  complexes), for samples presumed to have oxygen deficiencies [4], i.e.,  $y > 0$ , for  $x > 0.2$ , and for specimens [42] with  $y = 0$ , match the calculated curve for  $E_{\text{hop}} = 2.5$  meV (close to the 3 meV value reported for  $\text{LaSrCuO}_4$  by Goodenough et al. [24]), and  $\beta = 0.7$  (pair correlated). To illustrate the source of the parabolic-type relation<sup>25</sup> between  $T_c$  and  $x$ ,  $x_s$  is plotted as a function of  $x$  for  $T = 0$  in Figure 22, where the  $T_c = 0$  points occur at  $x_s(0) = x_t = 0.037$  for which  $x_0 = 0.075$  and  $0.31$ . At  $x = 0.2$ , the observed point of maximum  $T_c$  in Figure 21,  $x_s = 0.068$ . It therefore follows that this excess of supercarriers over the threshold minimum at  $x_t = 0.037$  is what allows superconductivity to survive to  $T \approx 40$  K. These parameter values for the  $\text{La}_{2-x}\text{Sr}_x\text{CuO}_{4-y}$  system will be used later in discussions of magnetic field and current density properties.

---

<sup>25</sup>Another possible contributing factor to this peculiar curve shape is the temperature-dependent population of the  $\text{Cu}^{3+}$  low-spin ions, which may be described in terms of a two-level Boltzmann function according to  $x_{\text{eff}} = x_s[1 + \exp(-\Delta_{ls}/kT)]$ , where  $\Delta_{ls}$  is the net low-spin state stabilization energy. For the  $\text{Cu}^{2+(3+)}$  combination at least, it may be assumed that  $x_{\text{eff}} \approx x_s$  because  $\Delta_{ls} \gg kT$ , as evidenced by the Goodenough et al. results at room temperature [24].

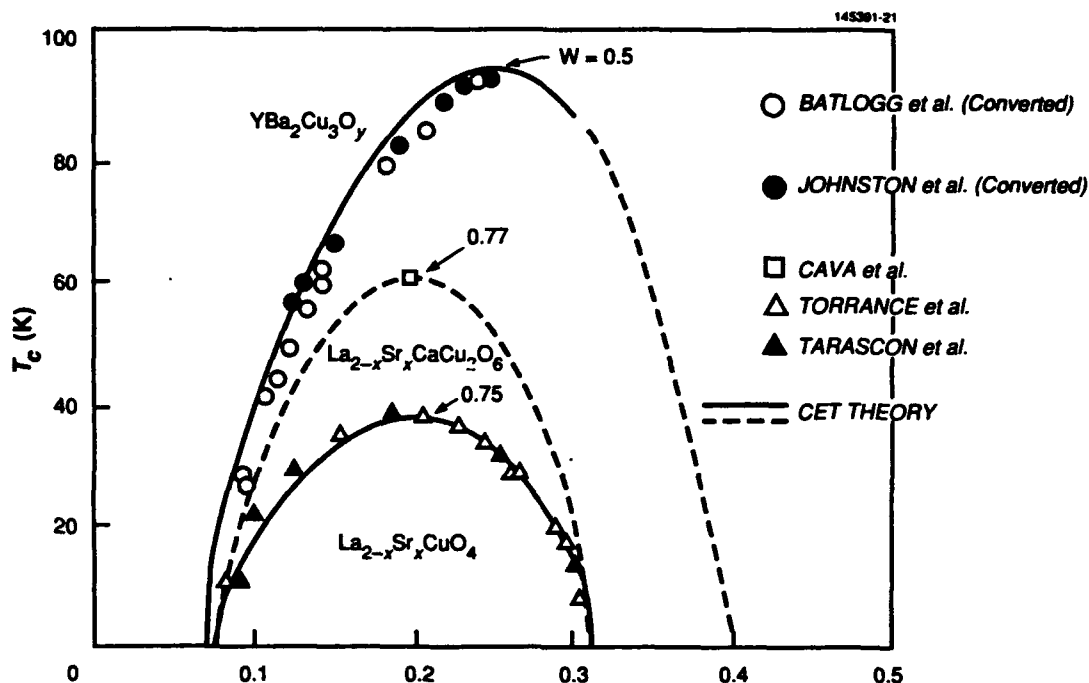


Figure 21. Critical temperature  $T_c$  versus  $x$  for  $\text{La}_{2-x}\text{Sr}_x\text{CuO}_4$ ,  $\text{La}_{2-x}\text{Sr}_x\text{CaCu}_2\text{O}_6$ , and  $\text{YBa}_2\text{Cu}_3\text{O}_y$  (where  $y$  has been converted to  $x$  using the linear model  $y = 0.25x - 1.5$ ); data of Tarascon et al. [4], Torrance et al. [42], Cava et al. [49], Johnston et al. [50], and Batlogg et al. [51].

Recent results [49] from a related series  $\text{La}_{2-x}\text{Sr}_x\text{CaCu}_2\text{O}_6$  with pyramidal  $\text{Cu-O}_5$  complexes that also features fixed polaron sources shed additional light on the origin of  $T_c$ . For  $z = 0.4$  (equivalent to the same polaron concentration of  $x = 0.2$ ), a maximum  $T_c = 60$  K was determined. As indicated by the dashed curve in Figure 21, this rise in  $T_c$  from 40 K may be explained by an increase in  $E_{\text{hop}}$  from 2.5 to 4 meV, with all other parameters unchanged. In Appendix D, the higher value of  $E_{\text{hop}}$  is discussed in terms of changes in crystal-field stabilization energies as the Cu coordination is truncated from a tetragonally distorted octahedron ( $\text{Cu-O}_6$ ) to a square-based pyramid ( $\text{Cu-O}_5$ ).

For the  $\text{YBa}_2\text{Cu}_3\text{O}_y$  system with maximum  $T_c = 95$  K, data of Johnston et al. [50] are compared in Figure 23 with a calculated curve based on the linear relations between  $x = 0.25y - 1.5$  derived in Dionne [1] (p. 83), for which  $x = 0.25$  at  $y = 7$  and  $x = 0$  at  $y = 6$ . (For comparison with the 40- and 60-K systems, the calculated curve is also plotted as a function of  $x$  in Figure 21). Because the superconduction occurs in the  $\text{Cu}(2)$  planes with pyramidal  $\text{O}_5$  coordination,  $E_{\text{hop}} = 4$  meV, as discussed in Appendix D,  $x_f = 0.035$ , and  $\beta = 0.57$ , which suggest improved polaron dispersal through the less-fixed oxygen vacancies as sources of polarons. As shown in Figure 22, the maximum  $x_f = 0.9$ , occurring at  $x = 0.25$ . The anomalous behavior of the  $T_c$  data beginning at  $y \approx 6.8$  suggests that the  $x$  versus  $y$  relations depart from linearity, reflecting a more rapid decrease in the pyramidally coordinated  $\text{Cu}^{3+}(2)\text{-O}_5$  concentration with

oxygen vacancy density, possibly due to structural changes caused by depletion of anions in the Cu(1)-O<sub>2</sub> linearly coordinated sublattice. Such an occurrence is also suggested by the anomalous dip in the room temperature  $\rho$  versus  $T$  data that corresponds to the  $T_c$  drop observed by Batlogg et al. [51].

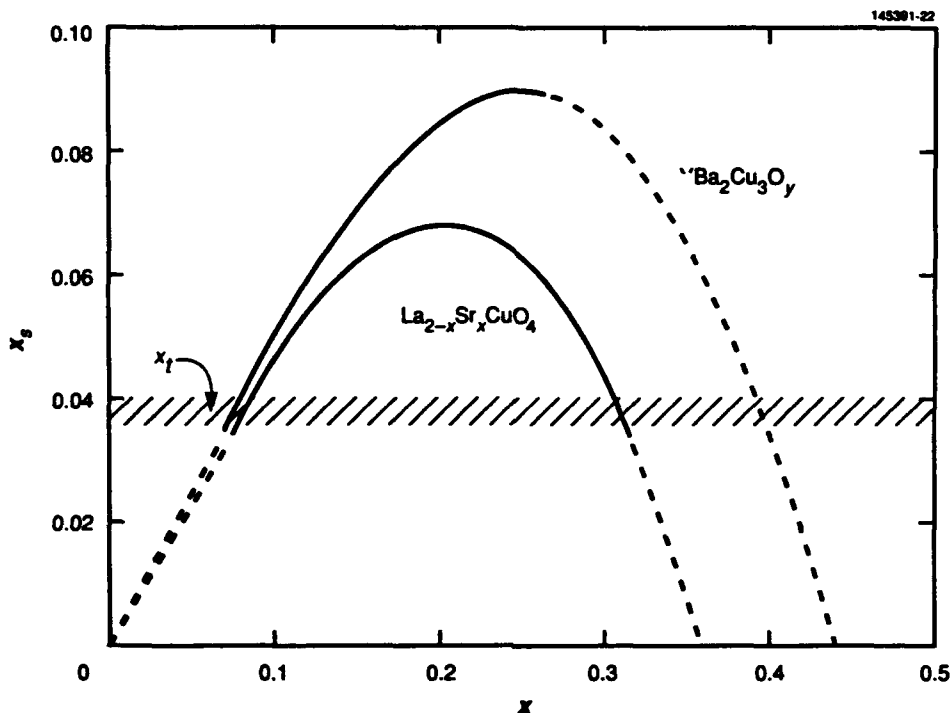


Figure 22. Supercarrier concentration  $x_s(0)$  versus  $x$  for the  $\text{La}_{2-x}\text{Sr}_x\text{CuO}_4$  and  $\text{YBa}_2\text{Cu}_3\text{O}_y$  systems of Figure 21.  $T_c = 0$  at  $x = 0.075$  and  $0.31$ , indicating the threshold for  $x_s(0) = x_t \sim 0.035$  to  $0.04$  in both cases, with corresponding percolation radii of about 14 transfer lengths ( $\sim 50$  Å).

The relative amounts of  $\text{Cu}^{3+}(2)$  and  $\text{Cu}^{1+}(1)$  as functions of  $y$  were determined by Brown [52] using the bond valence sum approach (which is compared with the original linear predictions of Dionne [1] in Section 7.1, where additional details of the chemistry and crystallography of this unusual system are examined). From Brown's results for  $x$ , corresponding  $T_c$  values were calculated from Equation (39) with the same parameter values that were used above, and are also plotted in Figure 23, where agreement with the Johnston et al. [50] data is close enough to serve as further verification for the validity of Equation (39).

In both of these Cu perovskite-related systems,  $b$  is again assumed to be  $0.43$  eV, and  $K = 15.6$ , a value typical for oxides containing these cations. For these values,  $x_t = 0.035$ , and the corresponding polaron radii become about 14 transfer lengths, or approximately  $50$  Å. The significance of this radius value and how it relates to the coherence length, which has been measured in these materials [53] as  $34$  Å (in-plane), are discussed in Section 6.7.

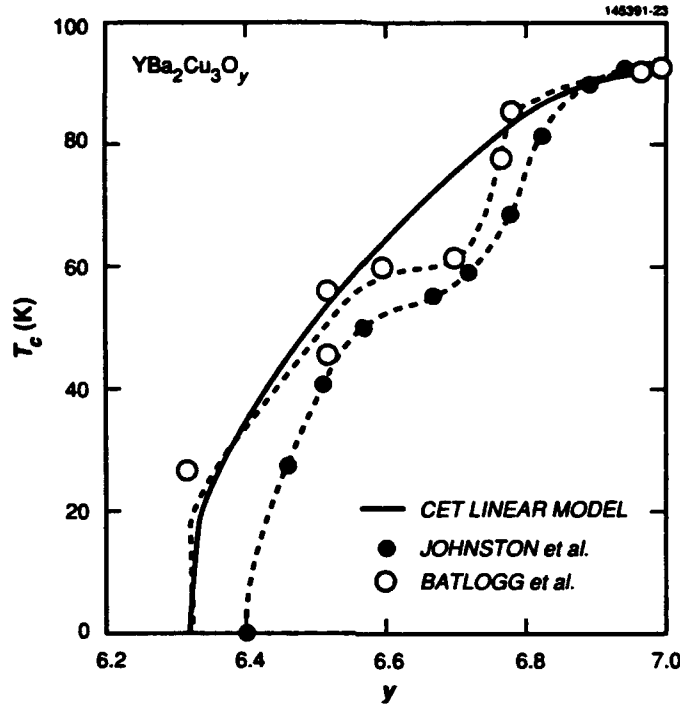


Figure 23. Comparison of theory with  $T_c$  versus  $y$  data from  $\text{YBa}_2\text{Cu}_3\text{O}_y$ . Theory is based on the linear valence model developed in Dionne [1]; data of Johnston et al. [50] and Batlogg et al. [51] reflect the nonlinearity determined from the valence bond sum analysis of Brown [52].

The more complex layered systems (see Section 7.1) are less amenable to this type of analysis, because polaron sources are not as well defined. For example,  $T_c$  of  $\text{Bi}^{3+}_2(\text{Sr}^{2+}, \text{Ca}^{2+})_3[\text{Cu}^{2+}_{1-x}\text{Cu}^{3+}_x]_2\text{O}_{8+\delta}$  reaches a value of 116 K for  $x = 0.33$  [6]. As plotted in Figure 24, where a family of  $T_c$  versus  $x$  curves is presented generically for  $E_{\text{hop}} = 4$  meV and  $x_i \approx 0.035$  with  $b$  ranging from 0 to 2, this higher temperature composition would have a dispersal parameter  $\beta = 0.45$ . It should be pointed out that some of the Cu ions have square-planar coordination ( $\text{Cu}-\text{O}_4$ ), which may result in  $E_{\text{hop}} > 4$  meV (see Appendix D). Another potentially important consideration for these compounds is the multivalent capability, e.g.,  $\text{Tl}^{1+}$  or  $\text{Tl}^{3+}$  ions, which may serve to explain the lower value of the dispersal parameter  $\beta$ .

From these projections, some preliminary conclusions might be considered. Because Madelung energy minimization would dictate that dispersal of polaron sources should be no worse than random,  $\beta$  should be  $\leq 1$ . To satisfy this condition,  $P_2$  defined in Equation (37b) must be used to interpret foregoing data, thereby indicating that double transfers are more likely, as single transfers would dictate the use of  $P_1$  from Equation (37a) and lead to values of  $\beta > 1$ . If the carriers transfer as pairs, in accord with the accepted convention of superconductivity and the discussion of magnetic contribution to  $E_{\text{hop}}$  in Section 3.3, it follows that the maximum effective polaron concentration would be  $x = 0.33$  (instead of 0.5 for individual transfers), as indicated by the dashed-line extrapolations that show declining  $T_c$  values in Figure 24 for  $x > 0.33$ . From the  $\beta = 0$  curve, this limit of  $x$  would therefore impose a maximum theoretical  $T_c$  of about 330 K. Values of  $E_{\text{hop}}$  clearly descend to the millielectron volt range in these superconductors, consistent with the idea that the elastic trapping energy that remains after magnetic frustration may be represented by the Debye energy, reduced by the coupling constant  $\alpha < 1$  (see Section 3.2).

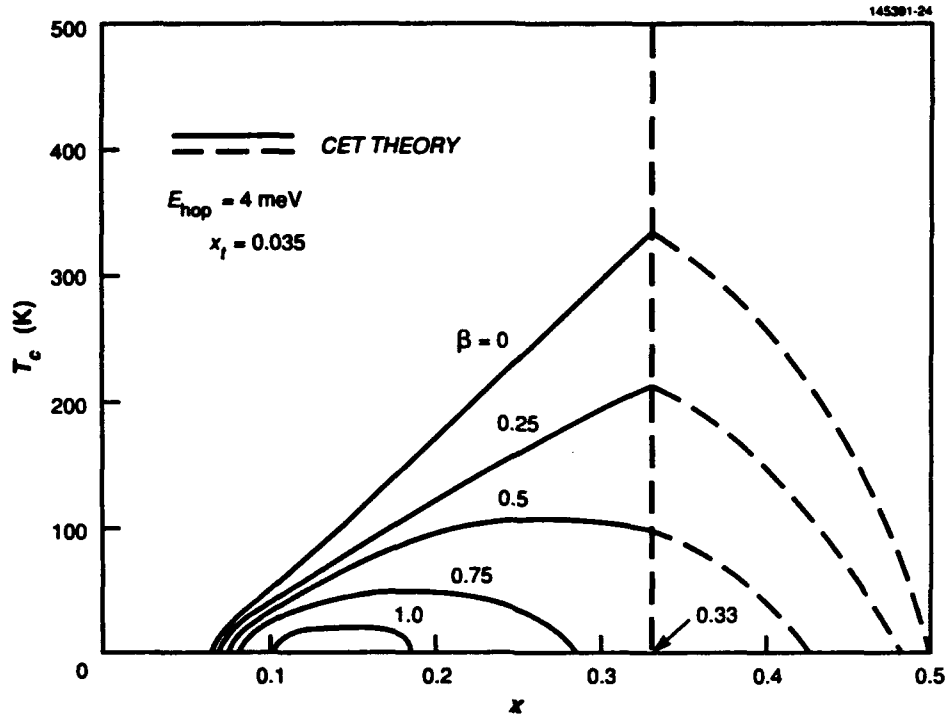


Figure 24. Projected  $T_c$  versus  $x$  curves based on CET theory over the range of  $0 \leq \beta \leq 2$  for individual carriers and  $0 \leq \beta \leq 1$  for pairs. Dashed curves indicate that the "real-space" pair model does not apply beyond  $x = 0.33$ .

## 5.2 RESISTIVITY VERSUS TEMPERATURE AND COMPOSITION

For transition-metal oxides, there are two mechanisms for electron transfer between mixed-valence cations — one permitted by covalent bonding and the other stimulated by lattice vibrations. In competition with the orbital transfer mechanism, normal conduction results from the thermally activated diffusion of an electron from its orbit on one cation to a higher-valence cation in a neighboring lattice site. Because the exponential activation factor causes the resistivity to decrease with temperature, mixed-valence oxides are considered to be (hopping) semiconductors, but differ from conventional collective carrier (band-model) semiconductors in the very short lifetimes and diffusion lengths of the hopping electrons that remain relatively localized to their polaron sources.

### 5.2.1 Origin of the Metallic $\rho$ - $T$ Slope

For metal oxides with mixed-valence cations (e.g.,  $\text{Li}^{1+}_x\text{Cu}^{2+}_{1-2x}\text{Cu}^{3+}_x\text{O}$ ), a measurable electrical resistivity exists and was determined by Heikes and Johnston [20] to obey the relation [from Equation (10)]

$$\rho = (Ne\mu)^{-1} ,$$

or

$$= (kT/Ne^2D) \exp(E_{\text{hop}}/kT) , \quad (43)$$



where  $\mu = (eD/kT) \exp(-E_{\text{hop}}/kT)$  is the activated mobility,  $N = x(1-x)/V$  is the effective polaron density expressed as the ratio of nominal concentration  $x$  to formula unit volume  $V$ , which is reduced to assure that  $0 \leq x \leq 1$ . The factor  $1-x$  represents the probability of hop completion at a given site, because the incidence of a completed hop is dependent on the availability of receptors [15], and  $eD/kT$  is the familiar Einstein relation for diffusion mobility. The diffusion constant  $D = d^2 v_{\text{hop}}$ , with  $d$  as the diffusion length (average hop distance) and  $v_{\text{hop}}$  as hopping frequency, related the Debye frequency. The symbols  $e$  and  $k$  represent the electron charge and Boltzmann constant, respectively. Because  $d$  should increase from  $a$  (the minimum distance between transfer sites) with the concentration of trapping centers, i.e., the average hop distance will increase with increasing competition for available receptor sites, the approximation  $d \approx aF(x) = a(1-x)^{-1}$  will be used over the range of interest in this discussion.<sup>26</sup> As a result, Equation (43) is expressed as

$$\rho = [CkT(1-x)/x] \exp(E_{\text{hop}}/kT) \quad , \quad (44)$$

where  $C = V/e^2 a^2 v_{\text{hop}}$ . [For  $\text{YBa}_2\text{Cu}_3\text{O}_7$ ,  $V \approx 1.5 \text{ a}^3$ ; for  $\text{La}_{2-x}\text{Sr}_x\text{CuO}_4$ ,  $V \approx (1+1/\sqrt{2})a^3 = 1.7 \text{ a}^3$ .]

The appearance of a resistivity minimum at  $T_{\text{min}} = E_{\text{hop}}/k$  that separates insulator/metal regimes may be determined from the  $\partial\rho/\partial T = 0$  condition applied to Equation (44). If  $E_{\text{hop}} \ll kT$ , Equation (44) may be simplified to the linear relation

$$\rho \approx [Ck(1-x)/x]T + CE_{\text{hop}}(1-x)/x \quad . \quad (45)$$

The metallic slope of the  $\rho$  versus  $T$  curve is readily apparent in Equation (45), and its presence has been discussed in connection with magnetic spinels as well as the simple oxides [20,21,54]. Figure 25 is plotted from Equation (45) to illustrate the  $\rho$  minimum and its relation to the asymptote slope and  $\rho$ -axis intercept  $\rho_i$ .

### 5.2.2 Mixed Normal and Superconduction Resistivity ( $T > T_c$ )

If one assumes that large-polaron cells also represent volumes of  $\rho \approx 0$  in the normal state prior to the carrier ordering that occurs with the condensation to the superconducting state, a possible refinement to this model would treat these zero resistivity regions as local short circuits. To estimate the resistivity above the critical temperature, consider the elementary approximation of a cylinder of length  $L$  and cross-sectional area  $A$  shown in Figure 26. If all of the uniformly dispersed cells are grouped in two separate regions, i.e., as two resistors of lengths  $L_n$  and  $L_s$  in series, the total resistance would be approximated by

$$R = \rho L/A = \rho_n L_n/A + \rho_s L_s/A \quad , \quad (46)$$

---

<sup>26</sup> It may be determined from elementary probability theory that the most probable hop distance (i.e., diffusion length) for polarons in a one-dimensional chain will be increased over the minimum distance by a factor  $F(x) \approx \sum x^{n-1} = (1-x)^{-1}$ , where  $n \geq 1$  is an integer. The dependence on  $(1-x)^{-1}$  serves to confirm and explain the empirical result of Miyata et al. [54] for mixed-valence ferrites.

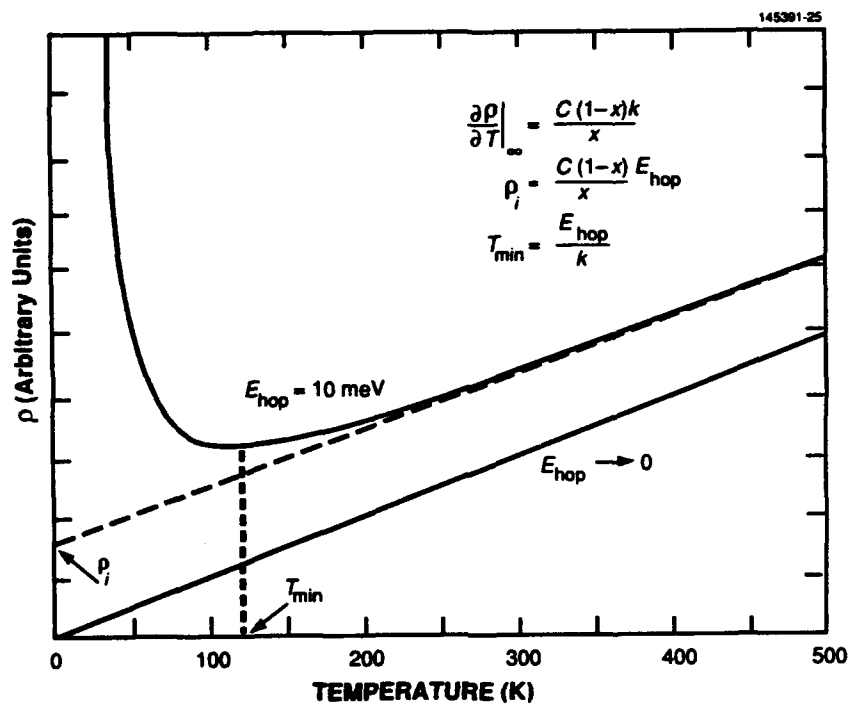


Figure 25. Generic plots of  $\rho$  versus  $T$  for  $E_{\text{hop}} = 0$  and  $10 \text{ meV}$ , defining relations for  $T_{\text{min}}$ , asymptote slope  $\partial \rho / \partial T \big|_{\infty}$  and intercept  $\rho_i$ .

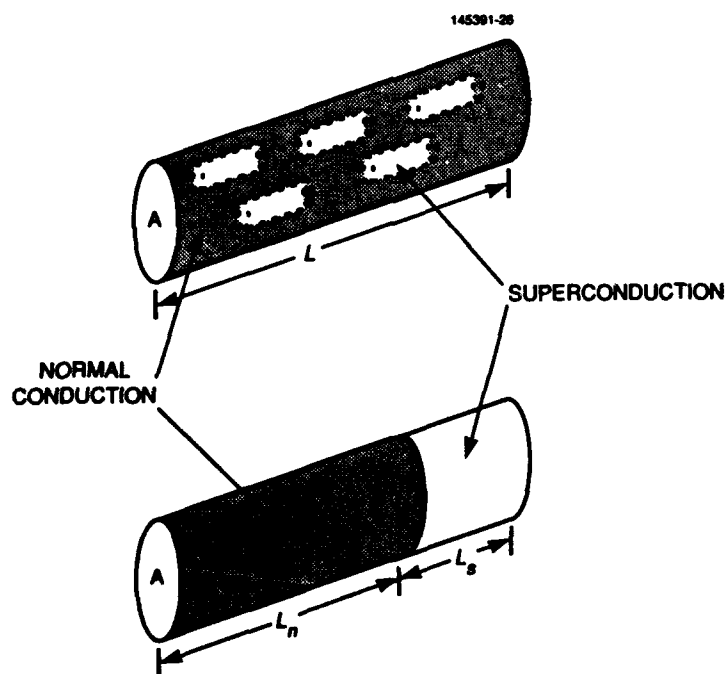


Figure 26. Simple model of the segregation of superconducting and normal regions for the purpose of estimating electrical resistivity above the transition temperature.

with  $\rho_s = 0$ ,

$$\rho = \rho_n [L_n / (L_n + L_s)] = \rho_n (1 - L_s / L) ,$$

or

$$= \rho_n (1 - V_s / V) . \quad (47)$$

$V$  and  $V_s$  are proportional to  $N$  and  $n_s$ , respectively, from Equation (30), and (47) becomes

$$\rho = [CkT(1-x)/x] [\eta P + (1 - \eta P) \exp(E_{\text{hop}}/kT)] . \quad (48)$$

If  $E_{\text{hop}} \ll kT$ , Equation (48) may be approximated by the linear relation

$$\rho = [Ck(1-x)/x]T + (1 - \eta P)CE_{\text{hop}}(1-x)/x , \quad (49)$$

which reduces to Equation (45) where  $\eta P \rightarrow 0$ . Thus, the slope remains the same, but  $\rho_i$  decreases with the increase in covalent transfer probability. In the limiting cases of  $\eta P = 0$  (no covalent transfer) and  $\eta P = 1$  (ideal transfer) respectively, Equation (48) reduces to:

$$\rho = [Ck(1-x)/x]T \exp(E_{\text{hop}}/kT) \text{ (hopping semiconductor)} , \quad (50a)$$

and

$$\rho = [Ck(1-x)/x]T \text{ (linear metal)} . \quad (50b)$$

Note that an ideal superconductor has no hopping effects present with a linear  $\rho$  versus  $T$  curve that passes through the origin. In practical cases, only metals with  $\eta P \sim 1$  and  $E_{\text{hop}} \sim 0$  are likely to approach this limit.

### 5.2.3 $T_c$ and the Insulator-Metal Phase Transition

A family of generic plots of Equation (48) is given in Figure 27, where the demarcations between semiconduction and metallic regimes are seen to occur at  $T_{\text{min}}$ , which varies as a function of  $\eta P$  according to the relation determined by differentiation of Equation (48),

$$\eta P / (1 - \eta P) = (1 - E_{\text{hop}}/kT_{\text{min}}) \exp(E_{\text{hop}}/kT_{\text{min}}) . \quad (51)$$

This transition temperature would not be expected to appear below 1000 K because  $E_{\text{hop}} > 0.1$  eV for hopping semiconductors with magnetic order. From Equations (39) and (51), a relation between  $T_c$  and  $T_{\text{min}}$  may be pointed out. The minimum in the  $\rho$  versus  $T$  curve can be observed only where  $T_c < T_{\text{min}}$ , and this threshold condition is expressed as

$$\eta P / (1 - \eta P) = (1 - W) \exp(W) , \quad (52)$$

recalling that  $E_{\text{hop}}/kT_c = W = \ln(1 - x_p/\eta Px)^{-1}$ .

Unfortunately, the variables  $\eta P$  and  $E_{\text{hop}}/kT_{\text{min}}$  in Equation (51) cannot be readily separated. A direct comparison with  $W$  is not convenient because this equation cannot be solved without an iteration procedure. Insight may be gained, however, if one considers that small values of  $\eta P$ , i.e., for a nonideal superconductor,

lead to higher  $T_{\min}$  and lower  $T_c$  values; in addition,  $T_c$  is further reduced where the polaron density approaches the threshold,  $x_f/x \rightarrow 1$ . As a consequence, observation of minima are most likely where  $W$  is larger through low polaron dispersal ( $\eta P \ll 1$ ), particularly for small  $x$ .

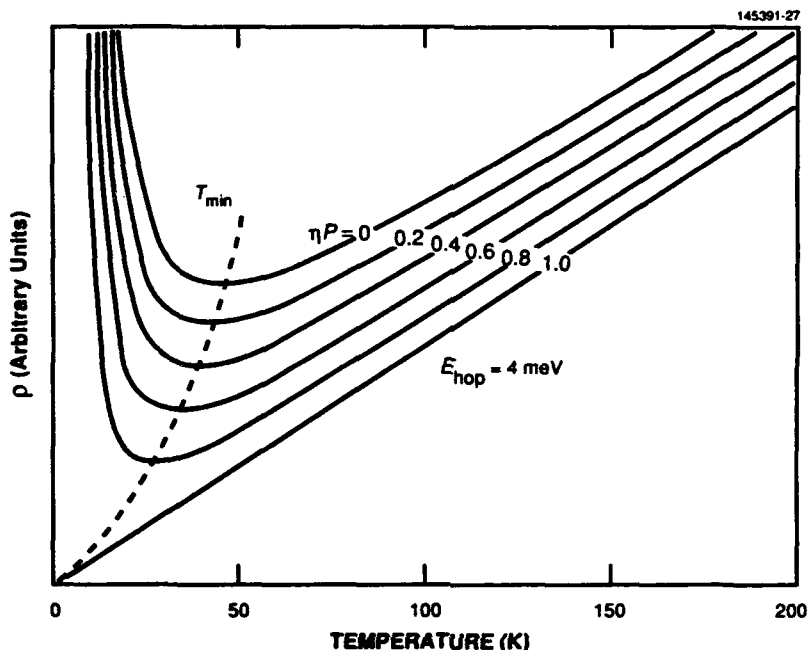


Figure 27. Resistivity versus temperature for  $0 \leq \eta P \leq 1$ , showing the influence of covalent transfer on the lowering of  $T_{\min}$  and  $\rho_i$ .

#### 5.2.4 Interpretation of $\rho$ versus $T$ Measurements

Earlier validation of this  $\rho$  versus  $T$  model was established with the  $\text{Li}_x\text{Ni}_{1-x}\text{O}$  system in a study of  $\text{Ni}^{2+} \rightarrow \text{Ni}^{3+} + e^-$  hopping conduction [55]. To compare theory with experiment for the high- $T_c$  materials, the data curves of Tarascon et al. [4] for the  $\text{La}^{3+}_{2-x}\text{Sr}^{2+}_x\text{Cu}^{2+}_{1-x}\text{Cu}^{3+}_x\text{O}_{4-y}$  system with  $x = 0.10, 0.15$ , and  $0.225$  are plotted in Figure 28 with the calculations based on Equation (48). Values of  $C = 16 \text{ m}\Omega \text{ cm/eV}$ ,  $E_{\text{hop}} = 2.5 \text{ meV}$ , and  $\beta = 0.7$  were found to provide a good fit. A similar agreement between theory and the data of Cava et al. [5] for  $\text{Y}^{3+}\text{Ba}^{2+}_2(\text{Cu}^{2+}_{3-3x}\text{Cu}^{3+}_{3x})\text{O}_y$  for  $y = 6.9$  (representing an average  $x = 0.267$  for charge balance) is shown in Figure 29, where the portion of the curve below  $T_c$  is extrapolated to show the minimum. In this case,  $C = 9 \text{ m}\Omega \text{ cm/eV}$ ,  $E_{\text{hop}} = 4 \text{ meV}$ , and  $\beta = 0.5$ . For both structures,  $a = 4 \text{ \AA}$ , and the  $C$  parameters require Debye frequencies  $2\pi\nu_D = \omega_D \sim 10^{14} \text{ rad/s}$ . (For double hops,  $a \approx 8 \text{ \AA}$  and the minimum diffusion length would therefore decrease, lowering the corresponding value of  $\omega_D$  by a factor of 4.) It is also significant that the ratio of the  $C$  values,  $16:9 = 1.78$ , is in close accord with the corresponding ratio of lattice cell volumes,  $(1+1/\sqrt{2}):1 = 1.71$ . As discussed in Section 5.3, the values of  $C$  are related to the microstructure. Because the specimens discussed above were polycrystals, the effects of randomly oriented grains are probably responsible for increased average diffusion lengths and higher  $C$  values.

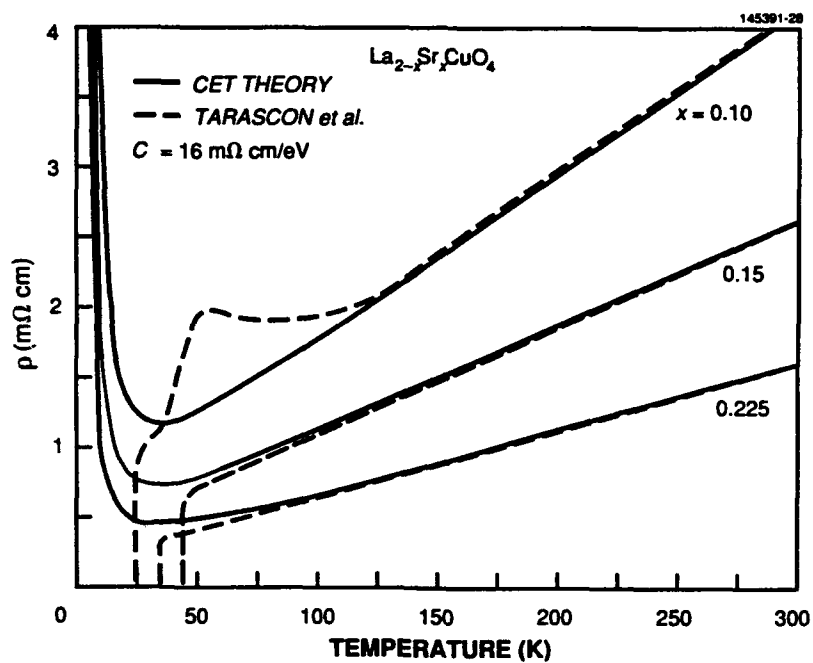


Figure 28. Comparison of theory with experiment for the  $\text{La}_{2-x}\text{Sr}_x\text{CuO}_4$  system (data of Tarascon et al. [4]).

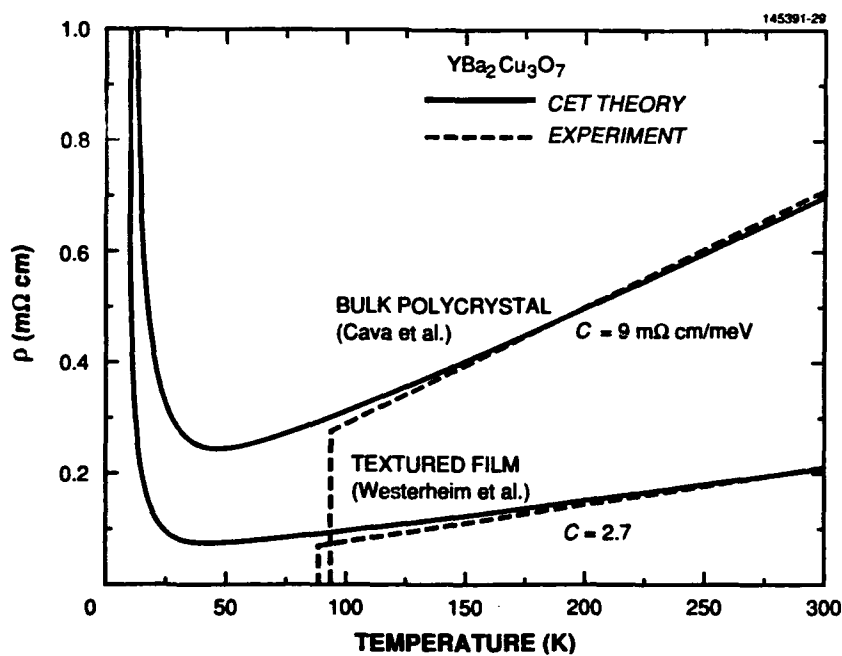


Figure 29. Comparison of theory with experiment for bulk polycrystalline and oriented film  $\text{YBa}_2\text{Cu}_3\text{O}_7$  (data of Cava et al. [5] and Westerheim et al. [61]).

For the  $\text{La}_{2-x}\text{Sr}_x\text{CuO}_4$  system, a  $T$  versus  $x$  phase diagram is proposed. In Figure 30 the material is either superconducting or metallic for  $T > E_{\text{hop}}/k$ . At large  $x$ , where  $E_{\text{hop}} \approx E_{\text{el}}$ , the insulating regime is at quite low temperatures; at small  $x$ , the boundary of this region rises sharply with the increase in  $E_{\text{hop}}$  as antiferromagnetic order sets in. Where  $\eta P \ll 1$ , a small range in which the material can be superconducting at  $T \approx 0$  begins at  $x = x_0$ , becomes insulating over a short  $T$  interval, and then reverts to metallic as  $T$  continues to rise. This effect represents the situation where a minimum appears in the  $\rho$  versus  $T$  curve described above.

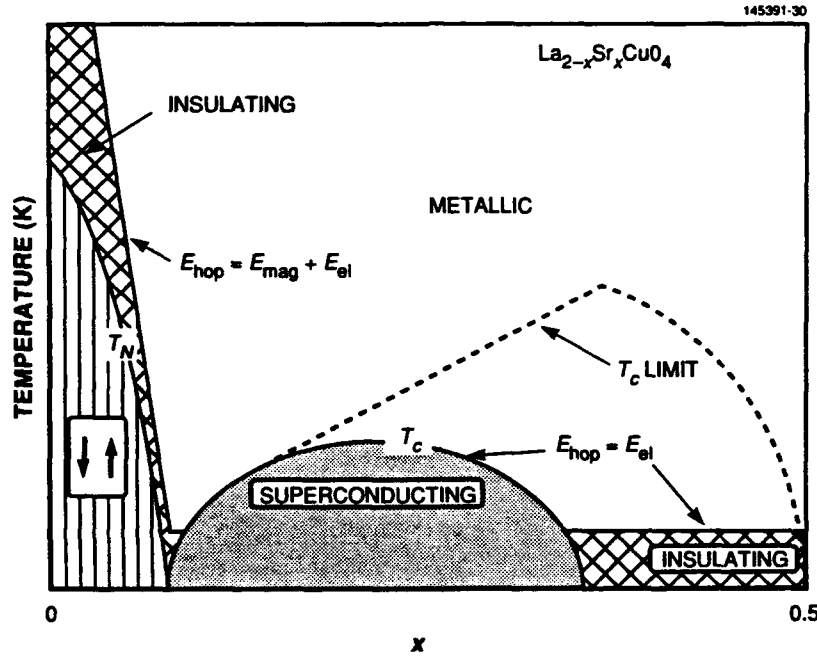


Figure 30. Proposed phase diagram for the  $\text{La}_{2-x}\text{Sr}_x\text{CuO}_4$  system.

In the  $x = 0.10$  curve of Figure 28, a minimum in  $\rho$  appears at  $T \approx 60$  K, together with evidence of two critical temperatures. This result suggests the presence of at least two phases, one of which has  $E_{\text{hop}} > kT_c$ . The case of superconductors with multiple phases is examined next.

### 5.3 RESISTIVITY OF MULTIPHASE SUPERCONDUCTORS

#### 5.3.1 Cylindrical Network Model

For practical systems, particularly polycrystalline specimens, phases with varying  $x$  that give rise to regions of different  $T_c$  values can produce a spectrum of  $\rho$  versus  $T$  curves [56,57]. Consider the multiphase network depicted in Figure 31, where semiconducting regions (resistivity  $\rho_0$ ) are shunted consecutively by different superconducting regions ( $\rho_n$ ) of varying sizes. If the fractional cross-sectional area of the  $\rho_0$  regions is  $f_n [= A_0/(A_0 + A_n)]$ , the effective resistivity of the network becomes

$$\rho = \sum_1^n g_n \frac{\rho_0 \rho_n}{(1-f_n)\rho_0 + f_n \rho_n} \quad , \quad (53)$$

where  $g_n = L_n/L$  and  $\sum g_n = 1$ .

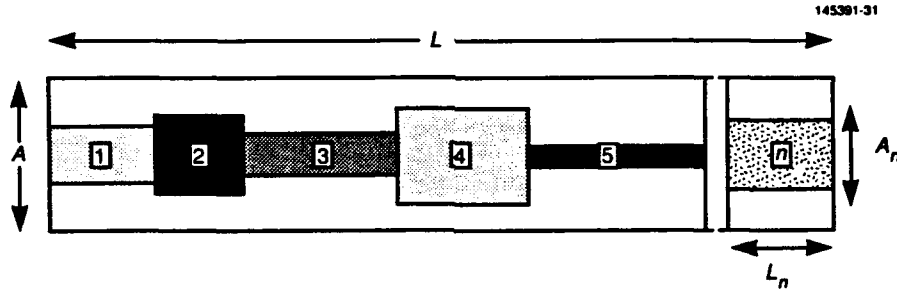


Figure 31. Cross section of a multiphase insulator/superconductor network.

In Figure 32, model curves based on Equations (48) and (53) for a two-phase system covering the range of  $0 \leq f \leq 1$  are presented for specimens with the following parameter values: For  $\rho_0$ ,  $E_{\text{hop}}^{(0)} = 35$  meV and  $x_0 = 0.06$  (partially frustrated, but not yet superconducting because  $x_0 < x_1$ ), and for  $\rho_1$ ,  $E_{\text{hop}}^{(1)} = 4$  meV and  $x_1 = 0.25$ . Based on these results, a partially superconducting material will retain its metallic slope until the amount of semiconducting phase exceeds 90%. Because the  $\rho$ -axis intercept of the high-temperature slope is defined in terms of superconductor phase parameters (it may be shown that  $\rho_i \approx CE_{\text{hop}}^{(1)}(1-x_1)/x_1(1-f)$  for slopes in the metallic regime), the intercept may serve as a qualitative diagnostic tool for characterizing the macroscopic homogeneity of specimen. Where the intercept is negative, as in the case of the  $\text{YBa}_2\text{Cu}_3\text{O}_y$  data of Cava et al. [5], there is the suggestion that trace amounts of even higher- $T_c$  phases may be present, perhaps regions with  $\beta \rightarrow 0$ .

An example of the departure from metallic slope with the presence of a large semiconducting region is seen in the comparison between single-crystal  $\text{Pb}_2\text{Sr}_2(\text{Dy,Ca})\text{Cu}_3\text{O}_8$  and multiphase polycrystalline  $\text{Pb}_2\text{Sr}_2(\text{Y,Ca})\text{Cu}_3\text{O}_8$  results [58] that are reproduced in Figure 33. In accord with the above predictions, the polycrystal has not only an insulator slope with <2% effective superconductor, here modeled with two different  $T_c$  phases, but a resistivity almost an order of magnitude greater than that of the single crystal specimen with about 35% superconductor. With  $\text{Cu-O}_5$  pyramidal complexes in the  $\text{Cu}(2)$  sublattice, similar to the structure of  $\text{YBa}_2\text{Cu}_3\text{O}_7$ , the  $E_{\text{hop}}$  value for the superconducting phase was also chosen as 4 meV. A slightly higher value of  $\beta$  ( $= 0.6$ ) or lower value of  $x_1$  ( $= 0.15$ ) could account for the lower  $T_c = 50$  K. An alternative mode of presentation is demonstrated by the curves of Figure 34, normalized to  $\rho$  at 300 K. From the data [59] for  $(\text{Tl}_{0.5}\text{Bi}_{0.5})(\text{Ca}_{1-z}\text{Y}_z)\text{Sr}_2\text{Cu}_2\text{O}_y$  in Figure 35, it is reasonable to suggest that substituting  $\text{Y}^{3+}$  for  $\text{Ca}^{2+}$  ions may be more a cause of inhomogeneity than a source of carriers.

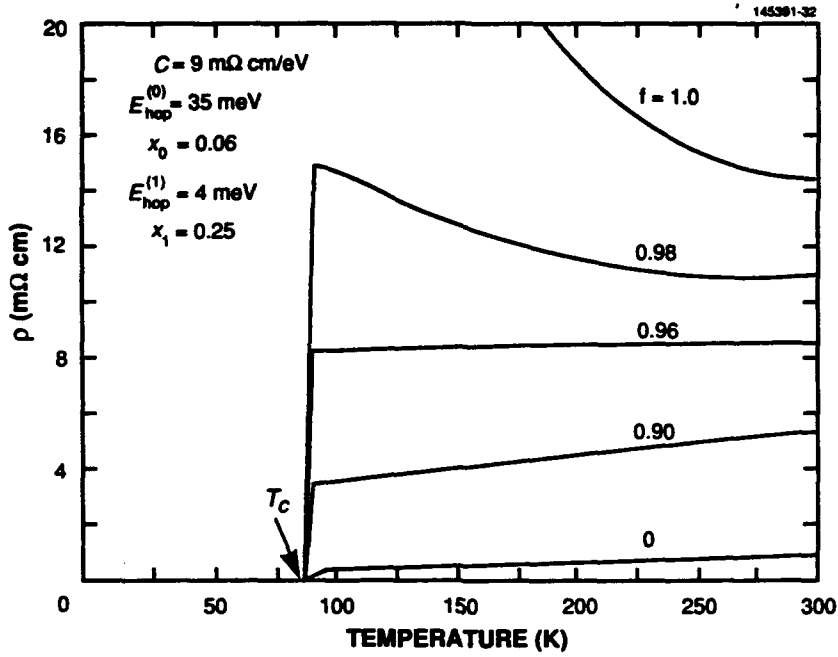


Figure 32. Sample resistivity versus temperature plots of a two-phase  $\text{YBa}_2\text{Cu}_3\text{O}_y$  system over the range  $0 \leq f \leq 1$ .

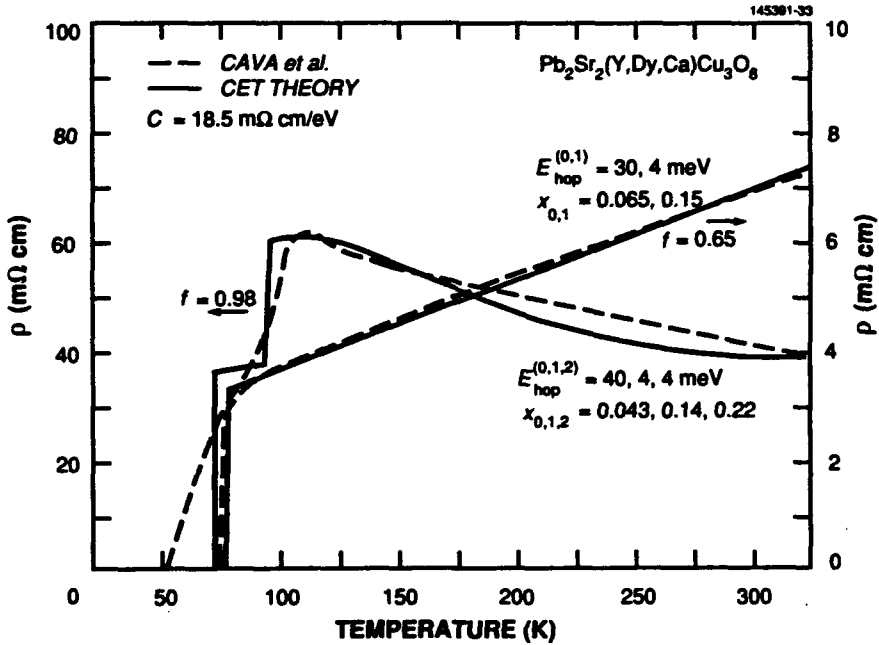


Figure 33. Theory fit to experiment for  $\text{Pb}_2\text{Sr}_2(\text{Dy,Ca})\text{Cu}_3\text{O}_8$  single-crystal ( $f = 0.65$ ) and  $\text{Pb}_2\text{Sr}_2(\text{Y,Ca})\text{Cu}_3\text{O}_8$  polycrystalline ( $f = 0.98$ ) specimens. Because grain boundary and orientation effects are absent, it is likely that the  $C$  parameter is smaller for the single crystal (data Cava et al. [58]).



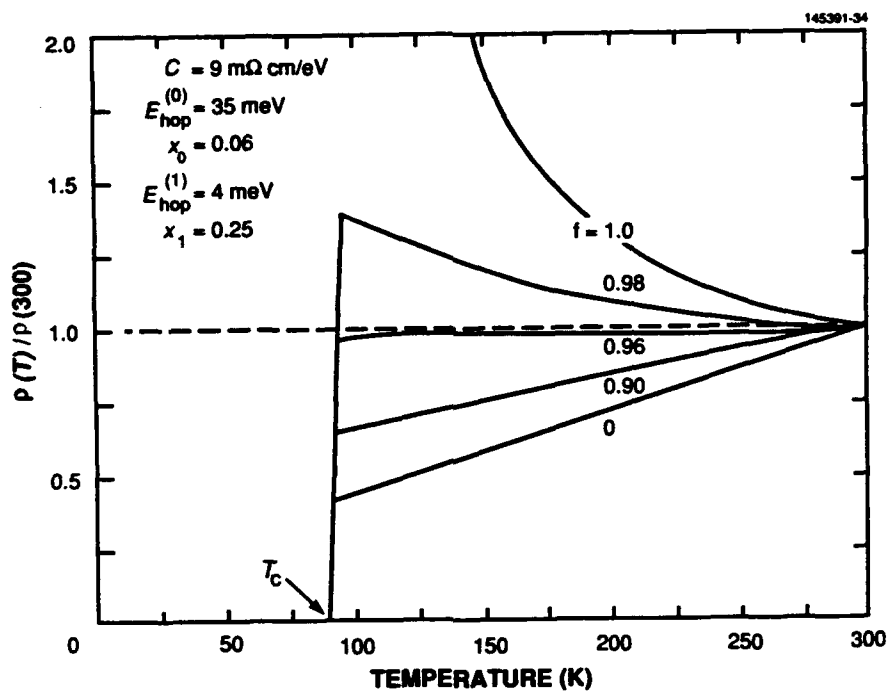


Figure 34. Curves of Figure 32, with  $\rho(T)$  normalized to  $\rho(300)$ .

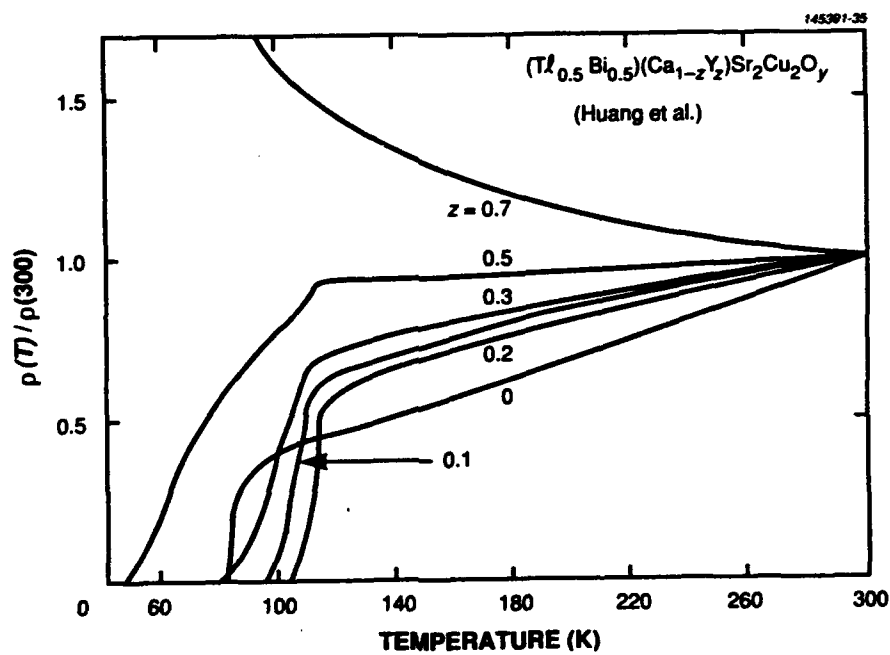


Figure 35.  $\rho(T)/\rho(300)$  versus  $T$  curves for the  $(\text{Tl}_{0.5}\text{Bi}_{0.5})(\text{Ca}_{1-z}\text{Y}_z)\text{Sr}_2\text{Cu}_2\text{O}_y$  family of mixed-phase superconductors (data of Huang et al. [59]).

### 5.3.2 Microstructure Effects

As discussed by Kingery [60], the effect of grain boundaries in ceramics is reflected in the diffusion constant and is usually of concern where the mean-free-path length is comparable to a grain dimension. Because the diffusion length is generally much smaller than a grain diameter in hopping electron semiconductors, the influence of grain boundaries appears as anomalous decreases in  $D$  over very short lengths, i.e., the grain boundary regions, and is usually ignored where  $\rho > 10^3 \Omega \text{ cm}$ . Where the resistivity is not high, however, as in the case of the high- $T_c$  oxides with very small  $E_{\text{hop}}$  values, the impedance introduced at grain boundaries is of greater concern.

In the foregoing interpretation of data, questions of resistance caused by scattering at boundaries between crystallographically misaligned grains were not considered. Because both grain orientation and lattice discontinuities at grain boundaries would lower carrier mobility through local reductions in diffusion length  $d$ , the semiempirical  $C$  parameter should be smaller for single crystals or highly oriented films. An example of this tendency is shown in the lower resistivity curve in Figure 29, where data [61] from a highly textured ( $c$ -axis oriented)  $\text{YBa}_2\text{Cu}_3\text{O}_7$  thin film (thickness  $\approx 2000 \text{ \AA}$ ) sputtered onto a  $\text{LaAlO}_3$  substrate are compared with the results for a polycrystalline bulk specimen of similar composition. In this case,  $\rho$  is about three times smaller than that of the corresponding bulk polycrystal.

A simple modification to parameter  $C$  that may semiempirically account for the anisotropy effects in these low-resistivity granular oxides may be constructed as follows:

$$C = (C_0 / \langle \cos \phi \rangle) [(1 - \delta_{gb}/\delta_g) + (\delta_{gb}/\delta_g)(D_g/D_{gb})] \quad (54)$$

where  $C_0$  is the perfect-alignment limit,  $\phi$  is an orientation angle,  $\delta_{gb}/\delta_g$  is the ratio of effective thickness of a grain boundary region to average grain diameter, and  $D_g/D_{gb}$  is the corresponding ratio of diffusion constants that is also dependent on  $\langle \cos \phi \rangle$ . The  $\langle \cos \phi \rangle$  factor outside the square bracket corrects for the general misalignment effect that would result in a longer average conduction path, i.e., effective specimen length. For ideal alignment,  $\phi = 0$ ,  $D_g/D_{gb} = 1$ , and  $C = C_0$ . Because  $\langle \cos \phi \rangle \approx 2/\pi$  for random orientation, an increase in  $C$  of about 50% might be expected regardless of microstructure details. From Equation (54), the principal contribution of grain boundaries would come from the  $(\delta_{gb}/\delta_g)(D_g/D_{gb})$  term, which represents a small number multiplied by a large one, and one may assume that grain dimensions would have a detectable influence despite  $\delta_{gb}/\delta_g \ll 1$ .

### 5.4 MICROWAVE SURFACE RESISTANCE $R_s$

The high-frequency electrical properties of superconductors are influenced by both  $n_s$  and  $n_n$ , and have accordingly been analyzed in terms of the Gorter-Casimir two-fluid model [62]. As derived, for example, in Van Duzer and Turner [63], the complex surface impedance is expressed as

$$\begin{aligned} Z_s &= R_s + j\omega L_s \\ &= (1/2) \omega^2 \mu_0^2 \lambda_L^3 \sigma_n + j\omega \mu_0 \lambda_L \end{aligned} \quad (55)$$

where  $\sigma_n$  is the conductivity due to normal electrons,  $\omega$  is the angular frequency,  $\lambda_L$  is the London penetration depth as defined in Section 2.1, and  $\mu_0 = 4\pi \times 10^{-7} \text{ H/m}$  [meter-kilogram-second (MKS) units used here].

For mixed-valence hopping electron perovskites,  $\sigma_n = \sigma(n_n/N)$ , as defined by Equations (10) and (44), and  $\lambda_L(t) = \lambda_L(0)[1 - \exp(W - W/t)]^{-1/2}$  [to be developed as Equation (65) in Section 6.3], with  $t = T/T_c$ . The MKS version of  $\lambda_L(0) = (m/\mu_0 n_s e^2)^{1/2}$  is used here with  $n_s$  given by Equation (30) and subsequently  $\eta P$  by Equation (38). From these relations, the intrinsic surface resistance  $R_s$  of Equation (55) for a bulk superconductor, defined as the surface losses per unit surface area per unit surface current density amplitude, becomes

$$R_s = \frac{1}{2} \frac{\mu_0^{1/2} m^{3/2}}{e^2 k} \frac{\omega^2 V^{3/2}}{C T_c x_i^{3/2}} \frac{x}{(1-x)} \frac{[1 - \exp(-W)]^{3/2} \exp(-W/t)}{t [1 - \exp(W - W/t)]^{3/2}}, \quad (56)$$

In Figure 36 calculations from Equation (56) are compared with  $R_s$  data (corrected to remove the asymptotic residual resistance contribution determined at  $T \rightarrow 0$ ) [64] of a  $\text{YBa}_2\text{Cu}_3\text{O}_7$  textured film similar to that of Figure 29 for  $\nu (= \omega/2\pi) = 1.5 \times 10^9$  Hz. For this particular film,  $T_c = 86.4$  K, which gives  $W = 0.54$  if  $E_{\text{hop}} = 4$  meV. The remaining parameter values used for the computations of Figure 36 are taken from those determined earlier in fitting  $T_c$  and  $p$  data:  $C = 2.7 \times 10^{-5} \Omega\text{m/eV}$ ,  $x_i = 0.035$ , and  $x = 0.25$ . Although the corrections to the raw data to account for film thickness were based on the penetration depth temperature dependence of the empirical two-fluid model (which differs somewhat from the CET version to be examined in Section 6), there is remarkable agreement between theory and experiment, with a discrepancy that is less than a factor of 2 across the entire range of  $0 \leq t \leq 1$ .

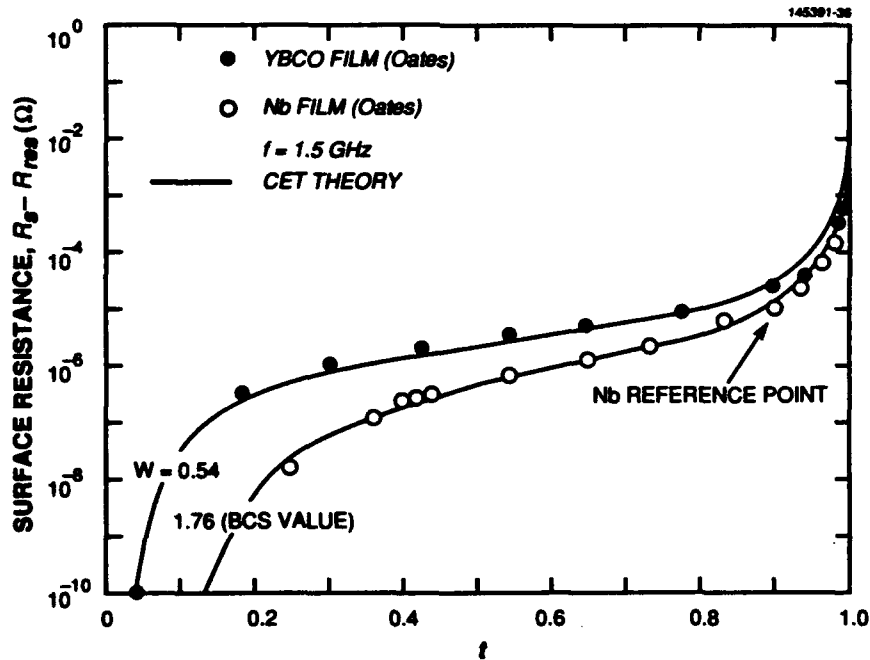


Figure 36. Comparison of CET calculations and measurements of microwave surface resistance  $R_s$  versus  $t$  for films of  $\text{YBa}_2\text{Cu}_3\text{O}_7/\text{LaAlO}_3$  and Nb (data of Oates and Anderson [64] and Sheen et al. [66], respectively).

It is instructive to compare Equation (56) with the surface resistance expression derived from the BCS theory,

$$R_s = (C' \omega^{3/2}/T) \exp[-\Delta(T)/kT] \quad ,$$

or

$$= (C' T_c \omega^{3/2}/t) \exp[-\Delta(t)/\Delta(0) (1.76/t)] \quad , \quad (57)$$

where  $C'$  is a constant. Because  $\Delta(t)/\Delta(0) \approx 1$  for  $t < 0.5$ , it may be determined that the temperature-dependent parts of Equations (56) and (57) approximate each other over this temperature range for  $W = 1.76$ . The frequency dependence of  $R_s$ , which differs between the two relations, appears to favor  $\omega^2$  of Equation (56), as determined by experiment [65].

To demonstrate further the difference in  $W$  between high- $T_c$  oxides and BCS-type metals, data corrected for residual resistance from an Nb film [66] is fitted to the temperature function of Equation (56), with  $W = 1.76$  (see Figure 36). Because values for  $C$ ,  $x_p$ , and  $x$  are not available (if indeed applicable here), the computed curve in this case has been arbitrarily adjusted to match  $R_s$  at  $T = 77$  K. Once again, however, the temperature trend agrees with experiment over the entire superconduction range.

As indicated by Equation (55),  $R_s$  depends jointly on  $\sigma_n$  and  $\lambda_L^3$ . One would expect these high- $T_c$  compounds to have lower microwave losses because polaronic oxides should have  $\sigma_n$  that is intrinsically smaller than that of metals. Unfortunately, the larger  $\lambda_L$  values that result from smaller  $n_s$  appear to more than offset this advantage, particularly in the temperature regime closer to  $T_c$ . With the high- $T_c$  compositions currently under development, losses comparable to those of metals near their low  $T_c$  limits may be achieved only at operating temperatures substantially lower than  $T_c$ . An unattractive scenario would be to have applications of these superconductors restricted to a low- $T_c$  regime.

## 6. SUPERCURRENTS AND MAGNETIC PHENOMENA

Although the basic requirement for zero resistance has been defined as  $n_s \geq n_p$ , which is largely controlled by temperature, this condition alone is not sufficient for superconduction. Superconductivity is a thermodynamic state of energy that is lower than normal and condensation to the superconducting state occurs when this stabilization energy is transferred to a supercurrent flow. In the following sections, the role of magnetic field in limiting this current is established, and the factors that determine critical magnetic field, critical current density, and related phenomena are examined.

### 6.1 SUPERCURRENT FORMATION AND EFFECTIVE SUPERCARRIER DENSITY $n_s^e$

It is important to repeat that a superconductor is not a perfect conductor. As stated earlier, perfect conduction implies simply zero electrical resistivity — the unrealizable case of universally unimpeded charge transport. For a material to be a perfect conductor, there can be neither scattering among carriers nor energy loss in the form of thermal dissipation through electron-phonon interaction. In reality, electrons in a solid can never be completely uncoupled from the lattice, and where so-called "free" electrons are involved, the state occupation limitations imposed by the Pauli exclusion principle create a repulsive action that also restricts current flow. Zero resistivity in the superconducting state, however, is achieved through spatial rigidity of the supercurrent that fulfills the  $E = 0$ ,  $B = 0$  conditions. As pointed out in the discussion of Equation (3), supercurrent rigidity ( $\nabla \cdot \mathbf{j}_s = 0$ ) requires both  $\nabla \cdot \mathbf{A} = 0$  (the London gauge) and  $\nabla n_s = 0$ . The latter is also a sufficient condition that implies real-space ordering of supercurrent carriers and may also involve some form of dynamic spin ordering. The spatial ordering of charges ( $\nabla n_s \rightarrow 0$ ) in an MO scheme will now be examined as the mechanism that creates fixed conduits for supercurrent flow.

If mixed valence can provide conduction among bound electrons delocalized within the directed lobes of their covalent bonds, it seems intuitive that some kind of electrostatic ordering of these carriers must exist; lattice periodicity alone would suggest a regularity to any carriers participating in the bonding. The charge balance requirements for optimizing the Madelung energy also impose such a spatial distribution of valence states. Because part of the trapping or stabilization energy of the carrier is from electrostatic attraction to its polaron source, i.e., the other half of its electric dipole, the carrier ordering is dictated by the dispersal of the fixed polaron sources, as depicted in Figure 37(a). For vanishingly small concentrations the carriers are isolated, with radially symmetric cell profiles in an  $x$ - $y$  plane (in reality, only the fourfold symmetry of a  $d_{x^2-y^2}$  orbital in the Cu-O<sub>4</sub> square-planar case). As the spatial density of polaron "cells" increases, the shapes of the overlapping regions converge into a chain to assume the minimum energy orientation of aligned electric dipoles. At a threshold density of fixed polaron sources, condensation of ordered chains would occur spontaneously in a manner depicted by Figure 37(b). A more realistic quantum mechanical picture of the resulting giant molecule structure that permits the ordered passage of carriers through the directed lobes of covalent bond MO wavefunctions is shown in Figure 38.

In the preceding sections, the necessary condition that  $\rho = 0$  was discussed in terms of a series of parallel, independent chains that could be represented by a one-dimensional model because only one completed chain would be required for zero resistance. For phenomena related to the buildup of supercurrent and its associated magnetic effects, however, orbital transfer can no longer be treated as an isolated linear chain but rather as a series of interconnected chains distributed across a macroscopic area.

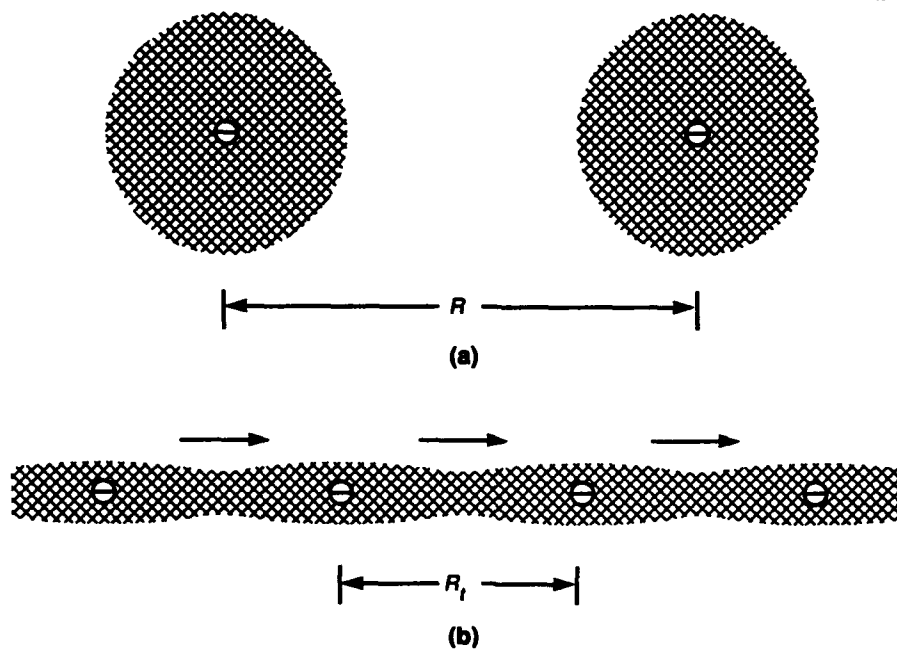


Figure 37. Two-dimensional model of polaron condensation to superconducting state: (a) below percolation threshold, and (b) after ferroelectric alignment with ordered supercurrent flow at threshold  $R = R_p$ .

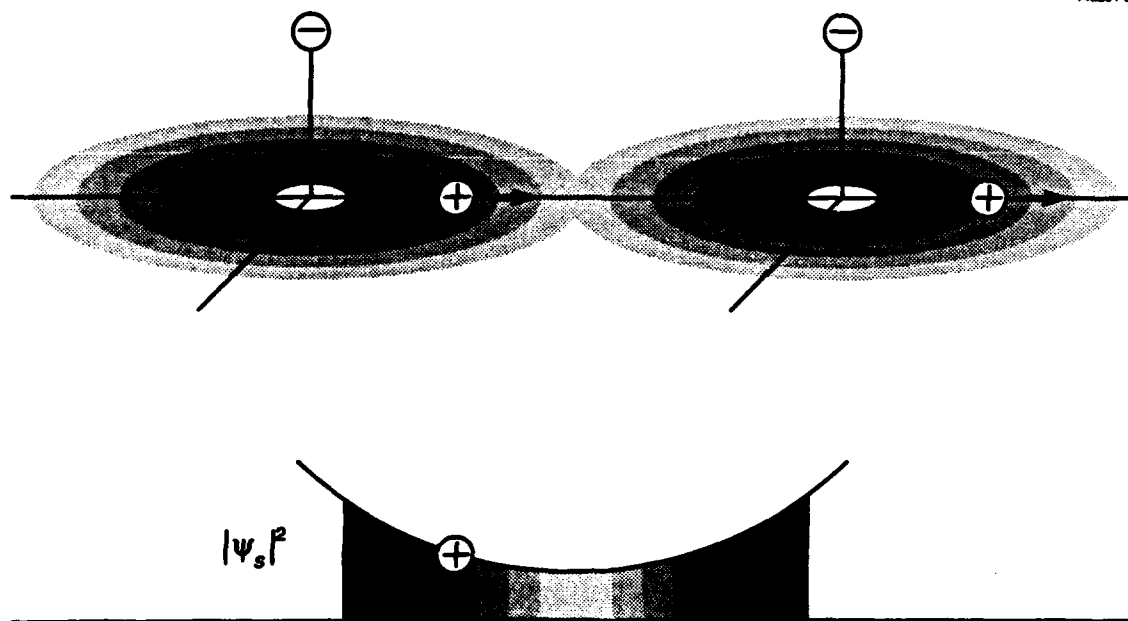
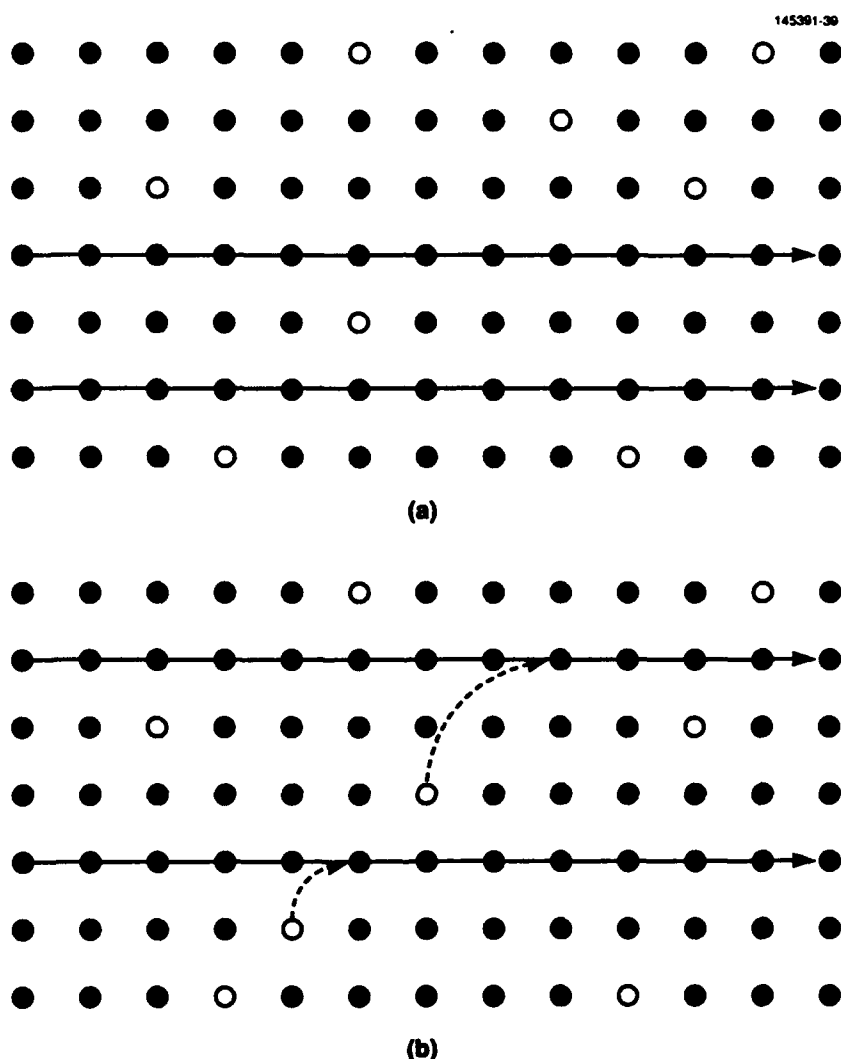


Figure 38. Superconducting polaron distribution and probability contour of the carrier density  $n_s = |\psi_s|^2$ .

It will be recalled from Equation (38) that the completion of a single path was contingent on the existence of a threshold supercarrier density  $n_r$ , occurring at  $T = T_c$ ; because a fraction of the electrons is in thermal activation at all times, the total  $n_r$  cannot be expected to complete every possible superconduction linkage simultaneously. Even if the chemical ordering were ideal ( $P = 1$ ), the incidence of electron-phonon encounters is still random. A possible analog to this effect would be the electrical breakdown of a gaseous medium, which begins with a single irregular striation that moves about as dictated by random molecular collisions. As the ionizing collisions increase with density (or pressure), multiple striations appear, and the gas is eventually transformed into a plasma continuum with a large fraction of the gas participating in the current. In Figure 39 this effect in a square-planar lattice is depicted by a Boltzmann population of hopping electrons that disrupt completed paths momentarily (a), only to reestablish new ones adjacent to (or including part of) the originals (b).



*Figure 39. Two-dimensional model of partially condensed supercurrent: (a) before disruption by hopping electrons, and (b) after establishment of new supercurrent paths.*

At this point it may be reasonably assumed that the current increases continuously from zero, with only the excess of  $n_s$  over  $n_i$  initially contributing to the supercurrent. An effective carrier density at  $T = T_c$  is therefore defined as  $n_s^e(T_c) = n_s(T_c) - n_i(T_c) = 0$ . At  $T = 0$ , however, there are no hopping electrons and one must assume that all of  $n_i$  is contributing to the supercurrent, i.e.,  $n_s^e(0) = n_s(0)$ . To satisfy these boundary conditions in the most direct manner, the above relation may be generalized to all temperatures according to

$$n_s^e(T) = n_s(T) - n_i(T) \quad , \quad (58)$$

where  $n_i(T) = n_i(T_c)[1 - n_s^e(T)/n_s^e(0)]$ . Thus, the fractional contribution of the threshold carrier density  $n_i(T_c)$  to the supercurrent increases in direct proportion to the buildup of the effective carrier density  $n_s^e(T)$  as  $T \rightarrow 0$ . The logic of Equation (58) is displayed pictorially in Figure 40, where the  $n_s^e(T)$  population is pictured as decreasing because of the proportionate decrease of  $n_s(T)$  and increase of  $n_i(T)$ . After rearrangement to isolate  $n_s^e(T)$ , Equation (58) becomes

$$n_s^e(T) = n_s^e(0) \left[ \frac{n_s(T) - n_i(T_c)}{n_s(0) - n_i(T_c)} \right] \quad . \quad (59)$$

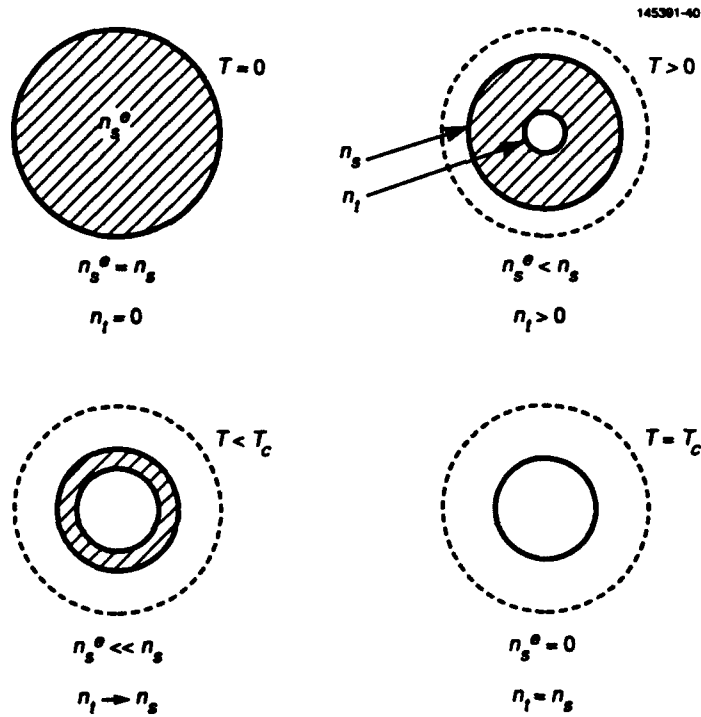


Figure 40. Pictorial representation of the simultaneous decrease of  $n_s^e(T)$  and the growth of  $n_i(T)$  as  $T \rightarrow T_c$ , where  $n_s$  and  $n_i$  converge to establish the threshold density for the onset of superconductivity.



Based on this relation for the effective carrier density that contributes directly to the supercurrent, it is now possible to proceed with an examination of the current- and magnetic-field related physical parameters derived from the London theory.

## 6.2 CONDENSATION ENERGY $\Delta G$

According to the London thermodynamic arguments [9], the condensation energy of the superconduction transition is the reduction in the Gibbs free energy per unit volume  $\Delta G$ . Inspection of Figure 37 reveals that this energy may be represented by the difference in energy between aligned and randomly oriented dipoles — not unlike ferroelectricity or the electronic analog to spin-ordering in spontaneous magnetism that was originally proposed by London [67] in defining his macroscopic molecule concept. Unlike spontaneous magnetism, however, there is no fixed population of dipoles and no strong exchange field that may lend itself to a Brillouin function variation with temperature. Instead, the fractional population of superconducting polarons is exponentially dependent on  $(kT)^{-1}$ , and because the polarons are transported by covalent transfer that is not directly phonon-coupled to the lattice, the conduction mechanism is temperature independent. This situation permits the electrostatic potential energy of the dipole array to be released adiabatically as kinetic energy of carriers in an ordered state, without the usual descent to random thermalization that produces the temperature change associated with the magnetocaloric or electrocaloric effects.

Because condensation occurs as a supercurrent is generated, a two-dimensional model is not only sufficient to describe the physical situation, but is probably more appropriate. For a planar array of dipoles with moment  $m_d$ , this function could be expressed as<sup>27</sup>

$$\begin{aligned}\Delta G &= G_n - G_s \sim (\langle m_d \cdot m_d \rangle / KR_d^3) n_s e \\ &\approx (m_d^2 \langle \cos \theta \rangle / KR_d^3) n_s e\end{aligned}\quad (60)$$

Because  $\langle \cos \theta \rangle = 1$  (perfect alignment),  $R_d = a/x_s e = a/n_s e V$ , and  $m_d = eR_d/2$  (at the midpoint between cell centers), Equation (60) may be approximated by

---

<sup>27</sup>This relation may be derived from the standard theory for the interaction energy density of a dipole array (with  $K = 1$ ),

$$E_d = \sum_{k>j} \frac{m_{dj} \cdot m_{dk}}{r_{jk}^3} - \frac{3(r_{jk} \cdot m_{dj})(r_{jk} \cdot m_{dk})}{r_{jk}^5},$$

where  $r_{jk}$  is the distance between neighboring dipoles  $j$  and  $k$ . For a linear chain of aligned dipoles, the energy per dipole is  $-2m_d^2/r_d^3$ , and for a square planar array, it is  $-m_d^2/r_d^3$ , similar to Equation (60) with  $K = 1$ . In the cubic case, the energy is zero to first order; smaller contributions come from quadrupole terms. If low symmetry yields high  $\Delta G$ , uniaxial and planar structures should feature larger critical fields and current densities, as discussed in Section 6.4 and 6.6.

$$\begin{aligned}\Delta G &\approx (1/4) (e^2 V/aK) (n_s^e)^2, \\ &\approx (1/4) (e^2/VaK) (x_s^e)^2,\end{aligned}\quad (61)$$

where the minimum value of  $R_d = R_t = 2a$  as shown in Figure 37(b). For  $a = 4$  Å,  $K = 16$ , and recalling that  $V = 1.7a^3$  for  $\text{La}_{2-x}\text{Sr}_x\text{CuO}_4$ , it may be estimated that  $\Delta G = 8.32 \times 10^8 (x_s^e)^2$  ergs/cm<sup>3</sup>. (For this computation and those that follow,  $e = 4.8 \times 10^{-10}$  esu.) Because  $x_s^e$  is a function of  $T$ ,  $\Delta G(T)$  may be evaluated at  $T = 0$ . With  $x_s^e(0) = 0.068$  for  $\text{La}_{1.8}\text{Sr}_{0.2}\text{CuO}_4$  (see Figure 22),  $\Delta G(0) = 3.77 \times 10^6$  ergs/cm<sup>3</sup>; for  $\text{YBa}_2\text{Cu}_3\text{O}_7$ , where  $x_s^e(0) = 0.09$  and  $V = 1.5a^3$  [considering only the Cu(2) sites], and  $\Delta G(0) = 7.54 \times 10^6$  ergs/cm<sup>3</sup>.

The formation of the spatially ordered carriers ( $\nabla n_s = 0$ ) in a molecular chain, therefore, results from the electrostatic dictates of the Madelung energy. For the creation of the supercurrent, however, the dynamic order of the carriers results from electrostatic repulsion between the mobile halves of the dipoles, possibly enhanced by the Pauli principle repulsive action. As the carriers transfer between cells, maintaining the required one carrier per cell ordering, there is no direct competition for quantum states and the Pauli repulsion serves as a propellant to charge transport rather than as a cause of carrier scattering. As a consequence, supercurrent rigidity follows naturally from the constraints of the directed bonding orbitals which act as conduits for the passage of electrons.

### 6.3 LONDON PENETRATION DEPTH $\lambda_L$

From the relation between current density and magnetic field stated in Equation (3), the London penetration depth is now defined in terms of  $n_s^e$ , according to

$$\lambda_L = (mc^2/4\pi e^2 n_s^e)^{1/2} = (mc^2 V/4\pi e^2 x_s^e)^{1/2}, \quad (62)$$

which provides  $\lambda_L(0) = 5.32 \times 10^5 V^{1/2} x_s^e(0)^{-1/2}$  cm, if the true electron mass is used. For the  $\text{La}_{1.8}\text{Sr}_{0.2}\text{CuO}_4$  perovskite in Figure 22,  $V = 1.7a^3$ ,  $a = 4$  Å, and  $x_s^e(0) = 0.068$ , which yields  $\lambda_L(0) \approx 2130$  Å, in good agreement with the 2000-Å value determined from experiment [68,69] for  $\text{YBa}_2\text{Cu}_3\text{O}_7$ , where  $V = 1.5a^3$  and  $x_s^e(0) = 0.09$ ,  $\lambda_L(0) \approx 1740$  Å, in accord with the 1670-Å value derived from microwave strip line resonance measurements [64]. The familiar ratio then reduces to the new two-fluid function,

$$[\lambda_L(0)/\lambda_L(T)]^2 = n_s^e(T)/n_s^e(0). \quad (63)$$

From Equations (30), (38), and (59), Equation (63) is developed as

$$\frac{n_s^e(T)}{n_s^e(0)} = \frac{\left[1 - \exp\left(-E_{\text{hop}}/kT\right)\right] - \left[1 - \exp\left(-E_{\text{hop}}/kT_c\right)\right]}{1 - \left[1 - \exp\left(-E_{\text{hop}}/kT_c\right)\right]}, \quad (64)$$

$$\text{which leads to } [\lambda_L(0)/\lambda_L(t)]^2 = n_s^e(t)/n_s^e(0) = 1 - \exp(W - W/t), \quad (65)$$

where  $t = T/T_c$ .

In Figure 41, generic curves of  $n_s^e(t)/n_s^e(0)$  from Equation (65) are plotted for a range of  $W$  values [including  $W = 1.76$ , i.e., the universal ratio between  $kT_c$  and the BCS energy gap  $\Delta(0)$ ] and compared with

curves of the empirical two-fluid  $(1 - t^4)$  and BCS models [70]. At this point, it is instructive to compare the basic critical-temperature relations for both models:

$$kT_c = \Delta(0)/1.76 \quad (\text{BCS}) \quad , \quad (66a)$$

and

$$kT_c = E_{\text{hop}}/W \quad (\text{CET}) \quad . \quad (66b)$$

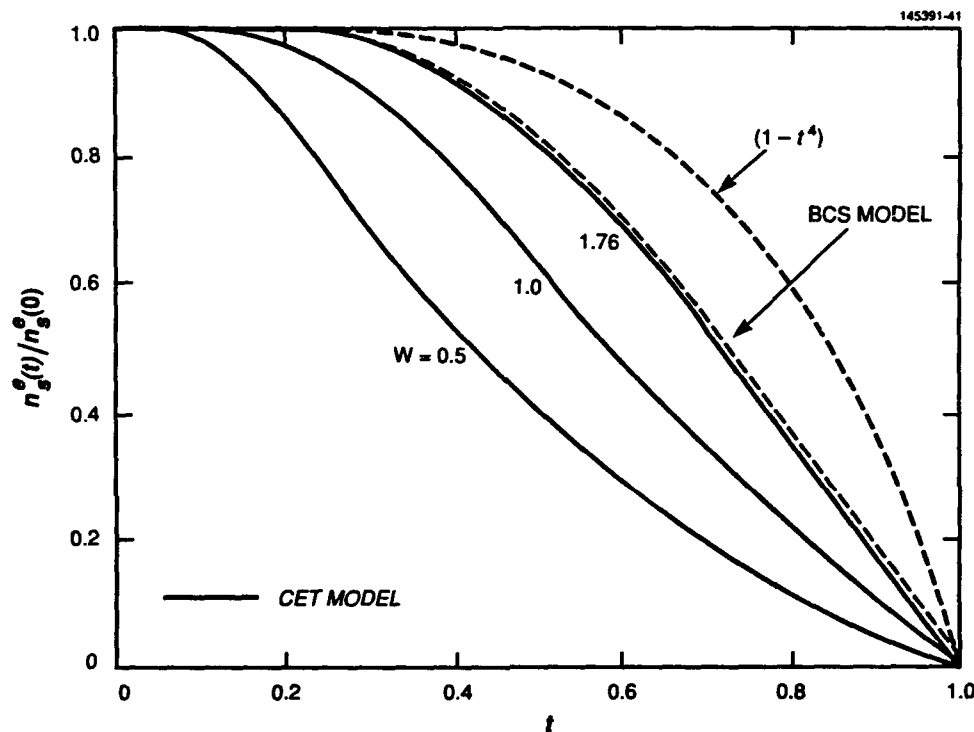


Figure 41. Comparison of  $n_s^e(t)/n_s^e(0)$  versus  $t$  for  $W = 0.5, 1$ , and  $1.76$  with the BCS function, and with the empirical  $(1 - t^4)$  two-fluid function.

With the  $\text{La}_{1.8}\text{Sr}_{0.2}\text{CuO}_4$  and  $\text{YBa}_2\text{Cu}_3\text{O}_7$  systems examined in Section 5.1, working values of  $W$  determined from fits to data are 0.75 and 0.5, respectively. For the BCS model, the denominator is the constant 1.76 calculated from  $\pi/\gamma$ , where  $\gamma$  is Euler's constant ( $\approx 0.577$ ). All the material-related information is contained in the gap parameter  $\Delta(T)$  computed at  $T = 0$  that appears in the numerator. This temperature-dependent gap energy, which determines the ratio of supercarriers to quasi-particles (normal electrons), is a maximum at  $T = 0$  and falls to zero in a Brillouin-type curve as  $T \rightarrow T_c$ . In the CET treatment, a gap equivalent would be the fixed numerator  $E_{\text{hop}}$ , but the denominator  $W$  is also a material-related variable that is strongly dependent on the polaron radius  $\gamma_p$ .

Although their meanings differ somewhat,  $\Delta(0)$  and  $E_{\text{hop}}$  represent energy separations (the former a condensation gap for electrons paired in  $k$  space and the latter a polaron trap barrier). The important

differences in the two relations of Equation (66) also lie in the  $W$  parameter versus the fixed denominator 1.76 of the BCS model. Comments on the agreement between the curves of Figure 41 for  $W = 1.76$  will be reserved for a later discussion.

Experimental evidence of the departure of  $n_s^e(t)$  from both the BCS model and the conventional two-fluid curve may be seen in the results of  $\lambda_L(t)$  measurements. The  $\ln[\lambda_L(t)/\lambda_L(0) - 1]$  data of Anlage et al. [71] plotted as a function of  $t^{-1}$  in Figure 42, where the ordinate variable in this instance was deduced from microwave phase velocity measurements [72] and applies to the regime  $t \leq 0.5$ . For purposes of comparison, the curves are adjusted to merge at  $t^{-1} = 2$ . All the  $\text{YBa}_2\text{Cu}_3\text{O}_7$  (YBCO) films are fitted to CET curves with  $W \leq 1$  and for the film with the  $\text{LaAlO}_3$  substrate,  $W = 0.5$ , consistent with the  $T_c$  results for bulk specimens and for the  $\text{LaAlO}_3$ -substrate specimens examined for the different superconductor variables throughout this report. It is also interesting that the slight departure from linearity that appears in the theoretical  $\ln[\lambda_L(t)/\lambda_L(0) - 1]$  function near  $t^{-1} = 2$  is also reflected in the measurements, thus confirming that the function is not just a simple BCS exponential. Further indication that a different two-fluid function is required for the high- $T_c$  oxides may be seen when fitting the CET model to the microwave resonance frequency data of Oates and Anderson [64], as is shown in Figure 43. With this technique, the resonance frequency  $f_o$  varies with the temperature dependence of the penetration depth, which in turn is sensed through the changes in kinetic inductance of a  $\text{YBa}_2\text{Cu}_3\text{O}_7/\text{LaAlO}_3$  stripline resonator. For a value of  $\lambda_L(0) = 1740$  Å, the agreement is reasonable for  $W$  in the 0.5 to 1.0 range up to 90% of  $T_c$ .

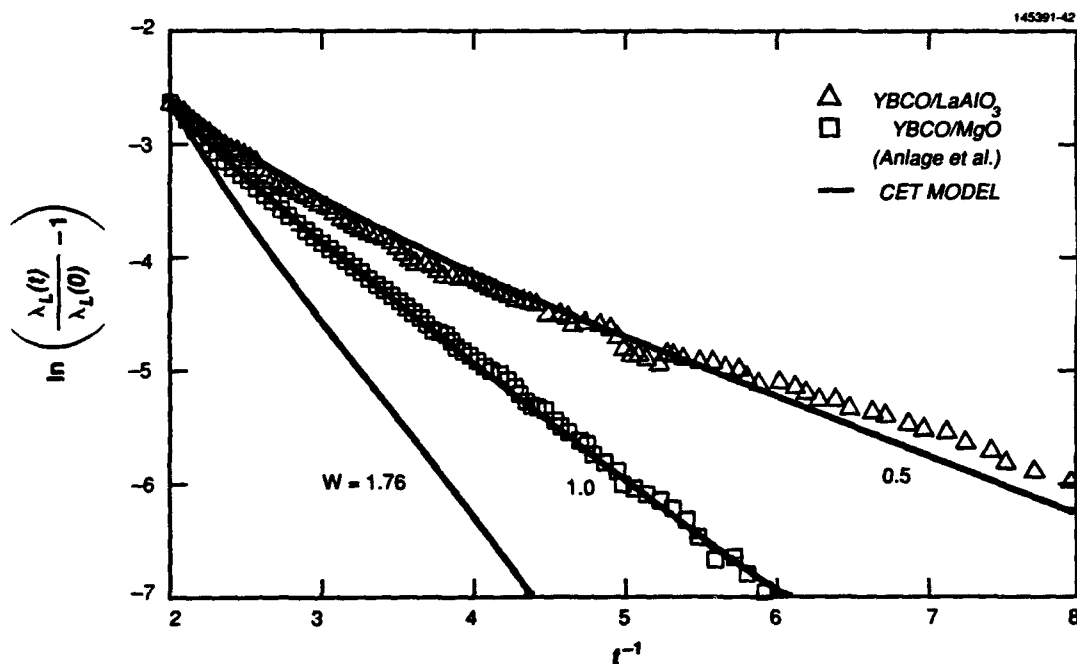


Figure 42. Comparison of calculated  $\ln[\lambda_L(t)/\lambda_L(0) - 1]$  versus  $t^{-1}$  curves with the  $\text{YBa}_2\text{Cu}_3\text{O}_7/\text{LaAlO}_3$  and  $\text{YBa}_2\text{Cu}_3\text{O}_7/\text{MgO}$  film data of Anlage et al. [71] for  $W = 0.5$  and 1.

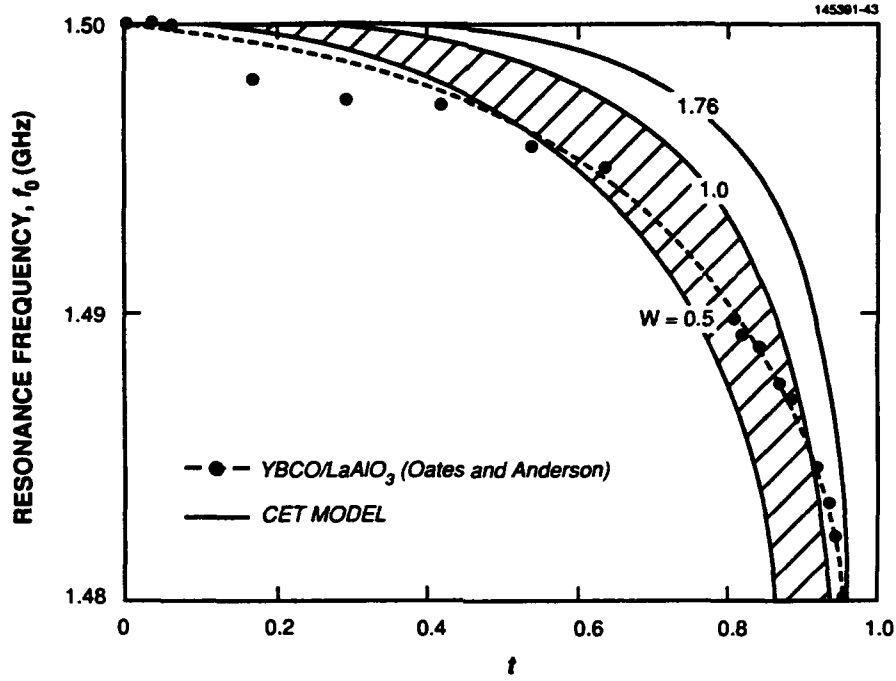


Figure 43. Comparison of calculated resonance frequency  $f_0$  versus  $t$  with  $\text{YBa}_2\text{Cu}_3\text{O}_7/\text{LaAlO}_3$  stripline resonator data of Oates and Anderson [64] for  $W = 0.5, 1$ , and  $1.76$ .

Although the regime in which the above analysis was focused is the clean limit  $\xi_0 \ll \lambda_L$  of the high- $T_c$  superconductors, for completeness it is appropriate to mention the relations for effective penetration depth  $\lambda$  and coherence length  $\xi$  that are used for the classes of superconductors introduced in Section 2.3. For the type-I pure limit with  $\xi_0 \gg \lambda_L$  (formally expressed as  $\xi^3 \gg \xi_0 \lambda_L^2$ ),  $\lambda = 0.65 \lambda_L (\xi_0 / \lambda_L)^{1/3}$ , and for the type-II (London or dirty) limit where  $\xi \rightarrow \ell$  (formally expressed as  $\xi^3 \ll \xi_0 \lambda_L^2$ ),  $\lambda = \lambda_L (\xi_0 / \xi)^{1/2} \approx \lambda_L (\xi_0 / \ell)^{1/2}$ .

#### 6.4 THERMODYNAMIC CRITICAL MAGNETIC FIELD $H_c$

If a bulk specimen is placed in a magnetic field  $H$ , the field will be expelled from the interior during a superconduction transition (the Meissner effect). Consequently, the superconduction Gibbs free energy  $\mathcal{G}_s$  will increase by the amount of the energy density  $H^2/8\pi$  of the expelled flux [73]. As a function of  $H$ ,  $\mathcal{G}_s$  becomes

$$\mathcal{G}_s(T, H) = \mathcal{G}_s(T, 0) + H^2/8\pi \quad . \quad (67)$$

For a nonmagnetic specimen in the normal state, however,  $\mathcal{G}_n(T, H) = \mathcal{G}_n(T, 0)$ , and because the condition for the return to the normal state is  $\mathcal{G}_n - \mathcal{G}_s = 0$ , the critical field may be defined according to Figure 44 as

$$\Delta\mathcal{G}(T, 0) = \mathcal{G}_n(T, 0) - \mathcal{G}_s(T, 0) = H_c(T)^2/8\pi \quad , \quad (68)$$

and

$$H_c(T) = [8\pi \Delta G(T,0)]^{1/2} , \quad (69)$$

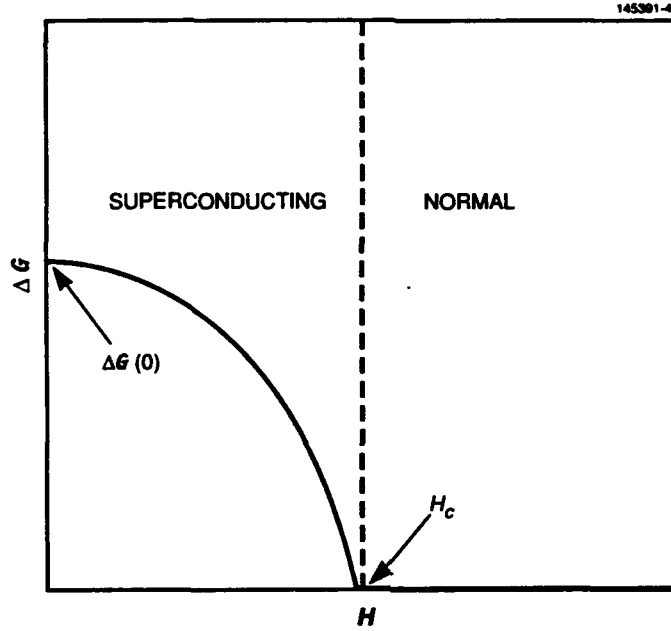


Figure 44. Change in Gibbs free energy as a function of  $H$ , indicating a decreasing energy available for conversion to the kinetic energy of supercurrent as  $H \rightarrow H_c$ .

where  $H_c(T)$  is the field at the surface [recalling from Equation (1) that  $H$  (and  $i_s$ ) decays exponentially, with penetration depth  $\lambda_L$ ]. After substitution from Equation (61),

$$\begin{aligned} H_c(T) &= (2\pi e^2 V / aK)^{1/2} n_s^e(T) , \\ &= (2\pi e^2 / VaK)^{1/2} x_s^e(T) . \end{aligned} \quad (70)$$

To determine  $H_c$ , it is important to realize that specimen cross-sectional dimensions should exceed the penetration depth in order to avoid the necessity of a correction  $(1 - A_{\text{eff}}/A)^{-1/2}$  to the effective volume of flux expulsion given in Appendix E. If  $A_{\text{eff}}/A \rightarrow 1$ , as in the case of a fine wire or thin film, the flux penetrates much of the material and the effective  $H_c$  is substantially greater than the true value.

From the estimates of  $\Delta G(0,0)$  beneath Equation (61), substitution into Equation (69) leads to  $H_c(0) \approx 10$  kOe for bulk  $\text{La}_{1.8}\text{Sr}_{0.2}\text{CuO}_4$ , and  $H_c(0) \approx 14$  kOe for  $\text{YBa}_2\text{Cu}_3\text{O}_7$ . An experimentally based value [5] of  $10 \pm 2$  kOe for bulk polycrystalline  $\text{YBa}_2\text{Cu}_3\text{O}_7$  was derived from conventional theory.

A universal relation follows directly from Equation (70):

$$H_c(T)/H_c(0) = [\lambda_L(0)/\lambda_L(T)]^2 = n_s^e(T)/n_s^e(0) \quad (71)$$

and

$$H_c(t)/H_c(0) = 1 - \exp(W - W/t) \quad , \quad (72)$$

to produce a temperature dependence that is the same as the two-fluid function of Equation (65). The curves plotted in Figure 45 for  $W = 1.76$  and 2 are, therefore, from the same family as those of Figure 41, but in this case it is more appropriate to compare them with the standard thermodynamic relation  $H_c(t)/H_c(0) = (1 - t^2)^{28}$  and also to examine the slopes at  $T = T_c$ . From the derivative of Equation (72) it may be shown that

$$[\partial H_c(t)/\partial t]_{t=1} = -H_c(0)W \quad , \quad (73)$$

or

$$\partial H_c(T)/\partial T = -W [H_c(0)/T_c] \quad \text{at } T = T_c \quad . \quad (74)$$

To match the slopes of the CET curve to the thermodynamic relation,  $W$  must therefore equal 2, slightly larger than the 1.76 BCS ratio. As indicated in Figure 45, the curves fit well over the upper quarter of the  $t$  range. Based on these results, one concludes that lower values of  $W$  substantially alter the shape of these curves that include the appearance of a tail and an inflection point at  $t = W/2$  (i.e., concavity begins to appear for  $W < 2$ ), and have an overall deleterious effect on the magnitudes of  $H_c$ .

At this point, it would be natural to continue with the subject of type-II superconductors, but this discussion must await the explanation of coherence in the context of the CET that is covered in Section 6.8.

## 6.5 SPECIFIC HEAT DISCONTINUITY $\Delta C$

For a magnetic field along the axis of a long thin specimen, a number of thermodynamic state variables may be directly related to  $H_c$  and  $\partial H_c/\partial T$ , as derived from the basic phenomenology of superconductivity [74]. The entropy per unit volume is given by

$$S = - (\partial G/\partial T)_H \quad , \quad (75)$$

---

<sup>28</sup> Note that the CET universal relations for  $H_c(t)/H_c(0)$  and  $[\lambda_L(0)/\lambda_L(t)]^2$  are identical according to Equation (71) but differ in their thermodynamic counterparts  $(1 - t^2)$  and  $(1 - t^4)$ , respectively.

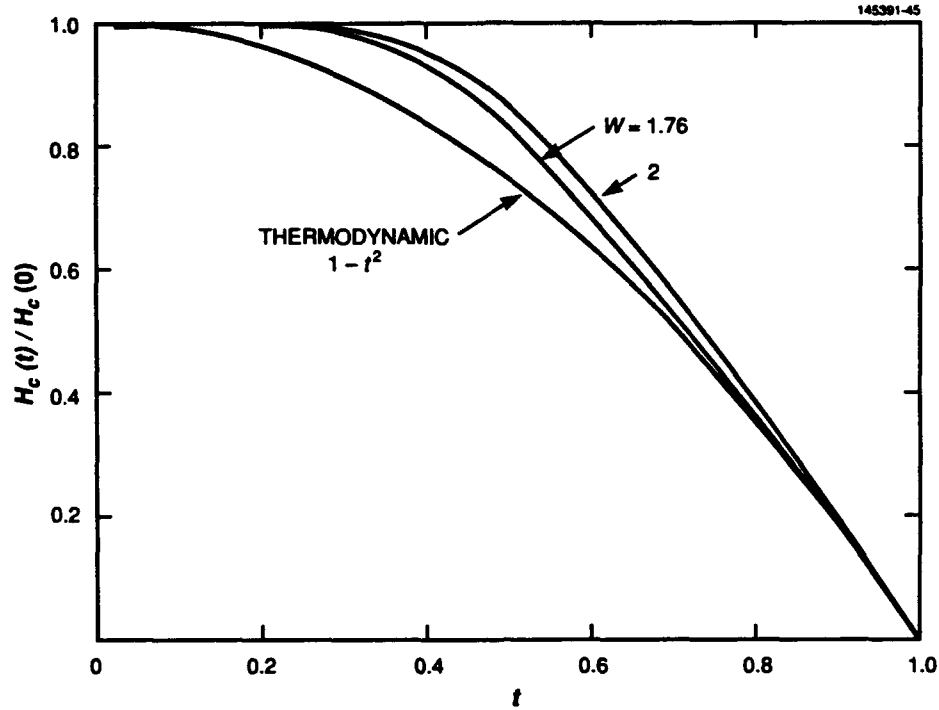


Figure 45. Comparison of  $H_c(t)/H_c(0)$  versus  $t$  for  $W = 1.76, 2$ , and the thermodynamic  $(1 - t^2)$  function.

where  $S$  is discontinuous at the critical point. The change in  $S$  then becomes

$$\Delta S = S_n - S_s = - (1/8\pi) (\partial H_c^2 / \partial T) \quad ,$$

or

$$= - (1/4\pi) H_c (\partial H_c / \partial T) \quad . \quad (76)$$

It may be shown that  $\partial H_c / \partial T = 0$  at  $T = 0$ , and that  $H_c = 0$  at  $T = T_c$ ; therefore,  $\Delta S$  must pass through a maximum somewhere between these two temperature limits. The latent heat per unit volume  $Q$  may, therefore, be related to the critical field by

$$Q = T \Delta S = - (1/8\pi) T (\partial H_c^2 / \partial T) \quad . \quad (77)$$

Because  $H_c = 0$  at  $T = T_c$ , both  $Q$  and  $\Delta S = 0$ , and the transition is adiabatic at the critical temperature. For  $T < T_c$ ,  $\partial H_c / \partial T$  is always negative,  $S_n > S_s$ , and this implies that superconduction is the more ordered state. There is also an anomalous decrease in specific heat  $C$  observed as  $T$  rises through  $T_c$ . Based on  $\Delta C = T \partial(\Delta S) / \partial T$ , differentiation of Equation (76) yields

$$\begin{aligned} \Delta C = C_n - C_s &= - (1/8\pi) T (\partial^2 H_c^2 / \partial T^2) \quad , \\ &= - (1/4\pi) T [H_c (\partial^2 H_c / \partial T^2) + (\partial H_c / \partial T)^2] \quad . \end{aligned} \quad (78)$$



Recalling that  $H_c(T_c) = 0$ , the absolute value of  $\Delta C(T_c)$  from Equation (78) may be determined by substituting the expressions for  $\partial H_c/\partial T$  at  $T = T_c$  from (74), and for  $H_c(0)$  from (70) with the result that

$$\begin{aligned}\Delta C(T_c) &= -(1/4\pi) T (\partial H_c/\partial T)^2, \\ &= -(1/4\pi) (H_c(0)^2/T_c) W^2, \\ &= -2 (\Delta G(0)/T_c) W^2, \\ &= -(1/2) (e^2 k V / a K E_{\text{hop}}) W^3 n_s^e(0)^2, \\ &= -(1/2) (e^2 k / V a K E_{\text{hop}}) W^3 x_s^e(0)^2.\end{aligned}\quad (79)$$

As a consequence,  $\Delta C$  should be smaller for oxides with small  $W$  and  $H_c(0)$  values, and large  $E_{\text{hop}}$ . For  $\text{La}_{1.8}\text{Sr}_{0.2}\text{CuO}_4$  with  $T_c \approx 40$  K and  $W \approx 0.75$ ,  $\Delta C \sim 1 \times 10^6$  ergs/cm<sup>3</sup>-K [see parameter values under Equation (61)]; for  $\text{YBa}_2\text{Cu}_3\text{O}_7$  with  $T_c \approx 95$  K and  $W \approx 0.5$ ,  $\Delta C \sim 4 \times 10^5$  ergs/cm<sup>3</sup>-K.

By substituting into Equation (78) the relations for  $\partial^2 H_c/\partial T^2$  derived from  $n_s^e(T)$  of (65),  $\Delta C$  relative to its discontinuity value at  $t = 1$  may be expressed as a function of reduced temperature by

$$\begin{aligned}\Delta C(t)/\Delta C(1) &= W^{-2} t \{ (2W/t^3 - W^2/t^4) \exp(W-W/t) \\ &\quad - (2W/t^3 - 2W^2/t^4) \exp[2(W-W/t)] \}.\end{aligned}\quad (80)$$

In Figure 46, generic curves of  $\Delta C(t)/\Delta C(1)$  are plotted for  $W = 1$  and 1.76 to illustrate the qualitative agreement with data of metals Sn [75] and Ga [76]. For the  $W = 1.76$  curve the sign reversal of  $\Delta C$  at  $t = 0.58$  matches exactly the London prediction that is based on reaching  $\Delta S$  maximum at  $T = T_c/\sqrt{3}$  [74]. It is also interesting that although the  $W = 1.76$  curve does not fit the Sn and Ga measured curves with high precision, this value of  $W$  also represents the best fit of the CET model over the full temperature range. For the high- $T_c$  Cu perovskites ( $W \leq 1$ ), the electronic contribution ( $\propto T$ ) to the specific heat may be masked by the lattice contribution ( $\propto T^3$ ) where  $T$  exceeds 30 K. Experimental results, therefore, may not bear a close resemblance to the calculated curve.

## 6.6 CRITICAL CURRENT DENSITY $i_c$

Pursuant to the hypothesis of dynamic ferroelectricity, critical current may be defined by equating carrier kinetic energy to condensation energy  $\Delta G$ . From Equations (68) and (69), one may assume [77]

$$\Delta G = (1/2) n_s^e m v_s^2 = H_c^2 / 8\pi = (1/4) (e^2 V / a K) (n_s^e)^2, \quad (81)$$

which leads to

$$v_s = [(1/2) e^2 V / m a K]^{1/2} (n_s^e)^{1/2},$$

or

$$= [(1/2) e^2 / m a K]^{1/2} (x_s^e)^{1/2}. \quad (82)$$

For  $\text{La}_{1.8}\text{Sr}_{0.2}\text{CuO}_4$  and  $\text{YBa}_2\text{Cu}_3\text{O}_7$ , with  $a = 4$  Å and  $K = 16$ ,  $v_s = 7.3 \times 10^6$  and  $8.4 \times 10^6$  cm/s, respectively. It should also be pointed out that the relation  $v_s \sim K^{-1/2}$  is consistent with the expected trends in local accelerating fields within materials of high or low dielectric constant, i.e., metals or insulators.

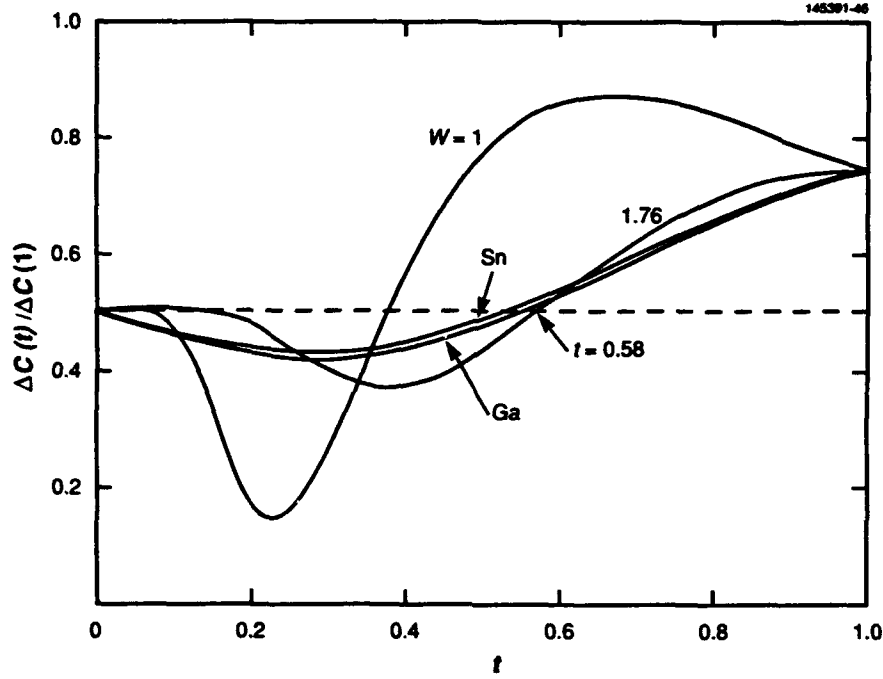


Figure 46. Generic curves of  $\Delta C(t)/\Delta C(1)$  versus  $t$  for  $W = 1$  and  $1.76$ , compared with data of Phillips from Sn [75] and Ga [76]. The  $W = 1.76$  curve provides the best fit to the Sn and Ga data over the complete  $t$  range and its sign reversal at  $t = 0.58$  matches the London theory [74].

Because the relation  $i_s = n_s e v_s$  represents the maximum possible supercurrent density for a given temperature and magnetic field, it may be described as the critical current density defined from Equation (82) as<sup>29</sup>

$$\begin{aligned}
 i_c &= [(1/2) e^4 V / m a K]^{1/2} (n_s e)^{3/2} , \\
 \text{or} \quad &= [(1/2) e^4 / m V^2 a K]^{1/2} (x_s e)^{3/2} , \\
 &= (5.4 \times 10^{-6}) V^{-1} (aK)^{-1/2} (x_s e)^{3/2} \text{ esu/s-cm}^2 , \\
 &= (1.80 \times 10^{-15}) V^{-1} (aK)^{-1/2} (x_s e)^{3/2} \text{ amp/cm}^2 .
 \end{aligned} \tag{83}$$

For the  $\text{La}_{1.8}\text{Sr}_{0.2}\text{CuO}_4$  and  $\text{YBa}_2\text{Cu}_3\text{O}_7$  superconductors of Figure 22 with  $K = 16$ ,  $a = 4 \text{ \AA}$ , and  $V = 1.7a^3$  and  $1.5a^3$ ,  $i_c(0) = 3.67 \times 10^8 \text{ amp/cm}^2$  and  $6.33 \times 10^8 \text{ amp/cm}^2$  are the upper theoretical current density limits, corresponding to  $x_s(0) = 0.068$  and  $0.09$ , respectively.

<sup>29</sup>From Equation (3) it will be recalled that  $i_s = (c/4\pi\lambda_L^2)A$ . If  $A_c = H_c\lambda_L$  (for specimens of dimensions greater than  $\lambda_L$ ), then Equation (83) may be derived directly from the London theory, with

$$i_c = (c/4\pi)(H_c/\lambda_L) = [(1/2) e^4 / m V^2 a K]^{1/2} (x_s e)^{3/2} ,$$

after  $\lambda_L = (mc^2/4\pi e^2 n_s e)^{1/2}$  from Equation (1) and  $H_c = (2\pi e^2 V / a K)^{1/2} n_s e$  from (70) are substituted.

From Equation (65), (83) may be converted to a universal curve,

$$i_c(t)/i_c(0) = [1 - \exp(W - W/t)]^{3/2} \quad (84)$$

In Figure 47, universal curves for  $i_c(t)/i_c(0)$  from Equation (84) are plotted for  $W = 0.5, 1$ , and  $2$ , once again displaying an increasing concave shape above  $t = 0.5$ , as  $W$  becomes smaller. (The traditional counterpart to Equation (84) is the Ginsburg-Landau function  $(1 - t)^{3/2}$ , considered to be valid near  $T_c$  [77].) Comparison with experiment (Figure 47) is first provided by the data of Hunt [79] for Sn and Clem et al. [80] for NbN (unoriented thin films), both BCS-type superconductors for which a good fit to theory is found with  $W \approx 2$ . Further indication of the applicability of the CET model is seen in the comparison with the data of Westerheim et al. [61] and Inam et al. [81] for highly  $c$ -axis oriented  $\text{YBa}_2\text{Cu}_3\text{O}_7$  (YBCO) thin films, where the points fall between the  $W = 0.5$  and  $1$  curves, the range established earlier in analyzing the electrical and microwave properties. In these latter cases, the intergranular current density  $i_c^{\text{exp}}(0) \approx 4 \times 10^7 \text{ amp/cm}^2$ , which is about a factor of 15 below the value suggested under Equation (83) as the theoretical limit for intragranular currents.<sup>30</sup>

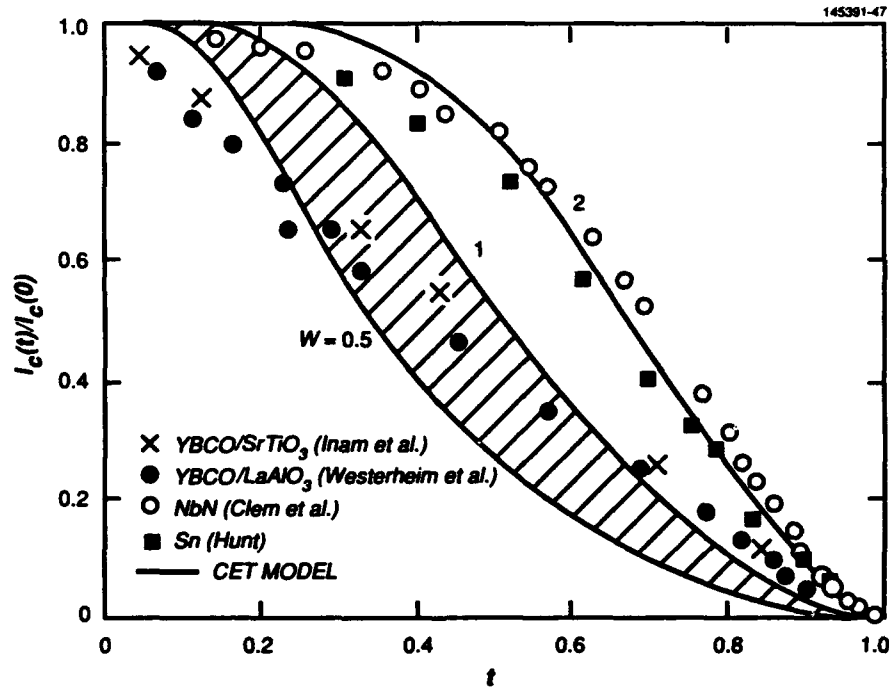


Figure 47. Normalized critical current density  $i_c(t)/i_c(0)$  versus  $t$  for  $W = 0.5, 1$ , and  $2$  plotted from Equation (84). Data for Sn are from Hunt [79], for NbN from Clem et al. [80], and for  $\text{YBa}_2\text{Cu}_3\text{O}_7$  from Westerheim et al. [61] and Inam et al. [81].

<sup>30</sup>Critical current measurements with polycrystalline (granular) specimens are hampered by the transport of current across grain boundaries. The density of condensed supercarriers is solely a function of temperature, therefore,  $i_c^{\text{exp}}(t)$  should scale in proportion to the true (intragranular) current, and the universal  $i_c^{\text{exp}}(t)/i_c^{\text{exp}}(0)$  versus  $t$  function for intergranular currents should not be affected by the impedance of the grain boundaries. Based on the discrepancy between theory and experiment, one might conclude that the grain boundaries even in highly oriented films could reduce the intergranular current density by an order of magnitude.

Because  $i_c$  is defined by Equation (2) as the density of supercurrent at the specimen surface, measurements must be corrected for the effects of small penetration depths as analyzed in Appendix E. Where the specimen cross-sectional area is not very much smaller than  $\lambda_L^2$ , the effective current density is reduced because the current is confined to layers within  $\lambda_L$  of the surface [78], and Equation (84) must be modified to fit experiment by

$$i_c^{\text{exp}}(t)/i_c^{\text{exp}}(0) = [1 - \exp(W-W/t)]^{3/2} A_{\text{eff}}(t)/A_{\text{eff}}(0) \quad , \quad (85)$$

with  $A_{\text{eff}} = 2\lambda_L[d_1(1-\exp(-d_2/2\lambda_L)) + d_2(1-\exp(-d_1/2\lambda_L)) - 2\lambda_L(1-\exp(-d_1/2\lambda_L))(1-\exp(-d_2/2\lambda_L))]$ , and  $d_1, d_2$  are the dimensions of a rectangular cross section (see Appendix E). In the opposite limit of  $d_1, d_2 \gg \lambda_L(0)$ , Equation (85) simplifies to

$$i_c^{\text{exp}}(t)/i_c^{\text{exp}}(0) = [1 - \exp(W-W/t)]^{3/2} \lambda_L(t)/\lambda_L(0) \quad ,$$

or from Equation (65),

$$i_c^{\text{exp}}(t)/i_c^{\text{exp}}(0) = [1 - \exp(W-W/t)] \quad , \quad (86)$$

the same as the relation for  $n_s^c(t)/n_s^c(0)$  from Equations (71) and (72).

In Figure 48, the data of Lessure et al. [82] for a bulk  $\text{YBa}_2\text{Cu}_3\text{O}_7$  specimen is plotted and compared favorably with Equation (86) for  $W = 1$ .

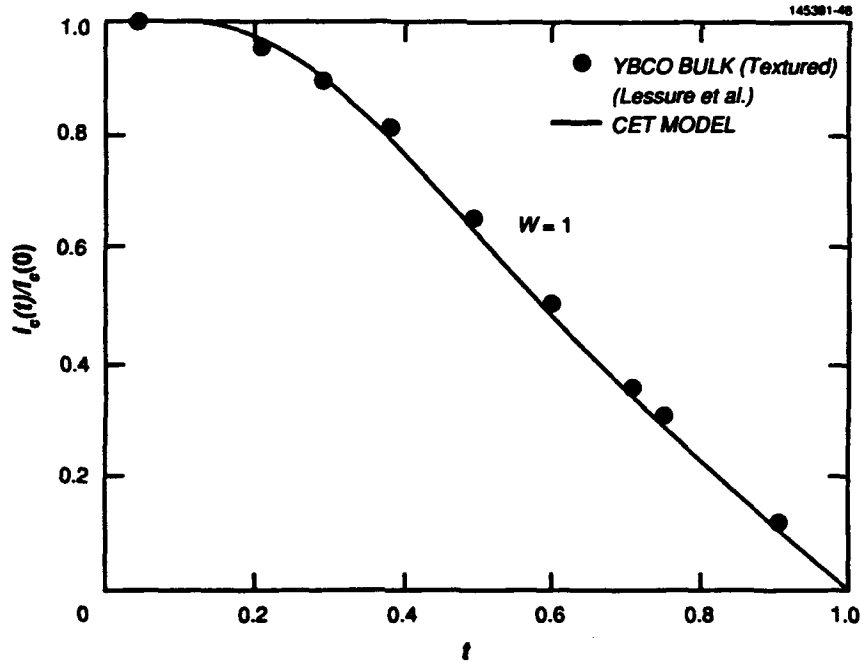


Figure 48. CET universal plot of  $i_c(t)/i_c(0)$  from Equation (86) for the bulk case with  $W = 1$ , compared with data of Lessure et al. [82].

In the presence of an external magnetic field  $H$ , part of the condensation energy density  $H^2/8\pi$  is required to expel  $H$  from the interior of the material as shown in Figure 44, and a more general expression for  $\Delta G(H)$  may be constructed from Equations (67) and (68):

$$\Delta G(H) = G_n(H) - G_s(H) = (H_c^2 - H^2)/8\pi \quad (87)$$

From Equations (82) and (87), Equation (81) for the kinetic energy density may be generalized to

$$\Delta G(H) = (1/2)n_s e m v_s^2 = (H_c^2 - H^2)/8\pi \quad (88)$$

If it is assumed that  $n_s e$  is unaffected by  $H$ ,<sup>31</sup> the reduction in  $\Delta G$  occurs as a decrease in carrier velocity and

$$v_s = [(H_c^2 - H^2)/4\pi m n_s e]^{1/2} \quad (89)$$

from which a universal relation for critical current density as a function of magnetic field may be deduced as

$$i_c(H)/i_c(0) \approx [1 - (H/H_c)^2]^{1/2} \quad (90)$$

Thus, it is seen that the supercurrent is limited by magnetic field which offsets the condensation energy, and by temperature, which controls the density of available carriers. It should be pointed out that Equation (90) describes the situation in the absence of a fluxoid lattice, i.e., type-I superconductors, where  $H_c$  is the thermodynamic critical field, and should not be expected to predict accurately the behavior of type-II superconductors, in which a variety of magnetic field-related effects may influence  $i_c(t, H)$  [84].

Because  $T_c = E_{\text{hop}}/kW$ , the superconduction critical temperature may be raised in two ways, by increasing  $E_{\text{hop}}$ , at the risk of introducing a magnetic exchange energy barrier that could upset the  $\hbar \geq E_{\text{hop}}$  requirement, or by reducing  $W$ , either through improved polaron dispersal ( $P \rightarrow 1$ ) or smaller polaron radii ( $n_t \rightarrow 0$ ) but at the expense of lowering the reduced values of  $H_c$  and  $i_c$  as  $T \rightarrow T_c$ .

## 6.7 INTRINSIC COHERENCE LENGTH $\xi_0$

A natural continuation from the above discussion of critical magnetic fields is the subject of coherence and its role in type-II superconductors. As discussed in Section 2.3, the notion of coherence was introduced by Pippard [11], who proposed that the nonlocal nature of the superelectron may be characterized in terms of the uncertainty principle. In this approach as applied to free-electron systems, the superconducting electrons are drawn from the population with energies within  $kT_c$  of the Fermi level. In order to obtain a relation for the individual carrier momentum  $p_s$  in the superconducting state, Pippard reasoned that their momentum range could be estimated by dividing the condensation energy, assumed to be equivalent to  $kT_c$ , by the Fermi velocity  $v_F$ , i.e.,  $\Delta p_s \sim kT_c/v_F$  [85]. As a consequence, the position uncertainty (coherence length) becomes  $\Delta x (= \xi_0) \geq (\hbar/2\pi)(v_F/kT_c)$ .

<sup>31</sup> In type-II superconductors there are situations where  $n_s e$  may be considered a function of  $H$  [83], such that  $\lambda_L(H) \rightarrow \infty$  as  $n_s e(H) = |\psi(H)|^2 \rightarrow 0$ .

Another definition of coherence length was provided by Ginsburg and Landau [12] from the solution of a Schrodinger-type equation with a nonlinear term. The resulting aggregate eigenfunction for this differential equation contained an exponential decay [see Equation (6)],  $\psi_s(x) \sim \psi_s(0)\exp(-x/\xi)$ , where  $|\psi_s|^2 = n_s^e$  is the expectation value of a spatially varying superconduction ensemble wavefunction of coherence length  $\xi$  that reduces to the Pippard result for  $T \ll T_c$ . Thus, the conceptual compatibility between Pippard and Ginsburg and Landau may be seen if it is simply viewed as the average distance a carrier travels before losing coherence with the ordered state. In reality, the carrier rarely reaches this limit, but the attendant velocity range may be used to define the degree of spatial order.

In its essentials the Pippard definition describes the coherence of a carrier chain composed of wavepackets with a spatial profile that may be assigned a de Broglie wavelength defined by

$$\lambda_{dB} = h/p_s \quad (91)$$

This concept is compatible with the basic CET model of a chain of localized wavefunctions that link to form a single MO function. Applying, therefore, the generalized form of the uncertainty relation for space packets, we obtain

$$\Delta p_s \cdot \Delta x \geq h/2\pi \quad (92)$$

or in this present context,

$$p_s \cdot \xi_0 \approx h/2\pi \quad (93)$$

where  $\Delta p_s$  is replaced by  $p_s$ <sup>32</sup>

In the CET model the condensation energy is not immediately determined by  $kT_c$ , so the use of the Pippard relation for  $\Delta p_s$  must be modified. The role of the energy trap is different from the conventional band theory approach in that it determines directly the population of available supercarriers but only indirectly their energy. As discussed in Section 6.2,  $\Delta G$  is determined by  $n_s^e(T)$  and is more closely associated with  $H_c$  than  $T_c$ . Because the CET model has conveniently produced a distinct relation for the carrier velocity, however, the question of estimating  $\Delta p_s$  by indirect means is unnecessary, and therefore, a coherence length similar to that of Pippard can be defined directly from the relation for superconductor carrier velocity of Equation (82),

$$\xi_0 = (h/2\pi)/p_s = (h/2\pi)/mv_s \quad ,$$

or

$$\begin{aligned} & \approx [(h^2/2\pi^2me^2)(aK/V)]^{1/2} (n_s^e)^{-1/2} \quad , \\ & \approx [(h^2/2\pi^2me^2)(aK)]^{1/2} (x_s^e)^{-1/2} \quad (94) \end{aligned}$$

<sup>32</sup>An alternative derivation of Equation (93) may be obtained from the standard quantum mechanics operator through the relation  $-j(h/2\pi)\nabla\psi_s$ , where  $p_s$  is a good quantum number for a stationary state. The ensemble wavefunction  $\psi_s(x) \sim \psi_s(0)\exp(-x/\xi_0)$  from Equation (6), therefore  $\nabla\psi_s = -(1/\xi_0)\psi_s$ , again arriving at  $p_s \cdot \xi_0 \sim h/2\pi$ . This result suggests that the ensemble concept of Ginsburg and Landau and the individual wavepacket idea of Pippard are equivalent as far as the notion of coherence is concerned.

If the parameter values used in the earlier discussion of critical phenomena in perovskites are also employed here, an intrinsic coherence length may be approximated by the following:

$$\begin{aligned}\xi_0 &\approx [(h^2/2\pi^2me^2) (aK)]^{1/2} (x_s^e)^{-1/2} , \\ &\approx 1.03 \times 10^{-4} (aK)^{1/2} (x_s^e)^{-1/2} .\end{aligned}\quad (95)$$

If Equation (95) is applied to the perovskites with  $K = 16$  and  $a = 4$  Å,

$$\xi_0(0) \approx 8.23 \times 10^{-8} x_s^e(0)^{-1/2} \text{ cm} . \quad (96)$$

For  $x_s^e(0) = 0.068$  ( $\text{La}_{1.8}\text{Sr}_{0.2}\text{CuO}_4$ ) and  $0.09$  ( $\text{YBa}_2\text{Cu}_3\text{O}_7$ ),  $\xi_0(0) \approx 32$  Å and  $27$  Å, respectively, in general agreement with experiment [53]. For type-I metal superconductors,  $\xi_0(0) \sim 10^4$  Å, which is also consistent with Equation (95) through the direct dependence of  $\xi_0$  on the dielectric constant ( $K^{1/2}$ ) that becomes very large in highly polarizable materials with loosely bound electrons.<sup>33</sup>

A discussion of the type-II superconductors follows, and it is appropriate to establish the analytical relationship between  $\xi_0$  and  $\lambda_L$  from Equations (94) and (62):

$$\begin{aligned}\xi_0 &= [(2h^2/\pi m^2 c^2) (aK/V)]^{1/2} \lambda_L , \\ &= 1.93 \times 10^{-10} (aK/V)^{1/2} \lambda_L \text{ cm} ,\end{aligned}\quad (97)$$

where  $\lambda_L$  is in centimeters. For the two perovskite systems,

$$\begin{aligned}\kappa &= \lambda_L/\xi_0 \approx 5.18 \times 10^9 (aK/V)^{-1/2} , \\ &\approx 67 \quad \text{for } \text{La}_{1.8}\text{Sr}_{0.2}\text{CuO}_4 , \\ &\approx 63 \quad \text{for } \text{YBa}_2\text{Cu}_3\text{O}_7 ,\end{aligned}\quad (98)$$

with the latter result closely agreeing with the value of 62 derived from experiment [5]. These results serve to confirm the expectation mentioned in Section 2.3 that the high- $T_c$  perovskites behave as natural type-II superconductors, with  $\lambda_L/\xi_0 \gg 1$ . (Metals with the large  $K$  values are Pippard superconductors, with  $\lambda_L/\xi_0 \ll 1$ .) Although  $\kappa$  is temperature independent, in accord with traditional theory [86], it must be recognized that both  $\lambda_L$  and  $\xi_0$  derive individual temperature dependencies through the supercarrier density; as  $T \rightarrow T_c$ ,  $\lambda_L$  and  $\xi_0 \rightarrow \infty$  through their mutual dependence on  $(n_s^e)^{-1/2}$  from Equation (30). Although Pippard's uncertainty principle arguments were used in these derivations of coherence length, the CET formalism yields the above temperature dependence of  $\xi_0$  that is more characteristic of the Ginsburg and Landau definition, which also produces a temperature-insensitive  $\kappa = \lambda(T)/\xi(T)$  [87].

<sup>33</sup> The dielectric constant in the context of conducting materials is viewed here as a parameter that represents the polarizability in a quasi-insulating state with at least some of the free electrons condensed back on their parent ions for covalent transfer. In the metallic state of course, macroscopic polarization effects can only be inferred, because any measurements are precluded by the presence of free electrons. This topic is examined further in Section 8 and Appendix G, where the  $K$  for Sn is discussed in terms of  $\kappa$ ,  $H_c(0)$  and the electron velocity through the relation  $v_s \sim K^{-1/2}$  of Equation (82).

If Pippard's use of the carrier mean-free-path  $d$  (here replacing  $\ell$  from Section 2.3 with  $d$ , which could be the thickness of a film or the diameter of a fine wire) is adopted to define a reduced effective coherence length  $\xi$ , we obtain

$$1/\xi = 1/\xi_0 + 1/d \quad , \quad (99)$$

for which  $\xi \rightarrow d$  where  $\xi_0 \gg d$ . If  $d$  represents the radius of a fluxoid domain in this model, i.e.,  $2d$  is the spacing between nonsuperconducting regions, a decline in superconduction efficiency can set in as  $d$  becomes increasingly smaller. Microscopic-scale  $d$  values can lower  $n_s$  by raising the polaron dispersal parameter  $\beta$ , thereby increasing  $W$  to cause a lower  $T_c$ . Another effect of short mean-free-paths would occur in the size of the large-polaron radius  $\gamma_p$  described by Equation (40). Because  $\gamma_p$  determines  $n_0$  (and hence  $n_s$ ), the nominal threshold density for superconduction, any decrease in its value would also increase  $W$ .

At this point the physical meanings and relationships of the large-polaron radius and the coherence length may be compared. The cell radius of an isolated polaron  $\gamma_p$  is a normal-state parameter that determines the minimum density for which a polaron chain may condense to the superconduction state and is directly dependent on the transfer integral  $b$ . The coherence length  $\xi_0$  on the other hand, emerges from the uncertainty principle as applied to the wave mechanical nature of the superconducting state, i.e.,  $\xi_0$  is larger for smaller momentum values, and because it varies as  $(n_s \epsilon)^{-1/2}$  according to Equation (94), it is dependent on the  $\beta$  dispersal parameter and is generally smaller for oxides, where  $x_s < 0.1$ .

## 6.8 TYPE-II SUPERCONDUCTORS

As introduced in Section 2.3, the three general categories of superconductors are distinguished by the relations between  $\xi_0$  and  $\lambda_L$ . In reality, only type-I materials (pure superconductors with  $\xi_0 \gg \lambda_L$ ) feature a single critical magnetic field in which the flux expulsion takes place completely once the thermodynamic  $H_c$  threshold is reached (in a bulk specimen). In materials of practical importance, however, flux expulsion occurs over a range of fields, with the limits defined by  $H_{c1} \leq H_c \leq H_{c2}$ . The spatial variation in  $H_c$  and  $\psi_s$  at a normal/superconductor interface, shown in Figure 49, indicates that type-II superconductors with  $\kappa \gg 1$  have interface regions set by  $\xi$  that is small enough and  $\lambda_L$  large enough to permit the bulk volume of the material to divide into islands of fluxoid domains that harbor magnetic flux in their normal cores at a field less than  $H_c$ . With the presence of fluxoid domains, the thermodynamic critical field  $H_c$  can no longer be measured directly. A larger field  $H_{c2}$  is required to offset the condensation energy defined in Equation (68) because the invasion of flux reduces the volume of material from which flux is expelled. As analyzed in detail by Abrikosov [88] and discussed by Kittel [89] and Tinkham [90], the critical magnetic fields for clean high- $T_c$  perovskite superconductors with  $\xi = \xi_0$  and  $\lambda = \lambda_L$  may be approximated by

$$H_{c1}/H_c \approx [(\sqrt{2})\kappa]^{-1} \ln \kappa \quad , \quad (100)$$

and

$$H_{c2}/H_c \approx (\sqrt{2})\kappa \quad . \quad (101)$$

With  $\kappa$  independent of temperature,  $H_{c1}$  and  $H_{c2}$  should track with  $H_c$  as functions of temperature. As shown in Figure 50, a universal curve with  $W = 0.8$  is fitted to the  $H_{c2}(\perp)$  data [91] from bulk polycrystalline  $(\text{Dy,Eu})\text{Ba}_2\text{Cu}_3\text{O}_y$ .



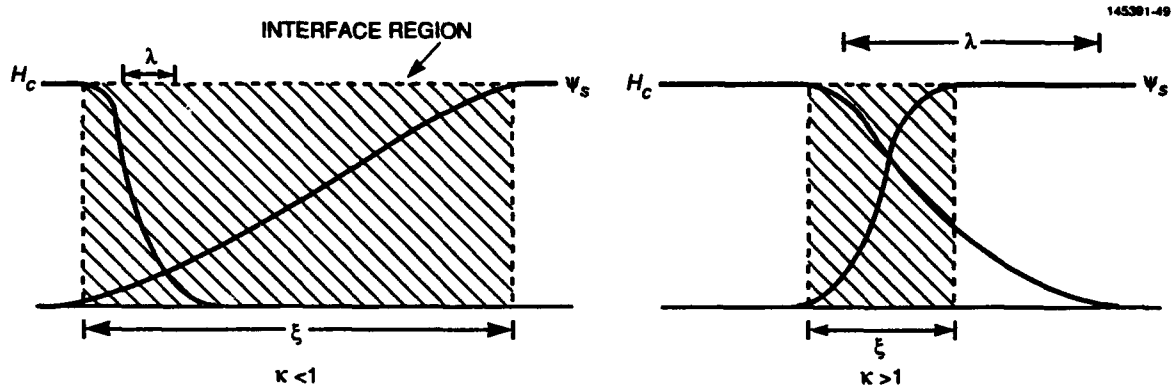


Figure 49. Variation of  $H$  and  $\psi_s$  at the fluxoid/superconductor interface for  $\kappa \ll 1$  (type I) and  $\kappa \gg 1$  (type II).

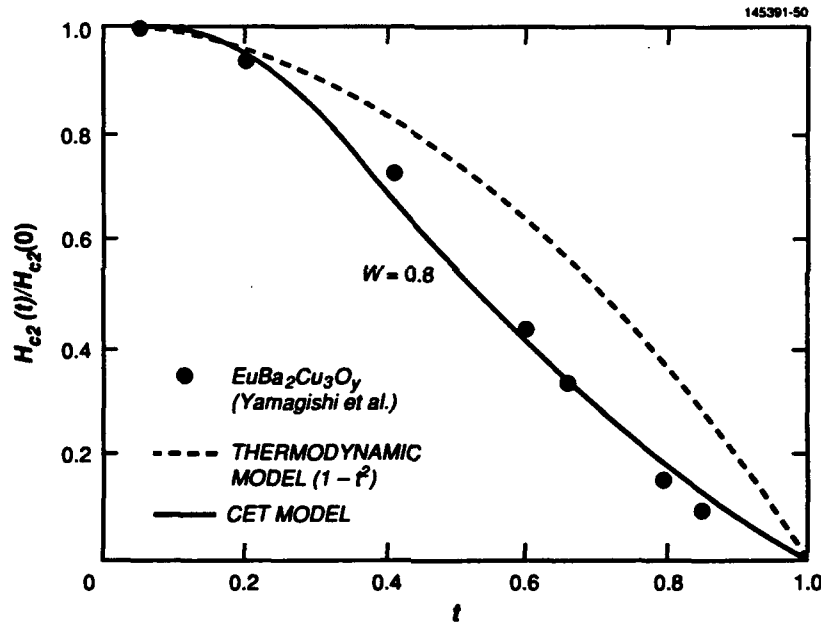


Figure 50. CET calculated curve of  $H_{c2}(t)/H_{c2}(0)$  versus  $t$  compared with data of Yamagishi et al. [91] for  $W = 0.8$ .

Another comparison with experiment may be carried out with the values of critical fields estimated from measurements of  $\partial H_c(T)/\partial T$  at  $T = T_c$ . For  $W = 1$ , the slope from Equation (74) is simply  $-H_c(0)/T_c$ , and the results of Finnemore et al. [92],  $\partial H_c(T)/\partial T = -165$  Oe/K for  $\text{YBa}_2\text{Cu}_3\text{O}_7$  conforms closely to the calculated estimate of  $-155$  Oe/K, with  $H_c(0) = 14$  kOe [computed beneath Equation (70)] and  $T_c = 91$  K. If Equations (100) and (101) are used with the above approximations and with  $\kappa = 63$  from Equation (98), the ratio  $\partial H_{c2}(T)/\partial T + \partial H_{c1}(T)/\partial T \approx 2\kappa^2/\ln\kappa = 1920$ , which closely matches the result of Cava et al. [5]:  $13$  kOe/K +  $7$  Oe/K =  $1860$ . It also follows from Equations (100) and (101) that for  $H_c = 14$  kOe,  $H_{c1} \approx 660$  Oe and  $H_{c2} \approx 1250$  kOe.

The question of the dirty superconductor may now be examined in the above context. Traditionally, a type-II superconductor is a metal with a  $\xi$  reduced to values below  $\lambda_L$  by the presence of inhomogeneities — “normal” regions that act as nucleation centers for the fluxoid lattice, in a manner similar to the formation of reverse magnetic domains about pores and grain boundaries in a ferromagnet. As pointed out in Equation (99), the situation for which  $\lambda_L/\xi \approx \lambda_L/d \gg 1$  occurs in metals where  $d \ll \xi_0$ , thus limiting the coherence length to a mean-free path. With the discovery of the high-temperature oxide superconductors with typical  $\xi_0 \sim 30$  Å, the  $\lambda_L/\xi \gg 1$  condition appears to exist naturally even in macroscopically homogeneous specimens.

The effect of local or dispersed inhomogeneities in the form of impurities or lattice defects has somewhat different implications for a metal and for an insulator. In metals, with the greatest charge screening effects,  $\xi_0 \gg \lambda_L$ , and the effect of inhomogeneities is significant in reducing  $\xi$  to set up the condition for establishing the fluxoid lattice, which can occur where  $d \ll \lambda_L$ . In effect, the impurities in a metal are required for the creation of a type-II superconductor through the nucleation and pinning of fluxoid regions at the impurity centers. In superconducting oxides with finite (measurable) dielectric constants, however,  $\xi_0 \ll \lambda_L$ , and the fluxoid lattice forms in the absence of impurities. Without pinning centers, they may be described as natural type-II superconductors.

Because the fluxoids are mobile, the inhomogeneities affect the fluxoid lattice only if  $d \leq \xi_0$ , at which point these impurities serve as pinning centers for the fluxoids. The use of induced inhomogeneities as a practical design strategy for increased magnetic field and supercurrent capabilities of high- $T_c$  materials may, therefore, be viewed as a method for stabilizing the fluxoid lattice by the pinning of domains about the inhomogeneities. Without these centers the fluxoid structure is likely to be fluid with the merging and collapsing of domains increasing as  $T \rightarrow T_c$ . The fluxoid lattice may “melt” well below the critical temperature even in materials with  $d > \lambda_L(0)$  because  $\lambda_L(T)$  increases more rapidly with  $T$  for small values of  $W$ .

To summarize the results of the above analyses, it has been shown that the magnitudes of  $\lambda_L$ ,  $H_c$ ,  $i_c$  and  $\xi_0$  are all determined by the effective density of supercarriers  $n_s^e(T)$ . The various relationships are organized in Table 6, where the parameter values determined in the foregoing analyses are listed with their corresponding measured values, where applicable.

## 6.9 MAGNETIC LEVITATION

Magnetic levitation is the most visually dramatic manifestation of superconductivity, occurring when the inducement of a diamagnetic supercurrent in a magnetic field attends the expulsion of flux from the interior of the specimen. An important distinction should now be recalled: A material qualifies as a superconductor where  $n_s \geq n_i$  (requiring that  $T \leq T_c$ ); however, it does not become superconducting until the carrier chain condenses to form a Meissner supercurrent for  $H \leq H_c$ . Thus, the supercarrier density is controlled by temperature, but the supercurrent by magnetic field.

Analogous to the concept of an image charge representing the effects of a metal plane beneath a real electric charge of opposite sign, the induced supercurrent in a specimen may be represented by a magnetic dipole, as shown in Figure 51. Because the current produces a diamagnetic moment, however, the dipole moment would be a mirror image of the external magnet, and the force between them is, therefore, repulsive.

TABLE 6

Superconductor Parameter Values and Dependence on Carrier Density

Parameter	$n_s^0$ Dependence	Theory	Experiment
$\Delta G(0)$	$(n_s^0)^2$	$8 \times 10^6$	$10^6$ to $10^7$ erg/cm <sup>3</sup>
$v_s(0)$	$(n_s^0)^{1/2}$	$8.4 \times 10^6$	cm/s
$i_c(0)$ (Film)	$(n_s^0)^{3/2}$	$6 \times 10^8$	$4 \times 10^7$ amp/cm <sup>2</sup>
(Bulk)	$(n_s^0)$		
$\lambda_L(0)$	$(n_s^0)^{-1/2}$	1740	1500 to 2000 Å
$\xi_0(0)$	$(n_s^0)^{-1/2}$	27	20 to 35 Å
$\kappa (= \lambda_L/\xi_0)$		63	62
$H_c(0)$	$n_s^0$	14	10 to 20 kOe
$T_c$	$n_s^0(0)$		
$\partial H_c/\partial T (T=T_c)$	$-H_c(0)/T_c (W=1)$	-155	-165 Oe/K
$(\partial H_{c2}/\partial T) + (\partial H_{c1}/\partial T)$	$2\kappa^2/\ln\kappa$	1920	1860
$R_s (T=77 \text{ K})$	$n_f/(n_s^0)^{3/2}$	$2 \times 10^{-5}$	$10^{-5} \Omega$

As pointed out earlier, the spatial ordering constraint of the covalent bond furnishes the eigenstate rigidity required for the  $\nabla\psi_s = 0$  condition. The celebrated levitation property of the Meissner effect can be appreciated, therefore, in the context of a magnetomotive force imparted to a current-carrying coil in an inhomogeneous magnetic field. In a superconductor, however, the current loop will be established on the specimen according to the disposition of the external field relative to the specimen. Similar to the coil, a superconducting object will assume an appropriate equilibrium position and attitude in an external field; unlike the coil, however, there are no restoring forces acting on the specimen when it is disturbed from its equilibrium position. Because the current path then adopts a different chain of covalent orbital lobes, a new equilibrium state may be established within the same specimen orientation by altering either the specimen position or magnetic field conditions.

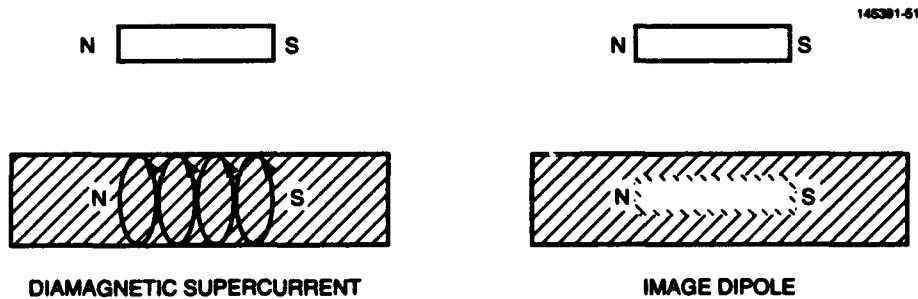


Figure 51. Diagrammatic representation of the Meissner flux expulsion/levitation effect from induced diamagnetism in a superconductor.

Without external mechanical assistance to alter the carrier condensation energy (or degree of polaron alignment)  $\Delta G (= H_c^2/8\pi)$ , the spatial relation between the specimen and magnet is fixed except for rotation about the magnetic field axis. Rotation about an axis perpendicular to the magnetic field or any translational adjustment requires an energy input to establish a new equilibrium current condition (thus precluding any restoring force effects).

The mechanical aspects of the Meissner effect, therefore, lend further credence to the conclusion that the supercarriers are part of the binding forces of the lattice and do not exist independently as unbound electrons.

## 7. LARGE-POLARON SUPERCONDUCTING SYSTEMS

A generic model of the MO energy levels for a metal cation ( $M$ ) in an octahedron of ligands ( $L$ ) is shown in Figure 52. For simple metal oxides, e.g., MgO, the lower energy bonding orbitals are principally oxygen states and are occupied by  $2p$  electrons of the stable  $O^{2-}$  ligands, while the higher energy antibonding orbitals represent  $3d$ ,  $4s$ , and  $4p$  states of the less stable metal ion (see Appendix A) and are occupied by the corresponding electrons of that particular cation.<sup>34</sup> The influence of the crystal field (important for ions of the transition elements) is indicated by the splitting of the five degenerate free ion  $3d$  states into  $e_g$  and  $t_{2g}$  terms. Where extended delocalization occurs from orbital overlaps that reach beyond nearest neighbors, multiplicities of these MO levels form the energy bands (see Figure 12) used for analyzing collective carrier systems (i.e., metals and band semiconductors) that involve unbound electrons and holes. For the collective carrier extreme, a partial band model version of Figure 52 that is adapted for  $Cu^{2+}$  is drawn in Figure 53. In the context of covalent electron transfer, the MO format will be used to survey specific ionic/covalent systems for which superconduction properties have been reported in mixed-valence (large-polaron) compositions.

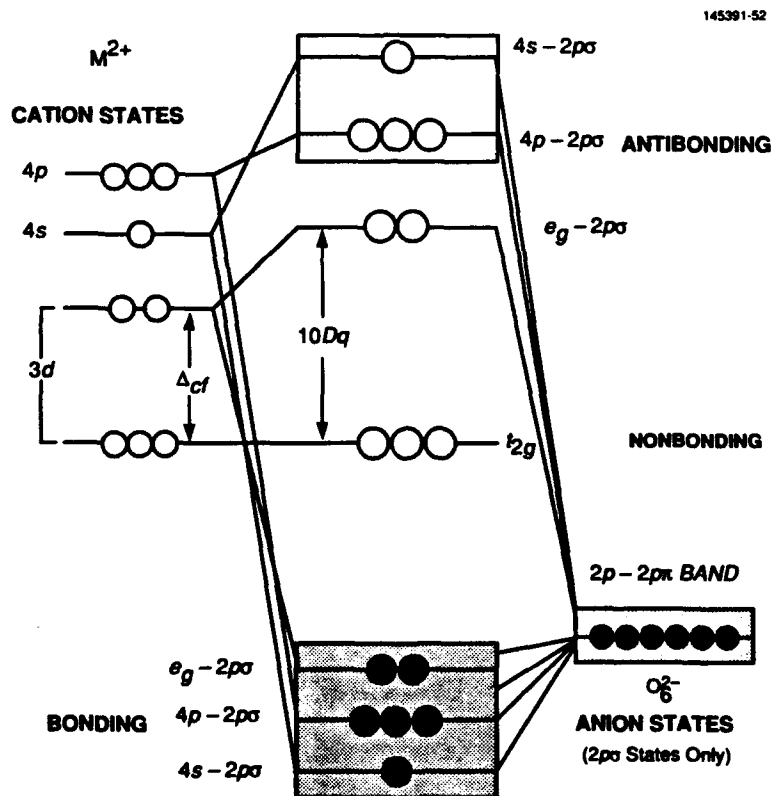


Figure 52. Generic MO energy level diagram for a  $d^0$  cation in an oxygen octahedral complex.

<sup>34</sup>In quantum mechanical terms, the lower energy of the free-ion ligand wave functions  $\chi_L$  provide the dominant contribution to the hybrid bonding state  $\phi_b = C_{11}\chi_M + C_{12}\chi_L$ , with  $C_{12} \gg C_{11}$ . For the higher energy antibonding state  $\phi_a = C_{12}\chi_M + C_{11}\chi_L$ , the reverse is true, with  $C_{11} \gg C_{12}$ . In more covalent combinations,  $\chi_M$  and  $\chi_L$  are closer in energy, and  $C_{11} \sim C_{12}$  in the resulting hybrid orbital.

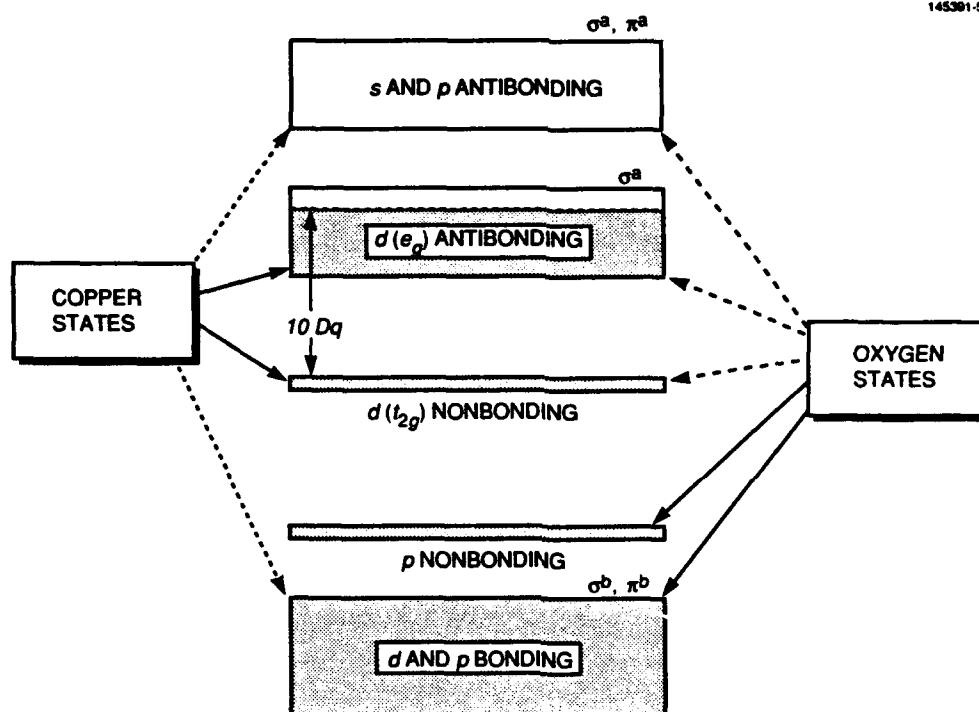


Figure 53. Band model approximation of the MO states of a Cu perovskite, indicating a partially filled antibonding band.

## 7.1 SYSTEMS WITH $3d-2p\sigma$ BONDS

### 7.1.1 $\text{Cu}^{2+}-\text{O}^{2-}-\text{Cu}^{3+}$ in $\text{A}_2\text{BO}_4$ and Layered Perovskites ( $p$ -Type)

Because the superconducting cuprates (Cu perovskites)<sup>35</sup> were the principal subject of the original work on this theory [1], it is appropriate to begin this discussion with a review of the orbital states and occupancies of the  $\text{Cu}^{2+}-\text{O}^{2-}-\text{Cu}^{3+}$  superexchange combination, which leads to superconduction that is confined to select  $\text{Cu}-\text{O}_4$  planes that occur as part of the  $B$ -lattice oxygen coordinations in perovskite-type lattices.

Although the large-polaron concept implies that the region of mixed-valence condition is local with carriers tethered to fixed polaron sources, it should be recognized that the valence state is not a fixed entity in cases where itinerant polarons exist through extended covalent delocalization. In accord with the  $(\text{CuO})^+$  molecular ion concept adopted in Appendix B, the transfer cations in these partially covalent compounds assume average (noninteger) valences lower than their nominal ionic assignments because the bonding

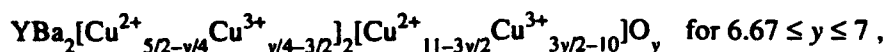
<sup>35</sup>In a generic sense, this means 180-deg cation-anion-cation bonds and would include a growing family of complex oxides with square planar  $(\text{Cu}-\text{O}_4)$  building blocks.

electrons become shared among the ions, both Cu and O, within the large-polaron cell.<sup>36</sup> Effects of covalent bonding have been estimated from the orbital reduction factors of transition-metal complexes as determined for paramagnetic resonance measurements of  $g$  factors and spin-orbit coupling constants. In the case of  $\text{Cu}^{2+}$  in Tutton salts, for example, the reduction is about 15% [94]; if applied to the oxide, the actual ionic charges would be  $\text{Cu}^{1.7+}\text{O}^{1.7-}$ . For want of a suitable systematic means to determine these effective valences, however, the integer valence values of the free ion oxidation states will be maintained in the discussions that follow.

To examine covalence involving the unfilled  $d$  shell of a transition series, it is first necessary to establish the crystal-field (point-charge model of ionic lattice) splittings for the particular system. In Figure 54, the order of energy levels for the five  $3d$  orbital states are displayed in the evolution from cubic ( $O_h$ ) through tetragonal/orthorhombic ( $D_{4h}/D_{2h}$ ) of the  $\text{La}_{2-x}\text{Sr}_x\text{CuO}_4$  system, to the extreme cases of pyramidal ( $C_{4v}$ ) and planar ( $C_{2h}$ , extreme  $D_{4h}$ ) coordinations of  $\text{YBa}_2\text{Cu}_3\text{O}_4$  and the more complex layered compounds. In the planar model, only the  $x$ - $y$  plane is involved, so the last remnant of the cubic crystal field is  $10 Dq$  between the  $d_{x^2-y^2}$  and  $d_{xy}$ . In the generic MO diagram (Figure 52), the  $10 Dq$  splitting is explained by the energy instability of the antibonding  $e_g$  relative to the nonbonding  $t_{2g}$  states [95]. Under the further influence of the orbital overlaps, the upper  $d_{x^2-y^2}$  (and to a lesser extent  $d_{z^2}$ ) then divides into bonding and antibonding states, while the remaining  $d$  states are presented as unchanged in energy and become nonbonding (actually  $\pi$  bonding to the ligand), as shown in Figures 55 and 56 for the tetragonal and square-planar cases, respectively.

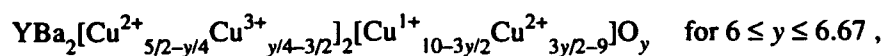
In the perovskites with anisotropic superconductivity, the Cu sites are either tetragonal (with an orthorhombic component under some conditions, possibly caused by a Jahn-Teller stabilization that occurs as part of the condensation process) or square planar, and the occupancies of the  $d$  states are shown in Figure 57. As previously reported [1], the  $d_{z^2}$  orbital state directed along the crystallographic  $c$ -axis is empty, thereby precluding the possibility of  $c$ -axis superconduction. The  $d_{x^2-y^2}$  antibonding orbital state is the transfer path both for superconduction in the  $a$ - $b$  plane with single occupancy in the  $\text{Cu}^{2+}$  ( $d^9$ ) member and empty for the  $\text{Cu}^{3+}$  ( $d^8$ ) member in a low-spin ( $S = 0$ ) state. It should also be pointed out that because the  $\text{Cu}^{3+}$  ( $d^8$ ) ion represents a positively charged mobile hole with  $S = 0$ , it satisfies the requirements of a boson and could be viewed as such in any interpretation involving conventional superconduction theory.

The source of polarons differs among these compounds. In the simplest case [2] of the  $\text{La}^{3+}_{2-x}\text{Sr}^{2+}_x[\text{Cu}^{2+}_{1-x}\text{Cu}^{3+}_x]\text{O}_4$  system with maximum  $T_c \approx 40$  K,  $\text{Sr}^{2+}$  ions are fixed negative charges in the  $A$  sublattice, and the mixed valence occurs as tetragonally coordinated  $\text{Cu}^{3+}$  holes that are electrostatically tethered to the nearest  $\text{Sr}^{2+}$  ions, thus making the conductivity  $p$ -type. A modification of this system that introduces the pyramidal coordinations [49] is  $\text{La}^{3+}_{2-x}\text{Sr}^{2+}_x\text{Ca}[\text{Cu}^{2+}_{1-x}\text{Cu}^{3+}_x]_2\text{O}_4$  with maximum  $T_c = 60$  K. As discussed in Appendix D, this modification to the crystal field may explain the increase in  $T_c$ . For the  $\text{YBa}_2\text{Cu}_3\text{O}_y$  system with  $T_c \approx 95$  K [3], the situation is more complex. The mixed valence occurs here as a result of oxygen vacancies that establish polarons in both the planes of  $\text{Cu}(2)\text{-O}_5$  pyramids and  $\text{Cu}(1)\text{-O}_2$  linear chains; chemical formulas highlighting proposed Cu valence distributions that vary linearly with polaron concentration (see Appendix D of Dionne [1]) may be written:



<sup>36</sup>This traditional view has also been expressed by A.W. Sleight in a review of superconducting oxide chemistry [93].

and



with Cu(1) and Cu(2) site valences  $v(1) = 1.5y - 8$  and  $v(2) = 0.25y + 0.5$ , respectively.

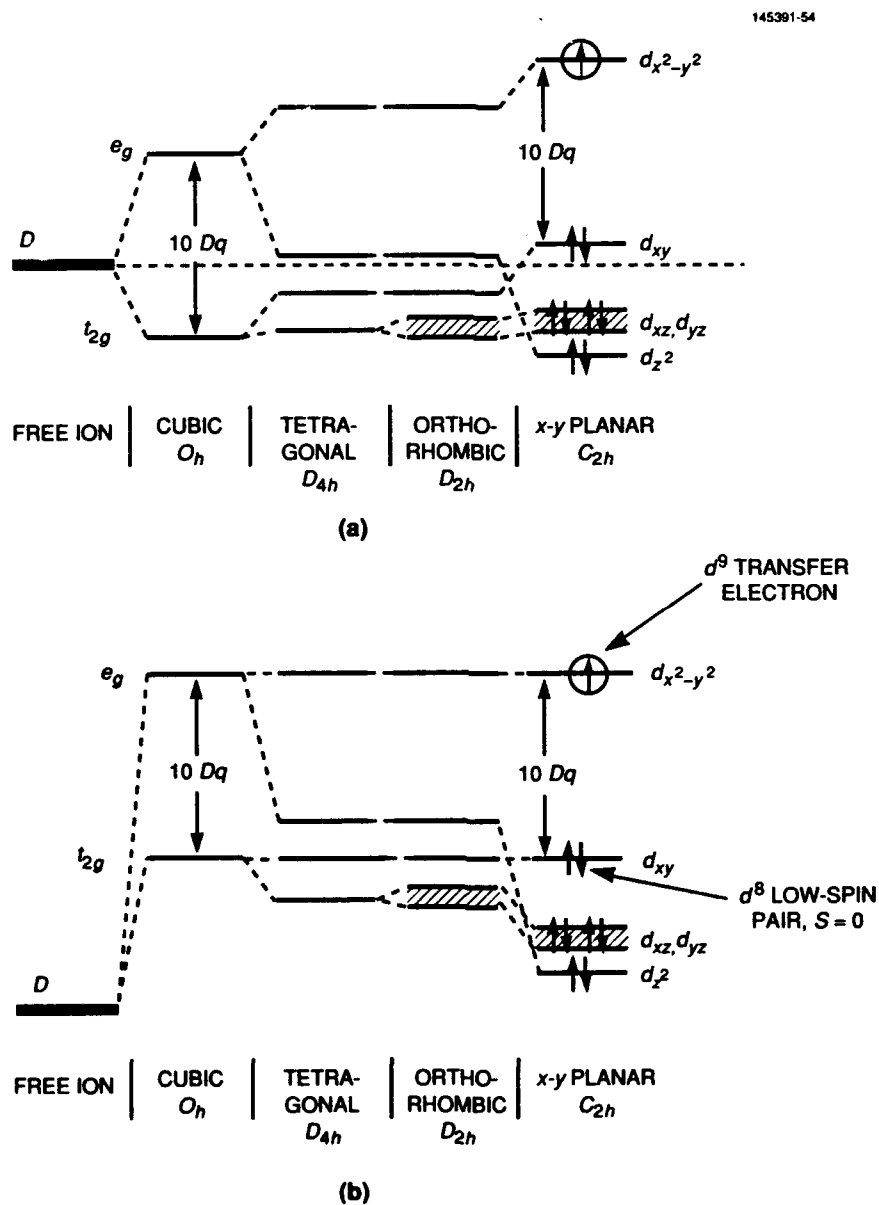


Figure 54. Crystal-field diagrams for the  $d^8$  low-spin ( $S = 0$ ) state: (a) free ion level as zero-energy reference and (b) least stable  $d_{x^2-y^2}$  level as reference.



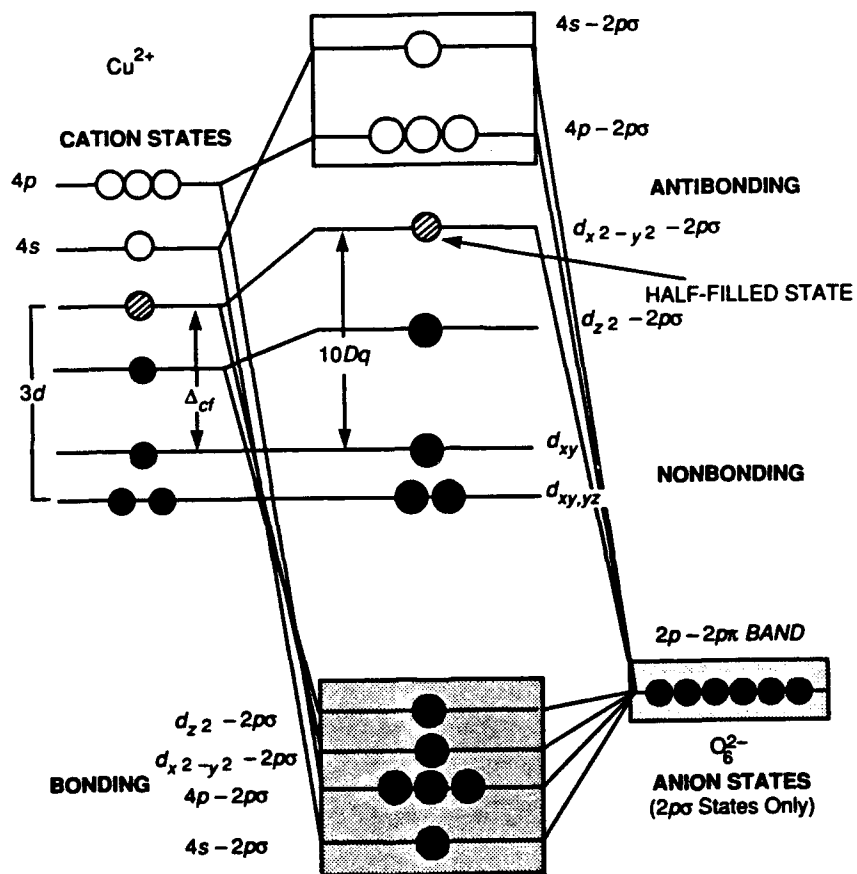


Figure 55. MO diagram for a tetragonally ( $D_{4h}$ ) distorted  $\text{CuO}_6$  complex.

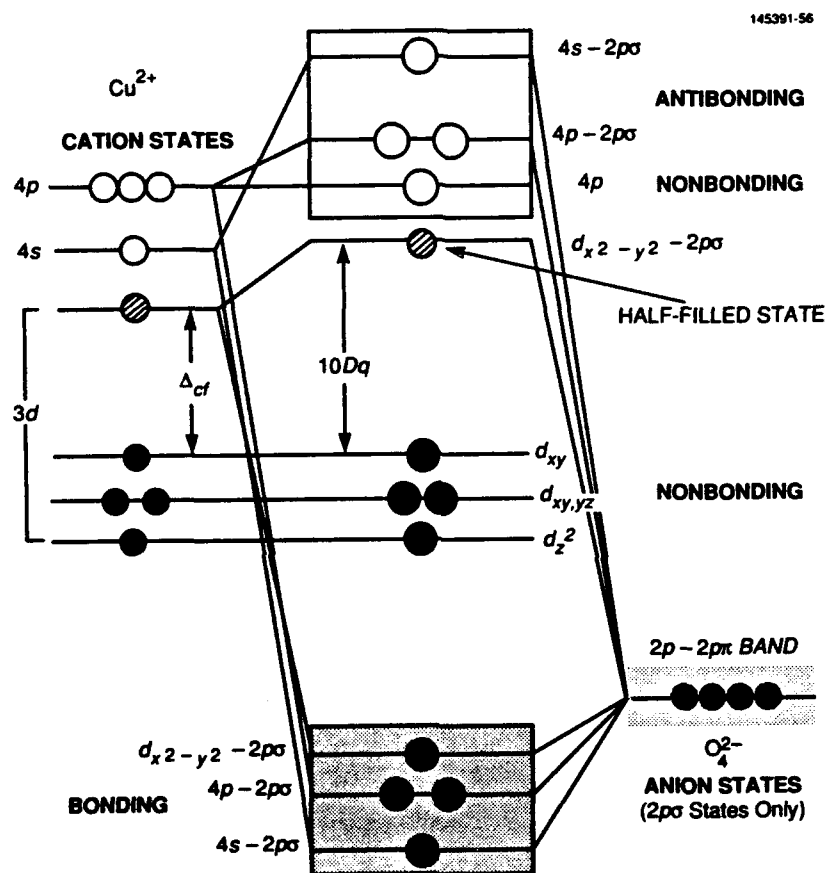


Figure 56. MO diagram for a square planar ( $C_{2h}$ )  $CuO_4$  complex.

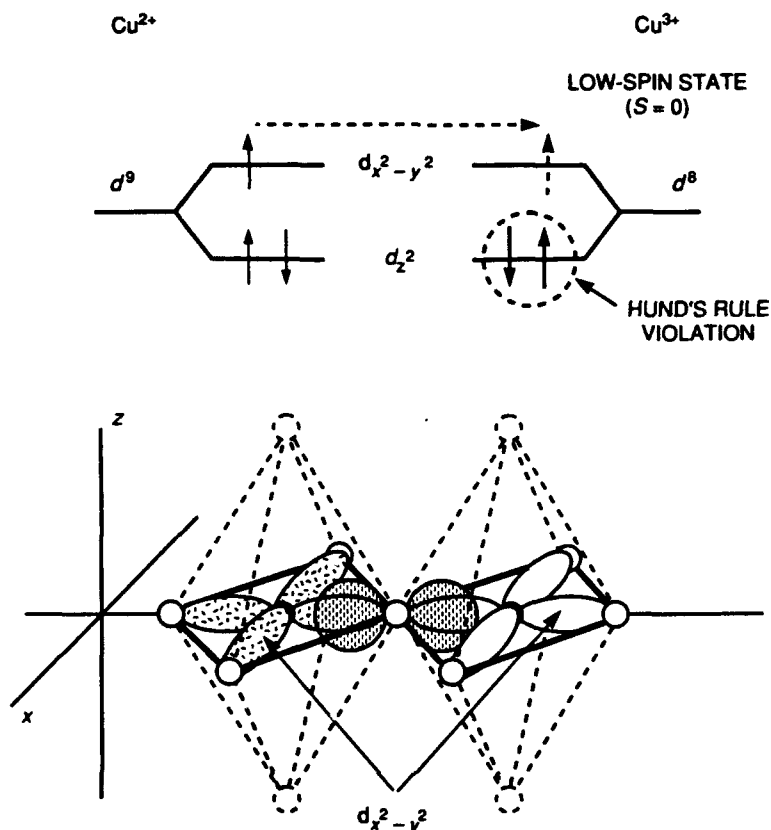


Figure 57.  $p$ -type  $3d_{x^2-y^2}-2p_y\sigma$   $\text{Cu}^{2+}-\text{O}-\text{Cu}^{3+}$  covalent transfer in 180-deg perovskite bond geometry for  $d^9 \rightarrow d^8$  (low-spin).

As suggested by Figure 58, superconduction is likely to occur in the  $\text{Cu}(2)\text{-O}_4$  planes of the pyramidal complex, because the  $\text{Cu}^{2+(3+)}$  content of the  $\text{Cu}(1)\text{-O}_4$  planes would phase over to  $\text{Cu}^{1+(2+)}$  at  $y = 6.67$  (see Figure 59) as a result of oxygen vacancies within the plane that create the  $\text{Cu}(1)\text{-O}_2$  chains. Moreover, these vacancies would break up the continuity of the transfer couplings necessary for superconduction. The origin of positive mobile polarons, therefore, would arise from the fixed negative charges of  $\text{O}^{2-}$  ions filling the vacancies, as  $y \rightarrow 7$ . In Sr-free  $\text{La}_2\text{CuO}_{4+\delta}$  [96], the excess oxygen is more correctly described by  $\text{La}_{2-x}[\text{Cu}^{2+}_{1-x}\text{Cu}^{3+}_x]\text{O}_4$ , which is brought about by La cation deficiencies. As determined earlier, a threshold value of  $x_0 \approx 0.08$  (or  $\delta \approx 0.04$ ) is all that is necessary for the onset of superconduction.

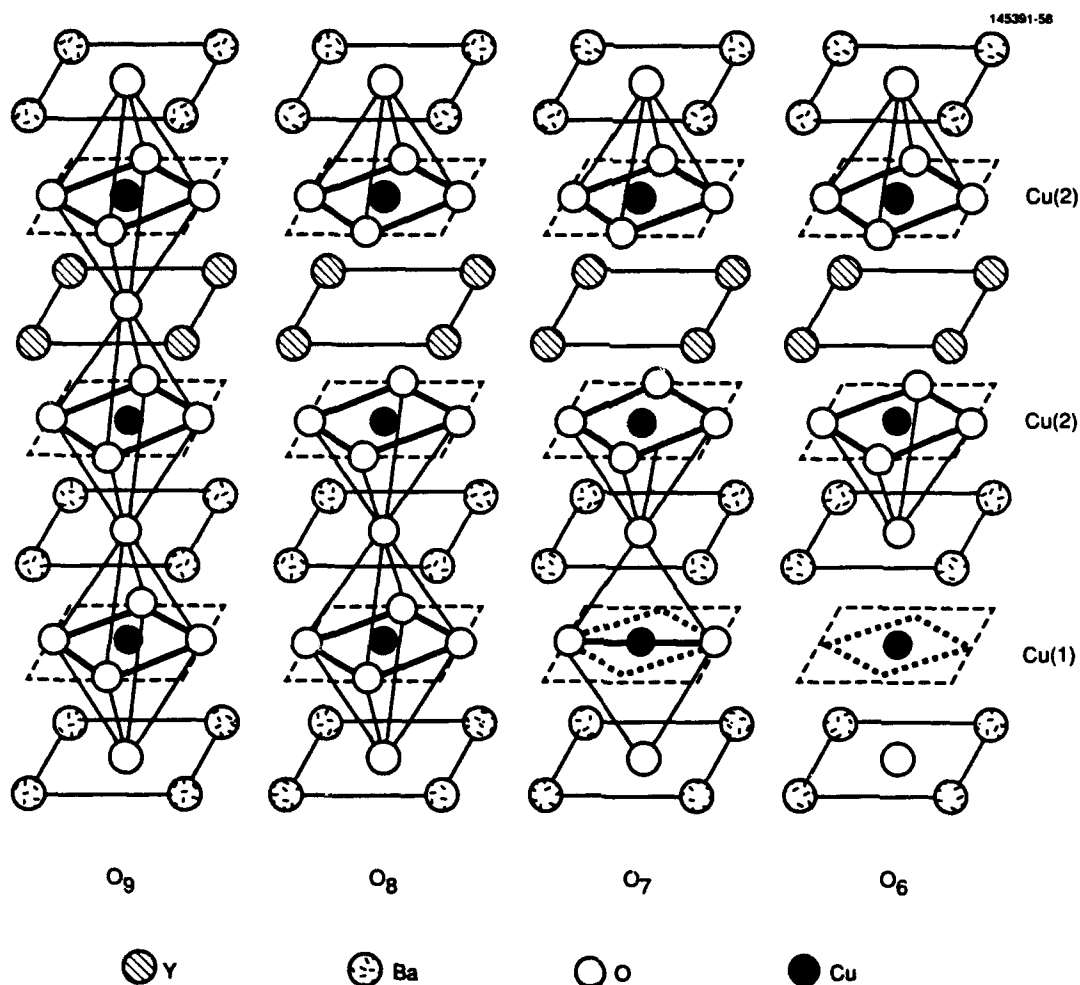


Figure 58. Ordered A-layer structure of  $YBa_2Cu_3O_y$ , showing breakdown of  $CuO_6$  complexes as  $y$  decreases from 9 (hypothetical in this case). At  $y = 8$ , oxygen is removed from  $YO_4$  planes and  $Cu(2)$  ions are square-pyramidally coordinated (i.e.,  $CuO_5$ ), but retain the  $C_4$  symmetry axis. At  $y = 7$ ,  $Cu(1)$  ions become linearly coordinated in the  $x$ - $y$  plane (orthorhombic phase) with uniaxial superconduction expected;  $Cu(2)$  ions retain square-planar coordination in the  $x$ - $y$  plane with planar superconduction possible. At  $y = 6$ ,  $Cu(1)$  planes are fully depleted of oxygen and  $Cu(2)$  ions lose mixed-valence with only  $2+$  species present (see Figure 59).

Partial verification of this valence model was reported by Tranquada [41], who determined experimentally that the average spin of the  $Cu(2)$  ions is 0.66 Bohr magnetons ( $\mu_B$ ) at  $y = 6$ , and that the  $Cu(1)$  sublattice is diamagnetic. This result indicates that most of the  $Cu(2)$  ions are  $2+$  (with some spin canting likely reducing the effective spin values) and that the  $Cu(1)$  ions are  $1+$ , which is consistent with the model in Figure 59. The occurrence of  $Cu^{1+}$  ions in the  $Cu(1)$ - $O_2$  chains should be expected, because its large radius ( $\sim 0.96$  Å) precludes occupancy of the  $Cu(2)$  pyramidal sites; furthermore, there is already ample evidence for  $d^{10}$  configurations to favor linear coordinations [97].

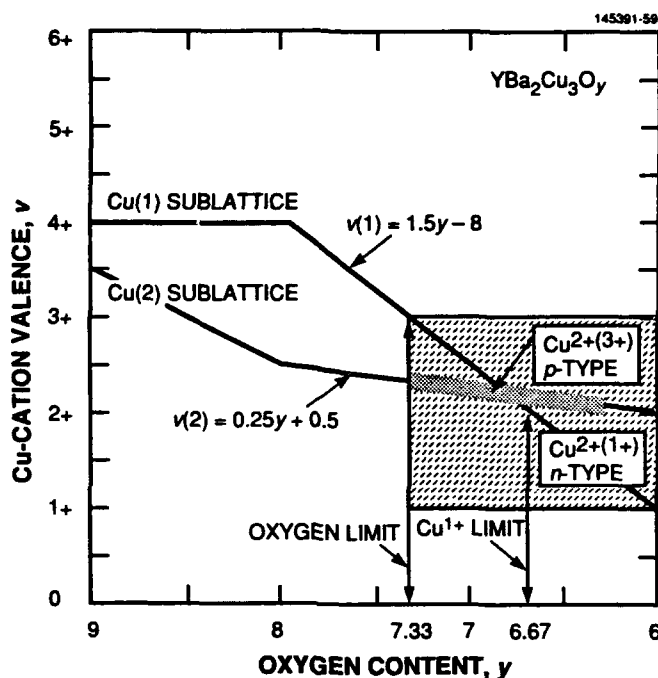


Figure 59. Proposed linear valence model of Cu(1) and Cu(2) as a function of the oxygen content variation and distribution depicted in Figure 58.

An even more intriguing confirmation of this originally proposed linear Cu valence distribution has come from the bond valence sum analysis of Brown [52]. The results plotted in Figure 60 indicate that the Cu valence distribution is basically linear, but with an oscillation about the relevant portion of the linear curve from Figure 59 that is added here for comparison. Among the implications of these results is the possibility that the apparent anomaly in the variation of  $T_c$  with  $y$  shown in Figure 23 may be explained entirely by the nonlinearity of the valence distribution with polaron concentration.

Together with the compounds discussed above, the parameters for more complicated layered structures are summarized in Table 7. In cases where the Cu resides principally in sites with  $O_4$  coordinations, which may provide  $E_{\text{hop}} > 4$  meV (see Appendix D),  $T_c \rightarrow 120$  K. For the  $\text{Bi}^{3+}_2(\text{Sr}^{2+}, \text{Ca}^{2+})_3\text{Cu}^{2+(3+)}\text{O}_{8+\delta}$  system [6], the optimum  $\text{Cu}^{3+}$  concentration  $x = 0.33$  occurs because of a combination of excess  $\text{O}^{2-}$  (i.e.,  $\delta = 0.17$ ) or the occurrence of monovalent calcium [98]. The  $\text{Tl}^{3+}_2\text{Ba}^{2+}_2\text{Ca}^{2+}_{n-1}\text{Cu}^{2+(3+)}_n\text{O}_{4+2n+\delta}$  compounds [99] derive their polaron sources from either fixed-valence cation deficiencies (i.e., excess  $\text{O}^{2-}$ ) or the mixed valence of Tl, which can appear as 1+ or 3+ to suit the ionic size or charge requirements of its locale. With such a dual-mixed-valence condition present, the likelihood of higher polaron ordering, i.e., smaller  $\beta$ , is also increased.

Another source of the enhanced  $T_c$  values could be larger  $b$  values that result from a covalent coupling between the  $d_{x^2-y^2} - 2p\sigma$  antibonding state and the  $6s$  orbital of  $\text{Bi}^{3+}$  or  $\text{Tl}^{1+}$ . An increased exchange integral would give rise to a smaller  $x_p$ . A measurement of the  $W$  parameter for the compositions with maximum  $T_c$  could help to sort out these possibilities.

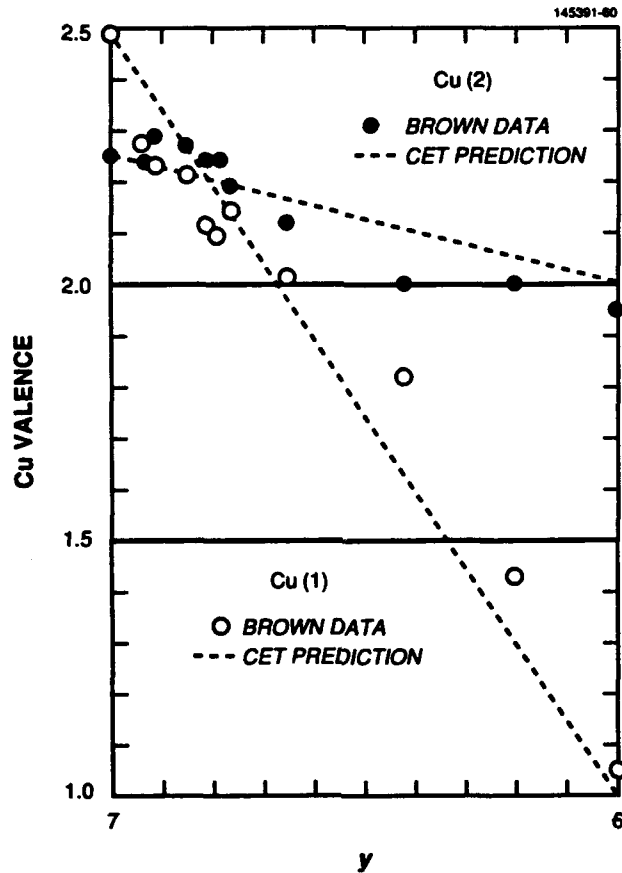


Figure 60. Nominal Cu valence as determined from linear model of Figure 59 compared with valence bond sum analysis of Brown [52] for  $\text{YBa}_2\text{Cu}_3\text{O}_y$ .

### 7.1.2 $\text{Cu}^{1+}\text{-O}^{2-}\text{-Cu}^{2+}$ in $\text{A}_2\text{BO}_4$ Perovskites and Layered $\text{ABO}_2$ (*n*-Type)

Through  $\text{Ce}^{4+}$  substitutions in A sites and the creation of  $\text{O}^{2-}$  vacancies by a reducing atmosphere anneal, Tokura et al. [100] reported superconductivity with  $T_c \approx 24$  K in  $\text{Nd}^{3+}_{2-z}\text{Ce}^{4+}_z(\text{Cu}^{2+}_{1-z-2y}\text{Cu}^{1+}_{z+2y})\text{O}_{4-y}$ , for  $z = 0.15$  and  $y = 0.04$ . As a consequence, stoichiometry is maintained with a  $\text{Cu}^{1+}$  concentration of  $x = 0.23$ .

Although the critical temperatures of this system are not particularly large, and because  $\text{Nd}^{3+}$  is a magnetic rare-earth ion with  $S = 3/2$ , superexchange involving the A sublattice may result in  $\text{Ce}^{4+}$  clustering that would lead to larger  $\beta$  parameters. These results are very significant and provide insight about the microscopic mechanism of superconductivity. The substitution of tetravalent cations into the A sublattice creates negative polarons (electrons), and the appearance of superconduction verifies the prediction of *n*-type  $\text{Cu}^{1+(2+)}$  orbital transfer published in the initial report on the CET model ([1], Table 1). As shown in the orbital transfer diagram of Figure 61, the  $d_{x^2-y^2}$  orbital is again the transfer

path. Here the  $\text{Cu}^{1+}$  ions provide the  $S = 0$  states required for spin transfer and the onset on magnetic frustration in the  $\text{Cu}^{2+}$  host lattice with  $S_L = 1/2$  (see Table 5). In addition, the existence of  $n$ -type superconduction significantly weakens the argument that high- $T_c$  phenomena are based on hole transport through the oxygen sublattice, i.e., local peroxide  $\text{O}^{1-}$  formation. For the oxygen ligands to provide conduits for electrons,  $\text{O}^{3-}$  ions would have to be postulated, which is a situation even more unlikely than the peroxide case.

**TABLE 7**  
**Cu Perovskite Superconduction Parameters**

Compound	Coordination	$T_c$ (max) (K)	$x$ (max)	$E_{\text{hop}}^a$ (meV)	$\beta^a$
<b>p-Type</b>					
$\text{La}_{2-x}\text{Sr}_x\text{CuO}_4$	$\text{O}_6$	~40	0.2	2.5	0.7
$\text{La}_{2-x}\text{Sr}_x\text{CaCu}_2\text{O}_4$	$\text{O}_5$	~60	0.2	4	0.7
$\text{YBa}_2\text{Cu}_3\text{O}_y$	$\text{O}_5$	~95	0.25	4	0.57
$\text{Bi}_2(\text{Sr,Ca})_3\text{Cu}_2\text{O}_{8+\delta}$	$\text{O}_4$	~120	~0.33	(>4)	(<0.5)
$\text{Tl}_2\text{Ba}_2\text{CuO}_{6+\delta}$	$\text{O}_6$	~80		(2.5)	(<0.5)
$\text{Tl}_2\text{Ba}_2\text{CaCu}_2\text{O}_{8+\delta}$	$\text{O}_5$	~110		(4)	(<0.5)
$\text{Tl}_2\text{Ba}_2\text{Ca}_2\text{Cu}_3\text{O}_{10+\delta}$	$\text{O}_5, \text{O}_4$	~120		(>4)	(<0.5)
<b>n-Type</b>					
$\text{La}_{2-x}\text{Ce}_x\text{CuO}_y$	$\text{O}_6$	24	0.23	(2.5)	(>0.7)
$\text{Sr}_{1-x}\text{Nd}_x\text{CuO}_2$	$\text{O}_4$	40	0.14	(4)	(>0.3)
<sup>a</sup> ( ) Indicate suggested values					

Another interesting feature of these compounds is the necessity to create oxygen defects as part of their preparation. In this case the  $\text{Cu}^{1+}$  ions occupy square planar sites ( $\text{Cu}-\text{O}_4$ ) with an occasional missing oxygen. As shown in Figure 58 for  $\text{YBa}_2\text{Cu}_3\text{O}_y$ , the Cu(1) sites that are proposed to harbor  $\text{Cu}^{1+}$  ions are also square planar to linear, as  $y$  falls below 7. Because  $\text{Cu}^{1+}$  ions are usually not accepted in sites of higher coordination, e.g., octahedral  $\text{O}_6$ , due to their large radii ( $\sim 0.96 \text{ \AA}$ ), this result is entirely consistent with traditional metal-oxide chemistry.

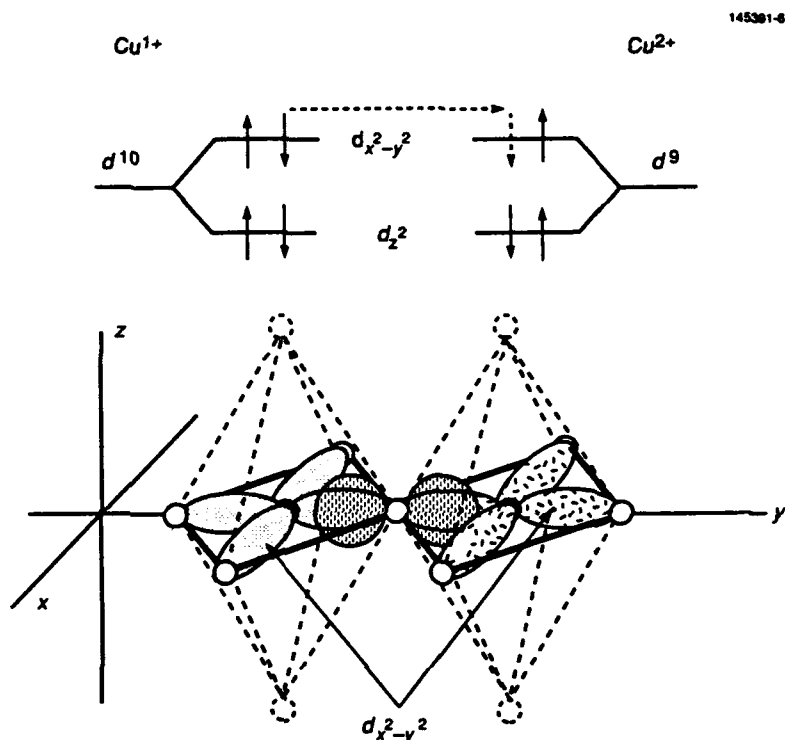


Figure 61.  $n$ -type  $3d_{x^2-y^2}-2p_{\sigma}$   $\text{Cu}^{1+}-\text{O}-\text{Cu}^{2+}$  covalent transfer in 180-deg perovskite bond geometry for  $d^{10} \rightarrow d^9$ .

More recently, a primitive layered  $n$ -type family  $\text{Sr}^{2+}_{1-x}\text{Nd}^{3+}_x(\text{Cu}^{2+}_{1-x}\text{Cu}^{3+}_x)\text{O}_2$  was reported by Smith et al. [101]. In this case, the Cu ions reside in planar coordinations with the A-sites forming oxygen-free layers that are interleaved between  $\text{Cu}-\text{O}_4$  planes. The  $n$ -type compositions are noteworthy because of the increased  $T_c = 40$  K and the lower value of  $x_{\text{max}} \approx 0.14$ . In the context of the foregoing discussion, these results may be explained by an  $E_{\text{hop}}$  that is higher than that of the compound containing  $\text{Ce}^{4+}$ , but with a larger  $\beta$  parameter, as compared in Table 7. This interpretation remains in accord with the general CET conclusions that  $T_c$  through  $E_{\text{hop}}$  has a crystal-field dependence related to oxygen coordination (discussed in Appendix D) and that polaron dispersal is essential for high  $T_c$ .

To conclude this discussion of the layered cuprate compounds, their superconduction anisotropy that was explained in the first report [1] will be reviewed. Apart from the fact that these materials feature mainly uniaxial crystallographic symmetry, there are two specific causes for the absence of superconductivity along the  $c$  axis, i.e., normal to the  $x$ - $y$  plane. First, the required  $\text{Cu}^{2+}-\text{O}^{2-}-\text{Cu}^{2+}$  covalent linkages are not present in the  $z$  direction. This condition in  $\text{YBa}_2\text{Cu}_3\text{O}_y$  may be confirmed by inspection of Figure 58 for  $y \leq 7$ . A second reason for the conduction to be confined to the  $x$ - $y$  plane is that the  $d_{z^2}$  orbital wavefunction (not shown in Figures 57 and 61, but included in Figure 62 for the nickelate case) is fully occupied in the  $\text{Cu}^{1+}$ ,  $\text{Cu}^{2+}$ , and low-spin  $\text{Cu}^{3+}$  ions, and therefore could not provide a transfer path in the  $z$  direction even if the bonding geometry requirements were satisfied.



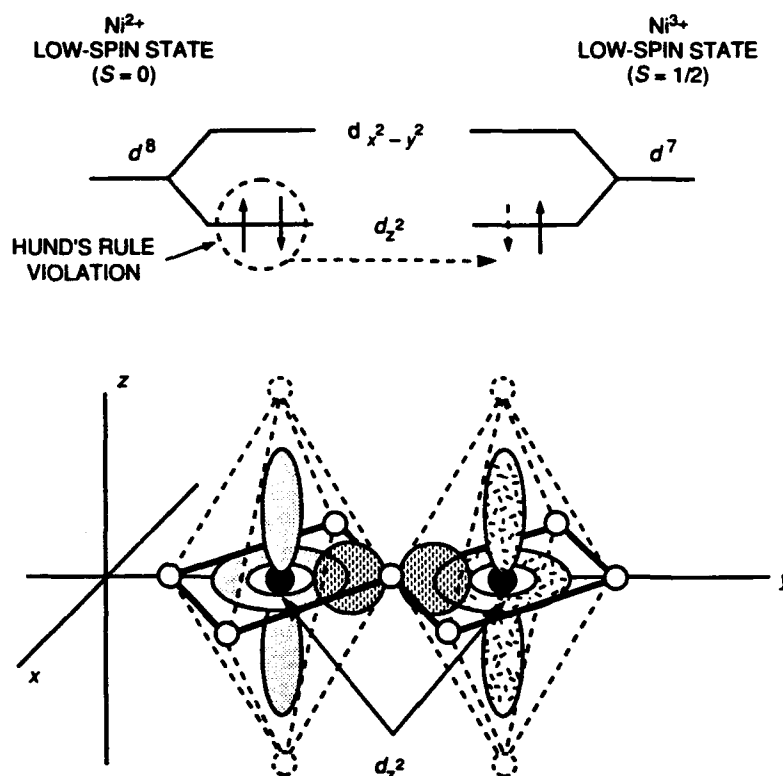


Figure 62.  $n$ -type  $3d_{z^2-2p_y}\sigma$   $\text{Ni}^{2+}$ - $\text{O}$ - $\text{Ni}^{3+}$  covalent transfer in 180-deg perovskite bond geometry for  $d^8$ (low spin)  $\rightarrow$   $d^7$ (low-spin).

### 7.1.3 $\text{Ni}^{2+}$ - $\text{O}^{2-}$ - $\text{Ni}^{3+}$ in $\text{A}_2\text{BO}_4$ Perovskites ( $p$ -Type)

Another entry in Table 5 that merits attention is  $\text{La}^{3+}_{2-x}\text{Sr}^{2+}_x(\text{Ni}^{2+}_{1-x}\text{Ni}^{3+}_x)\text{O}_4$ , for which planar superconduction effects were reported [37] at  $T \leq 70$  K with  $x = 0.2$ . In this system, the transfer orbital is  $d_{z^2}$  (see Figure 62), and the low-spin state must occur partially on both  $\text{Ni}^{2+}$  ( $S = 0$ ) and  $\text{Ni}^{3+}$  ( $S = 1/2$ ) cations [55], as explained in Appendix F.

Although the occurrence of conditions for superconduction with the nickelate compounds is probably tenuous at best, the effects reported lend further credence to the notion that covalence involving  $d$  electrons create  $S = 0$  configurations to produce superconductivity in oxides.

## 7.2 SYSTEMS WITH $6s$ , $6p$ - $2p\sigma$ BONDS

In the foregoing Cu and Ni cases, the superconductivity is confined to planar "sheets," e.g.,  $\text{Cu-O}_4$  complexes, and consequently is two dimensional. This constraint results from the chemical bonding involving the  $d_{x^2-y^2}$  orbital that is peculiar to  $\text{Cu}^{2+(3+)}$  in crystal fields of tetragonal or orthorhombic symmetry. There are, however, cubic metal oxide superconductors with isotropic properties.

### 7.2.1 $\text{Bi}^{4+}\text{-O}^{2-}\text{-Bi}^{5+}$ in $\text{ABO}_3$ Perovskites ( $p$ -Type)

The discovery of high- $T_c$  superconductivity ( $T_c \sim 30$  K) in the diamagnetic cubic perovskite [102]  $\text{Ba}^{2+}_{1-x}\text{K}^{1+}_x[\text{Bi}^{4+}_{1-x}\text{Bi}^{5+}_x]\text{O}_{3-\delta}$  brings into focus two important aspects of this phenomenon:

- $d$  electrons are not required for superconduction, because  $\text{Bi}^{4+}$  has only a single electron in the isotropic  $6s$  shell outside its closed  $5d^{10}$  shell and  $\text{Bi}^{5+}$  has an empty  $6s$  shell.
- Cooperative magnetic ordering is not required because neither ion participates in magnetic exchange (although  $\text{Bi}^{4+}$  is paramagnetic with the unpaired  $6s$  electron).

In this case, the orbital transfer path is  $6p\text{-}2p\sigma\text{-}6p$ , and the directionality of the conduction is three dimensional but restricted to the  $x$ ,  $y$ , and  $z$  axes of the  $p_{x,y,z}$  lobes. The corresponding MO diagram with electron occupancies is given in Figure 63, with the single electron transfer occurring between the antibonding  $6p\text{-}2p\sigma$  antibonding states, again separated in energy by  $E_{\text{hop}}$ . Although it is convenient to think in terms of  $s$ -electron transfer because the outer valence electron of  $\text{Bi}^{4+}$  occupies the  $6s$  orbital state, the actual transfer orbital becomes  $6p$  when the order of energy levels is determined from an MO calculation.

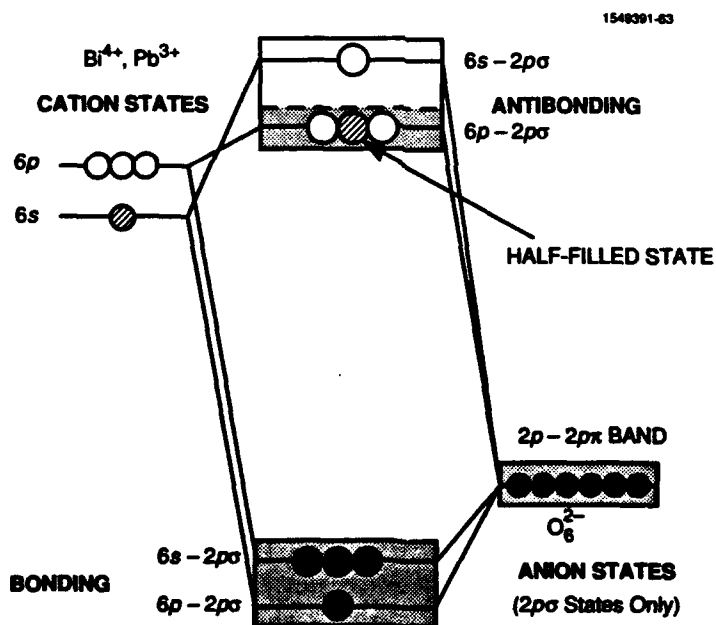


Figure 63. MO diagram for a  $\text{Bi}^{4+}, \text{Pb}^{3+}$  in an octahedral  $\text{O}^{2-}_6$  complex.

In this series, the nominal  $\text{K}^{1+}$  concentration for optimum  $T_c$  was initially found to be  $z = 0.4$ , which would very likely produce a  $p$ -type polaron concentration  $x < 0.33$  if an oxygen deficiency  $\delta$  of only 0.04 were present. Later measurements [103] on the same system confirmed that the polaron concentration for the highest  $T_c$  is  $x \approx 0.3$ , with  $T_c$  falling off quickly as  $x \rightarrow 0.5$ . These results are also consistent with

$E_{\text{hop}} < 2.5$  meV and  $h \sim 0.5$  to  $0.6$ , typical of the Cu perovskites; for  $x < 0.25$ , the cubic phase of this family is lost, and there are, unfortunately, no  $x_0$  data to estimate the concentration threshold  $x_f$ .

### 7.2.2 $\text{Pb}^{3+}\text{-O}^{2-}\text{-Pb}^{4+}$ in $\text{ABO}_3$ Perovskites ( $p$ -Type)

An earlier version of this cubic perovskite contained  $\text{Pb}^{3+(4+)}$  as the transfer pair in the formula  $\text{Ba}^{2+}[\text{Bi}^{5+}_z\text{Pb}^{3+}_{z(1-z)/(1+z)}\text{Pb}^{4+}_{(1-z)/(1+z)}]\text{O}_3$  and showed  $p$ -type superconduction over a composition range  $0.05 \leq z \leq 0.35$ , or  $0.045 \leq x \leq 0.26$ , because  $x = z/(1+z)$  [104]. In this series the curve of  $T_c$  versus  $x$  bears a resemblance to Figure 21 for  $\text{La}_{2-x}\text{Sr}_x\text{CuO}_4$  with a maximum  $T_c = 13$  K at  $x \approx 0.23$ , and then a sharper fall to zero at  $x = 0.26$ , thereby suggesting a  $\beta \sim 0.7$  that is characteristic of the  $\text{Cu}^{2+(3+)}$  materials. Pb immediately precedes Bi in the periodic table, therefore the  $\text{Pb}^{3+(4+)}$  pair has its electron configuration identical to  $\text{Bi}^{4+(5+)}$  with nearly identical ionic mass and similar ionic radius. In this case, however, the  $B$ -site  $\text{Bi}^{5+}$  ions act as the polaron sources, rather than  $A$ -site  $\text{K}^{1+}$  (or  $\text{Ba}^{2+}$ ) ions of the  $\text{Bi}^{4+(5+)}$  compound.

## 7.3 SYSTEMS WITH $3d\text{-}2p\pi$ OR $3d\text{-}3d\sigma$ BONDS

For the lower part of a  $d^n$  transition series, only  $t_{2g}$  orbitals are occupied in octahedral coordinations, and there is no cation-anion  $\sigma$  bonding. There are, however, two other possibilities that are diagrammed in Figure 64: First,  $(t_{2g}\text{-}2p\pi)\text{-(}2p\pi\text{-}t_{2g})$  bonding that is usually ignored in MO first approximations where  $e_g\text{-}2p\sigma$  bonding is dominant, and second, direct cation-cation  $t_{2g}\text{-}t_{2g}\sigma$  bonding with  $t_{2g}$  orbital lobes that reach across the face diagonals of the cubic cell.

### 7.3.1 $\text{Ti}^{3+}\text{-Ti}^{4+}$ in $\text{ABO}_3$ Perovskites ( $n$ -Type)

The first example of superconductivity in a mixed-valence oxide was reported by Schooley et al. [105] with the cubic perovskite  $\text{Sr}^{2+}[\text{Ti}^{4+}_{1-x}\text{Ti}^{3+}_x]\text{O}_{3-y}$  ( $T_c = 0.25$  K), where  $x = 2y$ . As stated, it should be pointed out that the polaron would be negative for  $y \leq 1$ , and the superconductor would be  $n$ -type. In this case the active part of the MO diagram (see Figure 65) is a simple two-level bonding/antibonding combination with the unpaired spin of the  $\text{Ti}^{3+}$  ion stabilized in the bonding state. For the cubic perovskite structure, the face of a unit cell is shown in Figure 64(a), where the  $t_{2g}$  orbital lobes are seen to be separated by  $\sqrt{2}a \approx 5.6$  Å. With such a long throw across the diagonals, direct  $d_{xy}\text{-}d_{xy}\sigma$  overlap should be negligible, and the transfer efficiency  $\eta$  would be much smaller than in the  $\text{Cu}^{2+}\text{-O}^{2-}\text{-Cu}^{2+}$  superexchange systems, which may account for the very small value of  $T_c$ . In this case,  $(t_{2g}\text{-}2p\pi)\text{-(}2p\pi\text{-}t_{2g})$  bonds may be the more efficient transfer paths. As listed in Table 5, other ionic candidates for this type of transfer are  $\text{V}^{4+(5+)}$ ,  $\text{Nb}^{4+(5+)}$ , and  $\text{Ta}^{4+(5+)}$ .

### 7.3.2 $\text{Ti}^{3+}\text{-Ti}^{4+}$ in $\text{AB}_2\text{O}_4$ Spinel ( $p$ -Type)

In the spinel  $\text{LiTi}_2\text{O}_4$ , the distance between cations across the cube face in Figure 64(b) is one-half that of the perovskite. Consequently, the  $h$  integral for  $d_{xy}\text{-}d_{xy}\sigma$  bonds is substantially larger, and the resulting higher carrier density could explain the critical temperatures greater than 10 K. As reported by Johnston et al. [106], a  $p$ -type Li-deficient series with generic formula  $\text{Li}^{1+}_{1-z}\text{Ti}^{4+}_z[\text{Ti}^{3+}_{1+3z}\text{Ti}^{4+}_{1-3z}]\text{O}_4$  was found to be superconducting for smaller values of  $z$ . In this case,  $\text{Ti}^{4+}_z$  are fixed polaron sources in the  $A$  sublattice. With  $z = 0.2$ , a  $B$ -sublattice polaron concentration of  $x = (1 - 3z)/2 = 0.2$  was found

to have  $T_c = 12.2$  K. A maximum  $T_c$  of 13.7 K was observed in a two-phase specimen. With fixed sources in a different sublattice, this situation is very similar to the large-polaron  $\text{Cu}^{2+}\text{-O}^{2-}\text{-Cu}^{3+}$  cases, where the positive carriers have  $S_p = 0$  and the host lattice ions have  $S_L = 1/2$  (see Table 5).

Another composition regime of interest for this system is where  $n$ -type conduction is created by substituting excess Li. Because superconduction is observed when  $x \rightarrow 0.5$  ( $c \approx 0$ ), the material behaves more in the manner of a metal and will be treated as such in Section 8.5.

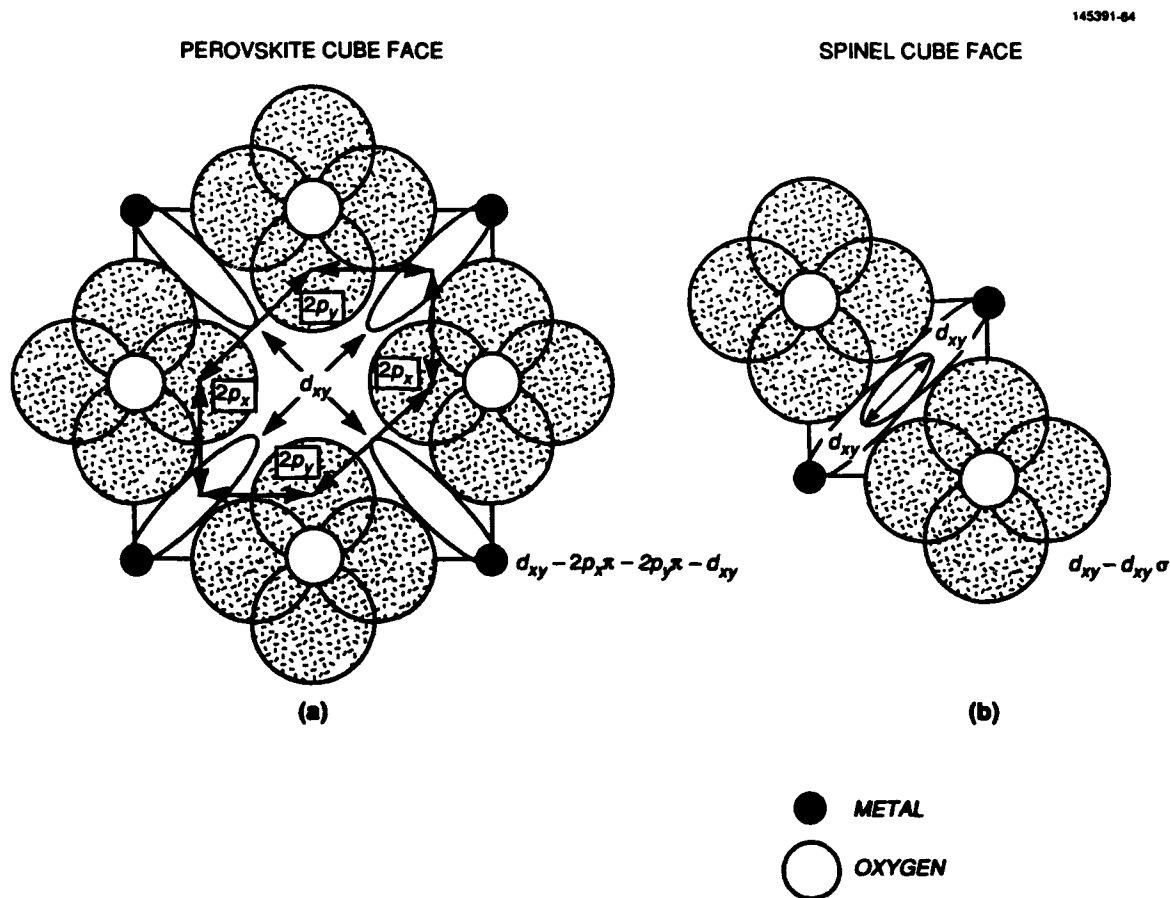


Figure 64. Covalent transfer paths for  $t_{2g}$ -occupied cations: (a) perovskites with  $t_{2g}\text{-}t_{2g}\sigma$  (weak) or  $t_{2g}\text{-}2p\pi\text{-}2p\pi\text{-}t_{2g}$  (moderate, if  $\pi$  overlaps are significant), and (b) spinels with  $t_{2g}\text{-}t_{2g}\sigma$  (moderate).

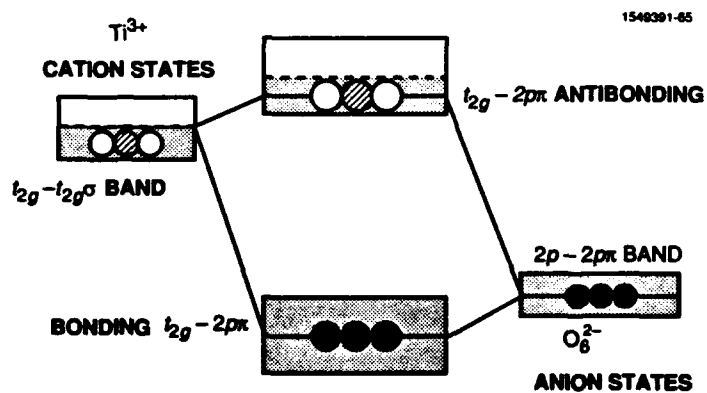


Figure 65. MO diagram for the octahedral  $\text{Ti}^{3+}\text{O}_6^{2-}$  complex  $t_{2g}-2p\pi$  states.

## 8. COVALENT ELECTRON TRANSFER IN METALS

Although the principal subjects of this report are the origin and properties of superconductivity in the high- $T_c$  metal oxides, for which theories that apply well for metals fail to explain the occurrence of superconductivity above  $T \sim 30$  K, speculation on how the CET theory may apply to systems with conduction electrons would not be unreasonable.

In Section 3.1 it was pointed out that extrinsic semiconductors might be superconducting at high impurity concentrations. At temperatures below the excitation threshold, the carriers are bound to their impurity sources and could be thought of as small polarons. With very high impurity densities, itineracy through covalent transfer or tunneling may be sufficient to establish the type of real-space carrier correlation discussed earlier. A more interesting (and real) situation occurs in metals, where the free carriers could be considered to result from excitation gaps of energies in the millielectron volt range within the conduction band, i.e., the concept of a metal as very narrow-band semiconductor. If the theory of mobility-activated conduction is generalized to include metals,<sup>37</sup> the transition from insulators to metals would occur at  $T = E_{\text{hop}}/k$ , as shown in the curves computed from Equation (43) and plotted in Figure 66. One could, therefore, argue that all materials eventually become insulators before  $T$  reaches 0 K. Of the many facets to this theory, the one that must serve as a common denominator for all materials is the notion that localized covalence is present in the relation of carriers to their lattice sites. For materials with a free electron gas at normal temperatures, this would imply that the free electrons are actually activated valence (hopping) electrons that recombine with their ion sources as the material approaches an insulating condition prior to condensation into a superconducting state in the limit as  $T$  falls to  $T_c$ .<sup>38</sup> In this sense,  $E_{\text{hop}}$  would represent either a gap energy or an activation energy, depending on whether a collective or isolated carrier approach is used.

### 8.1 THE GOODENOUGH $b$ PARAMETER MODEL

To introduce the subject of ordered conduction in collective electron systems, it is appropriate to review some important earlier work by Goodenough on metallic oxides in which relationships of electrical conduction to covalent bonding were proposed. In two comprehensive reviews of metal oxides [7,42], Goodenough discussed a model for electrical conduction that served as part of the basis for the CET theory. The main theme of his concept was that the energy of the covalent transfer integral relative to the energy level separation (or band gap) for the ionization reaction  $M^{n+} \rightarrow M^{(n-1)+} + e^- - U$ , i.e.,  $b/U$ , determines the transition from the localized (small polaron) condition of electron hopping to the beginning

---

<sup>37</sup>At low temperatures an exponential function representing ionization to the free-electron state may be expected to modify the product of carrier density  $N$  and temperature-dependent mobility such that  $\sigma \sim N\mu(T)\exp(-E_{\text{hop}}/kT)$ , where  $E_{\text{hop}}$  would represent a local pair-breaking gap energy.

<sup>38</sup>This is not a new concept, having roots in the earliest theories of electrical conduction. See, for example, Schoenberg's introduction [78].

of collective (large polaron to band) behavior among  $d$  electrons in unfilled shells at  $b \rightarrow b_c$ . For values of  $b > b_c$ , additional thresholds were defined, as shown in the energy  $E$  versus  $N(E)dE$  population charts of Figure 67. For static magnetic ordering,  $b \rightarrow b_m$  where the bands begin to overlap. Eventually,  $b$  approaches the higher threshold  $b_{cs}$ , and a necessary condition for the occurrence of a BCS-type of superconduction is established as the two bands merge to a single half-filled conduction band. Within this format, the material systems were also characterized according to  $(n_i \pm c)$ , where  $n_i$  is an integral number of electrons in an unfilled shell and  $0 < c < 1$  is a parameter to represent the nonintegral case. In the analysis that followed, both the  $c = 0$  and  $c \neq 0$  cases were discussed in reference to a complete spectrum of properties.

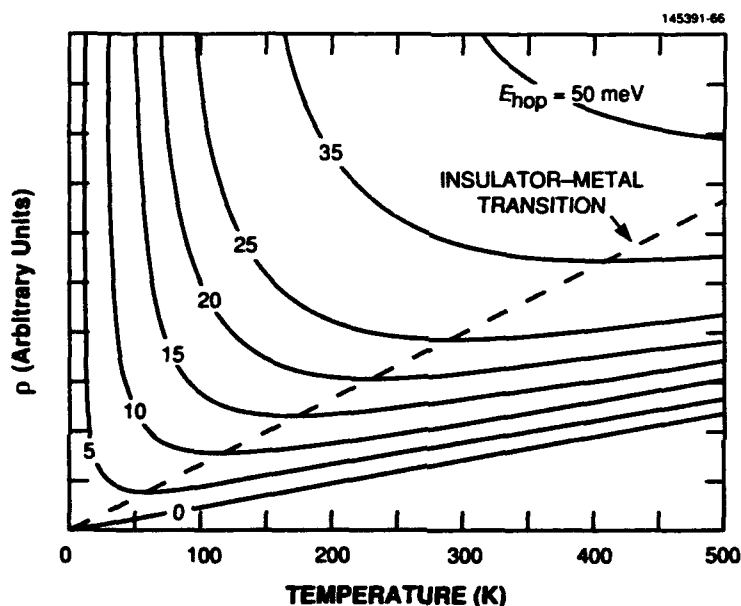


Figure 66. Variation of resistivity minimum as a function of  $E_{hop}$ .

In the context of the CET theory,  $c \neq 0$  is the mixed-valence case, and the conclusions of both concepts are generally compatible. As mentioned earlier, however, for the covalent conditions of the Cu perovskites, where  $1/2 < c < 1$ , single energy levels were used to approximate the narrow bonding and antibonding  $e_g$  bands for the apparent case of  $b \geq b_c$ . For the mixed-valence situation, the energy parameter  $U$  is not involved, being replaced by the small-polaron activation energy  $E_{hop}$ , but the  $b = b_m$  threshold is a consideration because it represents the point of band overlap ( $b \sim U$ ) for the  $c = 0$  case. This could mean that magnetic ordering should be expected to be correlated with covalent transfer, a condition that was discussed at the end of Section 3.5. Because static magnetic order threatens the  $b \geq E_{hop}$  requirement by increasing  $E_{hop}$ , this argument lends further support to the notion that superconduction can only occur with magnetic dilution enhanced by  $S_p = 0$  polarons. One of the points made clear by the Goodenough approach is the difficulty in describing the state that is intermediate between localized and collective extremes. In collective covalent systems, where individual orbits broaden into bands, a

band theory formalism becomes appropriate. Unfortunately, with the overlapping of energy states and (Hartree-Fock) solutions of periodic potentials in  $k$  space, local information regarding impurity states and the influence crystallographic geometries is lost. The BCS theory, despite its profound success in interpreting many important facets of superconductivity, does not directly account for effects related to local electronic structure and chemical bonding.

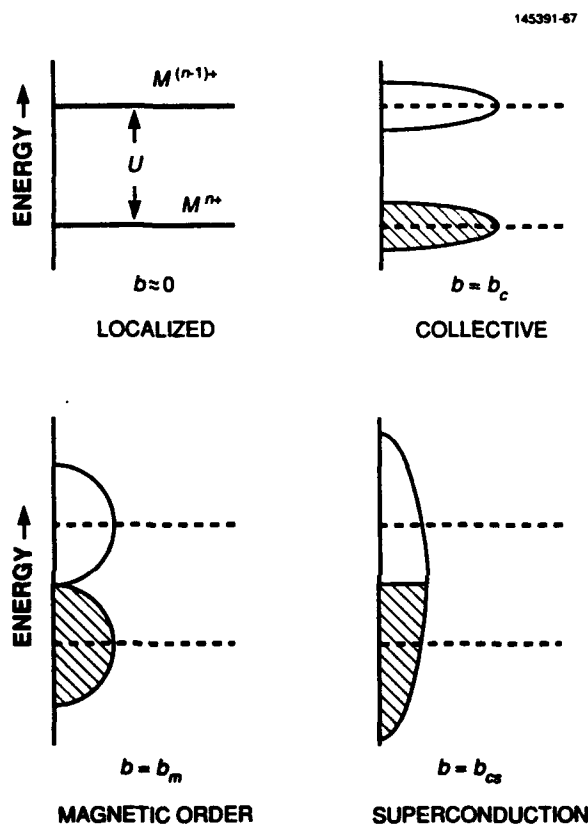


Figure 67. Energy-band diagram based on Goodenough's  $c = 0$  case of excited charge transfer ( $\Delta U \neq 0$  from Figure 2).

With the CET theory applied to oxides, dipoles occur from the mixed valence created by the chemistry and off-stoichiometry of a particular system (the Goodenough  $c \neq 0$  case). This model is based on the localized extreme, which makes it possible to examine the bonding and electron exchange transfer in real space for specific compounds where crystallographic considerations are of paramount importance. In pure metals  $c = 0$ , and there are no fixed polaron sources; the question of local ordering and large-polaron radii overlapping is therefore moot, and a collective model may be applied. There is, however, a need to retain the CET formalism of real-space covalent interactions to examine another possibility that arises from the exchange stabilization energy associated with spin-pairing in orbital states.



Although relationships between the CET theory for mixed-valence ( $c \neq 0$ ) oxides and the more general treatment described above can provide additional insights, the depth and complexities of Goodenough's analyses include a variety of physical properties that extend well beyond the present discussion, and interested readers are encouraged to consult the referenced texts. The main reason for introducing these concepts here lies more in the implications of the  $c = 0$  case (no fixed polaron sources), which is the usual situation in a metal. Here there are two possibilities, that differ according to whether the valence electrons per atom are odd or even numbers.

## 8.2 REAL-SPACE PAIRING IN METALS

For superconductivity in the collective carrier extreme, spin-pairing is required to satisfy the Pauli exclusion principle. To be consistent with the CET theory the pairing must occur in real space. Unlike the isolated dipoles of mixed-valence oxides, however, the dipoles in pure metals or intermetallic compounds that would cause dynamic ferroelectric condensation could not arise from mobile ions electrostatically bound to fixed sources. If dipole formation is postulated in metal structures, they would have to exist locally between adjacent atoms as part of the general bonding scheme through which the spontaneous electron transport would be dominant at low temperatures  $T < E_{\text{hop}}/k$  which is the insulator resistivity regime of Figure 66 for normal carriers.  $E_{\text{hop}}$  would be the energy required to break a pair and create free electrons (quasi-particles in the BCS sense). At higher temperatures (the metallic resistivity regime of Figure 66), the normal state conduction would be the result of electrons continuously activated out of their traps to create the partially filled conduction band depicted in Figure 14.

In systems composed of atoms with unpaired valence electrons, pairing must occur through virtual dipoles as part of the condensation process; for systems with even numbers of valence electrons per atom the pairing requirement is already satisfied and condensation would be associated with the formation of correlated polarization of the atomic medium.

### 8.2.1 Odd Electrons (Virtual Ionic Dipoles)

Consider the simple case of two covalently linked, half-filled orbital states (odd numbers of valence electrons) that form the one-dimensional antiferromagnetic chain through polarization exchange as pictured in Figure 68(a). If the electrons become localized on their atoms at low temperatures, their spins would be aligned according to the dictates of the  $J$  constant; however, if stabilization is gained by the creation of dipoles through the reaction



where  $M$  is an atom with a single  $s$  or  $p$  electron ( $\uparrow-$ ) outside a closed shell, and  $\Delta U$  is the net energy that combines ionization potentials, closed-shell stabilization, and Coulomb attractive energy of the quasi-ionic bond. For the reaction of Equation (102) to be stable,  $\Delta U > 0$ . In the CET context, therefore, the activation energy becomes

$$E_{\text{hop}} = \Delta U \quad , \quad (103)$$

and  $\Delta U$  is used to set the statistical partitioning for  $n_s$  in Equation (30), from which  $n_s^e$  and finally  $\Delta G$  are determined through Equations (59) and (60), respectively.

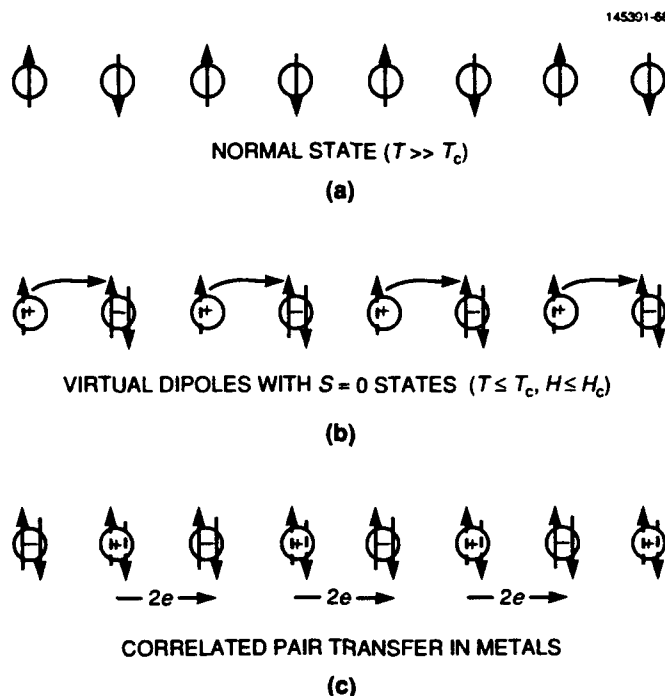


Figure 68. Conceptual model of the condensation of virtual dipole with  $S = 0$  sites: (a) uncondensed state,  $T > T_c$ , (b) formation of dipoles, and (c) correlated pair transfer in real space.

Where antiferromagnetic alignment is favored as suggested in Equation (102), a pattern of virtual dipoles may occur as depicted in Figure 68(b). The conversion of  $\Delta G$  to the energy of current density may be represented by the momentary snapshot of a dipole chain depicted in Figure 68(c) with odd electrons now paired on the same ion in  $S = 0$  configurations. Exceptions to this rule, of course, would be the ferromagnetic metals, e.g., Fe, Co, and Ni, where  $J$  imposes parallel spin alignments ( $\uparrow\uparrow$ ).

The establishment of the superconducting state would then take place first through virtual dipole condensation and then by dipole alignment of the kind described earlier for the ordered large polarons of the  $c \neq 0$  case. Similar to the  $c \neq 0$  case of fixed polarons in an antiferromagnetic lattice,  $E_{\text{hop}}$  for the chain of "condensed" dipoles would also be the energy for thermal activation of an individual electron and consequently the break-up energy of a real-space electron pair.

As implied above, virtual dipole formation is not likely in an insulator because electrostatic fields, local or externally applied, are subject to less screening by electrons. Consequently, the dipole formation in insulators would be more energy expensive than in metals where  $K$  is greater, thereby reversing the sign of  $\Delta U$ . In addition, ionic lattices may not readily tolerate the size variations required to accommodate, for example, fixed  $\text{Cu}^{1+}$ - $\text{Cu}^{3+}$  combinations on a large scale. Moreover, insulators with  $b$  values sufficient to allow covalent transfer must be derived from  $\sigma$  bonds, which unfortunately involve the partially filled  $e_g$  states that are also responsible for antiferromagnetic ordering. With  $T_N \sim 500$  K for these compounds, the magnetically ordered state would be highly stable at low temperatures, and would preclude the occurrence of the frustration necessary for superconduction.

### 8.2.2 Even Electrons (Polarized Atoms)

For the classic soft-metal superconductors, Hg, Pb, and Sn, the outer shells of the individual atoms have  $6s^2$ ,  $6s^2p^2$ , and  $5s^2p^2$  valence configurations, respectively. These elements are of the unfilled  $p$  shell category defined by Matthias [108] and described in Section 8.4. In their collective conduction states these paired electrons become thermally excited to form a "free" electron gas, but at very low temperatures phonon excitations are greatly diminished and relocalization of the valence electrons to their original sites could create a chain of polarized atoms. This result would represent the simplest example of a real-space pair at each lattice site for transfer through the bonding states in the particular system. In this case  $E_{\text{hop}}$  would also represent the pair-breaking energy associated with the creation of a normal electron without being reduced by the energy required to establish the virtual dipole.

With both types of metal superconductors proposed, the dipoles formed as part of the condensation would link covalently within very short distances. Because very high ordering would exist in the absence of scattered polaron sources, nearly complete participation of the dipoles would be required before supercurrents could begin to flow.

### 8.3 $T_c$ AND THE $W$ PARAMETER

To compare the superconduction parameters of metals with those of the high- $T_c$  oxides, it is necessary to examine the basic relation for the critical temperature, now a combination of Equations (11) and (39),

$$T_c = (\alpha/2) (h\nu_D)/kW$$

or

$$T_c = (\alpha/2) \Theta/W, \quad (104)$$

where it is assumed that  $E_{\text{hop}} = E_{\text{el}}$  and  $k\Theta = h\nu_D$ . In metals, the Debye temperature is usually less than 500 K and often less than that of its corresponding oxide, particularly for heavy metals like Hg and Pb. The elastic coupling constant  $\alpha$  is also smaller in metals for reasons that relate to the tendency for covalent compounds to have smaller coefficients (see Table 1), and also because of the larger electron screening effects in metals (large effective  $K$ ), discussed further in Section 8.5 and Appendix G.

Perhaps a more intriguing reason for the smaller  $T_c$  values in metals lies in the larger values of the  $W$  parameter. One immediate result of the assumption that virtual dipoles may form spontaneously in an ordered chain is that the cell radius in elemental metals is limited to a single lattice parameter, i.e.,  $\gamma_p (= x_0^{-1}) \sim 1$ .<sup>39</sup> In addition, because large polarons cannot form in metals  $x_0/x \rightarrow 1$  and  $x_{\text{eff}} \rightarrow 1$ . The question of polaron source dispersal is moot in a pure substance,  $P \sim 1$ ; therefore if the  $h$  integral is reasonably large, it may also be assumed that  $\eta \sim 1$ . As a consequence,  $W$  should be substantially larger than that of an oxide, based on a simple estimate from Equation (39). Based on the earlier observation

---

<sup>39</sup>In cases where there are no ligands, the definition of  $\gamma_p$  changes from Equation (40); because every site would be contributing carriers, the maximum  $x$  is 1 instead of 0.5 for the oxide case. Where the metal has a filled  $s$  shell, there are two available carriers per atom, and the supercarrier density would be potentially a maximum.

that  $W = 1.76$  provided a good fit to the universal  $n_s^c(T)n_s^c(0)$  versus  $T/T_c$  curve in Figure 41,  $x_i/x_{\text{eff}}$  is readily computed to be 0.83 from the complete relation for  $W = \ln[1-x_i/x_{\text{eff}}]^{-1}$  which must apply here because  $x_{\text{eff}} \sim x_i$ . The variation of  $W$  with  $x_i/x_{\text{eff}}$  is plotted in Figure 69. For this situation, one may assume that  $x_i \approx x_0$ , and that  $x_{\text{eff}} \sim x$ .

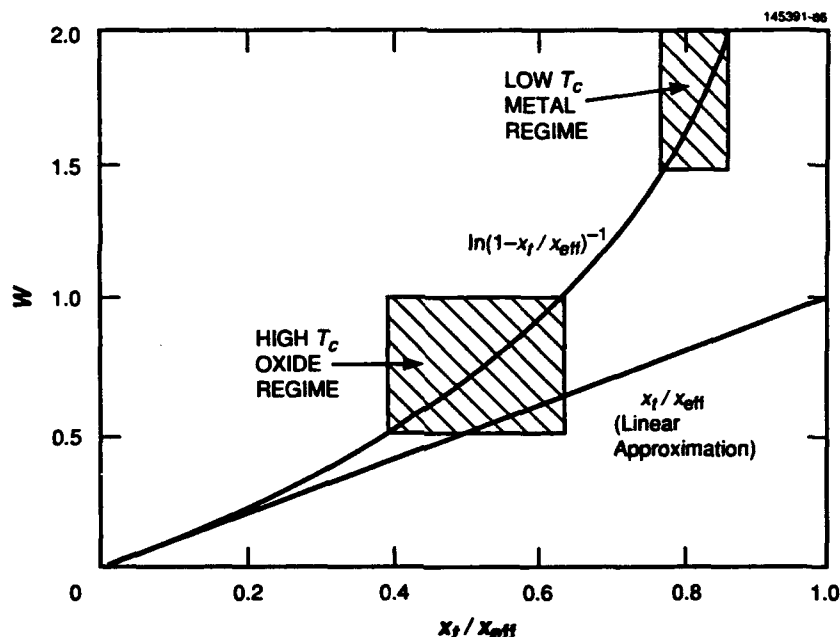


Figure 69.  $W$  parameter as a function of  $x_i/x_{\text{eff}}$  with regimes of oxides and metals indicated. Note that the linear approximation may apply only to certain oxides.

In summation, the  $T_c$  values for metals could be small because of an inherently low  $E_{\text{hop}}$  and a larger  $W$ . To estimate a practical limit, consider upper limits for  $\alpha$  of 0.01 and  $\Theta$  of 500 K. If  $W = 1.76$ , then  $T_c$  should not be expected to reach values much greater than 25 K. The smaller  $W$  value ( $\sim 0.5$ ) and higher  $T_c$  values for oxides reflects the fact that superconduction can be established with fewer carriers, i.e.,  $x_i/x \sim 0.1$ . Whereas the available carrier density  $N$  is even further reduced in the  $\text{ABO}_3$  and  $\text{A}_2\text{BO}_4$  perovskite families because of the presence of several noncontributing sites, critical fields and current densities are not only fundamentally lower in magnitude but suffer an earlier fall off as  $T \rightarrow T_c$  because of the lower  $W$  values (see for example, Figure 41).

#### 8.4 THE MATTHIAS MODEL AND THE PERIODIC TABLE

Prior to Goodenough's work the influence of chemical bonding and the importance of unfilled  $p$  and  $d$  electron states in superconductivity had already been inferred by the observations of Matthias [108], who produced an empirical model for predicting the likely occurrence of superconductivity in many metals and alloys, as well as for estimating the critical temperatures, according to

$$T_c \sim (V^2/M) F(n) \quad , \quad (105)$$

where  $V$  is the volume and  $M$  the mass per atom,  $n$  is the number of valence electrons, and  $a$  is a constant between 4 and 5. The most curious aspect of this model, however, is the empirical function  $F(n)$  that is reproduced in Figure 70. Simply stated,  $F(n)$  means that a first requirement for superconductivity is the existence of an unfilled  $p$  or  $d$  orbital shell. Refinements then place an  $n$  dependence on  $T_c$ , which oscillates across the  $d$  shell, peaking at odd  $n$  values (suggesting that polarization exchange between two half-filled orbits may increase  $E_{\text{hop}}$ ) but growing monotonically across the  $p$  shell.

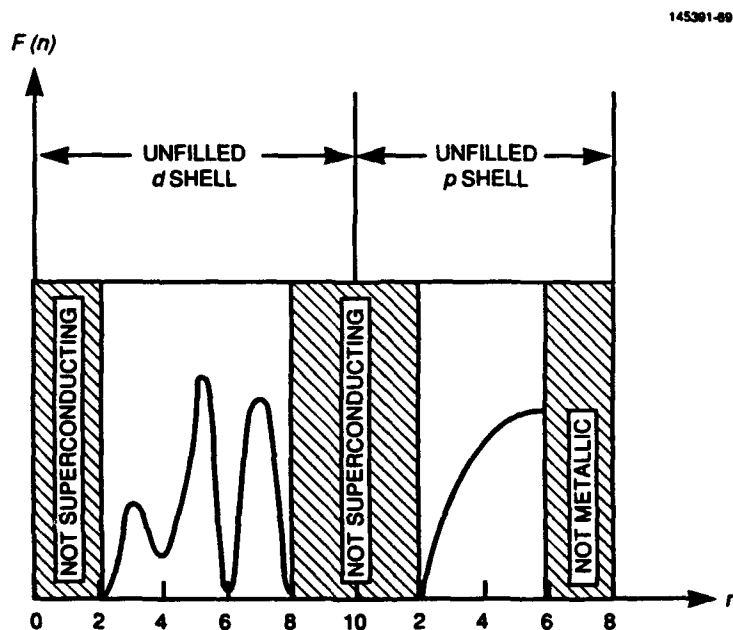


Figure 70. Matthias empirical function  $F(n)$  relating  $T_c$  to the average number  $n$  of valence electrons per atom.

The success of the Matthias criteria for superconductors extends even to alloys and intermetallic compounds in which none of the individual constituents alone meet the conditions but in chemical reaction produce the required  $d$  or  $p$  electron occupation. Like all theories, empirical or otherwise, this model does not apply universally. Nevertheless, it is sufficiently successful to suggest some important conclusions that conform not only to the mounting evidence derived from experiment, but also to the basic premises of CET theory:

- Elements with only  $s$  valence electrons, i.e., alkali metals and alkaline earths, are not likely superconductors, suggesting that free electrons by themselves do not contribute to the superconducting state.
- Elements with unfilled  $d$  or  $p$  shells are more probable candidates. This is consistent with the covalent bond and macroscopic molecule concepts and points to the importance of

crystallographic geometries. Where  $s$  electrons exist in outer atomic shells, it should be recalled that these electrons descend to  $p$  or  $d$  MO antibonding bands, as discussed in Section 7.2.1.

- Ferromagnetic elements from the upper half of the  $d$  shell, i.e., Mn, Fe, Co, and Ni, where  $e_g$  orbitals influence the exchange in typical octahedral coordinations, do not generally produce superconduction (unless through superexchange with  $d-p\sigma$  bonds), supporting the CET contention that superconduction and static magnetic ordering are mutually exclusive. These observations based on the Matthias model can be seen by inspection of the periodic table presentation in Figure 71.

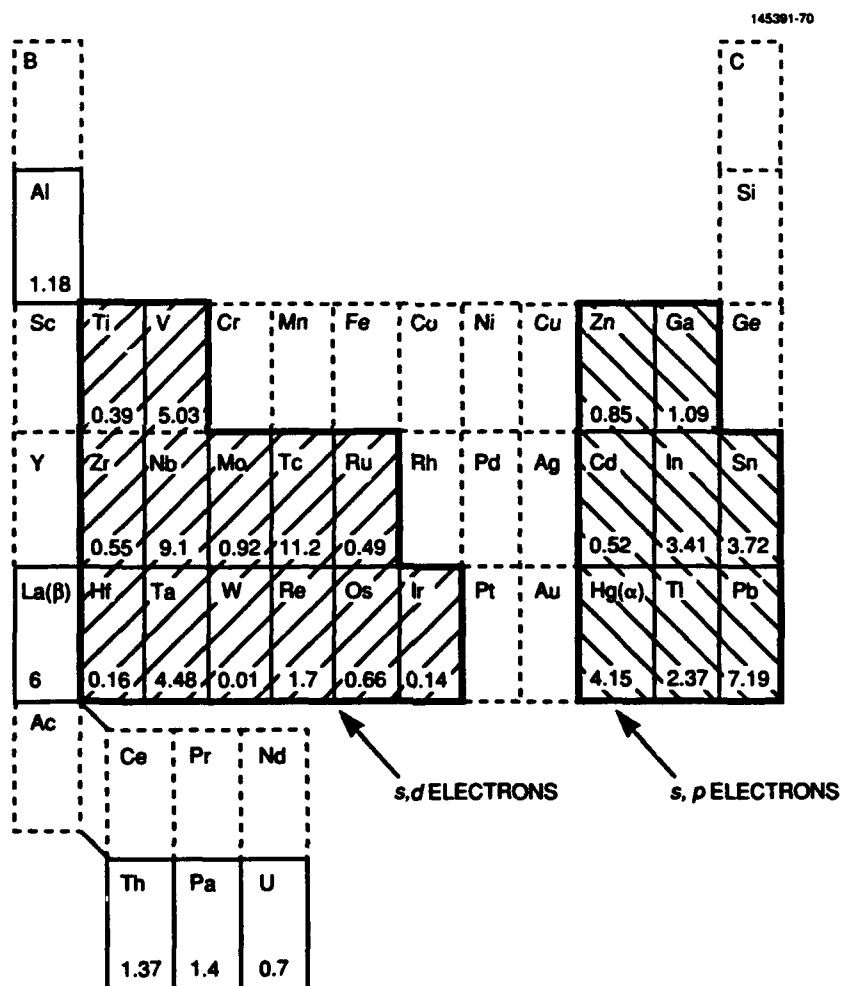


Figure 71. Superconducting elements in the periodic table ([73], p. 338).  $T_c$  values are included where available.

If conduction electrons are not necessarily the principal charge carriers in the superconducting state, and condensation can involve those electrons residing in directed orbitals with overlapping covalent bonds, the role of the conduction band  $s$  electrons remains an open question. Clearly they serve to reduce local electric fields and increase effective local dielectric constants. In most cases, particularly the transition elements, overlapping bands may provide the possibility of  $s$  electrons condensing into the empty states of the  $p$  or  $d$  bands as part of the overall formation of the superconducting state. [Note that crystal field splittings may not be important in metals, and the  $5d$  orbitals may be degenerate. Nonetheless, internal spin polarization (Hund's rule) and the highest energy state as the state for transfer must be considered. This means that the more  $d$  electrons, the larger the downward cascade during transfer, and implies a monotonic increase in  $E_{\text{hop}}$  (or  $E_{\text{mag}}$ ) with  $n$ .]

## 8.5 THE ISOTOPE EFFECT

As part of this general topic, the initial realization of the importance of the crystal lattice in superconductivity should be mentioned. Historically, it arose through the electron-lattice interaction theory of Fröhlich [109,110] that was celebrated by the discovery of the isotope effect and later by its adoption in the electron-phonon mediation of Cooper pairs that form the basis of the BCS theory. The presence of an isotopic dependence may also be seen in the above review of the Matthias model, where an  $M^{-1}$  factor exists in Equation (105) for  $T_c$ .

Without burdening this text with the details of Fröhlich's formal analysis, his result for the electron-phonon coupling in terms of the critical temperature is stated as  $T_c \sim (m/M)^{1/2}$ . Experimental support for this relation was initially found in the simple metals Hg, Pb, and Sn, but universal appearance of the  $M^{-1/2}$  dependence has not been forthcoming, particularly in transition metals where the isotope effect is generally absent (see Table 8). Because there are no polarons here,  $E_{\text{hop}}$  is only a pair-breaking energy without elastic components, meaning that the coupling constant  $\alpha \sim 0$ . Thus, the BCS model (or part of it) may apply best here with  $E_{\text{hop}} \sim \hbar \nu_D$ .

**TABLE 8**  
**Isotope Effect in Superconductors**

Nontransition Metals		Transition Metals	
Material	Exponent	Material	Exponent
Zn	-0.45	Ru	0
Cd	-0.51	Os	-0.15
Sn	-0.47	Mo	-0.33
Hg	-0.50	Nb <sub>3</sub> Sn	-0.08
Pb	-0.49	Mo <sub>3</sub> Ir	-0.33
Tl	-0.61	Zr	0
Source: Kittel [73], p. 347.			

The notion of electron coupling by phonon mediation later became a lynchpin of the BCS theory, where a lattice atom mass dependence turned up again through the Debye temperature  $\Theta$  ( $\sim M^{-1/2}$ ) in the relation  $T_c \sim \Theta \exp[-1/N(0)V]$ , derived from the following relations [111]:

$$\begin{aligned}\Delta(0) &= (h/2\pi)\omega_c [\sinh(-1/N(0)V)]^{-1} \approx 2(h/2\pi)\omega_c \exp[-1/N(0)V] , \\ 1/N(0)V &= 1.14 (h/2\pi)\omega_c/kT_c , \\ kT_c &\approx 1.14 (h/2\pi)\omega_c \exp[-1/N(0)V] ,\end{aligned}$$

or

$$T_c \sim \Theta \exp[-1/N(0)V] , \quad (106)$$

for coupling constant  $N(0)V \ll 1$  (weak limit), where  $N(0)$  is the density of states per unit energy at the Fermi level for electrons of one spin orientation,  $(h/2\pi)\omega_c$  is the Cooper pair binding energy  $\sim k\Theta$ , and  $V$  is the approximate magnitude of the Cooper pair scattering potential that is generally constant, but suffers a cutoff and drops to zero for states of energy  $k\Theta$  away from the Fermi level. By inspecting Equation (106) it may be seen that  $N(0)V$  (typically  $\leq 0.3$ ) varies directly with  $\Theta$  through the exponential function, and it is apparent why the BCS theory does not easily account for  $T_c$  values in the 100-K regime, particularly when  $\Theta$  itself is above 500 K only for light elements.

In the foregoing explanation of the source of  $E_{el}$ , CET also invoked some of Fröhlich's work, but this time the starting point was his polaron theory for nonmetals [13]. The relation between critical temperature and trapping energy for the magnetically frustrated situation may be inferred from Equation (11):

$$T_c \propto E_{el} \approx (\alpha/2) (h\nu_D) , \quad (107)$$

where  $h\nu_D = k\Theta \sim M^{-1/2}$ . In the Fröhlich derivation of the coupling constant  $\alpha$ , however, there is an additional dependence of  $\nu_D$  through the relation for the density of the polaron phonon cloud

$$\alpha = 2e^2(\pi^3 m/h^3)^{1/2} K_{eff}^{-1} \nu_D^{-1/2} , \quad (108)$$

where  $K_{eff} = KK_{op}/(K - K_{op})$  is the effective dielectric constant. Here  $K$  and  $K_{op}$  are the static and optical frequency dielectric constants, and  $(K - K_{op}) \approx K_{ion}$ , the ionic dielectric constant of the plateau that appears in the infrared or lattice vibration frequency band. In more general terms,  $K_{eff}$  may be considered as proportional to an effective polarizability, which is expected to increase with valence charge and ionic bond length and with the polarizabilities of the individual ions, e.g.,  $Ag^{1+}$  with a closed 4d shell is more polarizable than  $K^{1+}$  with an argon core even though they have the same radius.

It may be easily shown [112] that the dipole moments of an ionic lattice should be independent (in theory) of  $M$  or  $\nu_D$ , and vary according to

$$m_d = q^2 E/2C , \quad (109)$$

where  $E$  is the electric field at the ions and  $C$  is the elastic constant, so that the dependence on the mass of the lattice ions would reduce here to  $M^{-1/4}$ . To account for the  $M^{-1/2}$  dependence of Fröhlich's original prediction, a  $\nu_D^{1/2}$  dependence would have to be assigned to  $K_{eff}^{-1}$  in order to cancel the  $\nu_D^{-1/2}$  factor in Equation (108). This possibility is supported to some extent by the properties of diatomic compounds listed in Table 9, where a definite monotonic increase in  $K_{eff}$  with  $\nu_D^{-1/2}$  suggests the existence of at least an indirect dependence of  $K_{eff}$  on nuclear mass that might contribute to an isotope effect.



**TABLE 9**  
**Dielectric Data for Ionic Compounds [23]**

	$K$	$K_{op}$	$K-K_{op}$	$K_{eff}$	$\nu_D$ $\times 10^{12} \text{ s}^{-1}$	$\nu_D^{-1/2}$ $\times 10^{-6} \text{ s}^{1/2}$	$\Theta$ K
LiF	9.27	1.92	7.35	2.42	19.6	0.226	941
NaF	5.3	1.75	3.55	2.61	12.2	0.286	586
NaCl	5.62	2.25	3.37	3.75	7.79	0.358	374
NaBr	5.99	2.62	3.37	4.66	6.11	0.404	294
NaI	6.60	2.91	3.69	5.20	5.26	0.436	254
KCl	4.68	2.13	2.55	3.90	6.16	0.403	296
KBr	4.78	2.33	2.45	4.55	4.97	0.449	239
KI	4.94	2.69	2.25	5.91	4.39	0.477	212
RbCl	5	2.19	2.71	3.89	5.76	0.417	276
RbBr	5	2.33	2.67	4.36	4.23	0.486	204
RbI	5	2.63	2.37	5.54	3.37	0.544	162
CsCl	7.2	2.60	4.60	4.06	5.25	0.436	252
CsBr	6.5	2.78	3.72	4.85	3.66	0.523	176
CsI	5.65	3.03	2.62	6.53	2.70	0.608	130
AgCl	12.3	4.04	8.26	6.01	5.86	0.413	280
AgBr	13.1	4.62	8.48	7.13	4.38	0.478	210
ZnO	8.5	3.73	4.77	6.64	19.9	0.224	960
ZnS	8.3	5.07	3.23	13.0	11.6	0.293	580

Since the time of the original prediction and verification of the isotope effect, its significance as a test for superconductivity theories has probably diminished. Examples of the measured exponent values in Table 8 reveal a variation from 0 to 0.61. In particular, the elements listed may be separated into two groups, already made familiar by the Matthias model. For the nontransition elements with closed  $d^{10}$  shells, the exponent is approximately  $-1/2$ , thereby suggesting that  $K_{eff} \sim \nu_D^{-1/2}$ . For the transition metals with largely unpolarizable cores of closed  $p^6$  shells (i.e., noble gases), the magnitude of the exponent is smaller, closer to the CET average of  $-1/4$ , and in some cases effectively zero. This latter category would include the high- $T_c$  oxides, where multication lattices may also dilute any isotope effect [113].

#### 8.6 SUPERCONDUCTING COMPOUNDS WITH $c \approx 0$

Continuing the discussion of  $p$ -type  $\text{LiTi}_2\text{O}_4$  spinel from Section 7.3, it is appropriate to describe some further work on this system [114,115] in which positive polaron sources were created by excess Li diluting the  $B$  sublattice to produce  $n$ -type  $\text{Li}^{1+}[\text{Li}^{1+}_z\text{Ti}^{3+}_{1-3z}\text{Ti}^{4+}_{1+2z}]\text{O}_4$ . Superconductivity with  $T_c \approx 11$  K was observed [114] or a range of  $0 \leq z \leq 0.1$ ; since  $x = (1-3z)/(1-z)$ , the polaron concentration range translates into  $0.4 \leq x \leq 0.5$ . Here the concentration is greater than  $1/3$ , which is the limit anticipated for the real-space pairing (the double transfer concept) in a lattice with  $S_L > 0$ , the question of spin-pairing must be viewed in a broader context.

If one considers the  $z = 0$  case, where  $\text{Ti}^{3+}$  and  $\text{Ti}^{4+}$  ions may alternate through the lattice in perfect order, polaron trapping is still intact but the system is now collective, with no possibility of an isolated transfer. If one electron changes sites, either covalently or by hopping, it will immediately encounter an exchange requirement from its new neighbor. This process would mean that an antiferromagnetic alignment must already be available, or that the neighbor must also transfer away to restore the original ionic distribution. The implications for correlated covalent transfer in these  $n$ -type materials, where  $S_L = 0$ , suggest a conduction mode more like metals with a partially filled conduction band [116], and the spin alignments may be arranged according to  $\text{Li}^{1+}[\text{Ti}^{3+}(\uparrow-)\text{Ti}^{4+}(-)]\text{O}_4 \Rightarrow \text{Li}^{1+}[\text{Ti}^{2+}_{0.5}(\uparrow\downarrow)\text{Ti}^{4+}_{1.5}(-)]\text{O}_4$ , where a superconducting electron pair occupies every fourth  $B$  site.

An argument for the  $2\text{Ti}^{3+} \rightarrow \text{Ti}^{2+} + \text{Ti}^{4+}$  reactions is based on the comparative instability of the  $\text{Ti}^{3+}$  ion. Because  $\text{Ti}^{4+}$  is the most stable titanium oxidation state, and  $\text{Ti}^{2+}$  can be further stabilized by spin-pairing, the above reaction could result in a net energy reduction during a transition to the ordered superconducting state.

In addition to the semiconducting  $\text{LiTi}_2\text{O}_4$  spinels, there are a number of metallic binary transition-metal compounds, e.g.,  $\text{NbO}$ ,  $\text{NbN}$ ,  $\text{Nb}_3\text{Sn}$ ,  $\text{V}_3\text{Ga}$ , that probably represent situations that are partially  $c \neq 0$  cases. These materials have  $T_c$  values in the 10- to 25-K range and suggest a type of superconductor that is intermediate between the high and low  $T_c$  categories.

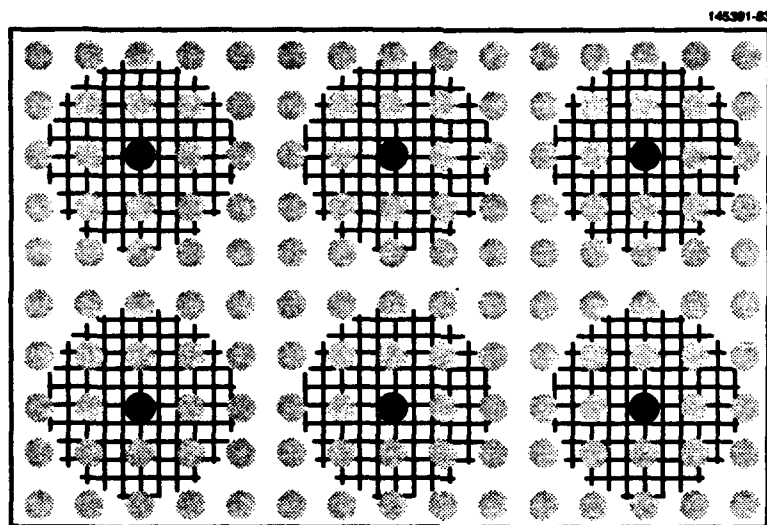
## 8.7 COMPARISON OF METAL AND OXIDE SUPERCONDUCTORS

From the above discussions it is now possible to contrast the superconductivity of metals with that of the high- $T_c$  oxides. As viewed from the CET perspective, the generic difference between the two classes of superconductors prior to the onset of condensation is suggested in Figure 72 by the randomly distributed local dipoles of metals as opposed to the array of large polarons centered about fixed charges that characterizes the oxides. In both instances the population and distribution of the dipoles are dynamic and controlled by thermal activation processes.

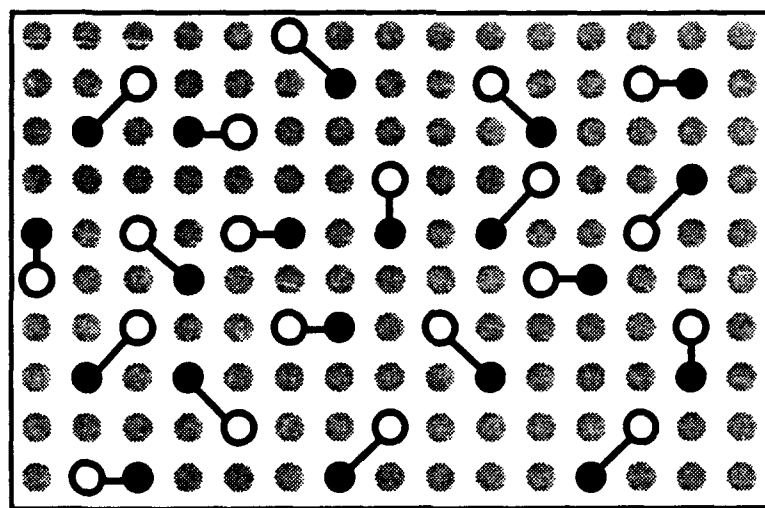
In metals there are no large polarons, and the dipoles themselves are mobile; therefore, superconductivity occurs only at the lowest temperatures, after almost every available dipole has condensed, i.e., large  $x_r$ . Moreover, critical temperatures are further reduced because the activation energy  $E_{\text{hop}}$  is small owing to the large electron screening effects (highest dielectric constants). With this situation it also follows that the carrier density  $n_f^e(0)$  is a maximum, and the dispersal parameter  $\beta \rightarrow 0$ .

On the contrary, metallic oxides feature higher critical temperatures for two reasons. First, the  $E_{\text{hop}}$  values are larger because of lower dielectric constants. A second less obvious cause is that the large polarons allow the superconducting state to survive at even higher temperatures because ordering of the carriers can occur at much lower densities, i.e., small  $x_r$ . However, this latter feature of the high- $T_c$  compounds also imposes a limitation on carrier densities. Because the highest temperatures at which superconductivity occurs are achieved with a minimum of carriers, the superconducting state is tenuous in this temperature range, and its properties reflect this fragility through reduced  $W$  values that were shown earlier in Figure 47 to limit critical current densities near the  $T_c$  regime. Thus, it may be concluded that although larger  $E_{\text{hop}}$  values are present in the oxides, it is the polaronic nature of the conduction that

creates the small  $x_c$  thresholds that allow the exaggerated  $T_c$  values that occur through reduced  $W$  ratios, as indicated by Equation (39). With  $W = 1.76$  typical of metals, the high- $T_c$  cuprates would have critical temperatures well below 77 K.



(a)



(b)

**Figure 72.** Dipole arrangements before superconduction condensation: (a) dispersed polarons in a mixed-valence oxide, and (b) random local dipoles in a metal.

Compared with metals, the oxides also have intrinsically lower carrier densities by the nature of their chemical and electronic structure. It is interesting to note how intermetallic compounds offer a  $T_c$  range (10 to 25 K) that is intermediate between the elemental metals and the complex layered cuprates. In accord with the CET theory, this would suggest that  $n_s^e(0)$ ,  $E_{\text{hop}}$ ,  $x_t$ , and  $\beta$  would also fall into the intermediate categories proposed in Table 10.

**TABLE 10**  
**Qualitative Comparison of Superconduction Parameters**

Material Class	$n_s^e(0)$	$T_c$	$E_{\text{hop}}$	$x_t$	$\beta$
Metals	Large	< 10 K	Small	Large	0
Intermetallics	Medium	10 to 25 K	Medium	Medium	$\geq 0$
Oxides	Small	> 25 K	Large	Small	0.5

One may conclude, therefore, that the promise of high- $T_c$  superconductors for high current applications could be somewhat illusory because of the sparseness of supercarriers at the higher temperatures. On the other hand, critical fields are intrinsically larger than in metals as a result of the reduced electrostatic screening (smaller  $K$ ). In the present state of the art, critical temperatures of the oxides may be increased further by seeking out compounds with higher  $E_{\text{hop}}$  and by improving the dispersal of the fixed polaron sources [1]. As shown in Figure 73, where model curves of  $n_s^e$  versus  $T$  based on Equation (65) and normalized to the approximate  $n_s^e(0) = N_{\text{max}}$  value for  $\text{YBa}_2\text{Cu}_3\text{O}_7$  are plotted for different  $\beta$  values,<sup>40</sup> the advantages of improving the polaron ordering are illustrated. Smaller  $\beta$  values increase the effective carrier density at low temperatures, but they also further reduce the  $W$  parameter, thereby causing even earlier falloffs in the  $n_s^e(T)$  function. For  $\beta < 0.375$  the optimum carrier concentration  $x = 0.33$ , which is the value proposed in Section 5.1.5 as the maximum possible for the real-space pairing option. Consequently, the low temperature enhancement of  $n_s^e$  would vanish when  $\beta$  is reduced below this level, but the advantages of better polaron dispersal persist at higher temperatures because of the increased  $T_c$  values.

To place these estimates in a clearer perspective, a proposed supercarrier region for metals is drawn in Figure 73, emphasizing their dramatic difference with the oxides and their inherent advantages for high current density applications and low temperatures. Based on the estimates for the high- $T_c$  cuprates, the current density limit for  $\text{YBa}_2\text{Cu}_3\text{O}_7$  could be raised by a factor of 2 over the value  $4 \times 10^8$  amp/cm<sup>2</sup> at  $T = 0$  K (calculated in Section 6.6) and by a factor of 5 at  $T = 77$  K. Based on the data presented in Figure 47, a  $\text{YBa}_2\text{Cu}_3\text{O}_7$  superconducting film with ideal crystallographic homogeneity and optimized polaron dispersal would have a critical current density of approximately  $5 \times 10^7$  amp/cm<sup>2</sup> at  $T = 77$  K.

<sup>40</sup>Equation (65) may be modified according to  $n_s^e(T) = n_s^e(0)[1 - \exp(-E_{\text{hop}}/kT) \cdot \exp(W)]$ , where  $W$  is defined by Equation (39). For each calculated curve of Figure 73,  $E_{\text{hop}} = 4$  meV,  $x_t = 0.04$ , and the transfer efficiency  $\eta$  was assumed to be unity at the concentration values for peak  $T_c$ , which are defined by  $x_{\text{max}} = (8\beta)^{-1}$  for  $x$  up to 1/3 (see Figure 24). For  $\beta \leq 3/8$  (or 0.375), the  $\beta$  values have no further influence on  $x_{\text{max}}$ , and therefore permit no additional enhancement of carrier or current densities at  $T = 0$ , as indicated in Figure 73.

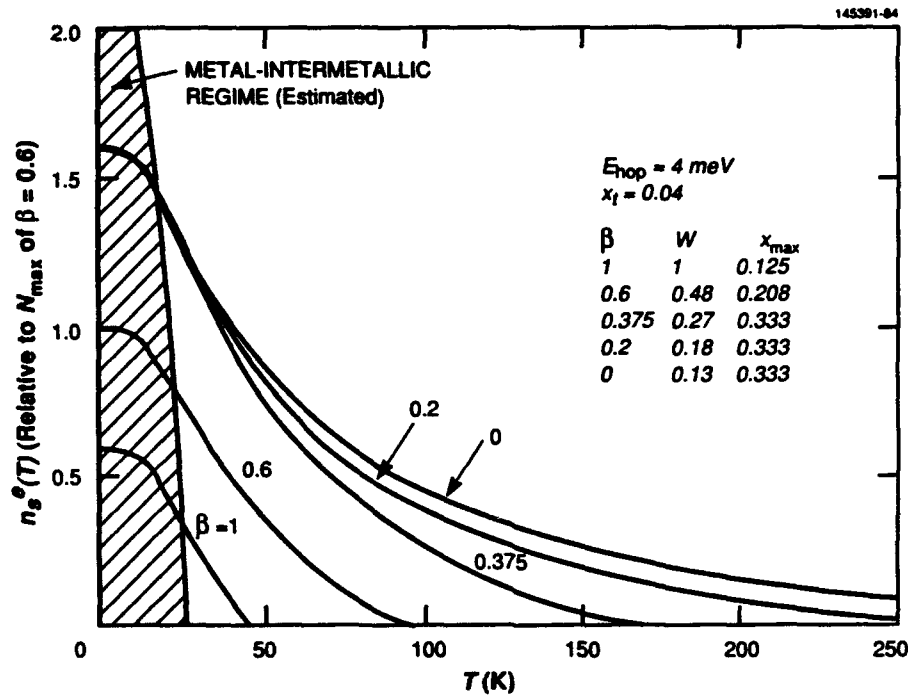


Figure 73. Temperature dependence of supercarrier density for values of dispersal parameter  $\beta = 1, 0.6, 0.375, 0.2$ , and 0.  $n_s(T)$  curves are referenced to  $N_{\max}$  of the  $\beta = 0.6$  curve, typical of  $\text{YBa}_2\text{Cu}_3\text{O}_7$ .

Perhaps a better basis for comparison would be the product  $T_c W (= E_{\text{hop}}/k)$ , which may be thought of as a figure-of-merit temperature  $T_{\text{fom}}$ . For example, intermetallic compounds such as  $\text{Nb}_3\text{Sn}$  that feature  $T_c \sim 18 \text{ K}$  and  $W \sim 2$  yield  $T_{\text{fom}} \sim 36 \text{ K}$ , while high- $T_c$  polaronic cuprates have  $T_c \sim 90 \text{ K}$  and  $W \sim 0.5$  to give  $T_{\text{fom}} \sim 45 \text{ K}$ . Although these two material types differ substantially in their regimes of applicability,  $T_{\text{fom}}$  in either case could be raised by increasing the gap or trap energy  $E_{\text{hop}}$ . As discussed in Sections 3.2 and 8.5, this could mean lower dielectric constants to increase the polaron coupling constant  $\alpha$  and (as Matthias suggested) smaller atomic masses to raise the Debye frequency  $\nu_D$ .

## 9. SUMMARY AND CONCLUSIONS

In this study of superconductivity, a reassessment of the mechanisms for creation of the ordered conduction state has been presented, inspired by the unexpected discovery of the phenomenon in traditional perovskite insulators. The CET theory was initially an interpretation of the electrical measurement data gathered from these materials. In a broader sense, however, it represents a departure from conventional thought on the subject of superconductivity that is based on the idea that the superconduction mechanism is intimately tied to chemical covalent bonding in all systems. The fact that its earliest observation happened to be in metals probably obscured this possibility and led to the assumption that supercarriers were exclusively derived from a free electron gas. According to the CET theory, superconduction occurs in insulators because of bound electrons delocalized from their parent ions and in metals because of free electrons returning to their parent ions.

Although macroscopic concepts like the two-fluid model and the microscopic theory of electron pairing in  $k$  space correctly observe that some constraint to the free-electron gas is required for compatibility with the London equations, the link to chemical bonding suggested empirically by Matthias [108] and explored qualitatively by Goodenough [7] as part of his comprehensive study of metallic oxides has been largely ignored.

The covalent transfer concept is deduced from previous contributions outlined in the partial evolution of superconduction theory illustrated in Figure 74. Beginning with the phenomenology of superconductivity, the chart defines the two basic origins as the

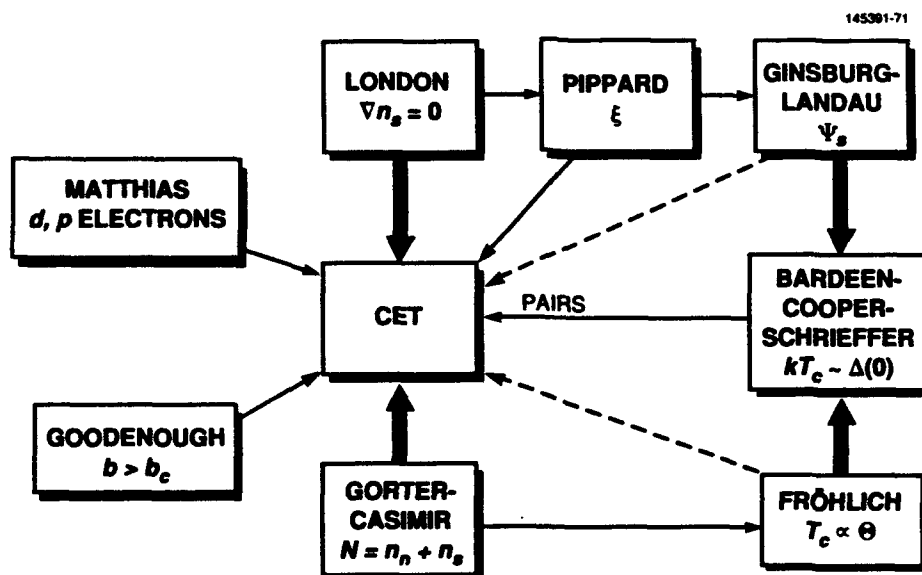


Figure 74. Partial historical summary of superconductivity theory development.

- Two-fluid model of Gorter and Casimir, whereby normal and superconducting carriers co-exist with a condensation to the superconducting state occurring below a critical temperature.
- London equations [9], which define the spatially ordered carrier constraint  $\nabla n_s = 0$  that serves as the basis for the Meissner effect and from which evolved the concepts of penetration depth (London) and coherence length (Pippard [11]).

Later theory by Ginsburg and Landau [12] generalized the notion of coherence with the introduction of a quantum mechanical wave function for the ensemble of supercarriers through the solution of a Schrodinger-type equation. The role of electron-phonon interactions in combination with the idea of an energy gap was introduced by Fröhlich [109,110], whose efforts led to the prediction of the isotope effect. From this background evolved the microscopic models, particularly that of Bardeen, Cooper, and Schrieffer [8], which have successfully explained many of the experimental mysteries associated with this remarkable phenomenon in metals.

As indicated in Figure 74, the CET theory evolves from the conventional track in most respects, but departs from the microscopic models through its assumption that only electrons in bonding states participate in superconduction. With this premise, the macroscopic molecule and two-fluid concepts follow directly, and the electron-lattice interaction is accounted for by thermally activated electron hopping that represents the conduction mechanism for normal electrons.

There are two aspects of CET that are fundamental in comparing it with the BCS theory. The first is the role of phonons, which limit the number of carriers available for superconduction through thermally activated hopping and destroy superconduction when the density of hopping electrons exceeds a limit determined by the large polaron radius and the degree of polaron dispersal. Unlike the BCS theory, however, there is no requirement for phonons to mediate the pairing of electrons in  $k$  space, and, consequently, no need for their existence as  $T \rightarrow 0$  K. In the BCS theory superconduction is destroyed by  $k$ -space pairs breaking up as a result of temperature increases that reduce the pair gap energy  $\Delta(T)$ . In the CET case pairing is in real space, resulting from local magnetic exchange between neighboring ions and is destroyed by thermally activated hopping. The second important aspect of the CET approach is the requirement for  $S = 0$  ions in a medium of long-range magnetic disorder (frustration), where the activation or pair-breaking energy  $E_{\text{hop}}$  is reduced to the low millielectron volt range. Although there is no temperature-dependent energy gap for paired electrons,  $E_{\text{hop}}$  represents a counterpart but differs in its invariance with temperature — a trap instead of a gap.

Another important parameter of this model is  $W$ , the ratio  $E_{\text{hop}}/kT_c$ . In collective electron systems (metals),  $W$  is typically 2, approximating the BCS ratio  $\Delta(0)/kT_c = 1.76$ . For polaronic materials  $W$  can be smaller, depending on the polaron range and dispersal, and it is shown how the  $T_c$  values can be higher than in a collective system. It also follows, however, that there can be a price for this  $T_c$  advantage in the form of lower critical magnetic fields and current densities as  $T \rightarrow T_c$ .

In spite of the simple exponential diffusion function employed to partition normal electrons from the total electron population, agreement between theory and experiment in several areas is remarkably good. The fits of theory to data for critical temperature as a function of carrier concentration; the

agreement between normal resistivity as a function of temperature; the variations of critical fields and current densities with temperature; the experimentally verified values for penetration depth, coherence length, and microwave surface resistance; and the prediction of the coexistence of  $T_N$  and  $T_c = 0$  that signals the simultaneous extinction of magnetic order and the onset of superconduction, offer strong evidence that the model may represent a large part of the reality involved. Of the physical parameters for which values were assigned in the calculations,  $E_{\text{hop}}$ ,  $x_p$ ,  $a$ ,  $K$ , and  $b$  fall well within the range of measurement or expectation for the perovskite crystal systems. Because there is no independent method of determining  $\beta$ , its value was chosen for best fit to the data. The values of  $\beta < 1$  (real-space pairing case) are reasonable, however, indicating that the polarons are dispersed better than in a random distribution in accord with Madelung electrostatic energy considerations.

Principal features of the CET theory are summarized as follows:

- *The critical temperature  $T_c$*  is directly dependent on the concentration of available supercarriers. In polaronic oxides, this concentration has a maximum of  $x$  that is set by the chemical composition, and the effective supercarrier concentration  $x_{\text{eff}}$  is determined by the efficiency of the covalent transfer mechanism and the degree of polaron dispersal.
- *Thermal activation of electrons into a collective continuum* is a basic process that limits the supercarrier concentration in all superconducting materials, not only mixed-valence ionic compounds, and represents the cumulative result of electron-phonon interactions. At higher temperature (or lower  $E_{\text{hop}}$ ), randomized hopping can create carriers that produce metallic resistivity behavior in the normal state, with a positive linear slope for high- $T_c$  materials above  $T \approx E_{\text{hop}}/k$ . Temperature characteristics of normal conduction, therefore, result from two competing factors: a mobility that decreases with temperature and a mobility-activated carrier population that increases with temperature.
- *The electrostatic/elastic polaron trapping energy  $E_{\text{el}}$*  is inversely dependent on the effective dielectric constant that screens the local electric fields, i.e.,  $K_{\text{eff}}^{-1}$ , through the  $\alpha$  coupling constant, which may partly explain why the  $T_c$  values of metals are lower than for oxides. Although polarizabilities are expected to increase with valence charge and ionic bond length (or with the polarizabilities of the individual ions, e.g.,  $\text{Ag}^{1+}$  with a closed  $4d$  shell is more polarizable than  $\text{K}^{1+}$  with an argon core even though they have the same radius), elements with the covalent capability required for superconduction also tend to be more polarizable. Therefore the task of raising  $T_c$  may reduce to the search for a material with lower  $K_{\text{eff}}$  that has enough covalent electrons for superconductivity.
- *The transfer integral  $b$*  of the covalent bond is a fundamental parameter for determining whether superconduction is possible. If the stabilization energy from the covalent bond ( $\sim b$ ) permits a transfer mechanism capable of overcoming the thermal activation (or pair-breaking) energy  $E_{\text{hop}}$ , the London macroscopic molecule may then form as the basis for the superconducting state, which permits spontaneous electron transfer without requiring the stimulation of lattice vibrations. Large  $b$  values not only help to optimize the value of  $x_{\text{eff}}$  but also lower the threshold polaron density  $x_p$ , which, in turn, raises the value of  $T_c$  through the approximation  $T_c \sim (E_{\text{hop}}/k) (x_{\text{eff}}/x_p)$ .



- *Long-range magnetic frustration*, antiferromagnetic in oxides or ferromagnetic in metals, is a prerequisite to superconduction because the exchange contributions to  $E_{\text{hop}}$  are large enough to negate the basic  $h > E_{\text{hop}}$  condition. The most convincing experimental evidence of this effect is the simultaneous observation of  $T_N, T_c = 0$  in the high- $T_c$  perovskites at a concentration threshold where large polarons merge to form an ordered chain of covalently linked cells.
- $S = 1/2$ ,  $S = 0$  *adjacent cation pairs*, representing the mobile molecular ion of an isolated polaron, are necessary to establish the magnetic frustration condition in mixed-valence oxides and to provide boson carriers for statistical compliance with the requirements of a superfluid state.
- *Polaron dispersal* in the perovskites (characterized by the probability-related parameter  $\beta$ ) can have a great influence on the effective number of supercarriers through a direct relationship to the  $W$  parameter. Where dispersal is less complete, as in the case of the  $\text{La}_{2-x}\text{Sr}_x\text{CuO}_4$  system, a parabolic-type of  $T_c$  versus  $x$  curve occurs with a resulting peak in  $T_c$ .
- *The occurrence of  $\text{Cu}^{3+}$  in the  $\text{Cu-O}_5$  pyramidal sites* of  $\text{YBa}_2\text{Cu}_3\text{O}_7$  may be approximated by the linear function proposed originally [1], in general accord with the results of valence bond-sum analysis [52]. Also modeled by a similar linear function,  $\text{Cu}^{1+}$  ions appear almost exclusively in the linearly coordinated sites of the nonsuperconducting  $\text{Cu-O}_2$  chains.
- *Electron pair carriers* exist in real space because of local Pauli principle requirements. Because ordered states are not generally subjects for statistical analysis, the occasion for pairing, which appears to be well established by the double electron charge effects observed in flux quantization and Josephson junction phenomena, must lie beyond simply a requirement to satisfy Bose-Einstein statistics. As summarized in Table 11, the pairing occurs between spins ( $S = 1/2$ ) of adjacent cations and as paired electrons in outer orbits, occurring naturally or as part of induced dipoles. In antiferromagnetic systems, a dynamic or spin wave ordering might be anticipated.
- *The decrease in Gibbs free energy  $\Delta G$*  results from a dynamic dipole ordering similar to a ferroelectric transition but with the energy converting to kinetic instead of thermal, thereby maintaining the adiabatic nature of the condensation. Dipole ordering satisfies the necessary and sufficient  $\nabla n_s \rightarrow 0$  condition of the London theory. In this model  $\Delta G$  derives its temperature dependence through its quadratic relation to  $n_s^c$ . Furthermore,  $\Delta G$  is not directly related to either  $E_{\text{hop}}$  or  $T_c$ , thus differing from the BCS version that depends on the gap energy  $\Delta(T)$  as indicated by Equation (G-1). Larger  $\Delta G$  from the low symmetry of high- $T_c$  cuprate lattices (see footnote 27) may account for higher  $H_c$  values and the possible enhancement of other parameters that depend on the condensation energy.

**TABLE 11**  
**Superconduction Pairing Arrangements**

Ion Mix	Bonding	Transfer Spin Arrangement	Carrier	Example
$c \neq 0$	$e_g$ - $p\sigma$ Oxide	$(--)(\uparrow-)(-\downarrow)(\uparrow-) \Rightarrow (-\downarrow)(\uparrow-)(--)(\uparrow-)$	$p$ -Type	$\text{Cu}^{2+(3+)}$
	$s$ - $p\sigma$ Oxide	$(\uparrow\downarrow)(\uparrow-)(-\downarrow)(\uparrow-) \Rightarrow (-\downarrow)(\uparrow-)(--)(\uparrow-)$	$n$ -Type	$\text{Bi}^{4+(5+)}$ $\text{Pb}^{3+(4+)}$ $\text{Cu}^{1+(2+)}$
	$t_{2g}$ - $t_{2g}$ Oxide	$(--)(\uparrow-)(-\downarrow)(\uparrow-) \Rightarrow (-\downarrow)(\uparrow-)(--)(\uparrow-)$	$p$ -Type	$\text{Ti}^{3+(4+)}$ $\text{V}^{4+(5+)}$ $\text{Nb}^{4+(5+)}$ $\text{Ta}^{4+(5+)}$
$c = 0$	$t_{2g}$ - $t_{2g}$ Oxide	$(\uparrow\downarrow)(--)(--)(--)\Rightarrow (--)(--)(--)(\uparrow\downarrow)$ $(\uparrow\downarrow)(--)(\uparrow\downarrow)(--)\Rightarrow (--)(\uparrow\downarrow)(--)(\uparrow\downarrow)$	$n$ -Type $n$ -Type	$\text{Ti}^{4+(3+)}$ $\text{Ti}^{4+(2+)}$
$c = 0$	Odd- $n$ $t_{2g}$ - $t_{2g}$ Metal	$(\uparrow\downarrow)(--)(\uparrow\downarrow)(--)\Rightarrow (--)(\uparrow\downarrow)(--)(\uparrow\downarrow)$	$n$ -Type	Nb, Ti
$c = 0$	Even- $n$ $s^2, s^2p^2$ Metal	$(\uparrow\downarrow)(\uparrow\downarrow)(\uparrow\downarrow)(\uparrow\downarrow)\Rightarrow (\uparrow\downarrow)(\uparrow\downarrow)(\uparrow\downarrow)(\uparrow\downarrow)$	$n$ -Type	Hg, Pb, Sn

- *Parameter values depend on the effective supercarrier density  $n_s^e$  (as summarized in Table 6). Among the significant results are the dependences of  $H_c$  and  $i_c$  on  $n_s^e$ , which lead to exponential tails in the  $i_c(T)/i_c(0)$  versus  $T/T_c$  curves that include an inflection point at  $T/T_c = W/2$  on the  $H_c(T)/H_c(0)$  curve. For materials with smaller  $W$  values, such as the high- $T_c$  perovskites, the critical fields and current densities are correspondingly smaller as  $T \rightarrow T_c$ ; therefore, it may be concluded that higher critical temperatures achieved with fewer carriers occur at the expense of reduced magnetic field and current carrying capabilities.*
- *The ratio  $\kappa (= \lambda_L/\xi_0)$  in perovskites is independent of  $n_s^e$  (and therefore temperature) with values  $\gg 1$  for the high- $T_c$  compounds, thus suggesting that these materials are natural type-II superconductors. As a consequence, the fluxoid lattice that exists at magnetic fields above  $H_c$  would be unstable because the domains are not pinned to impurity sites or nonsuperconducting regions. The occurrence of the smaller coherence lengths supports the proposal that carrier velocities are larger in these semiconductors because of higher local electric fields that result from lower dielectric constants, i.e.,  $v_s \sim K^{-1}$ .*
- *The periodic table may serve as a map for discerning superconductor categories. Where  $c \neq 0$ , transition cations in oxides with unfilled  $e_g$  orbitals at the upper end of the  $d^n$  series, or mixed-valence combinations of Pb and Bi in oxides may form high- $T_c$  compounds. At the low end of the  $d^n$  series, elements with unfilled  $t_{2g}$  orbitals (odd-electron case) may provide a CET mechanism by direct cation-cation transfer either in oxides or metal structures. In metals where electron pairing already exists in the atomic states ( $s^2$  or  $s^2p^2$ ), direct real-space pair covalent transfer may occur via combinations of  $s$  and  $p$  orbitals.*

In summation, all superconduction properties are controlled fundamentally by the volume density of superelectrons. The total number of conduction electrons is determined by chemical composition (including substitutions). The fractional population available for superconduction is principally a function of temperature within the limits imposed by the trap energy ( $E_{\text{hop}}$ ), imperfect polaron dispersal ( $P < 1$ ), and covalent transfer efficiency ( $\eta \leq 1$ ). Finally, the density of superelectrons actually participating in a supercurrent is controlled by the magnetic field. Based on this view, ideal superconductivity would require a small dielectric constant (to increase  $E_{\text{hop}}$ ), strong covalence between participating lattice sites ( $\eta = 1$ ), and perfect chemical and structural homogeneity ( $P = 1$ ).

Among the superconducting materials currently known, interesting contrasts exist between the high- and low- $T_c$  groups. The oxides are principally ionic with a covalent component and feature lower  $K$  constants to provide the larger  $E_{\text{hop}}$  energies necessary for the high  $T_c$  values. With their small  $x_i$  thresholds, the reduced  $W$  values that result cause an additional enhancement of  $T_c$ . Unfortunately, the density of superelectrons in these materials is limited by the multication chemical formulation and the imperfect cation ordering that further reduce the maximum current density at higher temperatures through reduced  $W$  values. On the other hand, low- $T_c$  metals and intermetallic compounds have intrinsically higher carrier densities and close to ideal chemical order but suffer from the high dielectric properties of free-electron conductors.

For metals, the problem of low  $T_c$  must be solved without reducing  $W$ , requiring reduction in polarizability without decreasing carrier density. For polaronic materials, the problem of low  $W$  must be solved without reducing  $T_c$ , requiring an increase in carrier density without increasing polarizability. In this latter case, the effective carrier density could be increased by improving polaron dispersal. The resulting increase in  $T_c$ , however, would be accompanied by an unwanted decrease in  $W$ .

## APPENDIX A

### SELF-CONSISTENT MOLECULAR-ORBITAL THEORY

In this study of charge transfer between  $\sigma$ -bonding orbitals of adjacent ions, the energy level structure and corresponding molecular orbital functions that are composed of linear combinations of the individual eigenstates may be calculated by the self-consistent (Hartree-Fock) approximation [117]. For the present purposes the analysis of the two-level model in Figure A-1 is sufficient to describe both the formation of bonding and antibonding MO states, as well as the physics of electron (or hole) exchange transfer among similar ions in a region surrounding a polaron source.

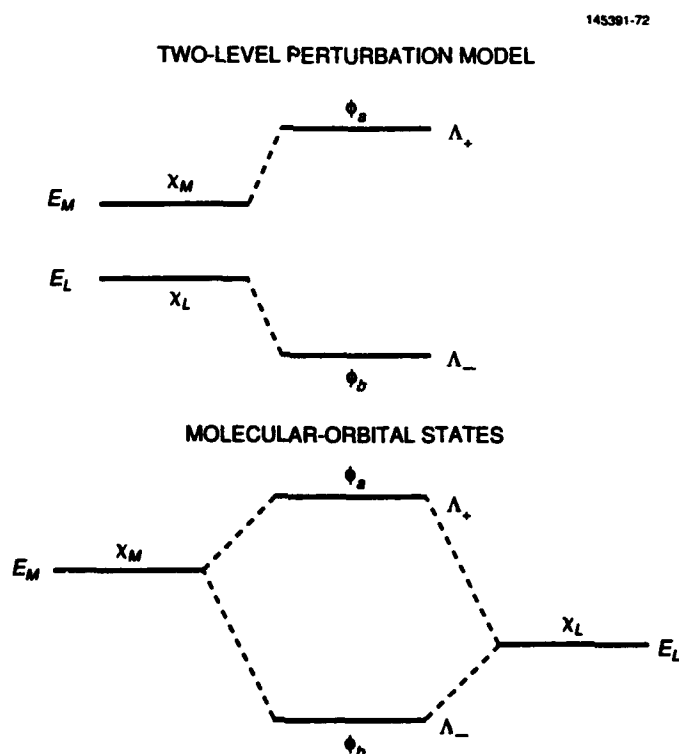


Figure A-1. Definitions of MO bonding  $\Lambda_-$  and antibonding  $\Lambda_+$  states: (a) conventional perturbation format, and (b) molecular-orbital format.

To treat this system by perturbation theory, the Hartree-Fock Hamiltonian is expressed as

$$H = H_L + H_M \quad , \quad (\text{A-1})$$

where  $H_L$  and  $H_M$  are the respective metal and ligand Coulomb energies in the lattice before applying exchange stabilization. In the usual manner, the Hermitian matrix elements  $H_{ij} = \langle \chi_i | H | \chi_j \rangle$  between the  $i$  and  $j$  unperturbed wavefunctions are formed, and the secular determinant becomes [117]

$$\begin{vmatrix} H_{11} - \Lambda & H_{12} \\ H_{21} & H_{22} - \Lambda \end{vmatrix} = \begin{vmatrix} E_L - \Lambda & B - \Lambda S \\ B - \Lambda S & E_M - \Lambda \end{vmatrix} = 0, \quad (\text{A-2})$$

where

$$\begin{aligned} B &= \langle \chi_L | H | \chi_M \rangle = (E_L + E_M)S && (\text{exchange integral}) \\ S &= \langle \chi_L | \chi_M \rangle && (\text{overlap integral}) \end{aligned} \quad (\text{A-3})$$

The eigenvalues follow as

$$\Lambda_{\pm} = \frac{(E_L + E_M)(1 - 2S^2) \pm [(E_L - E_M)^2(1 - S^2) + B^2]^{1/2}}{2(1 - S^2)}. \quad (\text{A-4})$$

The coefficients  $c_{ij}$  of the MO eigenvectors  $\phi_i = \sum_j c_{ij} \chi_j$  are thus found from the row  $\times$  column products summarized by the relation

$$\sum_j (H_{ij} - \Lambda_i \delta_{ij}) c_{ij} = 0, \quad (\text{A-5})$$

where  $\sum_j c_{ij}^2 = 1$ .

Accordingly, the determination of  $\phi_1$  and  $\phi_2$  follows from Equation (A-5):

$$(E_L - \Lambda_-) c_{11} + (B - \Lambda_- S) c_{12} = 0, \quad c_{11}^2 + c_{12}^2 = 1,$$

and

$$(B - \Lambda_+ S) c_{21} + (E_M - \Lambda_+) c_{22} = 0, \quad c_{21}^2 + c_{22}^2 = 1. \quad (\text{A-6})$$

An exact solution of Equation (A-6) yields the coefficients

$$c_{11} = \frac{-(E_L + E_M - \Lambda_-)S}{\sqrt{[(E_L + E_M - \Lambda_-)^2 S^2 + (E_L - \Lambda_-)^2]}},$$

$$\begin{aligned}
c_{12} &= \frac{E_L - \Lambda_-}{\sqrt{[(E_L + E_M - \Lambda_-)^2 S^2 + (E_L - \Lambda_-)^2]}} , \\
c_{21} &= \frac{-(E_M - \Lambda_+)}{\sqrt{[(E_L + E_M - \Lambda_+)^2 S^2 + (E_M - \Lambda_+)^2]}} , \\
c_{22} &= \frac{(E_L + E_M - \Lambda_+)S}{\sqrt{[(E_L + E_M - \Lambda_+)^2 S^2 + (E_M - \Lambda_+)^2]}} .
\end{aligned} \tag{A-7}$$

If  $S^2 \ll 1$ , the coefficients of Equation (A-7) can be put in the more useful form of

$$\begin{aligned}
c_{11} &= (1/\sqrt{2}) \left| 1 + \frac{1}{\sqrt{[1 + S^2 + Q^2(1 + 5S^2) + 2QS(1 + S^2)\sqrt{(1+Q^2)}]}} \right|^{1/2} , \\
c_{12} &= (1/\sqrt{2}) \left| 1 - \frac{1}{\sqrt{[1 + S^2 + Q^2(1 + 5S^2) + 2QS(1 + S^2)\sqrt{(1+Q^2)}]}} \right|^{1/2} , \\
c_{21} &= (1/\sqrt{2}) \left| 1 - \frac{1}{\sqrt{[1 + S^2 + Q^2(1 + 5S^2) - 2QS(1 + S^2)\sqrt{(1+Q^2)}]}} \right|^{1/2} , \\
c_{22} &= -(1/\sqrt{2}) \left| 1 + \frac{1}{\sqrt{[1 + S^2 + Q^2(1 + 5S^2) - 2QS(1 + S^2)\sqrt{(1+Q^2)}]}} \right|^{1/2} ,
\end{aligned} \tag{A-8}$$

where  $Q = B/(E_L - E_M)$ , and the minus sign before the  $2QS$  corresponds to the antibonding state defined below. As discussed in Ballhausen and Gray [117], correction factors are required to reestablish orthonormality of the eigenstates where  $S \neq 0$ :

$$C_{11} = c_{11}X, \quad C_{12} = c_{12}X; \quad C_{21} = c_{21}Y, \quad C_{22} = c_{22}Y , \tag{A-9}$$

where  $X = (c_{11}^2 + c_{12}^2 + 2c_{11}c_{12}S)^{-1/2}$ , and  $Y = (c_{21}^2 + c_{22}^2 + 2c_{21}c_{22}S)^{-1/2}$ . The normalized MO functions become

and

$$\begin{aligned}\phi_b &= C_{11} \chi_L + C_{12} \chi_M && \text{(bonding)} \\ \phi_a &= C_{21} \chi_L + C_{22} \chi_M && \text{(antibonding)}\end{aligned}\quad . \quad (\text{A-10})$$

## APPENDIX B

### THE $\text{Cu}^{2+}\text{O}^{2-}$ MOLECULE

When a charge unbalance is created by substituting a  $\text{Sr}^{2+}$  ion into the  $\text{La}^{3+}$  sublattice, a question arises immediately about the manner in which electrostatic neutrality is preserved. Because  $\text{La}_{2-x}\text{Sr}_x\text{CuO}_4$  is principally an ionic material, the hole is not excited but exists by virtue of the  $\text{Sr}^{2+}$  substitution — it is better described as a  $(\text{CuO})^+$  polaron bound to its  $\text{Sr}^{2+}$  source and transported through activated mobility. In polaron notation,  $\text{La}_{2-x}\text{Sr}_x\text{CuO}_4$  could be expressed as  $(\text{La}_{2-x}\text{Sr}_x)^{x-}(\text{CuO}_4)^{x+}$ ; therefore, analysis would logically begin with assignment of the hole to a lattice site adjacent to the  $\text{Sr}^{2+}$  source, with the simplified  $(\text{CuO})^+$  molecular ion as the polaron that moves among  $\text{CuO}$  molecular lattice in the attractive field of the negative charge represented by the  $\text{Sr}^{2+}$  acceptor [31]. This calculation begins with the derivation of the MO energy level scheme for the  $3d-2p\sigma$  states of the  $\text{CuO}$  molecule.

In the cuprate systems, the  $\text{Cu}^{2+(3+)}$  occupy tetragonal (slightly orthorhombic), pyramidal, or square-planar oxygen coordinations. To appreciate the origin of the molecular energy levels, a generic model is developed based on the point-charge crystal-field concept, as shown in Figure B-1. If the ionic character of the ligands is represented by their valence charges, the five  $d$  orbital states are split by an energy parameter  $\Delta_{cf}$  with the  $t_{2g}$  functions stabilized by  $(3/5)\Delta_{cf}$  and the  $e_g$  levels destabilized by  $(2/5)\Delta_{cf}$ . In cases where the crystal-field approximation is sufficient to describe the physical phenomena observed, e.g., optical spectroscopy, this quantity is called  $10 Dq$ . In reality, however,  $10 Dq$  also includes the splitting caused by the covalent interaction, because the ligands have an additional coupling with the cation in the form of orbital wavefunction overlaps, usually  $p$  orbitals that form  $\sigma$  bonds with the  $e_g$  states and weaker  $\pi$  bonds with the  $t_{2g}$  group. As a consequence, the  $e_g$  states are further destabilized by  $\Delta_{mo}$ , as determined by the calculation technique in Appendix A. To a first approximation, the  $\pi$ -bonded  $t_{2g}$  states are treated as unperturbed by the covalence, hence the term "nonbonding." As indicated in Figure B-1, a more correct relation for the main optical wavelength splitting is given by

$$10 Dq = \Delta_{cf} + \Delta_{mo} \quad , \quad (\text{B-1})$$

where  $\Delta_{mo}/10 Dq \approx 0.3$  based on the orbital reduction factors inferred from electron paramagnetic resonance (EPR) spectra [94].

Working MO diagrams for  $\text{Cu-O}_y$  are given in Figures 55 and 56. The basic building block is the  $\text{Cu}^{2+}\text{-O}^{2-}$  molecule, therefore calculations will focus on these two components with the relevant potential energies as depicted in the basic two-body model of Figure B-2. As noted, the lattice energy determined from the simple electrostatic attraction<sup>41</sup> (with a reduced Madelung constant  $M'$  to correct for the Born repulsion contribution shown in Figure B-3) is  $-M'q_{cu}q_{ox}e^2/r_0$ . The appropriate value for  $M' \approx 1.5$ , which is only slightly below the typical  $M$  of simple oxides [118], because  $E_{lat} = -43$  eV for  $\text{CuO}$  [118], for  $r_0 = 2$  Å in the  $\text{Cu-O}_4$  plane, and  $q_{cu} = +2$  and  $q_{ox} = -2$ .

<sup>41</sup> This approximation is being used in lieu of a more complete analysis based on the series summation of interactions over multiple groups of neighbors. Because the present exercise is intended mainly to illustrate a theoretical methodology for estimating the MO functions and the associated exchange integral  $b$  involved in the electron transfer, the analysis is limited to only the immediate ionic interactions.



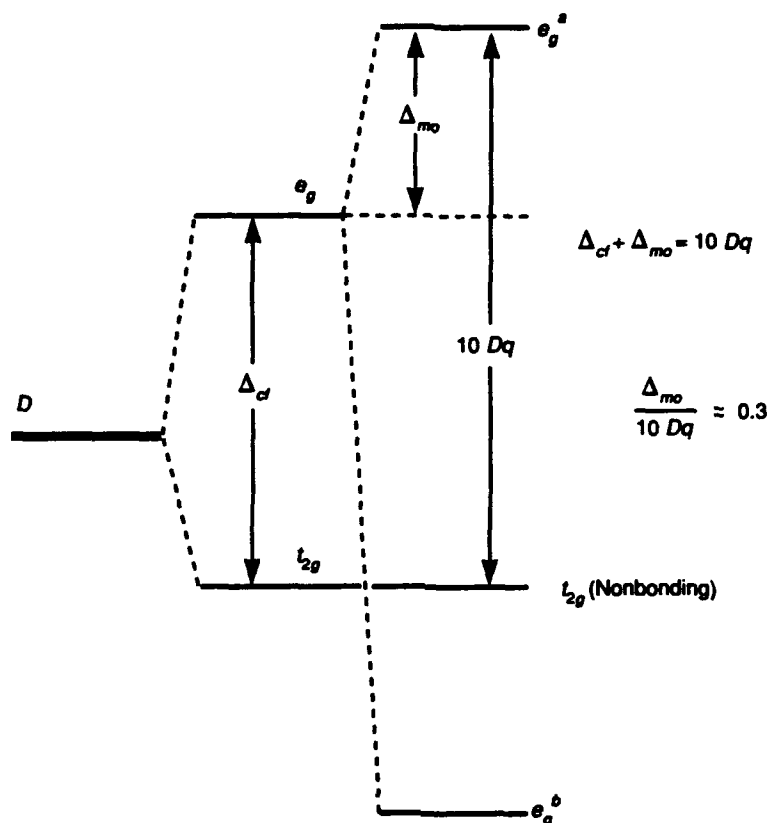


Figure B-1. Crystal field and covalent contributions to the semiempirical  $10 Dq$  splitting between  $t_{2g}$  and  $e_g^a$  bands:  $\Delta_{cf}$  arises from the basic point charge approximation; the additional  $\Delta_{mo}$  destabilization of  $e_g^a$  comes from  $e_g^-2p\sigma$  bonds. In this case, the ratio  $\Delta_{mo}/10 Dq$  is scaled to 0.3.

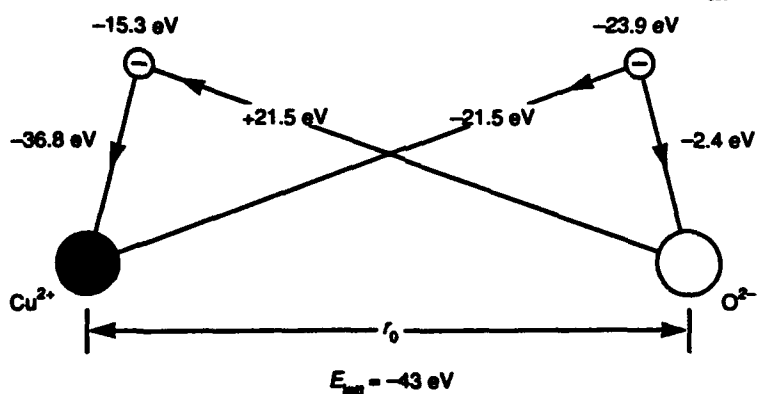


Figure B-2. CuO molecule approximation to the complete lattice energy  $E_{latt} = -43 \text{ eV}$ , using a Madelung constant  $M \approx 1.5$  to represent the effective electrostatic fields that determine the respective cation and anion energies.

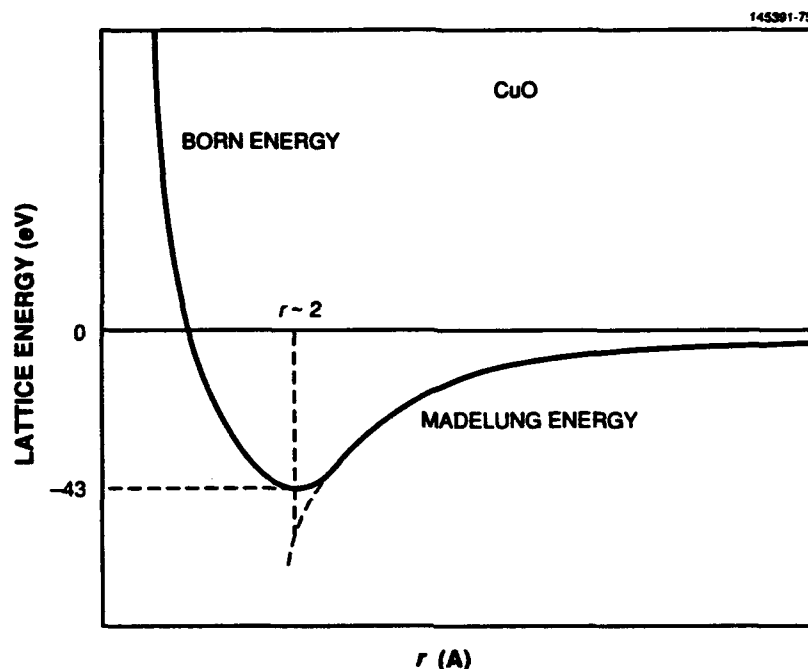
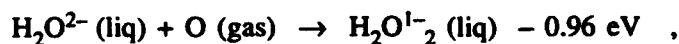


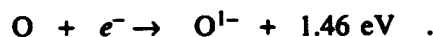
Figure B-3. Born-Mayer function for CuO, indicating corrected Coulomb attraction curve of Madelung energy to fit the  $E_{latt} \approx -43$  eV result. Correction is made by reducing  $M$  from 1.5 to 1.4.

If the Coulomb interactions within the CuO molecule are then based on this effective Madelung energy ( $-43$  eV), the stabilization energy of the outermost  $d$  electron on the  $\text{Cu}^{2+}$  ion may be taken as  $-15.3$  eV, found by combining the outermost electron stabilization energy of free  $\text{Cu}^{2+} = -36.8$  eV [118] (in this case the third ionization potential of neutral Cu) with the energy of the  $\text{O}^{2-}$  Coulomb repulsive potential energy  $M'q_{ox}e^2/r_0 = +21.5$  eV. Similarly, the stabilization energy of the outer  $2p$  electron on  $\text{O}^{2-}$  is chosen as  $E_L = -23.9$  eV, determined from the electron affinity of  $\text{O}^{1-} = 2.4$  eV,<sup>42</sup> combined with

<sup>42</sup> An estimate of the ionization potential for  $\text{O}^{2-}$  may be obtained by combining the heat of formation of hydrogen peroxide [119], with the electron affinity of the O atom, which has been well established at 1.46 eV, according to



and



Because the peroxide is formed by replacing the  $\text{O}^{2-}$  ion of the water molecule with what amounts to an  $\text{O}_2^{1-}$  ion (or a bonded pair of  $\text{O}^{1-}$  ions), still retaining the 110-deg bond angle, the repulsion energy of the two  $\text{O}^{1-}$  ions can be ignored, and the heat of formation reaction may be abbreviated as



therefore, the ionization potential  $\text{O}^{2-}$  is found to be 2.42 eV, as deduced from the subtraction of the above equations:



the stabilizing energy  $M'q_{cu}e^2/r_0 = -21.5$  eV of the attractive force between the outermost electron on the  $O^{2-}$  ion and the double positive charge on  $Cu^{2+}$ . If  $\Delta_{cf} \approx 1.25$  eV is estimated from the total  $10 Dq$ , it may be assumed that the uppermost  $d_{x^2-y^2}$  orbital is destabilized by  $\approx 0.75$  eV. The net stabilization energy of this orbital then becomes  $E_M = -14.55$  eV, and one may begin to examine the details of the energy levels in Figure B-4. With these values for the unperturbed energy parameters,  $B = (E_L + E_M)S = -38.45 S$  eV, and there remains only the assignment of a value to the overlap integral  $S$ .

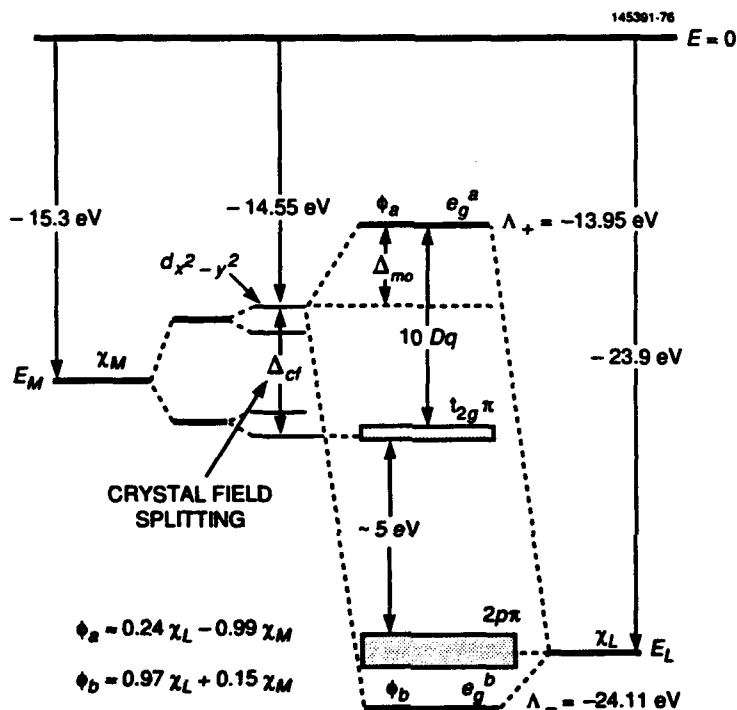


Figure B-4. Composite energy level diagram for CuO model, combining lattice energy estimates, point-charge crystal field splittings, and MO splittings.

It is probably judicious to treat  $S$  semiempirically, because  $10 Dq$  has been established by optical absorption as 1.57 eV ( $12,600 \text{ cm}^{-1}$ ) [120], and try for a reasonable fit through  $\Delta_{mo}$ . From Equation (A-4),

$$\Lambda_+ = \frac{(E_L + E_M)(1 - 2S^2) + \sqrt{[(E_L - E_M)^2(1 - S^2) + B^2]}}{2(1 - S^2)} \quad (B-2)$$

and

$$\Delta_{mo} = \Lambda_+ - E_M \quad (B-3)$$

Toward this purpose, a value of  $S = 0.10$  produced a result of  $\Delta_{mo} = 0.60$  eV, thus yielding a computed value of  $10 Dq = 1.25 + 0.60 = 1.85$  eV, approximately 18% higher than the value determined for the  $\text{Cu}(\text{H}_2\text{O})_6^{2+}$  ion. The calculated value for  $10 Dq$  appears quite reasonable, because this case places the  $\text{Cu}^{2+}$  ion in a strong tetragonal field with substantial covalence. Applying this value of  $S = 0.10$  to the foregoing analysis,

$$\begin{aligned} B &= -3.85 \text{ eV}, \\ \Lambda_+ &= -13.95 \text{ eV}, \\ \Lambda_- &= -24.11 \text{ eV}. \end{aligned} \tag{B-4}$$

A further indication of the reasonableness of these estimates may be seen from the energy separation between bonding and antibonding states,  $\Delta\Lambda = \Lambda_+ - \Lambda_- \approx 10$  eV, which is consistent with the band gap (between the bottom of the metal  $t_{2g}$  and the top of the oxygen  $2p\pi$  bands) values ( $\sim 5$  eV) for transition-metal oxides [121] after corrections for  $10 Dq$  and the widths of the upper and lower bands are taken into account. [Note that the magnitude of  $B \approx 4$  eV in Equation (B-4).]

Upon substituting the above parameter values into Equations (A-6) through (A-10), the resulting MO eigenfunctions become

$$\phi_a = 0.24 \chi_L - 0.99 \chi_M \quad (\text{antibonding})$$

and

$$\phi_b = 0.97 \chi_L + 0.15 \chi_M \quad (\text{bonding}) \quad . \tag{B-5}$$

From this result the probability of the ligand participating in the antibonding state is  $C_{21}^2 \approx 0.06$ , which means that the hole carrier in this model is, not surprisingly, greater than 90% associated with the Cu cations and that the influence of the covalence enters mainly through the destabilization of the  $e_g$  antibonding state. The delocalization of the unpaired electron, therefore, is largely within the Cu sublattice through the overlap of the  $e_g$  and  $p_x\sigma$  or  $p_y\sigma$  orbital wavefunctions. It should also be pointed out, however, that if different parameter values were assumed in the initial conditions, e.g., that the ligand  $\chi_L$  be less stable than the metal  $\chi_M$ , the MO calculation would place the hole more on the ligand sublattice.

An alternative approach to this last question is summarized in Table B-1, where the two extreme valence possibilities for  $(\text{CuO})^+$  molecular ion are compared in terms of traditional ionic bond energies:

- The hole is in the Cu sublattice (the conventional approach), according to  $(\text{LaSr})^--(\text{Cu}^{3+}\text{O}^{2-})^+$
- The hole is in the O sublattice (the peroxide scenario), according to  $(\text{LaSr})^--(\text{Cu}^{2+}\text{O}^{1-})^+$ .

Although both options may produce the  $S_p = 0$  requirement for  $T_N \rightarrow 0$ , i.e.,  $\text{Cu}^{3+}$  in a low-spin ( $d^8$ ) configuration or the individual  $\text{Cu}^{2+}$  and  $\text{O}^{1-}$  spins in an opposing alignment, these estimates also lead to the conclusion that the conventional approach is more likely because the ionic bonding stabilization energy  $E_{\text{ionic}}$  is greater by almost 30 eV. The Verwey rule that higher valence cations tend to seek out oxygen sites of highest coordination [122] is also based on Madelung energy considerations. A question

associated with the peroxide model is related to ligand-field conventions — how is the hole assigned to the anion group? Does it reside mainly on the lowest energy ligands (assuming distortions are present) or is it evenly distributed among them all?

For these reasons, the working assumption that the hole carriers are present principally in the Cu sublattice as  $\text{Cu}^{3+}$  ions will be adopted throughout this treatise. Regardless of which model is closer to reality, however, the carrier is not totally localized on either ion but treated as an entity belonging to the molecular chains that form conduits for the activationless ordered transfer called superconduction.

**TABLE B-1**  
**(CuO)<sup>+</sup> Ionic Stabilization Energies**

(CuO) <sup>+</sup> Options	$IP + EA^a$ (eV)	$E_{\text{latt}}^b$ (eV)	$E_{\text{ionic}}^c$ (eV)
$(\text{Cu}^{3+}-\text{O}^{2-})^+$	$36.8 - 3.8 = 33$	-63.8	-30.8
$(\text{Cu}^{2+}-\text{O}^{1-})^+$	$20.3 - 1.4 = 18.9$	-21.3	-2.4
<sup>a</sup> $IP$ = Cation ionization potential $EA$ = Anion electron affinity <sup>b</sup> $E_{\text{latt}} = M^* q_{\text{Cu}} q_{\text{Ox}} e^2 / a$ , where $a \sim 1.90$ Å, the CuO bond length, and $M^* \sim 1.5$ <sup>c</sup> $E_{\text{ionic}} = IP + EA + E_{\text{latt}}$			

## APPENDIX C

### THE FOUR-BODY ( $\text{Cu}^{2+}\text{O}^{2-}$ ) - ( $\text{Cu}^{2+}\text{O}^{2-}$ ) LINEAR MOLECULE

An extension of the MO model in Appendices A and B may now be applied to the superexchange case of  $\text{Cu}^{2+}\text{O}^{2-}\text{Cu}^{2+}$ . Because the carrier would, of necessity, occupy the highest energy  $d_{x^2-y^2}$  orbital in a  $d^9$  tetragonal complex, the approximations that follow focus on this state. As shown in the abbreviated MO diagram of Figure B-4, the antibonding state ( $\phi_a = 0.24 \chi_L - 0.99 \chi_M$ ) becomes the transfer orbital and represents the starting point for the calculation. For the three-body problem, the usual approach is to set up a  $3 \times 3$  matrix for  $\chi_M$ ,  $\chi_L$ , and  $\chi_M'$ , where  $\chi_M'$  represents the second  $\text{Cu}^{2+}$  ion, and redo the analysis in Appendix A. Apart from the obvious complexity introduced by the cubic equation of the secular determinant, there is also the difficulty that the  $\chi_M$  and  $\chi_M'$  states are at different polaron Coulomb energies and that this energy difference must be featured in the result. In reality, the second  $\text{CuO}$  molecule is an approximation to the  $(\text{CuO})^+$  ion raised to a higher energy ( $E_M' - E_M$ ) as a result of the field from the  $(\text{LaSr})^-$  polaron sources (see Figure 3).

To accommodate these objectives the results of the self-consistent MO calculations in Appendices A and B are presumed upon, and instead a four-body linear chain consisting of two consecutive  $\text{CuO}$  molecules is considered (see Figure C-1). With this approach, a resulting  $4 \times 4$  matrix includes bonding and antibonding states of both molecules with starting functions  $\phi_a$ ,  $\phi_a'$ ,  $\phi_b$ , and  $\phi_b'$  and matrix elements  $H_{ij} = \langle \phi_i | H | \phi_j \rangle$  reading as

	$\phi_a$	$\phi_a'$	$\phi_b$	$\phi_b'$
$\phi_a$	$\Lambda_+ - \lambda$	$b_a - \lambda s_a$	0	0
$\phi_a'$	$b_a - \lambda s_a$	$\Lambda_+' - \lambda$	0	0
$\phi_b$	0	0	$\Lambda_- - \lambda$	$b_b - \lambda s_b$
$\phi_b'$	0	0	$b_b - \lambda s_b$	$\Lambda_-' - \lambda$

(C-1)

where<sup>43</sup>

$$\begin{aligned}
 s_a &= \langle \phi_a | \phi_a' \rangle \\
 &= C_{21}C_{21}'\langle \chi_L | \chi_L' \rangle - C_{21}C_{22}'\langle \chi_L | \chi_M' \rangle - C_{22}C_{21}'\langle \chi_M | \chi_L' \rangle + C_{22}C_{22}'\langle \chi_M | \chi_M' \rangle, \\
 s_b &= \langle \phi_b | \phi_b' \rangle \\
 &= C_{11}C_{11}'\langle \chi_L | \chi_L' \rangle + C_{11}C_{12}'\langle \chi_L | \chi_M' \rangle + C_{12}C_{11}'\langle \chi_M | \chi_L' \rangle + C_{12}C_{12}'\langle \chi_M | \chi_M' \rangle, \\
 b_a &= \langle \phi_a | H | \phi_a' \rangle = (\Lambda_+ + \Lambda_+' )s_a,
 \end{aligned}$$

and

$$b_b = \langle \phi_b | H | \phi_b' \rangle = (\Lambda_- + \Lambda_-' )s_b. \quad (C-2)$$

<sup>43</sup> The usual nondegenerate approach for estimating transfer integrals results in a product  $[b_{ML}][b_{LM}]$ , which leads to a squaring of the direct metal-ligand transfer integral. In terms of the nomenclature used here,  $b \sim B^2$  (see, for example, Goodenough, *Magnetism and the Chemical Bond*, pp. 165-185).

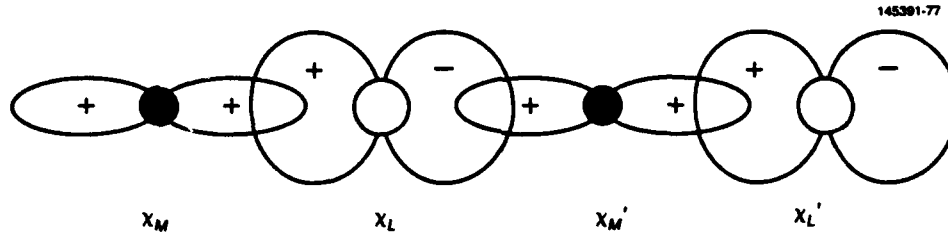


Figure C-1. CuO-CuO two-molecule chain.

The above determinant conveniently breaks up into a pair of  $2 \times 2$  matrices that directly follow the solution outlined in Appendix A. Only the solutions of the antibonding matrix (where it is assumed that the carrier resides) is the concern because the two resulting quadratic equations represent the perturbations of the original antibonding and bonding states, respectively.

$$\lambda_{\pm} = \frac{(\Lambda_+ + \Lambda_+')(1-2s_a^2) \pm [(\Lambda_+ - \Lambda_+')^2(1-s_a^2) + b_a^2]^{1/2}}{2(1-s_a^2)} \quad (C-3)$$

After substituting  $\lambda_{\pm}$  back into the secular equation, the corresponding eigenfunctions of the perturbation become

$$\begin{aligned} \psi_- &= X_a (k_{11} \phi_a + k_{12} \phi_a') \\ \psi_+ &= Y_a (k_{21} \phi_a + k_{22} \phi_a') \end{aligned} \quad (C-4)$$

where the  $k_{ij}$  weighting coefficients are similar in structure to Equation (A-8),

$$\begin{aligned} k_{11} &= (1/\sqrt{2}) \left| 1 + \frac{1}{\sqrt{[1 + s_a^2 + G_{12}^2(1 + 5s_a^2) + 2G_{12}s_a(1 + s_a^2)]\sqrt{(1+G_{12}^2)}}} \right|^{1/2}, \\ k_{12} &= (1/\sqrt{2}) \left| 1 - \frac{1}{\sqrt{[1 + s_a^2 + G_{12}^2(1 + 5s_a^2) + 2G_{12}s_a(1 + s_a^2)]\sqrt{(1+G_{12}^2)}}} \right|^{1/2}, \\ k_{21} &= (1/\sqrt{2}) \left| 1 - \frac{1}{\sqrt{[1 + s_a^2 + G_{12}^2(1 + 5s_a^2) - 2G_{12}s_a(1 + s_a^2)]\sqrt{(1+G_{12}^2)}}} \right|^{1/2}, \\ k_{22} &= -(1/\sqrt{2}) \left| 1 + \frac{1}{\sqrt{[1 + s_a^2 + G_{12}^2(1 + 5s_a^2) - 2G_{12}s_a(1 + s_a^2)]\sqrt{(1+G_{12}^2)}}} \right|^{1/2}. \end{aligned} \quad (C-6)$$

The normalization constants follow as  $X_a = (1 + 2k_{11}k_{12}s_a)^{-1/2}$ ,  $Y_a = (1 + 2k_{21}k_{22}s_a)^{-1/2}$ , and  $G_{12} = b_a/\Delta E_{12} + s_a$  with the polaron Coulomb energy  $\Delta E_{12} = E_M' - E_M \approx \Lambda_+' - \Lambda_+$ . Because  $s_a \ll 1$ , it may be assumed that  $G_{12} \approx b_a/\Delta E_{12}$ . Upon inspecting Figure C-1, Equation (C-2) for the magnitude of the orbital overlap parameter of the antibonding states reduces to  $s_a = C_{21}C_{22}' \langle \chi_L | \chi_M' \rangle \approx 0.24 \times 0.99$   $S = 0.024$ , for  $S = 0.1$ .

For  $\Lambda_+' + \Lambda_+ \approx -28$  eV, Equation (C-2) then yields  $b_a \approx -0.67$  eV, which has a magnitude about 50% greater than the 0.43 eV value determined from the Néel temperature of CuO that was used in the various covalent transfer computations throughout this report. This discrepancy should be considered surprisingly small when the assumptions implicit in this one-dimensional approximation are taken into account.

If it is now assumed that  $Q^2 \gg 1$ , with  $s_a \ll 1$ , the coefficients of the lower energy parts of Equation (C-6) reduce to

$$k_{11} = (1/\sqrt{2}) \left| 1 + \frac{1}{\sqrt{(1 + G_{12}^2)}} \right|^{1/2}, \quad (C-7)$$

$$k_{12} = (1/\sqrt{2}) \left| 1 - \frac{1}{\sqrt{(1 + G_{12}^2)}} \right|^{1/2}. \quad (C-8)$$

The normalization factors  $A$  and  $B$  also simplify through

$$2k_{11}k_{12}s_a \approx \left| 1 - \frac{1}{(1 + G_{12}^2)} \right|^{1/2} s_a = G_{12}s_a/\sqrt{(1 + G_{12}^2)} \approx s_a, \quad (C-9)$$

for  $G_{12}^2 \gg 1$ . (Note that although  $G_{12}$  is defined as the negative ratio  $b_a/\Delta E_{12}$ , with  $b_a < 0$  and  $\Delta E_{12} > 0$ , in these relations it emerges from under a square-root sign, for which the positive solution has always been chosen to fit the physical meaning.) It follows, therefore, that  $Y \approx X \approx 1 + s_a \approx 1$ .

The MO functions of Equation (C-4) may be expressed in terms of the basic four initial wavefunctions, by substituting Equation (B-5) according to

$$\begin{aligned} \psi_- &= 0.24 (k_{11}\chi_L + k_{12}\chi_L') - 0.99 (k_{11}\chi_M + k_{12}\chi_M') \\ \psi_+ &\approx 0.97 (k_{21}\chi_L - k_{22}\chi_L') + 0.15 (k_{21}\chi_M - k_{22}\chi_M') \end{aligned} \quad (C-10)$$

If the lower energy solution is chosen as the CET function, the relative participation of  $\chi_M$  and  $\chi_M'$  in the four-body MO function  $\psi_-$  is dependent on the respective magnitudes of  $k_{11}$  and  $k_{12}$ .

In Dionne [1], a transfer efficiency  $\eta$  was introduced but assumed to be unity. This approximation may now be refined by relating the transfer efficiency to the probability of a carrier occupying the  $\chi_M'$  state of a metal ion involved in the covalent transfer. The transfer efficiency between sites  $M$  and  $M'$  is defined  $\eta_{12} < 1$ , because the occupation probability of  $\chi_M'$  is  $k_{12}^2$ . In effect,  $\eta_{12}$  accounts for the



reduction from the mean carrier density (equivalent to the case of uniform density, where  $\hbar \gg E_{\text{hop}}$ ) between these two sites. For two adjacent sites, this ideal situation produces a maximum value of  $k_{12}^2 = 0.5$ , and the corresponding transfer efficiency then becomes

$$\eta_{12} = k_{12}^2/0.5 \approx 1 - 1/G_{12} \quad . \quad (\text{C-11})$$

## APPENDIX D

### OXYGEN-COORDINATION INFLUENCE ON $E_{\text{hop}}$

In Section 3.2 the origin of the electrostatic/elastic (nonmagnetic) contribution to the activation energy was described in terms of the polaron trap energy  $E_{\text{el}} \sim (\alpha/2)h\nu_D$ , where the coupling constant  $\alpha$  is related to the static and optical dielectric constants and tends to be smaller for covalent materials. Some type of isotope effect might be expected if this elastic trapping energy were the only contribution to  $E_{\text{hop}}$  because the Debye frequency  $\nu_D$  is dependent on  $M^{-1/2}$ . As pointed out in Section 8.5, the isotope effect has been largely absent in the high- $T_c$  cuprate compositions, particularly where  $T_c$  approaches or exceeds 100 K. In addition, the values of  $E_{\text{hop}}$  determined by theoretical fits to  $T_c$  data for the compounds listed in Table 7 indicate not only a direct relation to  $T_c$ , but also an apparent dependence on the oxygen coordinations at the Cu sites of the particular lattices, i.e., 2.5 meV for  $O_6$ , 4 meV for  $O_5$ , and probably  $> 4$  meV for  $O_4$ . This result logically raises the possibility of an oxygen-coordination influence on  $E_{\text{el}}$  through an enhancement of either  $\alpha$  or  $\nu_D$  by altering the dielectric constants or the normal vibronic modes.

Another and less obvious consideration, however, could be the presence of a third  $E_{\text{hop}}$  component in the form of a crystal-field stabilization energy difference  $E_{\text{cf}}$  between the  $\text{Cu}^{2+}$  and  $\text{Cu}^{3+}$  ions. From standard crystal-field considerations, the stabilization energy of transition-metal ions in octahedral-based sites increases with the valence charge of the cation, and also with the difference between the relative electron populations of the  $t_{2g}$  and  $e_g$  orbital states. Based on these factors,  $\text{Cu}^{3+}$  ( $d^8$ ) would have greater crystal-field stability than  $\text{Cu}^{2+}$  ( $d^9$ ). Consequently, if the net crystal-field stabilizations of the  $\text{Cu}^{3+}$  ions relative to the  $\text{Cu}^{2+}$  ions in undistorted octahedral sites are sufficient to tend to offset the Madelung destabilization caused by the creation of the  $(\text{LaSr})^--(\text{Cu}^{3+}\text{O}^{2-})^+$  polarons, the effect of crystal-field distortions may be discussed in terms of the model shown in Figure D-1.

With  $O_h$  symmetry, the orbital states are separated by the semiempirical energy parameter  $10 Dq$  into a lower triplet  $t_{2g}$  consisting of  $d_{xy}$ ,  $d_{xz}$ , and  $d_{yz}$ , and an upper doublet  $e_g$  containing  $d_{x^2-y^2}$  and  $d_{z^2}$ . As the crystal field distorts along the  $c$  axis ( $z$  direction),  $d_{x^2-y^2}$  and  $d_{xy}$  would be unaffected to first order, but the remaining orbitals with  $z$ -directed lobe components would be stabilized accordingly in proportion to the increase in tetragonal component, with  $d_{z^2}$  eventually becoming the ground state as the symmetry descends to square-planar with an  $O_4$  coordination. For the problem at hand, the  $t_{2g}$  group is fully occupied, with the  $\text{Cu}^{3+}$  low-spin stabilization  $\Delta$  occurring initially in the  $d_{z^2}$  orbital for moderate  $D_{4h}$  symmetry; for the pyramidal  $C_{4v}$  case, the stabilization increases further and finally reaches a limit of  $\Delta = 10 Dq$  after the crossover of the  $d_{z^2}$  and  $d_{xy}$  levels on the way to a square planar  $C_{2h}$  symmetry.

As the splitting  $\Delta$  increases beyond the point where low-spin stabilization is favored ( $\sim 0.2$  eV), i.e., where  $\Delta$  exceeds the Hund rule spin polarization energy  $E_{\text{Hund}}$ ,  $\text{Cu}^{3+}$  stabilization may result in a small  $E_{\text{cf}}$  component to  $E_{\text{hop}}$  that increases monotonically with  $\Delta$ , according to

$$\begin{aligned} E_{\text{hop}} &= E_{\text{el}} + E_{\text{cf}} , \\ &= (\alpha/2)h\nu_D + [(n_{3+}\Delta_{3+} - n_{2+}\Delta_{2+})R - E_{\text{Hund}}] , \end{aligned} \quad (\text{D-1})$$

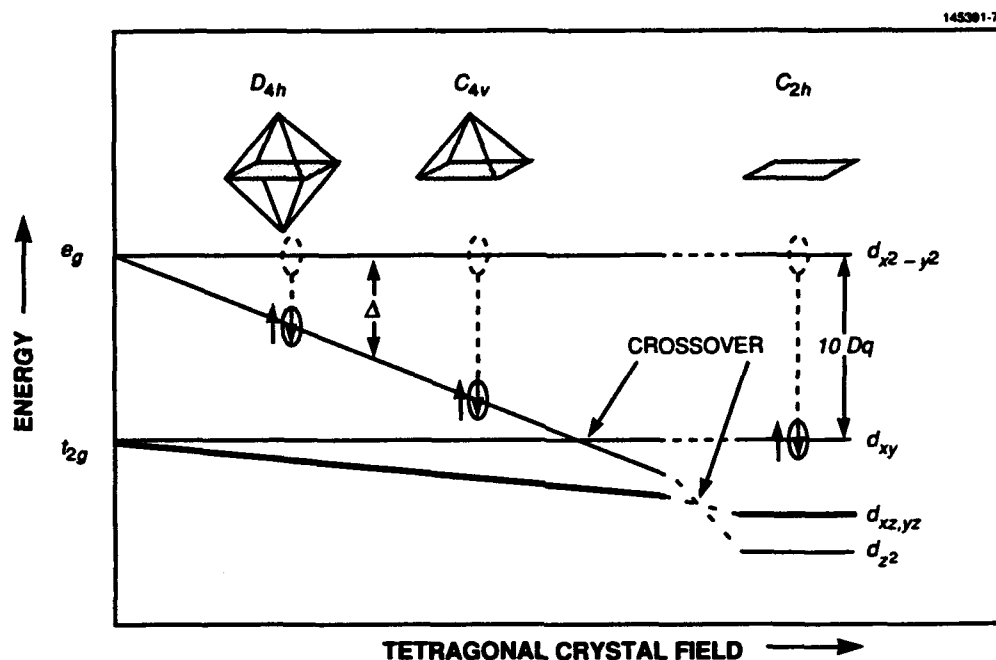


Figure D-1. Growth of  $e_g$  doublet splitting as the tetragonal crystal field component increases through  $D_{4h} \rightarrow C_{4v} \rightarrow C_{2h}$  to provide stabilization for the  $d^8$  low-spin state.

where  $\Delta_{3+}$  and  $\Delta_{2+}$  are the respective tetragonal splitting energies for  $\text{Cu}^{3+}$  and  $\text{Cu}^{2+}$ ;  $n_{3+}$  and  $n_{2+}$  are the corresponding numbers of net stabilized  $d$  electrons; and  $R$  ( $< 1$ ) is a semiempirical reduction factor that accounts for the lattice compensation adjustments to soften the effect of this crystal-field energy imbalance between the  $\text{Cu}^{3+}$  and  $\text{Cu}^{2+}$  ions. For the present case,  $\Delta_{3+}/\Delta_{2+} \approx 3/2$ ,  $n_{3+} = 2$  (low-spin case),  $n_{2+} = 1$ , so that Equation (D-1) may be simplified to

$$E_{\text{hop}} = (\alpha/2)h\nu_D + [2\Delta_{2+}R - E_{\text{Hund}}] \quad (\text{D-2})$$

$R$  must be considerably smaller than unity for  $E_{\text{cf}}$  to fall in this range because  $E_{\text{hop}}$  for the magnetically frustrated case is on the order of a few millielectron volts.

A final comment on the stabilization of the low-spin state concerns the occurrence of a lattice distortion that accompanies the reduction in ionic radius as the spin pairing takes place. In the Cu perovskites, a descent from tetragonal to orthorhombic symmetry has been reported in compounds that reach a polaron density sufficient to support a superconduction state. Although this small crystallographic phase change may be assigned to other causes, such as static Jahn-Teller effects, it is not unreasonable to consider that a Cu condensation from high spin ( $S = 1$ ) to low spin ( $S = 0$ ) may be the actual source.

## APPENDIX E

### EFFECTIVE AREA OF MAGNETIC FIELD AND SUPERCURRENT

For a superconductor of rectangular dimensions  $d_1$  and  $d_2$  as shown in Figure E-1, an area of magnetic field and current penetration may be calculated by integrating  $\exp(-x/\lambda_L)$  and  $\exp(-y/\lambda_L)$  distribution functions independently for the  $x$  and  $y$  directions, respectively:

$$\begin{aligned} d_2 d_1' &= 2d_2 \int_0^{d_1/2} \exp(-x/\lambda_L) dx = 2\lambda_L d_2 \left[ 1 - \exp(-d_1/2\lambda_L) \right] , \\ d_1 d_2' &= 2d_1 \int_0^{d_2/2} \exp(-y/\lambda_L) dy = 2\lambda_L d_1 \left[ 1 - \exp(-d_2/2\lambda_L) \right] . \end{aligned} \quad (\text{E-1})$$

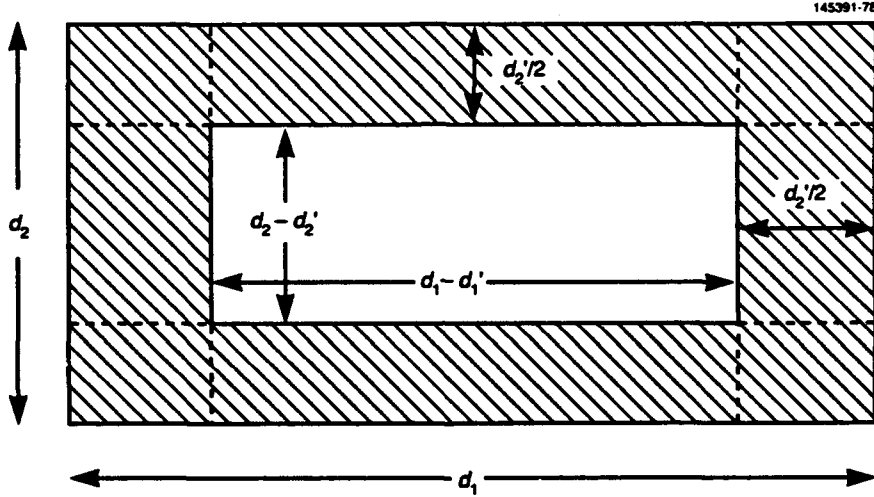


Figure E-1. Effective flux penetration regions for a rectangular cross-section model.

An interior area that is void of current may be defined as  $(d_1 - d_1')(d_2 - d_2')$  because  $d_1'$  and  $d_2'$  are equivalent to penetration depths of a square (rather than exponential) function. As a consequence, the effective area of penetration becomes

$$\begin{aligned} A_{\text{eff}} &= d_1 d_2 - (d_1 - d_1')(d_2 - d_2') , \\ &= 2\lambda_L [d_1(1 - \exp(-d_2/2\lambda_L)) + d_2(1 - \exp(-d_1/2\lambda_L)) \\ &\quad - 2\lambda_L(1 - \exp(-d_1/2\lambda_L))(1 - \exp(-d_2/2\lambda_L))] . \end{aligned} \quad (\text{E-2})$$

It is important to recognize two points related to Equation (E-2). First, depending on the relative magnitudes of  $\lambda_L$  and  $d_1, d_2$ , the value of  $i_c$  determined from experiment by dividing the measured total current by the nominal area is an apparent value that is smaller than the true current density. Second, because the  $i_c$  error is greatest at  $T = 0$  K, where  $\lambda_L$  is a minimum, an uncorrected curve of  $i_c(T)/i_c(0)$

versus  $T$  will track higher than the true curve, with the greatest error in the regime where  $T \rightarrow T_c$ . It is also important to remember that by definition  $i_c$  is the maximum value of current density at the surface, according to Equation (2).

Three limiting approximations to Equation (E-2) are worth deriving:

1.  $d_1, d_2 \gg 2\lambda_L$  (bulk specimen case),

$$A_{\text{eff}} \approx 2\lambda_L(d_1 + d_2 - 2\lambda_L) \approx 2\lambda_L(d_1 + d_2) \quad , \quad (\text{E-3})$$

and

$$A_{\text{eff}}/A \approx 2\lambda_L(1/d_1 + 1/d_2) \quad , \quad (\text{E-4})$$

and also

$$1 - A_{\text{eff}}/A \approx 1 - 2\lambda_L(1/d_1 + 1/d_2) \quad . \quad (\text{E-5})$$

2.  $d_1, d_2 \leq 2\lambda_L$  (~ fine wire case), with exponential series truncated after the second-order terms,

$$\begin{aligned} A_{\text{eff}} &\approx 2\lambda_L[d_1(d_2/2\lambda_L - (1/2)d_2^2/4\lambda_L^2) + d_2(d_1/2\lambda_L - (1/2)d_1^2/4\lambda_L^2) \\ &\quad - 2\lambda_L(d_2/2\lambda_L - (1/2)d_2^2/4\lambda_L^2)(d_1/2\lambda_L - (1/2)d_1^2/4\lambda_L^2)] \quad , \\ &\approx d_1d_2 - (1/4) d_1^2d_2^2/4\lambda_L^2 \quad , \end{aligned} \quad (\text{E-6})$$

and

$$A_{\text{eff}}/A \approx 1 - (1/4) d_1d_2/4\lambda_L^2 \quad , \quad (\text{E-7})$$

and also

$$1 - A_{\text{eff}}/A \approx (1/4) d_1d_2/4\lambda_L^2 \quad . \quad (\text{E-8})$$

3.  $d_1 \leq 2\lambda_L, d_2 \gg 2\lambda_L$  (thin-film case),

$$\begin{aligned} A_{\text{eff}} &\approx 2\lambda_L[d_1 + d_2(d_1/2\lambda_L - (1/2)d_1^2/4\lambda_L^2) \\ &\quad - 2\lambda_L(d_1/2\lambda_L - (1/2)d_1^2/4\lambda_L^2)] \quad , \\ &\approx d_1d_2 - d_1^2d_2/8\lambda_L + d_1/2d_2 \quad , \end{aligned} \quad (\text{E-9})$$

and

$$A_{\text{eff}}/A \approx 1 - d_1/8\lambda_L \quad , \quad (\text{E-10})$$

and also

$$1 - A_{\text{eff}}/A \approx d_1/8\lambda_L \quad . \quad (\text{E-11})$$

## APPENDIX F

### THE LOW-SPIN STATES OF Ni CATIONS

As listed in Table 5, the  $d^8 \rightarrow d^7$  pair can provide the  $S = 0, 1/2$  combination required for covalent transfer if both ions are in a low-spin configuration. Such a possibility may be a reality under conditions created by the tetragonal/orthorhombic crystal-field environments of the  $O_6$ -coordinated  $Ni^{3+(2+)}$  ions in  $La^{3+}_{2-x}Sr^{2+}_x(Ni^{2+}_{1-x}Ni^{3+}_x)O_4$ . In some measurements of diamagnetism [37], indications of superconduction transition were reported at temperatures as high as 70 K in carefully prepared single crystals.

Before the earlier analysis [55] of this system is described, it is important to review previous work with the Li-diluted monoxide NiO, i.e.,  $Li^{1+}_xNi^{2+}_{1-2x}Ni^{3+}_xO$ . In the work of Goodenough et al. [36], ferrimagnetic behavior was observed for values of  $x \leq 0.3$ , resulting at least in part from the  $Ni^{3+}$  ions in low-spin ( $S = 1/2$ ) states. In addition to reducing the magnetic moment of the polaron, a low-spin  $d^7$  in an  $O_6$  coordination introduces two important features:

- It sets up the possibility of orbital transfer through  $\sigma$ -bonding orbitals by leaving only one electron in the  $e_g$  levels.
- It creates a static Jahn-Teller effect in an octahedral site, similar to  $Cu^{2+} (d^9)$ .

Because the  $d^8$  occupation can also violate Hund's rule in a planar or strongly tetragonal symmetry, the implications of the cooperative Jahn-Teller effect from  $Ni^{3+}$  ions becomes apparent where an enhanced tetragonal distortion is large enough to force the low-spin  $d^8$  configuration similar to  $Cu^{3+}$ . In this case, however, the cubic crystal-field splitting parameter  $Dq$  of  $Ni^{2+}$  is proportionately smaller than that of  $Cu^{3+}$  and would, therefore, require a larger elastic distortion to split sufficiently the two  $e_g$  states, as shown in Figure F-1. Nonetheless, the scenario of dual low-spin configurations in the  $Ni^{3+(2+)}$  transfer pair remains a distinct possibility.

For the orbital occupancy indicated in Figure 62, the lower  $d_{z^2}$  level would be filled for  $d^8$  ( $S = 0$ ) and half-filled for  $d^7$  ( $S = 1/2$ ). Unlike the  $Cu^{2+(1+)}$  or  $Cu^{2+(3+)}$  cases, the  $d_{x^2-y^2}$  orbital is not occupied; the  $d_{z^2}$  orbital, however, does interact covalently with the  $p_x\sigma$  and  $p_y\sigma$  ligand orbitals (with a transfer integral  $b$  estimated as 1/3 that of the  $d_{x^2-y^2}$  orbital case in the  $x$  or  $y$  directions, resulting from the donut ring waist of the orbital [26]) and could supply the covalent stabilization necessary for superconduction transfer. The transfer integral along the  $z$  direction would be 4/3 that of the  $d_{x^2-y^2}$  orbital in the  $x$  or  $y$  directions, but could not play a role in the tetragonal perovskite lattice because there are no Ni-O-Ni linkages along the  $c$  axis. Further indication that  $b$  is smaller may be inferred from the fact that condensation effects were not seen until  $x \geq 0.2$ , meaning that  $x_c$  would be about five times greater than that of the Cu case.

In Figure F-2, the data of Springthorpe et al. [28] are presented to illustrate the possible presence of low-spin  $Ni^{2+}$  in the  $Li^{1+}_xNi^{2+}_{1-2x}Ni^{3+}_xO$ . As explained in Section 3,  $S = 0$  ions would be detected by a decrease in the activation energy  $E_{hop}$ , caused by the breakdown of exchange ordering as reflected in Equations (16) and (17). If it is assumed that all the  $Ni^{2+}$  is high spin ( $S = 1$ ) at higher temperatures, where only dynamic Jahn-Teller activity cause localized vibronic lattice perturbations and that a gradual

transition to low-spin  $\text{Ni}^{2+}$  occurs as those effects become static and cooperative, a temperature-dependent two-phase resistivity model employing a Boltzmann exponential function may be constructed according to

$$\rho = 1/\sigma = [Ne(\mu)]^{-1} = \{Ne[f\mu_{hs} + (1-f)\mu_{ls}]\}^{-1}$$

or

$$\rho = C(kT)\{(1-x)/x\}[f \exp(-E_{\text{hop}}^{hs}/kT) + (1-f)\exp(-E_{\text{hop}}^{ls}/kT)]\}^{-1}, \quad (\text{F-1})$$

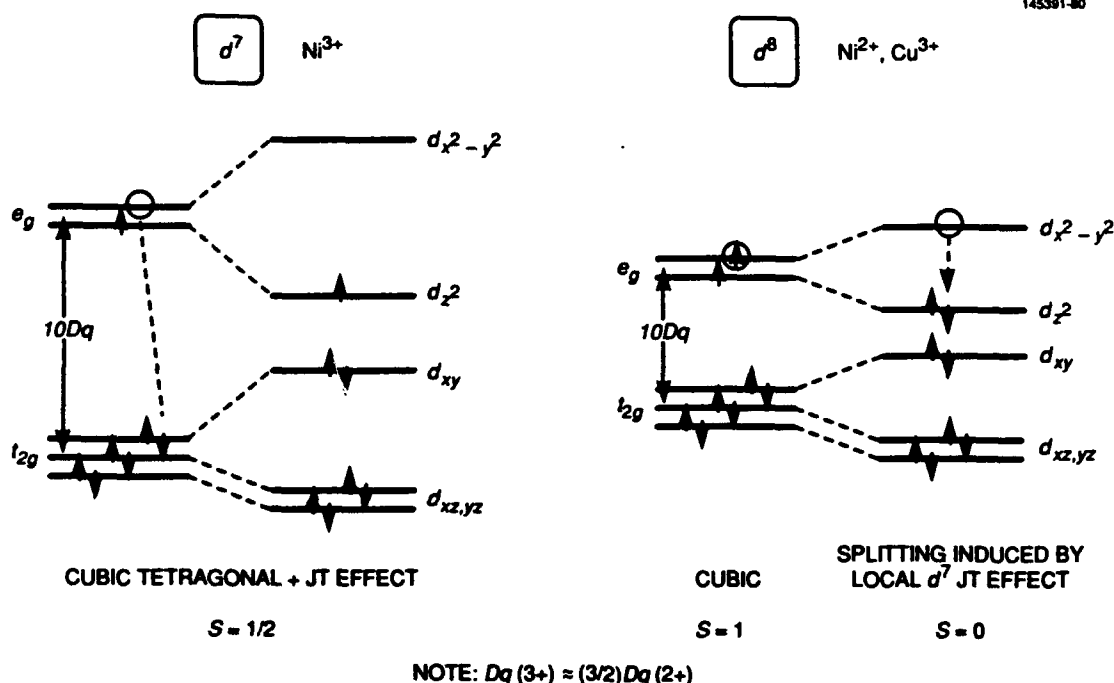


Figure F-1. Ground state crystal-field orbital occupancy diagrams for  $d^7$  and  $d^8$  spin states.

with  $N = x/V$ . The cell volume  $V = a^3$  and the diffusion length  $d$  is approximated by the distance of the double jump ( $2a$  for the linear chain case) required to preserve antiparallel spin alignments, so that  $C$  reduces to  $a/4e^2v_{\text{hop}}$ . The respective high- and low-spin mobilities are  $\mu_{hs}$  and  $\mu_{ls}$ ,  $E_{\text{hop}}^{hs}$  and  $E_{\text{hop}}^{ls}$  the corresponding activation energies, and the probability of high-spin occupancy is expressed semiempirically by  $f = \exp(-\epsilon/kT)$ , with  $\epsilon$  representing an activation energy parameter that determines the partition between the two spin states.

To test this model, computed curves are fitted to the measured data of Figure F-2, with  $a = 4 \text{ \AA}$ ,  $v_{\text{hop}} = 5.2 \times 10^{12} \text{ s}^{-1}$ , and  $E_{\text{hop}}^{ls} = 0.009 \text{ eV}$ . Although the partition function  $f$  is largely empirical, it does represent the physical tendency for the  $S = 0$  state to occur. As a result, it is not surprising that the parameter  $\epsilon$  is seen to increase with polaron concentration according to the relation  $\epsilon = (4 \times 10^{-17}) \exp(56\sqrt{x}) \text{ eV}$ . At higher temperatures, the decrease in  $E_{\text{hop}}^{hs}$  from 0.28 to 0.16 eV as  $x$  increases from

0.002 to 0.032 may be fitted mathematically with the function  $E_{\text{hop}}^{\text{hs}} \approx 0.33\exp(4\sqrt{x})$ . The sharper knee of the theoretical curve reflects the idealization of the  $\langle\mu\rangle$  approximation in Equation (F-1). For the high-temperature regime, spin canting from  $\text{Li}^{1+}$ -induced exchange isolation [29] could explain the activation energy decrease. Physical interpretation of the low-temperature effects, however, requires examination of the Ni cation magnetic states.

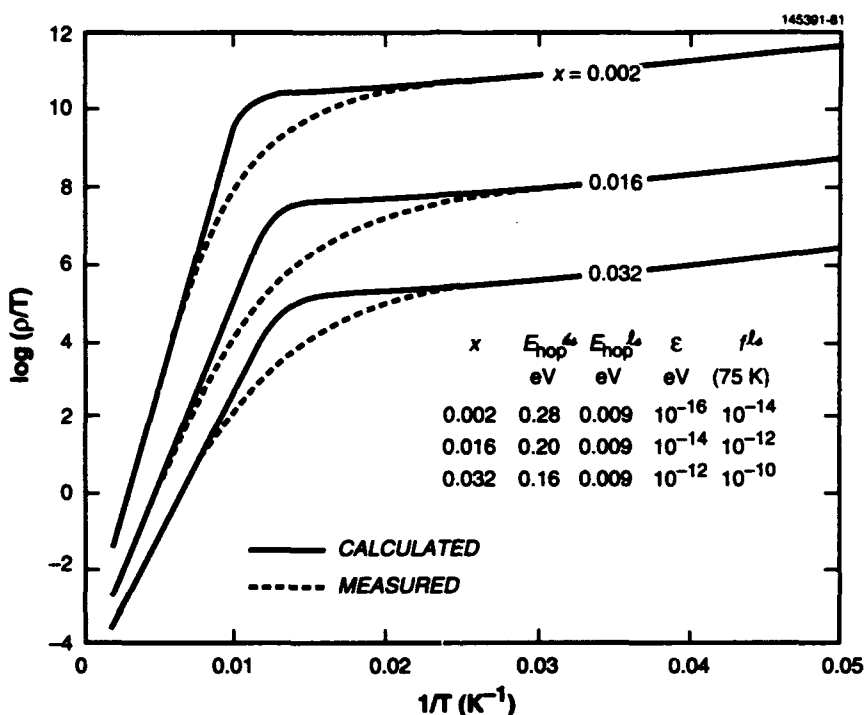


Figure F-2. Empirical fit of theory to data of Springthorpe et al. [28], indicating dual activation energies of  $\text{Li}_x\text{Ni}_{1-x}\text{O}$  system.

In the basically cubic NiO system, the occurrence of a tetragonal distortion large enough to create low-spin  $d^8$  ions is entirely dependent on the Jahn-Teller effect of the neighboring  $\text{Ni}^{3+}$  ions. For this reason the fraction of  $S = 0$  ions is expected to be very small and to cluster about the isolated  $d^7$  polarons of  $S = 1/2$  [see Figure F-3(a)]. In the configuration shown in Figure F-3(b), the  $\text{Ni}^{3+}$  polaron is "exchange isolated" by the zero-spin neighbors in a manner similar to that of  $\text{Co}^{2+}$  in  $\text{Ti}^{4+}$ -diluted  $\text{LiFe}_5\text{O}_8$  [29] and would transfer as a cluster that moves in double steps to preserve the integrity of the magnetic sublattices, as explained in Section 3. In the tetragonal perovskite, however, evidence of low-spin  $d^8$  configurations embodied in  $\text{Cu}^{3+}$  ions, even without the presence of Jahn-Teller  $\text{Cu}^{2+}$  ions, has been reported [24,34]. The possibility of covalent transfer for the  $\text{Ni}^{3+(2+)}$  pair is therefore directly dependent on the density of  $\text{Ni}^{3+}$  ions and the fraction of  $\text{Ni}^{2+}$  ions induced into  $S = 0$  states by the host site tetragonal symmetry, enhanced by the Jahn-Teller effect of the neighboring  $\text{Ni}^{3+}$  ions.<sup>44</sup>

<sup>44</sup> Further evidence of low-spin  $\text{Ni}^{3+}$  and its attendant local distortions is offered by Goodenough et al. [36] in a footnote relating the findings of Bongers [27] with  $\text{NaNiO}_2$  and  $(\text{Li}_{0.95}\text{Ni}_{0.05})\text{NiO}_2$ .



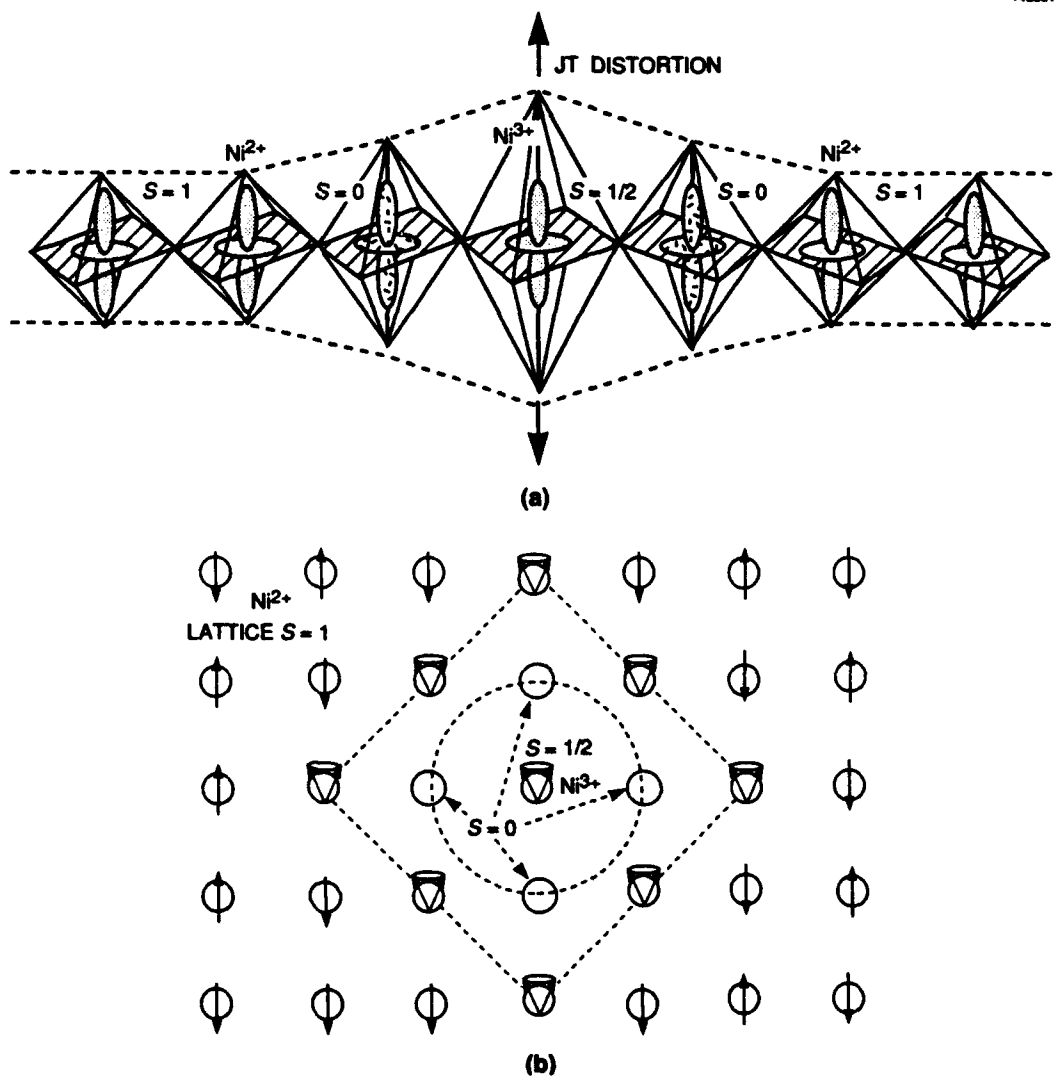


Figure F-3. Effects of Jahn-Teller distortion of  $\text{Ni}^{3+}$  (low spin) octahedral complex: (a) inducement of  $S = 0$  states on  $\text{Ni}^{2+}$  neighbors, and (b) magnetic frustration surrounding the low-spin  $\text{Ni}^{2+}$  grouping.

It should also be pointed out that interesting twists appear with this system. There are mixed magnetic exchange couplings and a less defined source of  $E_{\text{hop}}$  because  $\text{Ni}^{3+}$  has  $S_p = 1/2$ , and the  $\text{Ni}^{2+}$  lattice ions are a combination of  $S_L = 1$  and 0. In addition, with  $p$ -type polarons and the zero spin residing on the lattice ions, this system represents a case that is different from those in Table 5.

## APPENDIX G

### EFFECTIVE DIELECTRIC CONSTANT OF Sn

Another worthwhile exercise is to compare how the BCS and CET models relate the condensation energy to the thermodynamic critical field at  $T = 0$ . For the BCS theory [123],

$$\Delta G(0) = H_c(0)^2/8\pi = (1/2) N(0)\Delta(0)^2 \quad . \quad (G-1)$$

To evaluate  $H_c(0)$ , therefore,  $\Delta(0)$  may be determined experimentally, but  $N(0)$  is part of the coupling constant [see Equation (106)] for which there is no convenient measurement approach.

With CET, however,  $H_c(0)$  is related directly to  $\lambda_L(0)$  through  $n_s^e(0)$ . From Equations (62) and (70),

$$\begin{aligned} H_c(0)^2/8\pi &= (e^2V/4aK) n_s^e(0)^2 \quad , \\ &= (e^2V/4aK)(mc^2/4\pi e^2) \lambda_L(0)^{-2} \quad . \end{aligned} \quad (G-2)$$

The key parameter in Equation (G-2) is the electron screening or effective dielectric constant, which may now be expressed as

$$K = (1/8\pi) (mc^4a/e)^2 H_c(0)^{-2} \lambda_L(0)^{-4} \quad , \quad (G-3)$$

for  $V = a^3$ . From this relation the effective dielectric constant for Sn is calculated as  $K \approx 5 \times 10^6$ , for  $H_c(0) = 305$  Oe [124], and  $\lambda_L(0) = 360$  Å [125], and lattice parameter  $a \approx 2.7$  Å.

Another measurable parameter from which  $K$  may be estimated is the ratio  $\kappa = \lambda_L(0)/\xi_0(0)$ , expressed in Equation (98). After rearrangement and simplification,

$$K = (5.18 \times 10^9)^2 (a/\kappa)^2 \quad , \quad (G-4)$$

which yields  $K \approx 8 \times 10^5$  for  $\kappa = 0.156$  (based on the reported value for Sn [125] of  $\xi_0(0) = 2300$  Å), in qualitative agreement with the  $K$  value found from Equation (G-3).<sup>45</sup>

These results suggest that although electric fields in metals are screened, there are local internal contributions that propel current. This conclusion is consistent with the higher carrier velocities characteristic of the high- $T_c$  oxides, [through Equation (82)  $v_s \sim K^{-1/2}$ ] because lower  $K$  values mean higher internal fields.

---

<sup>45</sup>The value of  $K$  determined from Equation (G-3) is based on the assumption of a planar lattice (see footnote 27). Although the Sn lattice is not cubic, it is reasonable to expect that this  $K$  estimate should be smaller and, therefore, in closer agreement with the estimate determined from Equation (G-4).

## REFERENCES

1. G.F. Dionne, "Transition-Metal Oxide Superconductivity," MIT Lincoln Laboratory, Lexington, Mass., Technical Rep. 802 (20 April 1988). DTIC AD-A197069.
2. J.G. Bednorz and K.A. Müller, "Possible high  $T_c$  superconductivity in the Ba-La-Cu-O system," *Z. Phys. B* **64**, 189 (1986); also J.G. Bednorz, K.A. Müller, and M. Takashige, "Superconductivity in alkaline earth-substituted  $\text{La}_2\text{CuO}_{4-y}$ ," *Science* **236**, 73 (1987).
3. M.K. Wu, J.R. Ashburn, C.J. Torng, P.H. Hor, R.L. Meng, L. Gao, Z.J. Huang, Y.Q. Wang, and C.W. Chu, "Superconductivity at 93 K in a new mixed-phase Y-Ba-Cu-O compound system at ambient pressure," *Phys. Rev. Lett.* **58**, 908 (1987).
4. J.M. Tarascon, L.H. Greene, W.R. McKinnon, G.W. Hull, and T.H. Geballe, "Superconductivity at 40 K in the oxygen-defect perovskites  $\text{La}_{2-x}\text{Sr}_x\text{CuO}_{4-y}$ ," *Science* **235**, 1373 (1987).
5. R.J. Cava, B. Batlogg, R.B. van Dover, D.W. Murphy, S. Sunshine, T. Siegrist, J.P. Remeika, E.A. Reitman, S. Zahurak, and G.P. Espinosa, "Bulk superconductivity at 91 K in single-phase oxygen-deficient perovskite  $\text{Ba}_2\text{YCu}_3\text{O}_{9-\delta}$ ," *Phys. Rev. Lett.* **58**, 1676 (1987).
6. M.A. Subramanian, C.C. Torardi, J.C. Calabrese, J. Gopalakrishnan, K.J. Morrissey, T.R. Askew, R.B. Flippen, U. Chowdhry, and A.W. Sleight, "A new high-temperature superconductor:  $\text{Bi}_2\text{Sr}_{3-x}\text{Ca}_x\text{Cu}_2\text{O}_{8+y}$ ," *Science* **239**, 1015 (1988).
7. J.B. Goodenough, "Metallic oxides," *Prog. Solid State Chem.* **5**, 145 (1972).
8. J. Bardeen, L.N. Cooper, and J.R. Schrieffer, "Microscopic theory of superconductivity," *Phys. Rev.* **106**, 162 (1957); also "Theory of superconductivity," *Phys. Rev.* **108**, 1175 (1957).
9. F. London and H. London, "Supraconductivity and diamagnetism," *Physica* **2**, 341 (1935); also F. London, *Superfluids*, vol. 1, New York: John Wiley & Sons (1950).
10. F. Bloch, cited in London, *Superfluids*, p. 143.
11. A.B. Pippard, "An experimental and theoretical study of the relation between magnetic field and current in a superconductor," *R. Soc. London Ser. A* **216**, 547 (1953).
12. V.L. Ginsburg and L.D. Landau, "On the theory of superconductivity," *Zh. Eksp. Terr. Fiz.* **20**, 1064 (1950).
13. H. Fröhlich in *Polarons and Excitons*, C.G. Kuper and G.D. Whitfield (eds.), Edinburgh and London: Oliver and Boyd (1963), p. 1.
14. T. Holstein, "Studies of polaron motion. Part I. The molecular-crystal model," *Ann. Phys.* **8**, 325 (1959).
15. R.J.D. Tilley, *Defect Crystal Chemistry and Its Applications*, Glasgow and London: Blackie (1987), Chapter 6.
16. E.J.W. Verwey, P.W. Haaijman, F.C. Romeijn, and G.W. van Oosterhout, "Controlled-valency semiconductors," *Philips Res. Rep.* **5**, 193 (1950).

17. C. Zener, "Interaction between the d-shells in the transition metals. II. Ferromagnetic compounds of manganese with perovskite structure," *Phys. Rev.* **82**, 403 (1951).
18. P.-G. de Gennes, "Effects of double exchange in magnetic crystals," *Phys. Rev.* **118**, 141 (1960).
19. M.M. Schieber, *Experimental Magnetochemistry*, New York: John Wiley & Sons (1967), Chapters 4 and 6.
20. R.R. Heikes and W.D. Johnston, "Mechanism of conduction in Li-substituted transition metal oxides," *J. Chem. Phys.* **26**, 582 (1957).
21. M.I. Klinger and A.A. Samokhvalov, "Electron conduction in magnetite and ferrites," *Phys. Status Solidi B* **79**, 9 (1977).
22. C. Kittel, *Quantum Theory of Solids*, New York: John Wiley & Sons (1963), Chapter 7.
23. F.C. Brown in *Polarons and Excitons*, p. 323.
24. J.B. Goodenough, G. Demazeau, M. Pouchard, and P. Hagenmuller, "Sur une nouvelle phase oxygénée du cuivre +III: SrLaCuO<sub>4</sub>," *J. Solid State Chem.* **8**, 325 (1973).
25. J.B. Goodenough, *Magnetism and the Chemical Bond*, New York: Interscience Publishers, John Wiley & Sons (1963), p. 66.
26. P.W. Anderson, "New approach to the theory of superexchange interactions," *Phys. Rev.* **115**, 2 (1959).
27. P.F. Bongers, "Structure and Magnetic Properties of Several Complex Oxides of the Transition Elements," University of Leiden thesis (1957).
28. A.J. Springthorpe, I.G. Austin, and B.A. Austin, "Hopping conduction in Li<sub>x</sub>Ni<sub>1-x</sub>O crystals at low temperatures," *Sol. State Commun.* **3**, 143 (1965).
29. G.F. Dionne, "Theory of Co<sup>2+</sup> exchange isolation in ferrimagnetic spinels and garnets," *J. Appl. Phys.* **64**, 1323 (1988).
30. G.F. Dionne, "Molecular field coefficients of substituted yttrium iron garnets," *J. Appl. Phys.* **41**, 4874 (1970).
31. G.F. Dionne, "Magnetic frustration in high-T<sub>c</sub> superconductors," *J. Appl. Phys.* **69**, 5194 (1991).
32. A.M. George, I.K. Gopalakrishnan, and M.D. Karkhanavla, "Electrical conductivity of Ln<sub>2</sub>CuO<sub>4</sub> compounds," *Mater. Res. Bull.* **9**, 721 (1974).
33. L.E. Orgel, *An Introduction to Transition-Metal Chemistry: Ligand-Field Theory*, 1st Ed., New York: John Wiley & Sons (1960), p. 63.
34. G. Demazeau, C. Parent, M. Pouchard, and P. Hagenmuller, "Sur deux nouvelles phases oxygénées du cuivre trivalent: LaCuO<sub>3</sub> et La<sub>2</sub>Li<sub>0.50</sub>Cu<sub>0.50</sub>O<sub>4</sub>," *Mater. Res. Bull.* **7**, 913 (1972).
35. F.J. Morin, "Electrical properties of NiO," *Phys. Rev.* **93**, 1199 (1954).
36. J.B. Goodenough, D.G. Wickham, and W.J. Croft, "Some magnetic and crystallographic properties of the system Li<sub>x</sub><sup>+</sup>Ni<sub>1-2x</sub><sup>++</sup>Ni<sub>x</sub><sup>+++</sup>O," *J. Phys. Chem. Sol.* **5**, 107 (1958).

37. Z. Kakol, J. Spalek, and J.M. Honig, "Superconductivity and antiferromagnetism in  $\text{La}_{2-x}\text{Sr}_x\text{NiO}_4$ ," *J. Sol. State Chem.* **79**, 288 (1989).
38. G. Blasse, "Magnetic properties of mixed metal oxides containing trivalent cobalt," *J. Appl. Phys.* **36**, 879 (1965).
39. M. Pardavi-Horváth, A. Thavendrarajah, P.E. Wigen, and P. DeGasperis, "Canted ferrimagnetism in  $\text{Ca}^{2+}\text{Sc}^{3+}$  substituted yttrium-iron-garnet," *J. Appl. Phys.* **64**, 5656 (1988).
40. J.I. Budnick, B. Chamberland, D.P. Yang, Ch. Neidermayer, A. Golnik, E. Recknagel, M. Rossmanith, and A. Weidinger, "Dependence of the Néel-temperatures of  $\text{La}_2\text{CuO}_4$  on Sr-doping studied by muon spin rotation," *Europhys. Lett.* **5**, 651 (1988).
41. J.M. Tranquada, "Antiferromagnetism in  $\text{YBa}_2\text{Cu}_3\text{O}_{6+x}$ ," *J. Appl. Phys.* **64**, 6071 (1988).
42. J.B. Torrance, Y. Tokura, A.I. Nazzari, A. Bezing, T.C. Huang, and S.S.P. Parkin, "Anomalous disappearance of high- $T_c$  superconductivity at high hole concentration in metallic  $\text{La}_{2-x}\text{Sr}_x\text{CuO}_4$ ," *Phys. Rev. Lett.* **61**, 1127 (1988).
43. J.B. Goodenough and J.M. Longo, *Crystallographic and Magnetic Properties of Perovskite-Related Compounds*, vol. 4, New York: Springer-Verlag (1970), p. 126; also Goodenough, "Metallic Oxides," p. 245.
44. C.J. Ballhausen, *Introduction to Ligand Field Theory*, New York: McGraw-Hill (1962).
45. C.J. Ballhausen and H.B. Gray, *Molecular Orbital Theory*, New York: W.A. Benjamin, Inc. (1964).
46. C.J. Ballhausen and H.B. Gray, *Molecular Electronic Structures*, Reading, Mass.: The Benjamin/Cummings Publishing Co. (1980).
47. Goodenough, "Metallic Oxides," p. 277.
48. T. Holstein, "Studies of polaron motion," p. 335.
49. R.J. Cava, B. Batlogg, R.B. van Dover, et al., "Superconductivity at 60 K in  $\text{La}_{2-x}\text{Sr}_x\text{CaCu}_2\text{O}_6$ : The simplest double-layer cuprate," *Nature* **345**, 602 (1990).
50. D.C. Johnston, A.J. Jacobson, J.M. Newsam, J.T. Lewandowski, D.P. Goshorn, D. Xie, and W.B. Yelon, "Variation in the structural, magnetic, and superconducting properties of  $\text{YBa}_2\text{Cu}_3\text{O}_{7-x}$  with oxygen content," in *Chemistry of High-Temperature Superconductors*, D.L. Nelson, M.S. Whittingham, and T.F. George (eds.), Washington, D.C.: American Chemical Society (1987), p. 136.
51. B. Batlogg, R.J. Cava, C.H. Chen, et al., "Bulk superconductivity at 60 K in oxygen-deficient  $\text{Ba}_2\text{YCu}_3\text{O}_{7-\delta}$  and oxygen isotope effect in  $\text{La}_{1.85}\text{Sr}_{0.15}\text{O}_4$ ," in *Novel Superconductivity*, S.A. Wolf and V.Z. Kresin (eds.), New York: Plenum Press (1987), p. 653.
52. I.D. Brown, "A determination of the oxidation states and internal stresses in  $\text{Ba}_2\text{YCu}_3\text{O}_x$ ,  $x = 6-7$  using bond valences," *J. Solid State Chem.* **82**, 122 (1989). In Dionne ("Transition-Metal Oxide Superconductivity"), a linear estimate of polaron density predicted  $x = 0.25y - 1.5$  for  $\text{YBa}_2\text{Cu}_3\text{O}_y$ , yielding  $x = 0.1$  for  $y = 6.4$ . Analysis of data by Brown's bond valence sum method suggests a slightly lower value of  $x$ .

53. T.K. Worthington, W.J. Gallagher, and T.R. Dinger, "Anisotropic nature of high-temperature superconductivity in single-crystal  $\text{Y}_1\text{Ba}_2\text{Cu}_3\text{O}_{7-x}$ ," *Phys. Rev. Lett.* **59**, 1160 (1987).
54. N. Miyata, "Electric conduction of ferrites containing  $\text{Fe}^{2+}$ -ions," *J. Phys. Soc. Japan*, **16**, 206 (1961). The  $(1-x)/x$  dependence in Miyata's Equation (2) was found empirically for the resistivity of ferrites. The probability arguments used here may explain the origin of this factor.
55. G.F. Dionne, "Spin states and electronic conduction in Ni oxides," *J. Appl. Phys.* **67**, 4561 (1990).
56. G.F. Dionne, "Normal-state resistivity diagnostic for high- $T_c$  superconductors," *IEEE Trans. Magn.* **27**, 1190 (1991).
57. G.F. Dionne, "Resistivity of multiphase high- $T_c$  superconductors," *J. Appl. Phys.* **69**, 4883 (1991).
58. R. Cava, B. Batlogg, J.J. Krajewski, et al., "Superconductivity near 70 K in a new family of layered copper oxides," *Nature* **336**, 211 (1988).
59. Y.T. Huang, R.S. Liu, W.N. Wang, and P.T. Wu, "Bulk superconductivity of the  $(\text{Ti}_{0.5}\text{Bi}_{0.5})(\text{Ca}_{1-x}\text{Y}_x)\text{Sr}_2\text{Cu}_2\text{O}_y$  system," *Japan. J. Appl. Phys.* **28**, L1514 (1989).
60. W.D. Kingery, *Introduction to Ceramics* (1st Ed.), New York: John Wiley & Sons (1960), p. 682.
61. A.C. Westerheim, L.S. Yu-Jahnes, and A.C. Anderson, "Off-axis magnetron sputtering of YBCO films: The influence of atomic oxygen," *IEEE Trans. Magn.* **27**, 1001 (1991).
62. C. Gorter and H.B.G. Casimir, "Supraconductivity," *Physica* **1**, 306 (1934).
63. T. Van Duzer and C.W. Turner, *Principles of Superconductive Devices and Circuits*, New York: Elsevier (1981), pp. 128-131.
64. D.E. Oates and A.C. Anderson, "Surface impedance measurements of  $\text{YBa}_2\text{Cu}_3\text{O}_{7-x}$  thin films in stripline resonators," *IEEE Trans. Magn.* **27**, 867 (1991).
65. D.E. Oates, A.C. Anderson, and P.M. Mankiewich, "Measurement of the surface resistance of  $\text{YBa}_2\text{Cu}_3\text{O}_{7-x}$  thin films using stripline resonators," *J. Superconductivity* **3**, 251 (1990).
66. D.M. Sheen, S.M. Ali, D.E. Oates, R.S. Withers, and J.A. Kong, "Current distribution, resistance, and inductance for superconducting strip transmission lines," *IEEE Trans. Appl. Superconductivity* **1**, 108 (1991).
67. London, *Superfluids*, p. 150.
68. G. Aeppli, R.J. Cava, E.J. Ansaldo, J.H. Brewer, S.R. Kreitzman, G.M. Luke, D.R. Noakes, and R.F. Kiefl, "Magnetic penetration depth and flux-pinning effects in high- $T_c$  superconductor  $\text{La}_{1.85}\text{Sr}_{0.15}\text{CuO}_4$ ," *Phys. Rev.* **B35**, 7129 (1987).
69. W.J. Kossler, J.R. Kempton, X.H. Yu, H.E. Schone, Y.J. Uemura, A.R. Moodenbaugh, M. Suenaga, and C.E. Stronach, "Magnetic field penetration depth of  $\text{La}_{1.85}\text{Sr}_{0.15}\text{CuO}_4$  measured by muon spin relaxation," *Phys. Rev.* **B35**, 7133 (1987).
70. M. Tinkham, *Introduction to Superconductivity*, Malabar, Fla.: Robert E. Krieger Publishing Co., Inc. (1980), p. 81.

71. S.M. Anlage, B.W. Langley, H.J. Snortland, C.B. Eom, T.H. Geballe, and M.R. Beasley, "Magnetic penetration depth measurements with the microstrip resonator technique," *J. Superconductivity* **3**, 311 (1990).
72. B.W. Langley, S.M. Anlage, R.F.W. Pease, and M.R. Beasley, "Magnetic penetration depth measurements of superconducting thin films by a microstrip resonator technique," *Rev. Sci. Instrum.* **62**, 1801 (1991).
73. C. Kittel, *Introduction to Solid State Physics*, 3rd Ed., New York: John Wiley & Sons (1966), p. 352.
74. London, *Superfluids*, p. 20.
75. N.E. Phillips, "Heat capacity of aluminum between 0.1 K and 4.0 K," *Phys. Rev.* **114**, 676 (1959).
76. N.E. Phillips, "Low-temperature heat capacities of gallium, cadmium, and copper," *Phys. Rev.* **134**, A385 (1964).
77. Tinkham, *Intro. Superconductivity*, p. 118.
78. D. Schoenberg, *Superconductivity*, Cambridge University Press (1960), p. 176.
79. T.K. Hunt, "Critical-current behavior in narrow thin-film superconductors," *Phys. Rev.* **151**, 325 (1966).
80. J.R. Clem, B. Bumble, S.I. Raider, W.J. Gallagher, and Y.C. Shih, "Ambegaokar-Baratoff-Ginzburg-Landau crossover effects on the critical current density of granular superconductors," *Phys. Rev.* **B35**, 6637 (1987).
81. A. Inam, X.D. Wu, L. Nazar, et al., "Microwave properties of highly oriented  $\text{YBa}_2\text{Cu}_3\text{O}_{7-x}$  thin films," *Appl. Phys. Lett.* **56**, 1178 (1990).
82. H.S. Lessure, S. Simizu, P.J. Kung, B.A. Baumert, S.G. Sankar, and M.E. McHenry, "Intergranular  $J_c$  determination in toroidal high temperature superconductors using a soft-core closed magnetic circuit," *IEEE Trans. Magn.* **27**, 942 (1991).
83. Tinkham, *Intro. Superconductivity*, p. 124.
84. J. Mannhart, P. Chaudhari, D. Dimos, C.C. Tsuei, and T.R. McGuire, "Critical currents in [001] grains and across their tilt boundaries in  $\text{YBa}_2\text{Cu}_3\text{O}_7$  films," *Phys. Rev. Lett.* **61**, 2476 (1988).
85. Tinkham, *Intro. Superconductivity*, p. 7.
86. Tinkham, *Intro. Superconductivity*, p. 11.
87. Tinkham, *Intro. Superconductivity*, p. 113.
88. A.A. Abrikosov, "On the magnetic properties of superconductors of the second group," *Soviet Phys. JETP* **5**, 1174 (1957).
89. Kittel, *Solid State Physics*, p. 364.
90. M. Tinkham, "Effect of fluxoid quantization on transitions of superconducting films," *Phys. Rev.* **129**, 2413 (1963).

91. A. Yamagishi, H. Fuke, K. Sugiyama, M. Date, Y. Tajima, and M. Hikata, "High field measurements of whole profile of  $H_{c2}$  and normal resistivity of high- $T_c$  single crystal superconductors," *Physica B* **155**, 174 (1989).
92. D.K. Finnemore, M.M. Fang, J.R. Clem, R.W. McCallum, J.E. Ostenson, L. Ji, and P. Klavins, "Thermodynamic critical field of  $Y_1Ba_2Cu_3O_7$ ," *Novel Superconductivity*, p. 627.
93. A.W. Sleight, "Chemistry of high-temperature superconductors," *Science* **242**, 1519 (1988).
94. W. Low, *Paramagnetic Resonance in Solids*, Solid State Physics Suppl. 2, F. Seitz and D. Turnbull (eds.), New York: Academic Press (1960), p. 101.
95. Orgel, *Transition-Metal Chemistry Ligand Field*, p. 35.
96. J.M. Tarascon, L.H. Greene, B.G. Bagley, et al., "Chemical doping and physical properties of the new high temperature superconducting perovskites," *Novel Superconductivity*, p. 705.
97. Orgel, *Transition-Metal Chemistry Ligand Field*, p. 66.
98. Y. Fujiwara, S. Hirata, M. Nishikubo, T. Kobayashi, H. Nakayama, and H. Fujita, "Local atomic configuration and Auger valence electron spectra in BiSrCaCuO single crystals," *IEEE Trans. Magn.* **27**, 1166 (1991).
99. C.C. Torardi, M.A. Subramanian, J.C. Calabrese, J. Gopalakrishnan, K.J. Morrissey, T.R. Askew, R.B. Flippen, U. Chowdhry, and A.W. Sleight, "Crystal structure of  $Tl_2Ba_2Ca_2Cu_3O_{10}$ , a 125 K superconductor," *Science* **240**, 631 (1988).
100. Y. Tokura, H. Takagi, and S. Uchida, "A superconducting copper oxide compound with electrons as the charge carriers," *Nature* **337**, 345 (1989).
101. M.G. Smith, A. Manthiram, J. Zhou, J.B. Goodenough, and J.T. Markert, "Electron-doped superconductivity at 40 K in the infinite-layer compound  $Sr_{1-y}Nd_yCuO_2$ ," *Nature* **351**, 549 (1991).
102. R.J. Cava, B. Batlogg, J.J. Krajewski, R. Farrow, L.W. Rupp, Jr., A.E. White, K. Short, W.F. Peck, and T. Kometani, "Superconductivity near 30 K without copper: The  $Ba_{0.6}K_{0.4}BiO_3$  perovskite," *Nature* **332**, 814 (1988).
103. D.G. Hinks, B. Dabrowski, J.D. Jorgensen, A.W. Mitchell, D.R. Richards, S. Pei, and D. Shi, "Synthesis structure and superconductivity in the  $Ba_{1-x}K_xBiO_{3-y}$  system," *Nature* **333**, 836 (1988).
104. A.W. Sleight, J.L. Gillson, and P.E. Bierstedt, "High-temperature superconductivity in the  $BaPb_{1-x}Bi_xO_3$  system," *Sol. State Commun.* **17**, 27 (1975).
105. J.F. Schooley, W.R. Hosler, and M.L. Cohen, "Superconductivity in semiconducting  $SrTiO_3$ ," *Phys. Rev. Lett.* **12**, 474 (1964).
106. D.C. Johnston, H. Prakash, W.H. Zachariasen, and R. Viswanathan, "High temperature superconductivity in the Li-Ti-O ternary system," *Mater. Res. Bull.* **8**, 777 (1973).
107. Orgel, *Transition-Metal Chemistry Ligand Field*, p. 75.
108. B.T. Matthias, "Superconductivity in the periodic system," *Progress in Low-Temperature Physics*, vol. 11, C.J. Gorter (ed.), New York: Interscience Publishers, Inc. (1957), Chapter V.



109. H. Fröhlich, "Theory of the superconducting state. I. The ground state at the absolute zero of temperature," *Phys. Rev.* **79**, 845 (1950).
110. H. Fröhlich, "Isotope effect in superconductivity," *Proc. Phys. Soc.* **A63**, 778 (1952).
111. Tinkham, *Superconductivity*, pp. 28 and 34.
112. Kittel, *Solid State Physics*, p. 387.
113. B. Batlogg, R.J. Cava, A. Jayarman, et al., "Isotope effect in the high- $T_c$  superconductors  $\text{Ba}_2\text{YCu}_3\text{O}_7$  and  $\text{Ba}_2\text{EuCu}_3\text{O}_7$ ," *Phys. Rev. Lett.* **58**, 2333 (1987).
114. D.C. Johnston, "Superconducting and normal state properties of  $\text{Li}_{1+x}\text{Ti}_{2-x}\text{O}_4$  spinel compounds. I. Preparation, crystallography, superconducting properties, electrical resistivity, dielectric behavior, and magnetic susceptibility," *J. Low Temp. Phys.* **25**, 145 (1976).
115. M.R. Harrison, P.P. Edwards, and J.B. Goodenough, "The superconductor-semiconductor transition in the  $\text{Li}_{1+x}\text{Ti}_{2-x}\text{O}_4$  spinel system," *Phil. Mag.* **B52**, 679 (1985).
116. P.P. Edwards, R.G. Egdell, I. Fragala, J.B. Goodenough, M.R. Harrison, A.F. Orchard, and E.G. Scott, "A study of the spinel materials  $\text{LiTi}_2\text{O}_4$  and  $\text{Li}_{4/3}\text{Ti}_{5/3}\text{O}_4$  by photoelectron spectroscopy," *J. Sol. State Chem.* **54**, 127 (1984).
117. Ballhausen and Gray, *Molecular and Electronic Structures*, Chapter 2.
118. *Handbook of Chemistry and Physics*, 72nd Ed., Boca Raton, Fla.: CRC Press (1991-92).
119. J.W. Mellor, *Inorganic and Theoretical Chemistry*, vol. 1, New York: Longmans (1960), p. 930.
120. D.S. McClure, "Electronic spectra of molecules and ions in crystals. Part II. Spectra of ions in crystals," *Sol. State Phys.* **9**, 426 (1959).
121. Goodenough, "Metallic oxides," Section V.A.
122. E.J.W. Verwey and E.L. Heilmann, "Physical properties and cation arrangement of oxides with spinel structures," *J. Chem. Phys.* **15**, 174 (1947).
123. Tinkham, *Intro. Superconductivity*, p. 30.
124. B.W. Roberts, "Survey of superconductive materials and critical evaluation of selected properties," *J. Chem. Phys. Ref. Data* **5**, 581 (1976).
125. J. Bardeen and J.R. Schrieffer, "Recent developments in superconductivity," *Prog. Low Temp. Phys.*, C.J. Gorter (ed.), Amsterdam: North Holland (1961).

# REPORT DOCUMENTATION PAGE

Form Approved  
OMB No. 0704-0188

Public reporting burden for this collection of information is estimated to average 1 hour per response, including the time for reviewing instructions, searching existing data sources, gathering and maintaining the data needed, and completing and reviewing the collection of information. Send comments regarding this burden estimate or any other aspect of this collection of information, including suggestions for reducing the burden, to Washington Headquarters Services, Directorate for Information Operations and Reports, 1215 Jefferson Davis Highway, Suite 1204, Arlington, VA 22202-4302, and to the Office of Management and Budget, Paperwork Reduction Project (0704-0188), Washington, DC 20503.

1. AGENCY USE ONLY (Leave blank)		2. REPORT DATE 19 June 1992		3. REPORT TYPE AND DATES COVERED Technical Report	
4. TITLE AND SUBTITLE  Covalent Electron Transfer Theory of Superconductivity				5. FUNDING NUMBERS  C — F19628-90-C-0002 PE — 63250C PR — 227	
6. AUTHOR(S)  Gerald F. Dionne					
7. PERFORMING ORGANIZATION NAME(S) AND ADDRESS(ES)  Lincoln Laboratory, MIT P.O. Box 73 Lexington, MA 02173-9108				8. PERFORMING ORGANIZATION REPORT NUMBER  TR-885	
9. SPONSORING/MONITORING AGENCY NAME(S) AND ADDRESS(ES)  Air Force Systems Command Andrews AFB Washington, DC 20334				10. SPONSORING/MONITORING AGENCY REPORT NUMBER  ESD-TR-91-092	
11. SUPPLEMENTARY NOTES  None					
12a. DISTRIBUTION/AVAILABILITY STATEMENT  Approved for public release; distribution is unlimited.				12b. DISTRIBUTION CODE	
13. ABSTRACT (Maximum 200 words)  Following a brief review of phenomenological origins, a comprehensive discussion of the physics and chemistry of superconducting perovskite systems is presented. The covalent transfer theory developed in 1987, which was based on the normal-state electrical behavior of large polarons, is refined to include a molecular-orbital analysis of the electron transfer probability (assumed to be unity in the original model). An examination of the local magnetic superexchange interactions between $\text{Cu}^{2+}\text{-O}^{2-}\text{-Cu}^{2+}$ ions indicates that preconditions for the onset of superconduction include a breakdown in static antiferromagnetic order to eliminate the exchange contribution to the polaron trap energy. The occurrence of magnetic frustration is explained by the existence of mobile polaron ions in zero-spin states. By comparing the covalent transfer and electron hopping mechanisms, a new "two-fluid" function is derived for the temperature-dependent distribution of normal and superelectrons. From the population of carriers that are not thermally activated (hopping), condensation to the superconducting state occurs in the form of dynamic ferroelectric chains of ordered dipoles, with the condensation energy directly proportional to the square of the supercarrier population. With this relation, it is then possible to derive direct expressions between the measurable superconduction parameters and the effective supercarrier density as functions of temperature. Based on these concepts, computed values of critical temperature, magnetic field, and current density, as well as specific heat, penetration depth, coherence length, and microwave surface resistance all compare favorably with measured values, both in magnitude and as functions of temperature. The reported superconducting properties of the various high- $T_c$ systems are then examined in the context of this new model. To contrast with low- $T_c$ metals, the covalent transfer concept is applied qualitatively to systems with conduction electrons. Finally, the various topics are summarized and conclusions drawn concerning the limitations and applicability of existing superconductors, as interpreted by the covalent transfer theory.					
14. SUBJECT TERMS high temperature superconductivity polaron trapping energy magnetic frustration electron hopping			covalent electron transfer multiphase superconductors microwave surface resistance ferroelectric condensation		15. NUMBER OF PAGES 178
			parameter temperature dependences cation site distributions metal superconductivity dynamic ferroelectricity		16. PRICE CODE
17. SECURITY CLASSIFICATION OF REPORT Unclassified	18. SECURITY CLASSIFICATION OF THIS PAGE Unclassified	19. SECURITY CLASSIFICATION OF ABSTRACT Unclassified	20. LIMITATION OF ABSTRACT SAR		